Technische Universität München
Institut für Energietechnik

Lehrstuhl für Thermodynamik

Development of a Presumed Function Method of Moments with Application to Polydisperse Sprays

João Neuenschwander Escosteguy Carneiro

Vollständiger Abdruck der von der Fakultät für Maschinenwesen der Technischen Universität München zur Erlangung des akademischen Grades eines

DOKTOR – INGENIEURS

genehmigten Dissertation.

Vorsitzender:
Univ.-Prof. Dr.-Ing. Andreas Kremling
Prüfer der Dissertation:
1. Univ.-Prof. Wolfgang H. Polifke, PhD (CCNY)
2. Univ.-Prof. Dr.-Ing. Dominique Thévenin, Otto-von-Guericke-Universität Magdeburg

Die Dissertation wurde am 08.02.2011 bei der Technischen Universität München eingereicht und durch die Fakultät für Maschinenwesen am 18.05.2011 angenommen.

Acknowledgments

First of all, I would like to express my sincere gratitude to Prof. Polifke. I am not only thankful for his guidance throughout the course of the work, but also for the freedom and trust he gave me when entering this field of research. I am also grateful for the opportunity of acting as a teaching assistant at his lecture "Fundamentals of Multiphase Flows". I also thank Prof. Dr. -Ing. Dominique Thévenin for taking part in the defense committee and Prof. Dr. -Ing. Andreas Kremling for kindly accepting to chair the examination process.

My special thanks goes to Dipl.-Ing. Volker Kaufmann, whose collaboration greatly contributed to the development of this work. I also thank my other office colleagues Dr.-Ing. Thomas Steinhilber, Dipl.-Ing. Victor Fischer, Dipl.-Ing. Patrick Dems and Dipl.-Ing. Christoph Jörg for the motivating atmosphere. I am further indebted to all undergraduate students who, one way or the other, collaborated with workforce, ideas and discussions.

My gratitude goes also to Mrs. Bassett and Mrs. Schulz-Reichwald for the competent care of administrative tasks. Thanks are extended to all other colleagues at the Chair of Thermodynamics for contributing to the pleasant work environment.

Needless to say, I would certainly not be where I stand today without the unconditional support and love from my family – mom, dad and sister: you have been there for me consistently, through good and bad times. I truly thank you with all my heart.

An undeniable portion of success of this work goes also to my wife, Vanessa. First, for embracing our journey in Germany with such courage, but also for her love, companionship and patience with the many nights and weekends that occupied me for the completion of this thesis.

Last but not least, the birth of my lovely daughter Mariana gave me just the extra strength necessary to complete this written work. Thanks also to you, Mari!

This project was funded by the Brazilian National Council for Scientific and

Technological Development (CNPq), whose financial support is gratefully acknowledged .

To my wife Vanessa and daughter Mariana.

Contents

Abstract

Dispersed flows are very common in nature and are relevant to a great variety of industrial applications. Ranging from cloud physics in meteorology to spray combustion in turbines and engines, the simulation of these types of flows has been extensively used as a tool for understanding the basic phenomena involved, as well as the design and optimization of engineering processes. Yet challenges remain on the development of more efficient methods, which can also be applied to real, complex configurations, at the same type with an appropriate level of description and a reasonable degree of accuracy.

Recently, there has been a big effort towards the development of alternatives to the conventional Lagrangian or Multi-Fluid techniques for dispersed flows. Challenges are mainly associated to the multi-size/-velocity/-temperature treatment of the population of particles and closure for exchange terms with the continuous phase.

In the present work, a Method of Moments (PMOM) based on presumed functions for the particle size distribution and a novel relaxation approach for the size-velocity correlation was derived and tested for different configurations. The dependence of particle-velocity on -size is expressed as a first order expansion in terms of particle relaxation time around a reference velocity, which is obtained from the transport equations for particle phase momentum. A simple closure for the energy equation is developed by assuming that all particles have the same temperature.

The model is applied to a series of “proof-of-concept” test cases for polydisperse particle segregation using various reconstruction schemes involving Gamma and Beta distribution functions in order to study the effect of size-dependent particle velocity on particle and momentum transport. Cases comprising both small and large particle relaxation times are investigated, to which an extension of the relaxation approach is also proposed and tested. Results are compared to reference solutions computed with an Eulerian Multi-Fluid model.

A practical configuration consisting of a spray generated by an ultra-sonic atomizer was also assessed. Results for mono- and polydisperse simulations are compared to each other and to experimental data, for both non-evaporative and evaporative cases.

Zusammenfassung

In der Natur und Industrie treten sogenante disperse Strömungen sehr häufig auf. Sie sind durch die Koexistenz von Partikeln (Blasen, Tropfen oder Festpartikel) und einer kontinuierlichen Phase gekennzeichnet. Zahlreiche Anwendungen z.B. in der Meteorologie oder in der Energie- und Verfahrenstechnik belegen die hohe Relevanz der Materie. Die Entwicklung von effizienten und präzisen Simulationswerkzeugen gewinnt für die Beschreibung der Wolkenphysik oder die Optimierung und Auslegung von mit flüssigem Brennstoff betriebenen Turbinen und Motoren zunehmend an Bedeutung.

Lagrange'sche oder Multi-Fluid Modelle basieren auf einer Zerlegung des Partikelspektrums in diskrete Größenklassen. Um den damit verbundenen hohen Rechenaufwand zu vermeiden, wurden alternative Methoden zur Beschreibung der Dynamik der dispersen Phasen in letzter Zeit vermehrt untersucht. Diese Methoden basieren auf einer Beschreibung des Spektrums durch integrale Bilanzgrößen. Das Vorhandensein von Partikeln verschiedener Eigenschaften (Durchmesser, Geschwindigkeit, Temperatur) so wie die Schließung von Austauschtermen mit der kontinuierlichen Phase stellen hier eine besondere Herausforderung dar.

Diese Arbeit befasst sich mit der Herleitung und Verifizierung einer neuartigen, auf angenommenen Verteilungsfunktionen basierten Momentenmethode (PMOM) unter dem Paradigma der Euler'schen Betrachtungsweise der dispersen Phase. Mit Hilfe eines sogennanten Relaxationsansatzes wird die Abhängigkeit der Partikelgeschwindigkeit vom Partikeldurchmesser als Reihenentwicklung erster Ordnung im Relaxationszeitbereich näherungsweise beschrieben. Temperaturunterschiede zwischen den Partikeln werden vernachlässigt.

Das Modell wird in mehreren Testfällen zur polydispersen Partikelrelaxation, -entmischung und -sedimentation getestet, bei denen die Durchmesserabhängigkeit der Partikelgeschwindigkeit eine wichtige Rolle für Partikel- und Impulstransport spielt. Verschiedene Rekonstruktionsmethoden werden eingeführt, die sich nach der Form der Verteilungsfunktion (Gamma oder

Beta) und nach der Anzahl prognostischer Momente unterscheiden.

Zuletzt wird das Modell zur Beschreibung der Tropfenausbreitung und -verdampfung in einem Ultraschallzerstäuber angewendet und sowohl mit mono-dispersen (Zwei-Fluid Modell) Simulationsergebnissen als auch experimentellen Daten verglichen.

List of Figures

List of Tables

Nomenclature

Latin Characters

A	Surface area [m^2]
B	Beta function
$\mathbf{A}$	Force per unit mass in internal coordinate space [m/s^2]
C_0	Presumed function scaling parameter [$1/m^3$]
C_D	Drag coefficient [-]
c_p	Specific heat [J/kg-K]
C_t	Response coefficient [-]
C_k	Modified response coefficient [-]
D	Diameter [m]
f	Size distribution function [$1/m^4$]
$\tilde{f}$	Number density function [$1/m^3$]
$\boldsymbol{f}$	Fick's diffusive flux [m/s]
$\mathbf{F}$	Force [kg-m/s^2]
$\mathbf{g}$	Gravity [m/s^2]
G	Generation of turbulence kinetic energy [m^2/s^3]
h	Specific enthalpy [J/kg]
h_{tc}	Heat transfer coefficient [W/m^2-K]
h_m	Mass transfer coefficient [m/s]
i	Specific internal energy [J/kg]
I	Incomplete Beta function
$\boldsymbol{I}$	Unit tensor
k	Thermal conductivity [W/m-K]
l	Inter-particle spacing [m]
L	Latent heat [J/kg-K]

m	Particle mass [kg]
$\dot{m}$	Mass flow rate [kg/s]
$\mathbf{M}$	Momentum transfer term [kg/m^2-s]
$M^{(k)}$	Moment of order k [m^{k-3}]
N	Number of particles [-]
n	Number frequency distribution [-]
$\mathbf{n}$	Normal vector
p	Pressure [kg/m-s^2]
p	Gamma presumed function shape parameters [m]
p	Beta presumed function shape parameters [-]
q	Gamma and Beta presumed function shape parameters [-]
$\dot{Q}$	Heat transfer rate [J/s^2]
$\dot{q}$	Heat flux [W/m^2]
r	Radial coordinate [m]
$\mathbf{u}$	Velocity [m/s]
$\mathbf{u}_i$	Interface velocity [m/s]
$\mathbf{U}$	Mixture velocity [m/s]
$\mathbf{u}^{(k)}$	Transport velocity of $M^{(k)}$ [m/s]
$\mathbf{v}$	Center of mass velocity [m/s]
V	Volume [m^3]
S_d^k	Source term of turbulence kinetic energy [m^2/s^3]
S_d^ϵ	Source term of turbulence dissipation [m^2/s^4]
S_i	Interfacial area [m^2]
t	Time [s]
t	Beta function integration limit
T	Temperature [K]
T	Time interval
$\mathbf{x}$	Position [m]
X	Indicator function [-]
Y	Mass fraction [-]
W	Molar mass [g/mol]

Greek Characters

α	Volume fraction [-]
β	Response function parameter [-]
δ	Kronecker delta [-]
δ	Thickness [m]
Δ	Hankel-Hadamard determinant
ϵ	Turbulence dissipation [m^2/s^3]
ϕ	Property of the population of particles
Φ_v	Viscous dissipation [J/m^3]
Γ	Source term due to phase change
Γ	Gamma function
κ	Turbulence kinetic energy [m^2/s^2]
λ^*	Vaporization constant [m^2/s]
μ	Dynamic viscosity [kg/m-s]
ν	Kinematic viscosity [m^2/s]
Ψ	Arbitrary property of Eulerian phase
ρ	Density [kg/m^3]
τ	Relaxation time [s]
σ	Surface tension [$kg\ m^2/s^2$]
τ	Shear stress [$kg/m\text{-}s^2$]
ξ	Particle internal coordinate

Indices

∞	Free stream value
$\rightarrow 0$	Zero limit
0	Reference value for expansion
0	Initial value
α	Volume fraction
air	Air property
B	Body force
c	Continuous phase

d	Dispersed phase
eq	Equilibrium
D	Drag
$fuel$	Fuel property
F	Fluid
ϕ	Property of the population of particles
i	i-th particle class
$interp$	Interpolated value
k	Phase adjacent to interface
min	Minimum value
max	Maximum value
mix	Mixture property
$M^{(k)}$	Moment of order k
p	Particle property, as in $\mathbf{v}_p$
p	Pressure, as in $\mathbf{F}_p$
ref	Reference value
s	Directional coordinate
S	Surface
t	Total
T	Terminal value
v	Vapor
x	x coordinate
y	y coordinate

Superscripts

$*$	Characteristic quantity
$'$	Fluctuating quantity
$'$	Modified quantity
$''$	Flux quantity
$\cdot$	Quantity per unit time
eff	Effective property
(k)	Order of weighted average quantity

pt	pseudo-turbulence
t	Turbulent quantity
T	Transposed

Non-dimensional Parameters

B_m	Mass transfer number $[\frac{Y_S - Y_{v,\infty}}{1-Y_S}]$
Bi	Biot number $[h_{tc}D/2k_d]$
Le	Lewis number $[k/\rho c_p \mathscr{D}_{cd}]$
Nu	Nusselt number $[h_{tc}D/k]$
Pe	Peclet number [RePr]
Pr	Prandtl number $[\mu c_p/k]$
Re	Reynolds number $[\rho\|\mathbf{u}_c - \mathbf{v}\|D/\mu]$
Sc	Schmidt number $[\mu_c/\rho_c \mathscr{D}_{cd}]$
Sh	Sherwood number$[h_m D/\mathscr{D}_{cd}]$
St	Stokes number $[\tau/\tau_c]$

Abbreviations

CFD	Computational Fluid Dynamics
LHS	Left Hand Side
MOM	Method of Moments
PMOM	Presumed function Method of Moments
RHS	Right Hand Side

Operators

∇	Nabla operator
d	Lagrangian differential operator

D	Total differential operator
Δ	Variation of a given quantity
Π	Product operator
Σ	Sum operator
∂	Partial differential operator
$\cdot$	Inner product
$<>$	Volume average operator
$-$	Time average operator
$\tilde{}$	Phase average operator

Symbols

$\mathscr{D}_{cd}$	Binary diffusion coefficient [m^2/s]
$\mathscr{K}$	Coefficient of size-velocity correlation [1/m-s]
$\mathscr{V}$	Characteristic volume [m^3]

1 Introduction

1.1 Motivation

A large number of flows in nature and industry involve the simultaneous presence of continuous and dispersed phases. Their applications range from environmental sciences to numerous engineering problems. Several examples can be cited such as bubbly flows in aerated stirred vessels, atmospheric aerosols, cloud physics, oil and gas transport in pipelines, spray combustion, etc.

In contrast to other types of multiphase flows, such as those involving free surfaces for example, dispersed multiphase flows present a very distinguished characteristic: one is normally not interested in the detailed dynamics of the interface between continuous and dispersed phases. Apart from very few exceptions, the detailed resolution of exchange processes at the interfaces of several particles is either not relevant or demand a huge computational effort, such that it is normally advantageous to implicitly assume that a distribution of spherical drops, bubbles or solid particles exists, which evolves with time and space depending on the flow conditions.

As a result of the interaction between the different phases such flows are very difficult to describe theoretically. While for single-phase flows Computational Fluid Dynamics (CFD) has already a long history and it is nowadays a standard tool used both by researchers and engineers, the application of CFD in the design and optimisation of multiphase systems is rather young. Even though a lot of effort has been spent towards a better description of the highly complex physics involved, neither the modeling capabilities nor the numerical techniques have achieved the desired level of maturity.

Hence, it is clear that there is still need to further improve current simulation methods for the engineering design process involving these types of flows.

Some basic aspects concerning this task are given below:

- One should not underestimate the importance of a careful verification of new developed models in simple test cases in order to assess the properties of the system and confirm the expected behavior against reference solutions. Only then it makes sense to apply the simulation method to complex configurations and validate it against experimental data.
- Extensive verification against experiments in practical configurations is an essential, if not the most important step.
- It is very important to develop models that are also attractive in terms of computational costs, which often means to find a compromise between simplicity and accuracy.
- Last but not least, with the advent of parallel computing, the robust performance in highly parallelised systems became in the last years an almost indispensable characteristic, specially for Large Eddy Simulations (LES) and Direct Numerical Simulations (DNS) of turbulent multiphase flows.

A particularly challenging class of multiphase flows occur in spray applications. They have been the subject of intense investigation over the past decades, having also driven the improvement on the description of dispersed flows in a general way[1]. Understanding and predicting the behavior of sprays is a crucial aspect to the process of energy generation through liquid fuels. While emerging technologies explore the potential of renewable energies, one way to reduce fossil fuel consumption is the optimization of existing processes which are present, for example, in gas turbines and Diesel engines. Combustion efficiency and emission characteristics depend strongly on the fuel-air distribution over the combustion chamber's cross section. This is achieved through the dispersion and mixing of the atomized fuel, which is a result of

[1] This occurs specially for flows involving solid particles, but methods for the description of dispersed bubbly flows are also in many aspects similar, specially with regard to bubble population dynamics, eventhough relevant forces that influence bubble transport may differ

the turbulent transport of droplets by the gas phase as well as a complex population dynamics influenced by collisions, break-up, coalescence and evaporation. Many advances have been achieved in the description of these phenomena, yet challenges remain on the development of accurate and efficient simulation tools that are also applicable to real configurations.

In view of the points mentioned above, it seems reasonable to pursue a modeling framework which is able to describe overall quantities of engineering relevance accurately and at reasonable costs, in lieu of capturing all the details of the flow. In this context, field (Eulerian) formulations for average quantities of the dispersed phase have gained a lot of attention recently, becoming an alternative to the more detailed but more computationally expensive, discrete treatment. There is no doubt, however, that in order to achive an appropriate level of description of the phenomena involved, a considerable modeling effort has to be undertaken in the Eulerian context. Considerations on some of the specific requirements of such approaches will be given next.

1.1.1 Modeling requirements

Mass, momentum and energy exchange with the continuous phase is strongly influenced by the spectrum of particle[2] sizes present in a typical dispersed multiphase system, as represented in Fig. 1.1. For example, very small tracer particles tend to quickly adapt to the carrier phase velocity as a result of the dependence of inertial and drag forces on particle size. On the other hand, a big fuel droplet has a higher rate of evaporation than a small one in a hot gas environment. Both situations illustrate the importance of particle size on basic phenomena which exist in many dispersed systems. In the literature, the presence of multiple particle sizes and its influence on the flow dynamics and exchange with the continuous phase is normally referred to as *polydispersity* in a very broad context. Hence, one of the most important modeling requirements is the ability of capturing polydispersity and related effects – such as the ones mentioned above – in an efficient way.

[2] if not stated otherwise, the term “particle” is used in a general way throughout the text, and refers to either bubbles, drops or solid particles

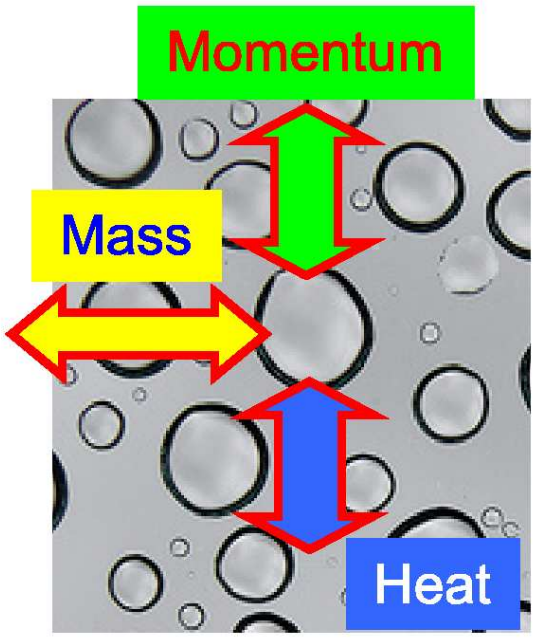

Figure 1.1: Population of drops.

In the past, the field of computational modeling of dispersed flows (specially solid particles and droplets) was dominated by Lagrangian methods. The description of the dispersed phase as a set of discrete entities with different sizes, that are tracked throughout the flow, has the advantage of incorporating polydispersity inherently. However, it is generally accepted that the integration of equations of motion for a large number of individual particles can be extremely expensive, specially when the gas phase is turbulent. The multi-size treatment in the Eulerian context is also possible, but is probably even more computationally intensive. This occurs because sets of transport equations for each size class, which are separetely treated as a different phase, have to be solved for the whole computational domain, even in regions where there are no particles present. However, it is the possibility of describing polydispersity without the segregation into size classes that makes the Eulerian treatment attractive and more efficient than its Lagrangian counterpart. The idea is to formulate field equations for overall quantities (e.g., total volume or surface area) of the particle cloud, which represent the population as a whole. Obvi-

ously, this necessarily leads to loss of information on phenomena that occur at scales that are not explicitly represented in this integral formulation. Hence, one has to resort to modeling in order to incorporate whatever effect might play an important role in the application in question.

Approaches that aim at describing the dispersed phase dynamics and its interaction with the continuous phase without the explicit discretization into size classes are usually grouped in the so called moment methods (often referred to as MOM – "Method of Moments"). These methods are characterized by the transport of moments (or some related information) of the size distribution function, rather than the distribution itself. There are a number of advantages of modeling the dispersed phase in this fashion. First, the number of equations being solved is significantly smaller than in any of the commonly used polydisperse models, making it more computationally efficient. Second, when compared to Lagrangian approaches, coupling with the continuous phase can be more easily accounted for by way of the formulation. Finally, a similar mathematical and numerical treatment of continuous and dispersed phases allows the development of simpler and more efficient parallelization schemes.

The challenge of MOM lies principally in the formulation of closure models for the transport of moments and exchange terms with the continuous phase, such as drag and turbulent dispersion forces, heat transfer and evaporation.

1.1.2 Scope of the work

The objective of the present work is the development, verification and validation of an Eulerian approach in the context of MOM to describe polydisperse flows and its implementation in the open source CFD library tool OpenFOAM. The mathematical formulation is achieved through the integration of the particle equations written in an Eulerian frame. Unclosed terms are modeled by means of a presumed Number Density Function (pNDF), with a novel relaxation approach for the convection velocity of the moments and closure of exchange terms with the continuous phase. The relaxation approach considers an expression for particle velocities as a first order expansion of the fluid ve-

locity scaled with the particle response time. It is able to describe the particle relaxation process towards equilibrium and provides an analytical closure for the overall Stokes drag term acting on the particle population. It is shown that the integration of the expression for the particle velocity also allows the direct determination of the convection velocities of the moments from reference velocities. The framework developed here is called Presumed function Method of Moments (PMOM), with reference to the presumed forms of both the size distribution function and the expression for the size-velocity correlation.

A careful verification of the model and its interdependencies is made with the help of simple test cases involving the segregation and sedimentation of particles due to drag and buoyancy. Results are compared either to analytical solutions or to Multi-Fluid simulations. Additionally, in order to validate the sub-models for spray simulations, comparison against experimental data is performed for configurations involving droplet dispersion and evaporation.

1.2 Outline of the thesis

A literature review on the modeling of multiphase dispersed flows with special attention to polydispersity is given in chapter two.

The third chapter is devoted to the thorough derivation of continuous and dispersed equations in an Eulerian framework, which constitute the basis of the Two- and Multi-Fluid formulations. In the following chapter, PMOM equations are then derived through the integration of the Eulerian dispersed phase equations over the size spectrum. Closure models for the PMOM equation set are also shown.

Chapters five and six contain the results obtained by the proposed model. In chapter five, the implementation of the methodology in OpenFOAM is briefly discussed, and a series of “proof of concept” test cases are presented, with comparison to the corresponding reference solutions. A practical configuration involving droplet dispersion and evaporation is presented in chapter six, where the model results were validated against experimental data for a spray

generated by an ultrasonic atomizer.

Conclusions and suggestions for future work are presented in chapter seven.

2 Dispersed Flows

2.1 Introduction

A “phase” refers to the thermodynamic definition of the solid, liquid or gaseous state of matter. A multiphase system consists of a mixture of two or more phases such as gas bubbles in a liquid, solid particles or liquid drops in a gas, and so on. The term “multi-component” is used to define systems with multiple chemical species. Thus, a water-steam mixture is two-phase, one-component, while a water-air mixture is a two-phase, two-component and a oil-water mixture one-phase, two-component. The latter is commonly regarded as two-phase flow since the components in the mixture are immiscible.

Unfortunately, at present, there is still no general framework which is able to handle all classes of multiphase flows. Perhaps the major difficulty involved in the prediction of these types of flows is that the physical arrangement of phases and/or components in the mixture is not known a priori, but is rather a part of the solution. Consider the flow of gas-liquid mixtures in pipes, for example, which is quite common in many industries (nuclear, oil and gas, etc). Unless the geometry of the interfaces can be defined, there is no practical way to proceed on the selection of an appropiate strategy for the modeling and simulation of such flows in order to determine parameters of engineering significance such as pressure drop, heat transfer coefficients, etc. Otherwise, there is no simulation model which can reasonably predict – as a natural outcome of the initial and boundary conditions chosen – whether bubbles will be uniformly distributed throughout the liquid, or will coalesce to form coherent gas structures, eventually flowing as a continuum core in the center of the pipe, while the liquid forms a film on the wall (this configuration is called “annular flow”). Another good example occurs in spray applications. The process

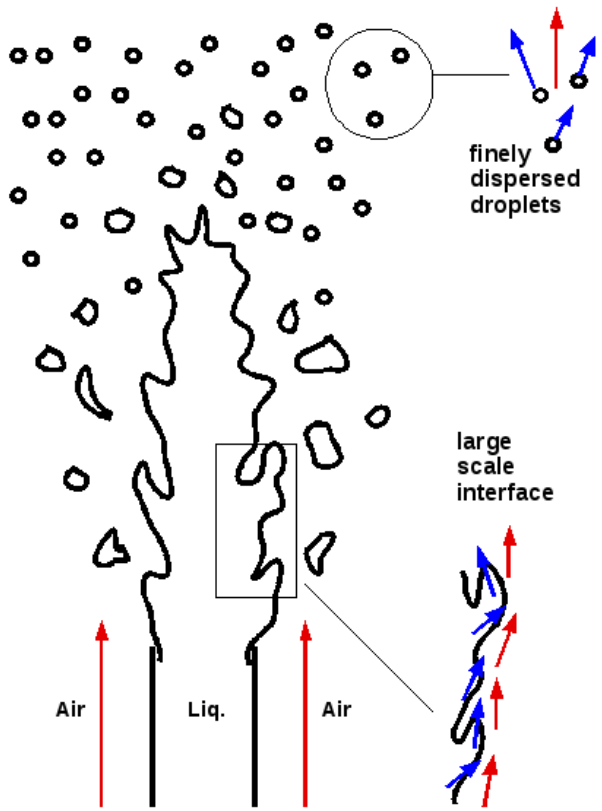

Figure 2.1: Schematic representation of jet-break up.

of fuel atomization involves the disintegration of a liquid phase in a gaseous environment. Very distinct regions can be identified here, ranging from a continuous liquid jet (or sheet) to finely dispersed droplets (see Fig. 2.1). Models that are developed to capture the evolution of the interface during the primary break-up process are not expected to perform well in regions where a population of very small droplets exist (and vice-versa). While for the first it is crucial to resolve phenomena happening at the scale of the interface, the flow inside and around each droplet would be very difficult and expensive to compute, being rather unimportant in the latter.

In this context, the present thesis is restricted solely to the description of what is called dispersed flows. The term “dispersed” refers to the presence of discrete elements immersed in a continuous medium. These elements can be

of the same phase of the continuum (in a dispersion of oil in water for example) or not (such as liquid droplets dispersed in air). Even though the behavior of the two can differ significantly, their modeling is usually similar. In the majority of cases of interest, length scales of the dispersed elements are sufficiently small so that surface tension effects are dominant. Hence, it is reasonable to assume that these elements are well represented by spherical particles. Therefore, knowledge of how the particles are distributed (how many and how big they are) at a given position allows to solve the problem of determining the interfacial geometry in some sense, and the computation of the exchange of mass, momentum and heat with the continuous phase is in theory possible. The key question is related to the importance of back coupling with the continuous phase, how to model exchange terms in general, and to whether particle-particle interaction is important or not. Since particles are not explicitly resolved, *a priori* criteria are extremely useful in order to determine which type of regimes are expected, given the flow conditions, and incorporate proper physical effects into the models. This will be discussed in the next section.

2.1.1 Classification of dispersed flows

For the characterisation of dispersed two-phase flow regimes, it is useful to define some properties which are summarized below.

The volume fraction of the dispersed phase (α_d) is the volume occupied by the particles in a characteristic volume of the mixture, $\mathcal{V}$. It is given by:

$$\alpha_d = \frac{\sum_i N_i V_i}{\mathcal{V}}, \tag{2.1}$$

with N_i the number of particles of a certain size class i, with volume $V_i = \pi D^3/6$.

The spacing l_p between particles is related to α_d by[1]:

[1] it is considered, for simplicity, that particles are represented by a unique diameter

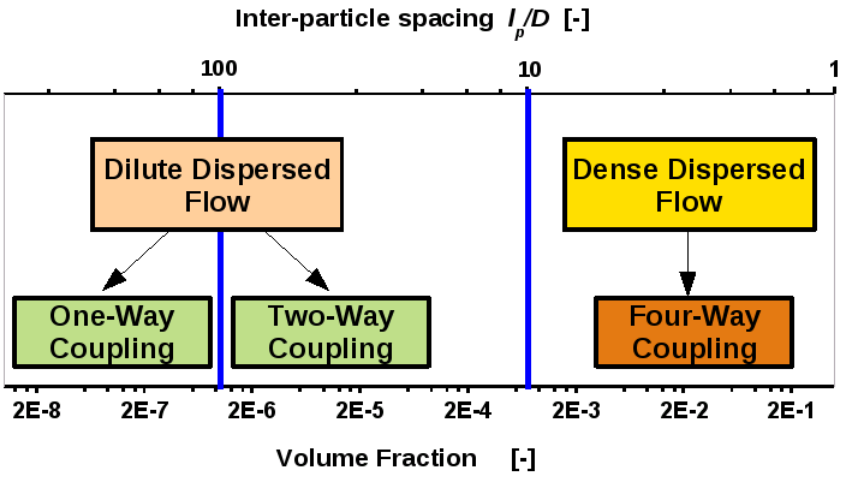

Figure 2.2: Dispersed flow regime classification.

$$\frac{l_p}{D} = \left(\frac{\pi}{6\,\alpha_d}\right)^{\frac{1}{3}}, \tag{2.2}$$

with D the particle diameter.

The characteristic response time τ of particles with respect to the fluid flow is defined as

$$\tau = \frac{\rho_d D^2}{18\mu_c}, \tag{2.3}$$

with ρ_d the dispersed phase density and μ_c the continuous phase dynamic viscosity.

Commonly, dispersed flows are separated in two regimes. In dilute systems τ is typically much smaller than the time between collisions. Thus, the spacing between particles is likely to remain sufficiently large, so that a direct interaction is rare. On the other hand, dense systems are those where particle transport is dominated by collisions and the inter-particle spacing is comparatively small. In this case, particles have relatively little time to react to fluid dynamic forces between successive collision events.

A classification of dispersed flows with regard to the importance of interaction

mechanisms was provided by Elghobashi [28]. Generally it is distinguished between dilute and dense flows as mentioned above (Fig. 2.2). A two-phase system may be regarded as dilute for volume fractions up to $\mathcal{O}(10^{-3})$ (i.e. $l_p/D \sim 10$). In this regime the influence of the particle phase on the fluid flow may be neglected for volume fractions smaller than $\mathcal{O}(10^{-6})$ (i.e. $l_p/D \sim 100$). When the volume fraction is increased, the influence of particles on the continuous phase needs also to be accounted for. This is often referred to as "two-way coupling". In the dense regime (i.e. for volume fractions greater than $\mathcal{O}(10^{-3})$) additionally inter-particle interactions (i.e. collisions and the effect of particle presence on the fluid dynamic forces acting on its neighbors) become important. This regime is characterized by the so called "four-way coupling"[2].

It is common practice in the literature to designate the collection of all dispersed particles simply as "dispersed phase", in contrast to "continuous phase". If the dispersed phase is characterized by a single size, the flow is called *monodisperse*. If a distribution of particle sizes is present, it is denominated *polydisperse* (as mentioned in 1.1.1). In the most general case, particles are likely to have distinct properties, such as different sizes, velocities or temperature. This obviously poses challenges to the modeling and computation of the coupled dynamics of continuum and dispersed phases and will be discussed later on with the different modeling strategies.

2.2 Modeling strategies

There are numerous techniques for the simulation of dispersed two-phase flows and the question of which one is more appropriate for a given problem does not have a simple answer. To help clarify the need for different methods, Ferry and Balachandar [30] propose the following analysis: imagine a monodisperse particle-laden flow with fixed density ratio and volume fraction in the dilute regime; how should the simulation technique be chosen?

They argue that the important parameter to be looked at is the ratio of the re-

[2] Loth [50] also distinguishes between three- and four-way coupling. While three-way coupling considers only the distorted flow fields due to the presence of particles on its neighbors (e.g. wake effects), four-way coupling includes also particle collisions.

sponse time τ of particles vs. the typical time scale of the continuous phase flow. Very small particles tend to adapt almost immediately to the surrounding flow and therefore the use of an Eulerian treatment for a single phase with modified density is sufficient. A passive scalar representing the particle concentration is then transported with the fluid velocity. For larger particle diameters the assumption of equal velocities is no longer valid, even though the Eulerian treatment still applies. The reason for that is the larger response time – $\tau \propto D^2$, see Eq. (2.3). For even bigger particles, the Eulerian approach ceases to be appropriate, mainly because the number of particles is too low (for a given volume fraction) to assign a meaningful mean value for the local Eulerian velocity. In this case, a Lagrangian treatment for individual particles is more accurate. If the particle sizes increase further, the Lagrangian parameterization for the exchange terms with the continuous phase probably becomes inaccurate and the resolution of the flow field around the particles becomes necessary.

A brief description of each of the above mentioned modeling frameworks will be given in the next sections, following the classification strategy presented by Balachandar and Eaton [4] (see Fig. 2.3). The degree of details captured by each approach will be gradually relaxed from the DNS level, going through Lagrangian and Eulerian approaches, including the treatment of polydispersity with moment methods, including the parameterization of exchange terms.

2.2.1 DNS

For particle sizes comparable or larger than the characteristic flow scales of the continuous phase, fully resolved DNS becomes the only option. In DNS techniques the temporal and spatial resolution is such that all details of the flow fields are captured, which makes possible the exact determination of forces experienced by the dispersed elements moving in a continuous phase. Unfortunately, computational costs are prohibitive for practical calculations. There are examples of calculations involving up to $\mathcal{O}(10^3)$ particles (see e.g. Pan and Banerjee [65] or Uhlmann [80]), but real applications typically involve far more than that. Hence, the use of fully resolved simulations is likely

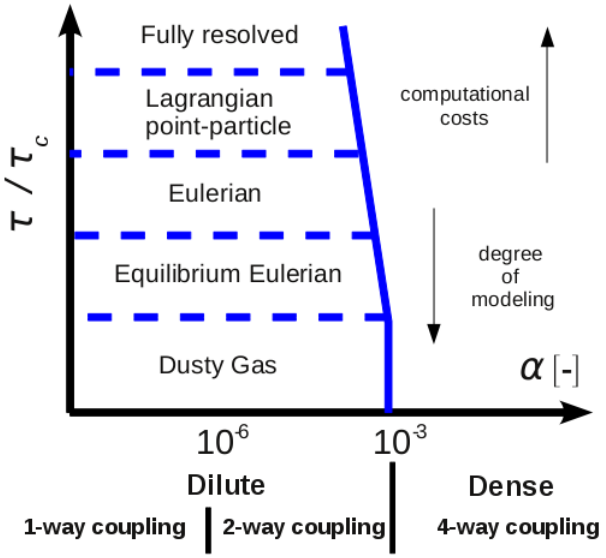

Figure 2.3: Different approaches to dispersed flows in terms of time scale ratio and volume fraction [4].

to be restricted to simple configurations in the near future. Nevertheless, these configurations are also extremely interesting in order to improve closure relations for the phase interaction terms required in either Eulerian-Lagrangian or Eulerian-Eulerian type of models which are in principle more suitable for engineering problems.

2.2.2 Eulerian-Lagrangian approaches

As mentioned in section 1, discrete particle methods[3] retain the intuitive Lagrangian description of particle motion in order to determine the position, mass, momentum and energy of particles along its trajectories. Individual particles are tracked through the gas phase grid (Fig. 2.4, left) by solving their own equations of motion. If the flow is dense and highly unsteady, it might be interesting to track groups of representative particles, in what is called “discrete element” method [22].

[3]These methods are often called Lagrangian point-particle approaches, because the whole mass of the particle is concentrated into a point

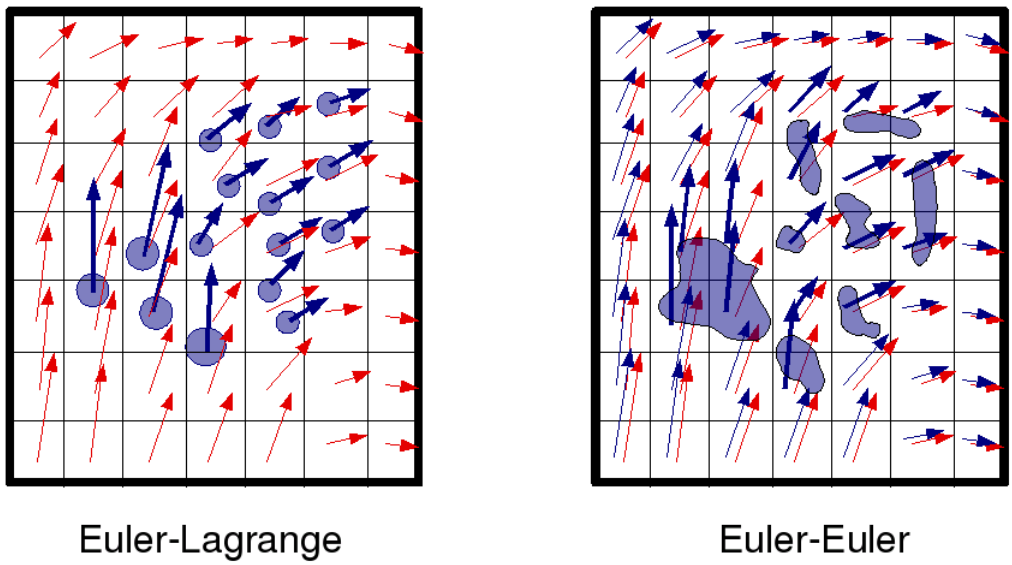

Figure 2.4: Schematic representation of Eulerian and Lagrangian strategies.

In the Lagrangian description, polydispersity is handled intrinsically. Additionally, multiplicity of particle characteristics (e.g. velocities and temperatures) within the same size class can be accounted for. This allows to capture, for example, effects of Particle Trajectory Crossing (PTC). This effect can be important in opposed jets configurations or when a spray interacts with a wall, but also due to velocity non-equilibrium characteristics of large particles in a turbulent flow field [22].

Coupling of the particles back to the carrier phase (two-way coupling) is achieved through source terms in the Eulerian level, which poses challenges regarding the distribution of source terms due to the presence of particles within a cell to the neighboring grid points. In contrast to one-way coupled simulations (as carried out, e.g. by Maxey [57] and Elghobashi [27]), two- and four-way coupled simulations are much more expensive and have been only more recently combined with LES by Yamamoto et al. [89] and DNS by Ferrante and Elghobashi [29] of the carrier phase.

An important aspect of the modeling of dispersed flows is the treatment of turbulent fluctuations on particle motion. If the turbulent flow field of the con-

tinuous phase is known, particle dispersion evolves directly from the discrete particle method. However, in the majority of cases, it is not possible to resolve all scales of the turbulent flow field and one has to resort either to Reynolds Averaged Navier Stokes (RANS) computations or LES. In order to model the fluctuating forces which act on the particles, the so called stochastic methods can be used. A very common approach is to assume that the velocity can be decomposed as the sum of the local time-averaged value and a fluctuating part [90], which is selected e.g. through a random number generator (Monte-Carlo method). Many improvements have been made in the calculation of the fluctuation velocity, such as in the works of Gosman and Ioannides [38] and Berlemont et al. [13]. However, these methods are much more expensive than the ones used in the Eulerian framework, where closure for terms involving turbulent fluctuations can be simply achieved as in single phase flows by assuming e.g. a gradient-diffusion hypothesis, which intrinsically allows to incorporate terms involving gradients of relevant variables in a field description.

Accurate representation of interphase exchange requires a large sample of particles to obtain statistically meaningful average quantities. If very fine resolved computations are conducted, very small time and spatial intervals for sampling are necessary and quality of results might be compromised by the level of statistical noise. To avoid this, the sample size must be increased, which can be very computationally expensive, specially if LES or DNS of the continuous phase is pursued.

The development of algorithms for parallel computations with Euler-Lagrange methods is a difficult task. If the domain is decomposed in many geometrical subdomains, particles must be tracked as they cross adjacent regions to account for the exchange between processors, which involves a relative large amount of "book keeping". Riber et al. [69] observed that the speed-up using several processors is not able to follow the increase on the workload, specially for unstructured grids. Furthermore, load imbalance is very common in Euler-Lagrange computations, since particles might be accumulated in a small part of the domain (near injectors, for example), but completely absent in others.

Therefore, as seen above, while the biggest advantage of Lagrangian meth-

ods is the ability to capture most relevant phenomena involved in dispersed flows, two- and specially four-way coupled simulations in engineering configurations normally means formidable computational costs, specially when combined with resolved turbulence simulations of the gas phase. The often non-satisfactory scaling behavior in parallel computing has also contributed to the motivation for the further development of techniques in the Eulerian framework, which will be treated in the next section.

2.2.3 Eulerian-Eulerian approaches

The movement of a collection of small (macroscopic) particles is in many aspects similar to that of gas molecules on the molecular scale (even though the relevant interaction forces have a different nature in the two cases). If scales much larger than the mean free path between collisions are considered, the discrete treatment is not strictly necessary; statistically invariant properties are assigned locally and a continuum formulation can be used instead. A similar idea has been used to treat dispersed flow systems as well; some earlier work on the subject was done by Travis et al. [79], for example. Thus, the principal difference to the Lagrangian approaches is that fields of local average properties of the dispersed phase exist by definition in the whole domain, even if no particles are present (Fig. 2.4, right).

In many of their classical versions, Eulerian multiphase models usually treat all phases as interpenetrating and interacting continua. Conservation equations are derived through some type of averaging procedure (ensemble, time, volume or a combination of them – as systematically derived by Ishii [42]) of the single phase equations, and sets of symmetrical equations result for the multiphase system, including continuous and dispersed phases. The outcome of the different averaging procedures are in most cases similar, but many controversies persist in the literature as to which approaches are more correct, as well as the physical interpretation of phase interaction terms that arise due to the presence of an interface. A discussion on the subject was given by Prosperetti [67]. Another issue lies on the meaning of stress terms when treating dispersed phases as continua. In the dense regime, it might be rea-

sonable to model the outcome of particle-particle interaction as stress-like terms, since particles are close to each other, are likely to collide and the interchange of momentum is high. One example of this type of modeling can be found in studies of Monahan et al. [60] and Monahan and Fox [59], where a bubble-pressure term is employed to take into account for the exchange of momentum arising from bubble-bubble interactions. In dilute mixtures, however, where inter-particle spacing is large and particle-particle interaction is rare, the physical meaning of dispersed phase pressure and shear stresses is questionable.

A comprehensive heuristic approach was developed by Crowe et al. [22], in which particle field equations are derived starting from the Lagrangian equations of motion transformed to Eulerian coordinates. A similar approach was also briefly discussed by Bataille and Lance [9]. The Eulerian field equations for a dispersed phase are then obtained in a physically sound manner by using directly the Lagrangian parameterization of interaction terms and performing a combination of volume and ensemble averaging. This avoids the appearence of stress-like terms in the dispersed phase equations. Continuous phase volume-averaged equations are then derived in the usual manner and the result is a set of field equations for both phases which are not strictly symmetrical.

Despite of the subtleties of the equation set and how it is derived, it is useful to discuss the level of description and computational costs of Eulerian approaches. According to Balachandar and Eaton's [4] classification (see Fig. 2.3), the following Eulerian methods can be mentioned:

- Dusty Gas

  The dusty gas approach was introduced by Carrier [20]. In this approach, particles are assumed to be sufficiently small in order to follow the carrier gas perfectly. Thus, the two-phase flow is actually considered as a single phase with modified density and, in addition to the mixture equations, only a tranport equation for the particle concentration has to be solved.

- Equilibrium Eulerian

The single-velocity hypothesis limits the range of validity to very small τ. Ferry and Balachandar [30, 31] extended the method on what was called "equilibrium Eulerian" approach, which is also computationally simple, even though particle and gas phases do not share the same velocity field. Instead, the particle velocity field is expressed as a first order expansion on the gas velocity, using particle relaxation time τ as dependent variable. The method was shown to be accurate, provided that the particle response times are not large. The same idea was successfully applied later for the temperature field of small particles [32].

- Two-Fluid and Multi-Fluid Models

  In the Two-Fluid Model, a set of conservation equations is solved for the dispersed phase, which allows to better reproduce the dynamic nature of coupling between continuous and dispersed phases than the previous approaches. However, the hypothesis of local existence of a single phase representative of the whole spectrum of sizes compromises the use of the Two-Fluid Model when multi-size treatment is important, since there is no information whether the volume fraction (the unique information available on the distribution) is a result of a few large bubbles or many small ones, for example.

  The logical extension to the Two-Fluid is the Multi-Fluid Model, where several size classes can be considered and each of them is treated as a different Eulerian phase. Thus, here the description of polydispersity is in theory possible, but the solution of multiple Eulerian phases might become very computationally expensive. In the homogeneous MUSIG of Lo [49], continuity equations are solved for each size, which share however the same velocity field. An extension to this model is the Inhomogeneous MUSIG of Krepper et al. [48], which subdivides the size classes in different velocity groups, for which different momentum equations are solved. These models have been extensively applied to bubbly flows with relative success, but even the use of few momentum equations (typically less than four) can be very expensive, specially when coupled through population balance processes such as break-up, coalescence and phase change.

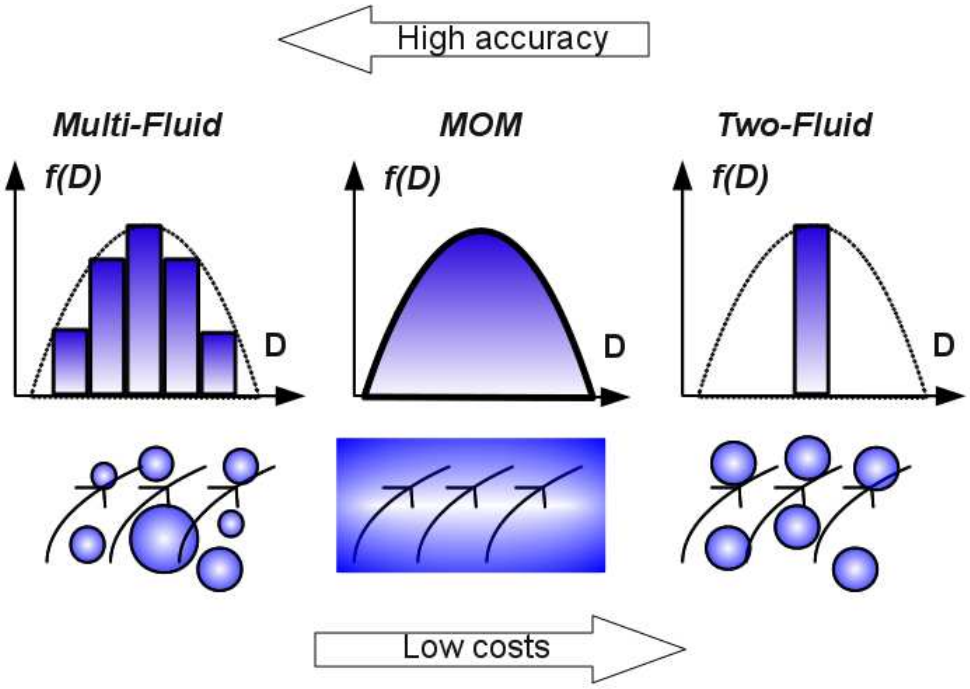

Figure 2.5: Schematic representation of Eulerian-Eulerian Models.

A critical comparison of Two-Fluid, Multi-Fluid and Lagrangian approaches in RANS context for spray simulations was done by Mostafa and Mongia [62]. Surprisingly, they found out that the use of a Monte Carlo technique to account for droplet turbulent dispersion can be sometimes even more expensive than the multi-size Eulerian treatment. While both models are accurate in comparison to the experimental data, the Two-Fluid Model is restricted to situations where the size distribution is not wide. Therefore, it seems reasonable to search for a solution which represents a compromise between the low costs of a Two-Fluid Model and the accuracy of a full Multi-Fluid Model – as schematically represented in Fig. 2.5. These models appear in the context of Moment Methods, which will be described next.

2.2.3.1 Moment methods

Recently, alternatives to the conventional Lagrangian or Multi-Fluid techniques have been developed, which make it possible to account for polydisperse particle transport and population dynamics more efficiently. Instead of discretizing the particle size distribution function in many size classes, most of these methods rely upon formulations involving its moments (or some other information) [12, 36, 45, 54, 73]. In the formulation of such types of models, there are essentially two paths to follow: a statistical derivation in the lines of the kinetic theory of gases; or, simply the integration of pre-established Eulerian Multi-Fluid equations (in the context of models described in the last section) over size or velocity space (or any other particle coordinate).

Statistical derivations of field equations can be found in several works in the literature [33, 55, 79]. Normally, a generalized population balance equation for a joint NDF $f(\mathbf{x}, t; \mathbf{u}, \xi)$ including one or more particle internal coordinates (such as size, velocity or temperature; denoted here as ξ) is used:

$$\frac{\partial f}{\partial t} + \nabla_{\mathbf{x}} \cdot (\mathbf{u} f) + \nabla_{\mathbf{u}} \cdot (\mathbf{A} f) + \nabla_{\xi} \cdot (\dot{\xi} f) = h(f), \tag{2.4}$$

where the first term is the accumulation in time, the second is the convection in physical space, the third and fourth represents the convection in internal coordinate space and $h(f)$ is the source term, which can incorporate break-up and coalescence, for example.

Moment transforms are then applied to the above equation in order to derive transport equations for integral quantities of interest (namely mass, momentum, etc). Specifically in the context of sprays, the Williams generalized transport equation introduced by Williams [88] is used in the development of these types of methods [1, 2, 55].

Beck and Watkins [11, 12] have shown that a formulation dependent on the moments can also be achieved by integration of Eulerian Multi-Fluid equations representing droplet classes over the size spectrum. The idea was to retain the Eulerian-Eulerian formulation, but to capture the full polydisperse nature of the spray while representing the population of droplets as a whole.

The liquid phase is parameterized by integral quantities defined by the moments. A similar framework concerning the derivation of their model is also used in this thesis.

Regardless of which derivation strategy is chosen, transport equations for moments of the size distribution function are normally solved in addition to the common conservation equations in the Eulerian-Eulerian framework. Depending on the physical laws of the exchange processes with the continuous phase (e.g. drag or evaporation) or particle-particle interaction, integral source terms which represent these processes are formulated in terms of the moments and need to be modeled and closed. This involves in general the determination of *a priori* unknown moments, which is usually done either by reconstructing the size distribution from presumed functional forms [12], by means of splines [24, 45], or using quadrature approximations [54]. Tagliani [78] developed a framework with the maximum entropy formalism for the reconstruction of a distribution function given a set of constraints (the moments). It has the main advantage that the form of the distribution function is an outcome of the reconstruction process itself. Archambault [2] applied a moment method with maximum entropy closure in quasi-one-dimensional-spray while Massot et al. [56] tackled the important problem of evaluation of disappearence rate of droplets with NDF reconstruction through a maximum entropy formalism. Beck [10] pointed out that approaches based on the maximum entropy formalism can be computationally expensive for real configurations – spray cases were analyzed with a CFD framework – because an optimization problem has to be solved for each grid cell and time step. However, Kah et al. [47] have shown in the simulation of a compressible polydisperse evaporating spray that the associated numerical expenses are actually not prohibitive.

Many moment methods commonly assume that the moments are transported with the velocity of the dispersed phase [37, 66]. Such approaches are also able to predict effects of polydispersity due to, e.g. break-up and coalescence processes, through the incorporation of source terms in the transport equations for moments. Particularly in the work of Gharaibah [36], mean and variance of the bubble size distribution are transported in a Two-Fluid framework, while

source terms are read from a look-up table in order to compute the change in the distribution function due to bubble coalescence or break-up in an aerated stirred vessel. Indeed, depending on the local flow conditions, these processes might lead to non-uniform size distribution functions in space and time. However, the effect that particles of different sizes have locally different velocities, which translates into different transport velocities for the moments, is not accounted for.

In order to account for the effect of particle size on the transport of moments, different approaches can be found in the literature. Manninen et al. [52] suggest the use of a Drift-Model to determine particle velocities in polydispersions, assuming local equilibrium and a constant expression for the slip-velocity. Wacker and Seifert [82] use a power-law functional form for the size-velocity correlation, applying their moment method to pure sedimentation of rain drops. Beck and Watkins [12], on the other hand, derive transport equations for the moment transport velocities, using for instance an approximate closure for the integral drag force acting on the population of droplets in a spray, where the relative velocity between the liquid and the gas was taken to be constant with diameter. Their model gave very realistic results for the spray configurations analysed, but the independent advection of more than two moments proved to destabilize the numerical method. This motivated the use of a two-moment scheme, while other moments were determined with help of a presumed function approach.

In the present work, a novel closure based on the equilibrium Eulerian method is presented, where particle velocities are expressed as a first order expansion of the fluid velocity scaled with particle relaxation times. This is a more accurate representation than simply setting a constant relative velocity for each particle size, since the relaxation process towards equilibrium can also be accounted for. The adaptation of this idea to the context of the Method of Moments allows the determination of moment transport velocities from reference velocities, which in turn can be obtained from the solution of proper momentum equations. Therefore, this method provides – in combination with a presumed distribution function approach – a possibility of analytical closure for the drag term and the determination of moment transport velocities. This

model can also be extended to larger relaxation times, as will be shown in the course of the text.

3 Continuous and Dispersed Phase Equations

3.1 Introduction

Multiphase flows can be in theory described by the Navier-Stokes equations within each phase, applying appropriate boundary conditions at the interfaces separating them. That is, if the position and velocity of these interfaces were known, the problem would be reduced to solving single-phase equations for a complex domain with varying shape. However, in the vast majority of cases, the interface dynamics is not known *a priori*; it is rather a part of the solution. Needless to say, this poses formidable mathematical and computational problems, as stated and discussed in the former chapters of this thesis in details.

In the past decades, much of the research in the area of multiphase flows was dedicated to the development of techniques to contract the problem to a form which is more tractable in both mathematical and numerical points of view. For instance, in single- and multiphase pipe flows (e.g. in oil and gas pipelines) it is common engineering practice to perform averages over the cross section and treat the problem from the perspective of the "mean flow". However, by doing that, knowledge input is normally required (through empirical or analytical models), so that missing details, which might be important to the description of relevant phenomena, can be to some extent reincorporated into the modeling process.

In the pipeline example, friction factors abbreviate the need for solving a complex problem in very long domains, while representing momentum exchange at the interfaces between phases (and between phases and the wall) by predefined correlations. In dispersed flows, a similar point of view can be used.

The parameterization of forces acting on particles with help of analytical and empirical results avoids having to compute the detailed fluid flow around each and every particle – an effort which goes far beyond present computing power. It is therefore very important to study the phenomenology of single particle motion in a detailed manner.

The following sections are dedicated to the description of the various phenomena governing particle motion. Once the most important forces acting on particles – as well as mechanisms of heat and mass exhange – are identified for the class of problems studied here, the averaging procedure can be worked out, as well as closure for the interphase exchange terms that arise in the averaged equations.

3.2 Phenomenology of dispersed flows

3.2.1 Particle-Fluid interaction: momentum exchange

The particle equation of motion is written according to Newton's second law:

$$m_i \frac{\mathrm{d}\mathbf{v}}{\mathrm{d}t} + \underbrace{\int_{S_i} \rho_d \left(\hat{\mathbf{u}} + \frac{1}{2}\dot{D}\mathbf{n}\right) \hat{\mathbf{u}} \cdot \mathbf{n} dS}_{\approx 0} = \mathbf{F}, \tag{3.1}$$

where m_i is the particle mass, $\mathbf{v}$ is the particle center of mass velocity, $\hat{\mathbf{u}}$ is the velocity with which the mass crosses the particle interface S_i (i.e., the velocity with respect to the regressing or advancing surface) and $\frac{1}{2}\dot{D}\mathbf{n}$ is the regressing/advancing rate with respect to the particle's center of mass; the integral on the LHS represents therefore the net flux of momentum on the particle surface due to loss/gain of mass during phase change (which is zero since spherical symmetry is assumed). $\mathbf{F}$ is the sum of all external forces acting on the particle. These forces can be divided in three different categories:

- Particle-fluid interaction: pressure and viscous forces acting on the interface between particle and fluid ($\mathbf{F}_F$)

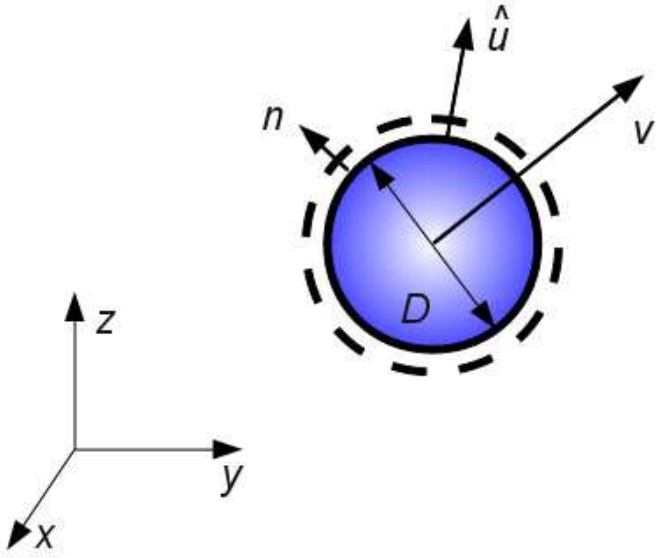

Figure 3.1: Particle moving with respect to a fixed reference frame.

- Particle-particle interaction: momentum exchange due to collision processes ($\mathbf{F}_P$)
- Body forces: such as gravity or Coulomb forces. ($\mathbf{F}_B$)

Attention will be restricted to the first type, since particle-particle interaction is out of the scope of this work and the treatment of body forces is straightforward. The force $\mathbf{F}_F$ exerted by the surrounding fluid on a particle is given exactly by the integral of normal and shear stresses over the particle surface. Thus:

$$\mathbf{F}_F = \int_{S_i} (-p\boldsymbol{I} + \tau) \cdot \mathbf{n} dS. \tag{3.2}$$

As mentioned in chapter 2, a DNS of a fluid containing dispersed particles is very difficult and demands a great amount of computing power. In addition to the resolution of the boundary layer around the particle, a full dynamic cou-

pling of fluid forces and particle movement described by Newton's second law is necessary. Although fully resolved simulations have been made for a small number of particles and small Reynolds numbers of the continuous phase, it remains impractical for the most systems of engineering relevance.

Fortunately, there is a practical way to proceed in parameterizing forces acting on the particle without explicit knowledge of pressure and shear stress distributions around the particle. Consider the continuity and momentum equations (Navier-Stokes equations) for the continuous phase, which govern the flow around the particle:

$$\frac{\partial \rho_c}{\partial t} + \nabla \cdot (\rho_c \, \mathbf{u}_c) = 0 \tag{3.3}$$

$$\frac{\partial (\rho_c \mathbf{u}_c)}{\partial t} + \nabla \cdot (\rho_c \, \mathbf{u}_c \mathbf{u}_c) \quad = \quad -\nabla p + \nabla \cdot \tau + \rho_c \mathbf{g}. \tag{3.4}$$

For an incompressible, Newtonian fluid with constant properties, the above equations can be simplified to:

$$\nabla \cdot \mathbf{u}_c = 0 \tag{3.5}$$

and

$$\begin{aligned} \frac{D\mathbf{u}_c}{Dt} = \frac{\partial \mathbf{u}_c}{\partial t} + \mathbf{u}_c \cdot \nabla \mathbf{u}_c \quad &= \quad -\frac{1}{\rho_c} \nabla p + \frac{1}{\rho_c} \nabla \cdot \tau + \mathbf{g} \\ &= \quad -\frac{1}{\rho_c} \nabla p + \nu_c \nabla^2 \mathbf{u}_c + \mathbf{g}. \end{aligned} \tag{3.6}$$

The momentum equation may be rendered dimensionless (neglecting gravity, for simplicity, but without loss of generality for the present purposes) with help of characteristic time and length scales $t^* \sim t/\tau$, $\mathbf{x}^* \sim \mathbf{x}/D$, velocity $\mathbf{u}_c^* \sim \mathbf{u}_c/(\mathbf{u}_\infty - \mathbf{v})$ and pressure $p^* \sim (p - p_\infty) D^2/(\mu_c |\mathbf{u}_\infty - \mathbf{v}| D)$, yielding the following expression:

$$\frac{\partial \mathbf{u}_c^*}{\partial t^*} + \mathrm{Re}_p\,(\mathbf{u}_c^* \cdot \nabla^* \mathbf{u}_c^*) = -\nabla^* p^* + \nabla^{*2} \mathbf{u}_c^*. \tag{3.7}$$

It can be infered from Eq. (3.7) that, if the particle Reynolds number is much smaller than unity (creeping flow condition)

$$\mathrm{Re}_p = \frac{|\mathbf{u}_c - \mathbf{v}|D}{\nu_c} \ll 1, \tag{3.8}$$

non-linearities have a marginal importance in the momentum equation. This is generally known as the Stokes hypothesis. In this case, a superposition of velocity and pressure fields that individually satisfy the Navier-Stokes equations is also a valid solution. Hence, the total force acting on the particle may be added up as

$$\begin{aligned}
\mathbf{F}_F &= \int_{S_i} -(p_1 + p_2 + p_3 ...)\boldsymbol{I} \cdot \mathbf{n} dS + \int_{S_i} (\tau_1 + \tau_2 + \tau_3 + ...) \cdot \mathbf{n} dS \\
&= \int_{S_i} (-\sum_i p_i \boldsymbol{I} + \sum_i \tau_i) \cdot \mathbf{n} dS) \\
&= \sum_i \int_{S_i} (-p_i \boldsymbol{I} + \tau_i) \cdot \mathbf{n} dS \\
&= \sum_i \mathbf{F}_{F,i}.
\end{aligned} \tag{3.9}$$

Therefore, particle movement in a complex flow field can be perceived to comprise of the combination of different types of elementary motions, of which the following will be considered here:

- Particle traveling with uniform velocity in a stagnant fluid ($\mathbf{F}_{F,D}$)
- Particle at rest in a pressure field ($\mathbf{F}_{F,p}$)
- Particle moving in a shear flow ($\mathbf{F}_{F,\tau}$)
- Archimedes' buoyancy force ($\mathbf{F}_{F,\mathrm{g}}$)

The resulting expression of these forces can be seen as closure laws which allow to predict particle motion without requiring any detailed knowledge of the influence of the particle on the flow. The linear splitting of the forces is frequently used even if the Stokes assumption is not strictly fulfilled. However, nonlinear coupling between the forces is often thought to be so small that it can be neglected. The various forces acting on particles and their behavior in different types of flow conditions have been reviewed by Crowe and Michaelides [21].

3.2.1.1 Steady state drag force

In most dispersed systems, the drag force dominates particle motion and consists of contributions from pressure ("form drag") and shear stress ("viscous drag") distributions. The flow field due to a spherical body in translational motion was first determined by Stokes [77]. With the hypothesis of sufficiently small Re_p, an analytical expression of the drag force can be derived simply by evaluating the integral on the particle surface given by Eq. (3.2). It results in:

$$\mathbf{F}_{F,D} = \underbrace{2\pi\mu_c D(\mathbf{u}_c - \mathbf{v})}_{\text{viscous drag}} + \underbrace{\pi\mu_c D(\mathbf{u}_c - \mathbf{v})}_{\text{form drag}} = 3\pi\mu_c D(\mathbf{u}_c - \mathbf{v}). \tag{3.10}$$

As seen in the above expression, in the Stokes regime the contribution of viscous drag is twice as important as the pressure contribution.

It is usual to express the drag force exerted on the moving particle by the fluid in terms of a dimensionless coefficient obtained by dividing the magnitude of the force by a dynamic pressure $\frac{1}{2}\rho_c|\mathbf{u}_c - \mathbf{v}|^2$ and by the area of the particle projected onto a plane normal to $\mathbf{u}_c - \mathbf{v}$; thus the drag coefficient is determined for small Reynolds numbers by

$$C_D = \frac{3\pi\mu_c D|\mathbf{u}_c - \mathbf{v}|}{\frac{1}{2}\rho_c|\mathbf{u}_c - \mathbf{v}|^2 \frac{\pi D^2}{4}} = \frac{24}{\mathrm{Re}_p}. \tag{3.11}$$

The dependence of the drag coefficient of a spherical particle on the Reynolds

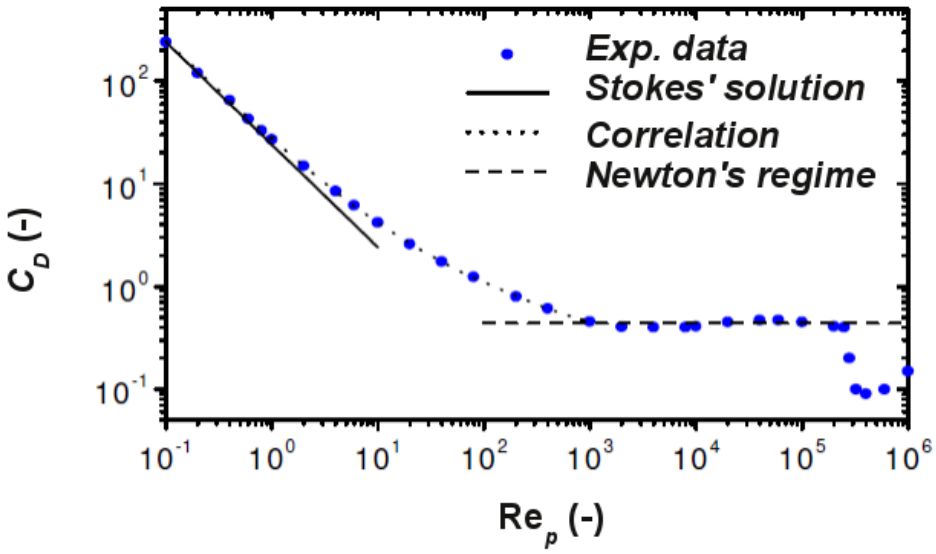

Figure 3.2: Drag coefficient as a function of particle Reynolds number (adapted from [76]).

number is shown in Fig. 3.2.

One may identify several regimes which are associated with the flow characteristics around the sphere. For small Reynolds numbers, viscous effects are dominating and no separation is observed. The analytical solution for C_D is presented above. In the transition region (i.e. $1 < \mathrm{Re}_p < 1000$) inertial effects become of increasing importance. Above a certain Reynolds number, separation patterns of the flow around the particle begin to be observed, which change pressure and shear stress distributions. Numerous correlations have been proposed in order to represent the experimental data. A frequently used correlation is that proposed by Schiller and Naumann [71], which fits the data up to $\mathrm{Re}_p = 1000$ reasonably well (see Fig. 3.2). The Schiller-Naumann correlation takes into account a correction to the Stokes expression, which is nonlinear in the Reynolds number:

$$C_D = \frac{24}{\mathrm{Re}_p}(1 + 0.15\mathrm{Re}_p^{0.687}) \tag{3.12}$$

Above this region and below a critical value of Re_p (i.e. $1000 < \mathrm{Re}_p < \mathrm{Re}_{p,crit}$), the so- called Newton's regime is observed, where form drag plays the decisive role and drag coefficient is nearly constant ($C_D \approx 0.45$). For $\mathrm{Re}_p > \mathrm{Re}_{p,crit}$, transition to a turbulent boundary layer occurs, leading to a drastic decrease of the drag coefficient, since the separation point moves significantly downstream at the particle surface.

3.2.1.2 Forces due to pressure and shear stresses

Local pressure and shear stress gradients in the flow give rise to additional forces on the particle. For example, a local pressure gradient tends to accelerate particles in the opposite direction of the pressure gradient. A shear stress distribution has a similar effect and generates a force in the direction of the divergence of the shear stress. Hence, combining both effects, one obtains:

$$\begin{aligned} \int_{S_i} (-p\boldsymbol{I} + \tau) \cdot \mathbf{n} dS \quad & \underbrace{\rightarrow}_{\substack{\text{Gauss' divergence theorem}}} \quad \int_{V_i} (-\nabla p + \nabla \cdot \tau) dV \\ \Rightarrow \mathbf{F}_{F,p} + \mathbf{F}_{F,\tau} \quad & = \quad V_i(-\nabla p + \nabla \cdot \tau) \end{aligned} \tag{3.13}$$

In the above relations, it is implicitly assumed that particles are sufficiently small, such that the global pressure and shear stress gradients are nearly constant over the particle volume.

3.2.1.3 Buoyancy

Buoyancy can be regarded as a pressure gradient force due to the hydrostatic pressure variation in a fluid. The pressure distribution in a fluid at rest is given by the hydrostatic equation:

$$\nabla p = \rho_c \mathbf{g}. \tag{3.14}$$

The total force due to the pressure distribution resulting from the above equation is simply given by the surface integral:

$$\int_{S_i} -p\,\boldsymbol{I}\cdot\mathbf{n}dS = \int_{V_i} -\nabla p dV = -\rho_c V_i \mathbf{g} \tag{3.15}$$

This is also known as the Archimedes' principle: the buoyancy force acting on the particle is given by the weight of the displaced fluid, in which the particle is immersed.

3.2.1.4 Relaxation time

The particle relaxation (or response) time is an extremely important parameter which may be used to characterize the capability of particles to follow changes in the velocity of the continuous phase. Being a characteristic time scale of particle motion, it will naturally appear as a central quantity in the model development.

Rewriting Eq. (3.1), considering the expression for the drag force in the Stokes regime presented above and the gravity/buoyancy contributions, results in:

$$m_i \frac{\mathrm{d}\mathbf{v}}{\mathrm{d}t} = 3\pi\mu_c D(\mathbf{u}_c - \mathbf{v}) + (\rho_d - \rho_c) V_i \mathbf{g}. \tag{3.16}$$

With help of the definition of the particle relaxation time (see section 2.1.1), the equation of motion becomes:

$$\frac{\mathrm{d}\mathbf{v}}{\mathrm{d}t} = \frac{\mathbf{u}_c - \mathbf{v}}{\tau} + \left(1 - \frac{\rho_c}{\rho_d}\right)\mathbf{g}. \tag{3.17}$$

The solution of this equation for a simplified case representing a jump in the fluid velocity from zero to $\mathbf{u}_c = (u_{c,x}, 0, 0)$ and an initial particle velocity of zero, gives the evolution of the particle axial velocity, v_x (no gravity acting in this direction). Hence:

$$v_x = u_{c,x}(1 - e^{-\frac{t}{\tau}}). \tag{3.18}$$

From this equation it is obvious that the particle relaxation time, τ, is the time required for a particle, released with zero velocity into a flow with $\mathbf{u}_c$, to reach $(1-1/e) = 63.2$ % of the terminal velocity (in this case, the continuous phase velocity). The solution of Eq. (3.17) is schematically represented in Fig. 3.3. Another interpretation for τ is the time that would be required to reach the terminal velocity if the initial acceleration was kept constant. This can be seen by manipulating Eq.(3.17):

$$\begin{aligned} \frac{\mathrm{d}\mathbf{v}}{\mathrm{d}t} &= \left.\frac{\mathrm{d}\mathbf{v}}{\mathrm{d}t}\right|_{t=0} = \frac{\Delta\mathbf{v}}{\Delta t} = \frac{\mathbf{u}_c}{\tau} \\ \Rightarrow \quad & t|_{\mathbf{v}\to\mathbf{u}_c} = \tau. \end{aligned} \tag{3.19}$$

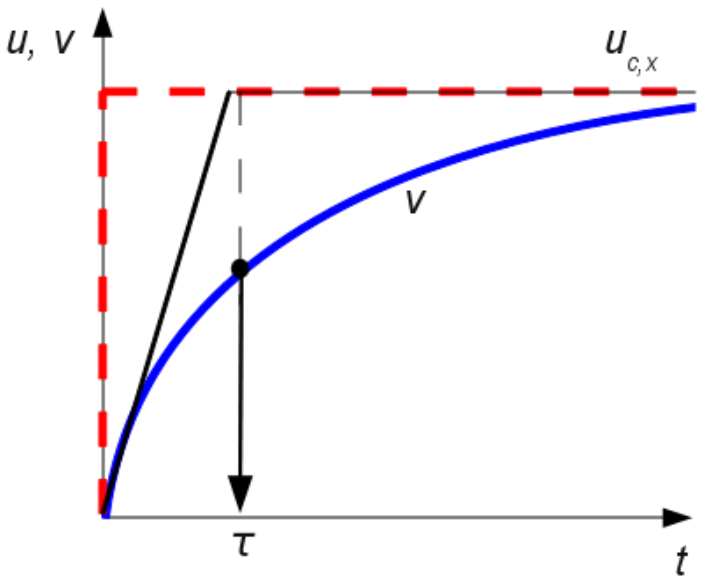

Figure 3.3: Schematic representation of the solution of Eq. (3.17).

Note that the solution of Eq. (3.17) for a constant $\mathbf{u}_c$, including gravity and buoyancy contributions, yields the following asymptotic value for the particle velocity (terminal velocity):

$$\mathbf{v}_T = \mathbf{u}_c + \left(1 - \frac{\rho_c}{\rho_d}\right) \tau \, \mathbf{g}. \tag{3.20}$$

As seen above, the relaxation time is a time scale which characterizes momentum exchange between particle and fluid due to drag. The Stokes number is defined as the ratio between τ and some characteristic time τ_c defined for the flow field:

$$\mathrm{St} = \frac{\tau}{\tau_c}. \tag{3.21}$$

If $St \ll 1$, particles will have sufficient time to respond to changes in the flow and are likely to adopt the fluid velocity very rapidly. On the other hand, for $St \gg 1$, particle movement is not affected by variations in the flow field because there is essentially not enough time to respond to fluid velocity changes.

3.2.2 Particle-Fluid interaction: heat exchange

In the present work, energy coupling between particles and fluid occurs through the mechanisms of heat conduction, advection and phase change. Kinetic energy changes due to efflux of mass (e.g. droplet evaporation) is usually very small compared to the enthalpy fluxes at the surface and shall be therefore neglected. Furthermore, due to the small temperatures considered here, radiative heat transfer will not be accounted for.

The particle temperature equation can then be written as:

$$m_i \, c_{p,d} \frac{\mathrm{d}T_i}{\mathrm{d}t} = \dot{Q}_c + \dot{m} L_v, \tag{3.22}$$

$c_{p,d}$ is the specific heat of the particle material, $\dot{Q}_c$ is the heat transfer rate from the continuous phase, $\dot{m}$ is the rate of mass transfer from the particle surface and L_v is the latent heat of vaporization. The above equation states that the internal energy variation of the particle is controlled by the heat exchange with

the continuous phase and the energy associated with change of phase. For example, if there is no heat transfer to an evaporating droplet, it tends to cool down as mass is evaporated from the surface. Also, at boiling conditions, the amount of heat exchanged with the continuous phase is exactly that required to produce the mass flow rate $\dot{m}$ of vapor at the droplet surface; i.e. $\mathrm{d}T_i/\mathrm{d}t = 0$.

The heat transfer rate $\dot{Q}_c$ at the surface of the particle is given by:

$$\dot{Q}_c = -\int_{S_i} \dot{q}_c dS, \tag{3.23}$$

where $\dot{q}_c$ is the heat transfer rate per unit area (heat flux) from the particle. It is determined by Fourier's law:

$$\dot{q}_c = -k_c \frac{\partial T_c}{\partial r}\bigg|_{r=D/2}, \tag{3.24}$$

k_c the thermal conductivity of the continuous phase, T_c represents its temperature.

Neglecting at first any volumetric sources of heat (i.e., $\dot{m} = 0$), the steady state boundary layer equation (in its non-dimensional form) for the internal energy of an incompressible continuous phase can be written as [41]:

$$\mathbf{u}_c^* \cdot \nabla^* T_c^* = \frac{1}{\mathrm{Re}_p \mathrm{Pr}_c} \nabla^{*2} T_c^*, \tag{3.25}$$

where the dimensionless temperature T_c^* is defined as $T_c^* = \frac{T_c - T_{i,S}}{T_{c,\infty} - T_{i,S}}$; $T_{i,S}$ is the temperature at the particle surface and $T_{c,\infty}$ is the free stream temperature of the continuous phase. The Prandtl number Pr_c can be interpreted as a ratio between the rates of diffusion of momentum and diffusion of thermal energy and is given by:

$$\mathrm{Pr}_c = \frac{\mu_c}{k_c / c_{p,c}}, \tag{3.26}$$

with $c_{p,c}$ the specific heat of the continuous phase.

The product of Reynolds and Prandtl numbers appearing in Eq. (3.25) is called the Peclet number (Pe) and is an important parameter, which defines the role of advection of heat by the fluid. Thus:

$$\mathrm{Pe} = \mathrm{Re}_p \mathrm{Pr}_c. \tag{3.27}$$

The case of Stokes flow implies $\mathrm{Re}_p \ll 1$. According to the above relationship, unless the Prandtl number Pr_c is very large (for air, for example, $\mathrm{Pr} = 0.7$), this condition also implies $\mathrm{Pe} \ll 1$. Under these circumstances, the problem simplifies to solving a conduction equation

$$\nabla^2 T_c = 0, \tag{3.28}$$

with the boundary conditions: $T = T_{i,S}$, for $r = D/2$; $T \to T_{c,\infty}$, for $r \to \infty$. In this case, the analytical temperature profile along the radial coordinate r is given by:

$$T_c(r) = T_{c,\infty} + \frac{D}{2r}(T_{i,S} - T_{c,\infty}). \tag{3.29}$$

It is also possible to determine the heat flux from the fluid to the particle:

$$\dot{q}_c = k_c \left.\frac{\partial T_c}{\partial r}\right|_{r=D/2} = \frac{2k_c}{D}(T_{c,\infty} - T_{S,i}). \tag{3.30}$$

The heat transfer at a surface is usually expressed with help of the concept of a convective heat transfer coefficient defined by Newton's law: $\dot{q}_c = h_{tc}(T_{c,\infty} - T_{S,i})$. With this definition, the heat transfer coefficient h_{tc} is given by:

$$h_{tc} = \frac{-k_c \left.\frac{\partial T_c}{\partial r}\right|_{r=D/2}}{T_{i,S} - T_{c,\infty}} = \frac{2k_c}{D}. \tag{3.31}$$

The Nusselt number (Nu) represents the dimensionless rate of heat transfer and is given by:

$$\mathrm{Nu} = \frac{\partial T_c^*}{\partial r^*}\Big|_{r^*=1} = \frac{h_{tc} D}{k_c}. \tag{3.32}$$

Based on the above analysis, the following expression for Nu is obtained:

$$\mathrm{Nu} = 2. \tag{3.33}$$

Consider now a particle moving in a fluid (with $\mathrm{Re}_p, \mathrm{Pe} \ll 1$) and that the particle temperature is nearly uniform in the interior and on the surface. This should be the case if the convective heat transfer coefficient is small compared to the internal heat transfer coefficient (due to conduction) calculated across the particle radius. This is measured by the so called Biot number (Bi), defined as

$$\mathrm{Bi} = \frac{h_{tc} D}{2 k_d}. \tag{3.34}$$

k_d is the thermal conductivity of the particle material. According to Eq. (3.31), Bi is given by the ratio of continuous and dispersed phase conductivities, $\mathrm{Bi} = \frac{k_c}{k_d}$. For water droplets in air, $\mathrm{Bi} \ll 1$, and $T_{i,S} \approx T_i$. The expression for the heat flux at the particle surface can be substituted in Eq. (3.23), yielding:

$$\dot{Q}_c = -\int_{S_i} \frac{2k_c}{D}(T_{c,\infty} - T_i)\, dS = \frac{2k_c}{D}(T_{c,\infty} - T_i)\, A_i, \tag{3.35}$$

with $A_i = \pi D^2$; i.e. the particle surface area. Finally, upon substitution of the above expression into the particle temperature equation:

$$m_i \frac{\mathrm{d}T_i}{\mathrm{d}t} = 2\pi D k_c (T_{c,\infty} - T_i). \tag{3.36}$$

The above equation can be generalized for non-creeping conditions:

$$m_i \frac{\mathrm{d}T_i}{\mathrm{d}t} = \mathrm{Nu}\,\pi D k_c (T_{c,\infty} - T_i), \tag{3.37}$$

with the Nusselt number usually given by the correlation due to Ranz and Marshall [68]:

$$\mathrm{Nu} = 2 + 0.6\mathrm{Re}_p^{\frac{1}{2}}\mathrm{Pr}^{\frac{1}{3}}. \tag{3.38}$$

3.2.3 Particle-Fluid interaction: mass diffusion

The particle continuity equation states that the rate of change of the particle mass equals the total mass efflux through the surface:

$$\dot{m} = \frac{\mathrm{d}m_i}{\mathrm{d}t} = \int_{S_i} \rho_d \,(\hat{\mathbf{u}} \cdot \mathbf{n}) dS = \dot{m}'' A_i. \tag{3.39}$$

In general, it is assumed that a binary mixture exists, consisting of the gas phase and the vapor of the particle liquid. Fick's law describes the mass flux at the surface of a particle in a binary mixture as:

$$\dot{m}'' = -\rho_c \mathscr{D}_{cd} \left.\frac{\partial Y_v}{\partial r}\right|_{r=D/2}, \tag{3.40}$$

with $\mathscr{D}_{cd}$ the binary diffusion coefficient associated to the mixture comprising of continuous and dispersed phases.

The non-dimensional form of the concentration equation reads:

$$\mathbf{u}_c^* \cdot \nabla^* Y_v^* = \frac{1}{\mathrm{Re}_p \mathrm{Sc}_c} \nabla^{*2} Y_v^*, \tag{3.41}$$

where Y_v^* is defined as $Y_v^* = \frac{Y_v - Y_S}{Y_{v,\infty} - Y_S}$; Y_S is the vapor mass fraction at the particle surface and $Y_{v,\infty}$ is the vapor mass fraction far from the surface.

The Schmidt number Sc_c represents the ratio of rates of diffusion of momentum and diffusion of mass:

$$\mathrm{Sc}_c = \frac{\mu_c}{\rho_c \mathscr{D}_{cd}}. \tag{3.42}$$

Since, for air, $\mathrm{Sc}_c \approx 1$, Stokes flow also implies that the convective transport of vapor from the particle surface is negligible compared to the diffusive transport. Thus, the solution of a diffusion equation allows the determination of the vapor mass fraction profile – which is analogous to the temperature profile determined in the previous section. A similar anaysis to the heat diffusion problem also allows the definition of the Sherwood number (Sh) – the equivalent of the Nusselt number for mass transfer – given by:

$$\mathrm{Sh} = \left.\frac{\partial Y_v^*}{\partial r^*}\right|_{r^*=1} = \frac{h_m D}{\mathscr{D}_{cd}}, \tag{3.43}$$

where h_m is a mass transfer coefficient, defined as:

$$h_m = \frac{2\mathscr{D}_{cd}}{D}\left.\frac{\partial Y_v^*}{\partial r^*}\right|_{r^*=1}. \tag{3.44}$$

Based on the above analysis, similarly to the heat transfer problem, the Sherwood number is given by:

$$\mathrm{Sh} = 2. \tag{3.45}$$

If convective transport of vapor from the droplet surface is significant (e.g. high relative velocity between particle and continuous phase), the Ranz-Marshall correlation can also be generalized for the mass transfer problem:

$$\mathrm{Sh} = 2 + 0.6\mathrm{Re}_p^{\frac{1}{2}}\mathrm{Sc}^{\frac{1}{3}}. \tag{3.46}$$

Finally, the particle mass conservation equation for the pure diffusive limit with no heat transfer associated can be written as:

$$\frac{\dot{m}}{A_i} = \dot{m}'' = -\mathrm{Sh}\,\pi D \rho_c \mathscr{D}_{cd}(Y_{v,\infty} - Y_S). \tag{3.47}$$

3.2.4 Coupled heat and mass exchange – Stefan problem

The coupled problem of heat and mass exchange appears for example in the description of droplet evaporation in sprays. Evaporation is the process of phase change at the droplet surface and the transport of vapor away from the surface. The driving force of evaporation is the gradient in concentration between the droplet surface and the free stream. Obviously, the gas phase must provide the sufficient amount of latent heat in order that phase change occurs at the surface.

The previous separate analysis for heat and mass exchange with the continuous phase provides the basis for the derivation of analytical expressions when both processes are coupled. Mass and energy balances at the interface between the droplet and the gas phase are written in this case as:

$$\dot{m}''(1 - Y_S) = -\rho_c \mathscr{D}_{cd} \left.\frac{\partial Y_v}{\partial r}\right|_{r=D/2}, \tag{3.48}$$

and

$$k_d \left.\frac{\partial T_{i,S}}{\partial r}\right|_{r=D/2,d} - k_c \left.\frac{\partial T_c}{\partial r}\right|_{r=D/2,c} = \dot{m}'' L_v, \tag{3.49}$$

respectively.

In Eq. (3.48), the mass flux is evaluated with respect to the regressing surface of the evaporating droplet, taking into account the Stefan convection. Equation (3.49) represents a balance of heat fluxes at the droplet surface: the difference in the conductive heat fluxes at both sides of the interface (droplet,

"d" and gas, or continuous phase, "c") equates the energy required for vaporizing the liquid at the interface. An additional condition is required for the relationship between the liquid heating rate and the interface temperature. As mentioned before, for Bi $\ll 1$, it is reasonable to assume that $T_{i,S} \approx T_i$ and $\partial T_{i,S}/\partial r|_{r=D/2,d} \approx 0$.

For the special case of unitary Lewis number (Le ≈ 1, i.e. $\rho_c \mathscr{D}_{cd} = k_c/c_{p,c}$), the coupled solution of energy and vapor mass fraction equations taking into account diffusion and Stefan convection (with respect to the droplet's moving surface) yields the following algebraic expression for the rate of vaporization:

$$\dot{m} = \frac{\mathrm{d}m_i}{\mathrm{d}t} = -2\pi D \frac{k_c}{c_{p,c}} \ln(1+B_m). \tag{3.50}$$

B_m is the Spalding mass transfer number:

$$B_m = \frac{Y_S - Y_{v,\infty}}{1-Y_S}. \tag{3.51}$$

The evaporative Sherwood (Sh) number is:

$$\mathrm{Sh} = 2\,\frac{\ln(1+B_m)}{B_m}. \tag{3.52}$$

The evaporative Nusselt (Nu) number is taken to be equal to the evaporative Sherwood number. Note that for the non-vaporizing limit, $B_m \to 0$ and the classical result for the heated sphere derived in the previous section is recovered (Nu = 2).

Equation (3.50) is frequently referred to in the literature as D^2-*Law*. The reason for that lies in the fact that the rate of decrease of the droplet surface is constant (i.e., it does not depend on the droplet size):

$$\frac{\mathrm{d}D^2}{\mathrm{d}t} = \lambda^* = -8\frac{1}{\rho_d}\frac{k_c}{c_{p,c}} \ln(1+B_m) = \text{ constant}. \tag{3.53}$$

The determination of the rate of vaporization given by Eq. (3.50) still requires knowledge of the mass transfer number B_m, which depends on the vapor mass fraction at the droplet surface, Y_S, as well as the free stream value $Y_{c,\infty}$. For the latter, a transport equation can be formulated, as will be seen later. Y_S can be determined using the Clausius-Clapeyron equation (assuming phase equilibrium at the interface):

$$Y_S = \frac{1}{1 + \frac{W_{mix}}{W_{fuel}}(\frac{p}{p_v} - 1)}, \tag{3.54}$$

with

$$\frac{p}{p_v} = e^{\frac{L_v}{R}\left(\frac{1}{T_i} - \frac{1}{T_{boil}}\right)} \tag{3.55}$$

and

$$W_{mix} = (1 - Y_{v,\infty})W_{air} + Y_{v,\infty}W_{fuel}. \tag{3.56}$$

In the above equations, W_{fuel}, W_{air} and W_{mix} represent the molar masses of fuel, air and mixture, respectively. p_v is the vapor pressure and R is the gas constant.

3.3 Continuous phase equations

The previous sections were concerned with the phenomenology of momentum, heat and mass exchange between phases at the scale of one particle. Various sub-models were presented and discussed. These are relevant to develop appropriate closure models for dispersed and continuous phase averaged equations, because the averaging procedure itself leads to loss of information at the scale of the particle size. Very small volume fractions will be considered in this work, i.e., the disperse flow will be essentially dilute. Hence, it will be assumed that these models will be considered valid even when a collection of particles exist.

Various approaches exist as to how to perform averaging of the single phase equations, such as time, volume and ensemble averaging (and combinations of them). There is still no consensus in the literature on the superiority of any of them versus the others, probably because the outcome of averaging is very similar in all cases, while differences are expected to be marginal comparing to the typical uncertainty of the closure relations required to close the averaged system of conservation laws. Volume averaging seems to be the most natural in a finite volume CFD context and will be used as basis for the development of averaged equations [22, 67]. In the volume averaging procedure, however, turbulent fluctuations are not explicitly involved and the equations retain their instantaneous form. Therefore, in the present work, a double averaging procedure with phase weighted quantities (analogous to Favre-averaging of variable density flows) will be used along the lines of Oliveira [63].

Consider a characteristic volume $\mathcal{V}$ as shown in Fig. 3.4. Note that the purpose is not to discretize the spatial domain, but to develop a set of averaged equations. For this reason, the characteristic volume does not need to be necessarily Cartesian; it is rather more important that its dimensions are much bigger than typical non-uniformities of the flow (e.g. velocity gradients of the flow around each particle), and at the same time much smaller than the global dimensions of the problem[1]. However, it is important to point out that a key assumption regarding Eulerian models for the dispersed phase is that there are many particles in a computational cell-volume, which implies that the control volume sizes are much greater than the average inter-particle spacing ($\mathcal{V} \gg l_p^3$).

Subdividing the total volume of the mixture into continuous phase and dispersed phase contributions ($\mathcal{V}_c$ and $\mathcal{V}_d$, respectively), such that:

$$\mathcal{V} = \mathcal{V}_c \cup \mathcal{V}_d. \tag{3.57}$$

It is useful to define an indicator function $X_c(\mathbf{x}, t)$ as follows:

[1] For simplicity, boundary particles (i.e. particles which are crossed by the control surface) will not be considered in the derivation, since they do not influence the basic structure of the resulting set of equations [22, 67]

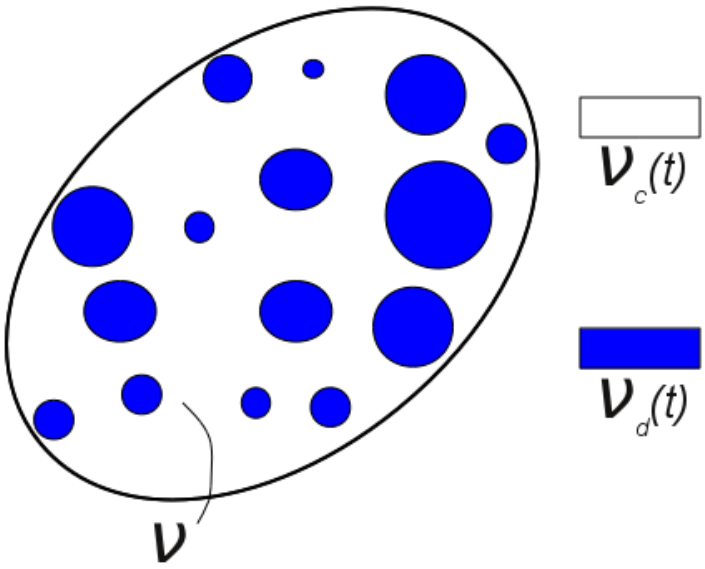

Figure 3.4: Characteristic control volume $\mathcal{V}$ enclosing both phases.

$$X_c(\mathbf{x}, t) = \begin{cases} 1 & \text{if } \mathbf{x} \in \mathcal{V}_c \\ 0 & \text{otherwise} \end{cases} \tag{3.58}$$

The topological equation describes the evolution of $X_c(\mathbf{x}, t)$ and is given by:

$$\frac{DX_c}{Dt} = \frac{\partial X_c}{\partial t} + \mathbf{u}_i \cdot \nabla X_c = 0, \tag{3.59}$$

with $\mathbf{u}_i$ the velocity of the interface and

$$\nabla X_c = \mathbf{n}_c \delta(\mathbf{x} - \mathbf{x}_i) \tag{3.60}$$

and

$$\mathbf{n}_c = -\frac{\nabla X_c}{|\nabla X_c|}\bigg|_i. \tag{3.61}$$

In the above equations, δ is the dirac-function and $\mathbf{x}_i$ denotes all points on the

surface S_i which describes the interface between phases; $\mathbf{n}_c$ is the unit vector normal to S_i and points from phase c outwards.

The variation of X_d (X_c is obviously analogous) and ∇ along a directional coordinate s is schematically represented in Fig. 3.5.

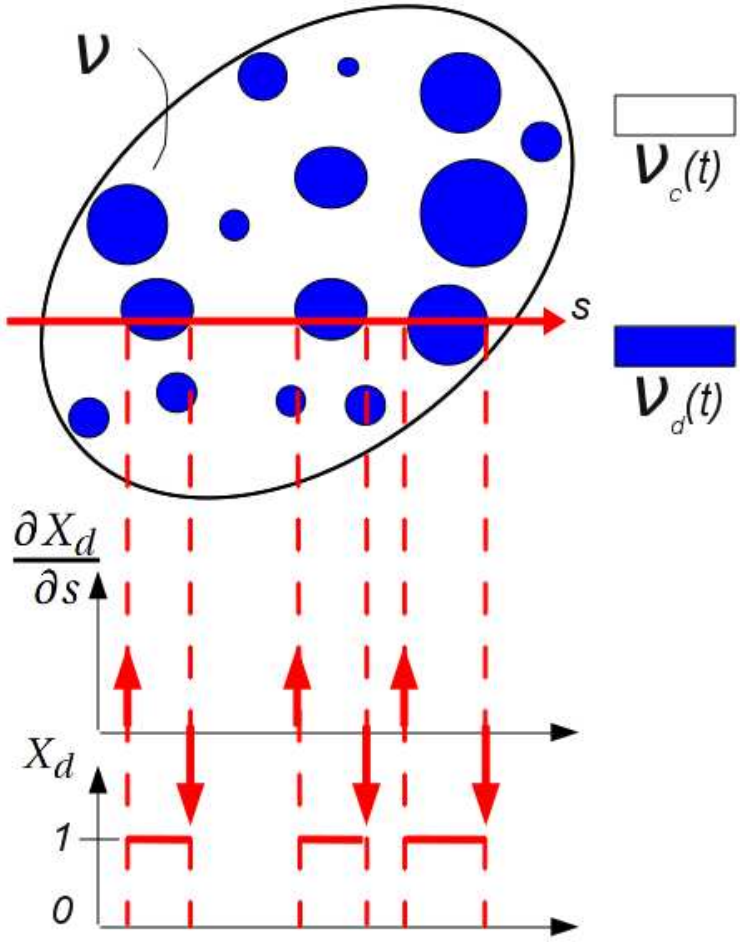

Figure 3.5: Characteristic control volume $\mathcal{V}$ and variation of X_d and ∇X_d along s, i.e. $\frac{\partial X_d}{\partial s}$.

$X_c(\mathbf{x}, t)$ can be averaged over the characteristic volume $\mathcal{V}$, which results in the volume fraction of the continuous phase:

$$\alpha_c = \frac{1}{\mathcal{V}} \int_{\mathcal{V}} X_c(\mathbf{x}, t)\, dV = \frac{\mathcal{V}_c(t)}{\mathcal{V}}. \tag{3.62}$$

The volume average over $\mathcal{V}$ of a general quantitiy (scalar or tensor) defined for the continuous phase is defined as follows:

$$\langle \Psi_c \rangle^{\mathcal{V}} = \frac{1}{\mathcal{V}} \int_{\mathcal{V}} \Psi_c(\mathbf{x}, t) X_c(\mathbf{x}, t)\, dV. \tag{3.63}$$

Analogously, the average over $\mathcal{V}_c$ is:

$$\langle \Psi_c \rangle^{\mathcal{V}_c} = \frac{1}{\mathcal{V}_c} \int_{\mathcal{V}_c} \Psi_c(\mathbf{x}, t) X_c(\mathbf{x}, t)\, dV. \tag{3.64}$$

It is possible to write:

$$\langle X_c \Psi_c \rangle^{\mathcal{V}} = \frac{1}{\mathcal{V}_c} \int_{\mathcal{V}} \Psi_c(\mathbf{x}, t) \underbrace{X_c(\mathbf{x}, t) X_c(\mathbf{x}, t)}_{X_c(\mathbf{x}, t)}\, dV = \alpha_c \langle \Psi_c \rangle^{\mathcal{V}_c}. \tag{3.65}$$

Therefore:

$$\langle X_c \Psi_c \rangle^{\mathcal{V}} = \alpha_c \langle \Psi_c \rangle^{\mathcal{V}_c}. \tag{3.66}$$

Concerning the gradient of Ψ_c, the following relation is valid (with $\langle \nabla \Psi_c \rangle^{\mathcal{V}} = \nabla \langle \Psi_c \rangle^{\mathcal{V}}$):

$$\langle \nabla \Psi_c \rangle^{\mathcal{V}} = \nabla \langle X_k \Psi_c \rangle^{\mathcal{V}} - \langle \Psi_c \nabla X_c \rangle^{\mathcal{V}}, \tag{3.67}$$

where the product rule was implicitly used. With Eq. (3.60), it follows that:

$$-\langle \Psi_c \nabla X_c \rangle^{\mathcal{V}} = \frac{1}{\mathcal{V}} \int_{\mathcal{V}} \Psi_c(\mathbf{x}, t) \delta(\mathbf{x} - \mathbf{x}_i, t) \mathbf{n}_c dV = \frac{1}{\mathcal{V}} \int_{S_i \cap \mathcal{V}} \Psi_{c,i}(\mathbf{x}, t) \mathbf{n}_c dS. \tag{3.68}$$

$\Psi_{c,i}$ denotes the values of Ψ along the continuous phase side of the surface and $S_i \cap \mathcal{V}$ is the interface between phases inside the characteristic volume $\mathcal{V}$.

Furthermore, with help of the topological equation:

$$\begin{aligned} -\langle \Psi_c \frac{\partial X_c}{\partial t} \rangle^{\mathcal{V}} &= \langle \Psi_c \mathbf{u}_i \cdot \nabla X_c \rangle^{\mathcal{V}} = \frac{1}{\mathcal{V}} \int_{S_i} \Psi_c \delta(\mathbf{x} - \mathbf{x}_i, t) \mathbf{u}_i \cdot (-\mathbf{n}_c) dS \\ &= \frac{1}{\mathcal{V}} \int_{S_i} \Psi_{c,i} \mathbf{u}_i \cdot (-\mathbf{n}_c) dS. \end{aligned} \tag{3.69}$$

The above relations form the basis for the derivation of volume-averaged equations for the continuous phase.

3.3.1 Continuity equation

Multiplying the continuity equation for the continuous phase by the indicator function and averaging over $\mathcal{V}$ results in:

$$\langle X_c \frac{\partial \rho_c}{\partial t} \rangle^{\mathcal{V}} + \langle X_c \nabla \cdot (\rho_c \mathbf{u}_c) \rangle^{\mathcal{V}} = 0. \tag{3.70}$$

The first term can be rewritten as

$$\langle X_c \frac{\partial \rho_c}{\partial t} \rangle^{\mathcal{V}} = \frac{\partial \langle (\rho_c X_c) \rangle^{\mathcal{V}}}{\partial t} - \langle \rho_c \frac{\partial X_c}{\partial t} \rangle^{\mathcal{V}}, \tag{3.71}$$

with

$$-\langle \rho_c \frac{\partial X_c}{\partial t} \rangle^{\mathcal{V}} = \langle \rho_c \mathbf{u}_i \cdot \nabla X_c \rangle^{\mathcal{V}} = \frac{1}{\mathcal{V}} \int_{S_i} \rho_{c,i} \mathbf{u}_i \cdot (-\mathbf{n}_c) dS. \tag{3.72}$$

The convective term becomes:

$$\langle X_c \nabla \cdot (\rho_c \mathbf{u}_c) \rangle^{\mathcal{V}} = \nabla \cdot \langle (X_c \rho_c \mathbf{u}_c) \rangle^{\mathcal{V}} - \frac{1}{\mathcal{V}} \int_{S_i} \rho_{c,i} \mathbf{u}_{c,i} \cdot (-\mathbf{n}_c) dS. \tag{3.73}$$

Rearrangement of the above relations yields (with $\rho_{c,i} = \rho_c$):

$$\frac{\partial \langle (\rho_c X_c) \rangle^{\mathcal{V}}}{\partial t} + \nabla \cdot \langle (X_c \rho_c \mathbf{u}_c) \rangle^{\mathcal{V}} = \frac{1}{\mathcal{V}} \int_{S_i} \rho_c (\mathbf{u}_i - \mathbf{u}_{c,i}) \cdot \mathbf{n}_c dS. \tag{3.74}$$

Finally, with help of Eq. (3.66):

$$\frac{\partial (\langle \rho_c \rangle^{\mathcal{V}_c} \alpha_c)}{\partial t} + \nabla \cdot (\langle \rho_c \mathbf{u}_c \rangle^{\mathcal{V}_c} \alpha_c) = \frac{1}{\mathcal{V}} \int_{S_i} \rho_c (\mathbf{u}_i - \mathbf{u}_{c,i}) \cdot \mathbf{n}_c dS. \tag{3.75}$$

A source term Γ can be defined as:

$$\Gamma = \frac{1}{\mathcal{V}} \int_{S_i \cap \mathcal{V}} \rho_c (\mathbf{u}_{c,i} - \mathbf{u}_i) \cdot \mathbf{n}_c dS, \tag{3.76}$$

i.e., $-\Gamma$ represents loss of mass, if $\mathbf{u}_{c,i} > \mathbf{u}_i$ ($\mathbf{n}_c$ points into the dispersed phase).

3.3.2 Momentum equation

With the above definitions and results, it may be written for the momentum equation:

$$\langle X_c \frac{\partial (\rho_c \mathbf{u}_c)}{\partial t} \rangle^{\mathcal{V}} + \langle X_c \nabla \cdot (\rho_c \mathbf{u}_c \mathbf{u}_c) \rangle^{\mathcal{V}} = -\langle X_c \nabla p \rangle^{\mathcal{V}} + \langle X_c \nabla \cdot \boldsymbol{\tau} \rangle^{\mathcal{V}} + \langle X_c \rho_c \mathbf{g} \rangle^{\mathcal{V}}. \tag{3.77}$$

The time derivative term takes the following form:

$$\begin{aligned} \langle X_c \frac{\partial (\rho_c \mathbf{u}_c)}{\partial t} \rangle^{\mathcal{V}} &= \frac{\partial \langle (X_c \rho_c \mathbf{u}_c) \rangle^{\mathcal{V}}}{\partial t} - \langle \rho_c \mathbf{u}_c \frac{\partial X_c}{\partial t} \rangle^{\mathcal{V}} \\ &= \frac{\partial (\alpha_c \langle \rho_c \mathbf{u}_c \rangle^{\mathcal{V}_c})}{\partial t} + \frac{1}{\mathcal{V}} \int_{S_i} \rho_c \mathbf{u}_{c,i} \mathbf{u}_i \cdot (-\mathbf{n}_c) dS. \end{aligned} \tag{3.78}$$

For the convective term, it is possible to write:

$$\begin{aligned}\langle X_c \nabla \cdot (\rho_c \mathbf{u}_c \mathbf{u}_c) \rangle^{\mathcal{V}} &= \nabla \cdot (\langle X_c \rho_c \mathbf{u}_c \mathbf{u}_c \rangle^{\mathcal{V}}) - \langle (\rho_c \mathbf{u}_c \mathbf{u}_c) \cdot \nabla X_c \rangle^{\mathcal{V}} \\ &= \nabla \cdot (\alpha_c \langle \rho_c \mathbf{u}_c \mathbf{u}_c \rangle^{\mathcal{V}_c}) + \frac{1}{\mathcal{V}} \int_{S_i} \rho_{c,i} \mathbf{u}_{c,i} \mathbf{u}_{c,i} \cdot \mathbf{n}_c dS.\end{aligned} \tag{3.79}$$

Pressure and shear stress terms are obtained in the following operations:

$$\begin{aligned}\langle X_c \nabla p \rangle^{\mathcal{V}} &= \nabla \langle X_c p \rangle^{\mathcal{V}} - \langle p \nabla X_c \rangle^{\mathcal{V}} \\ &= \nabla (\alpha_c \langle p \rangle^{\mathcal{V}_c}) + \frac{1}{\mathcal{V}} \int_{S_i} p_i \boldsymbol{I} \cdot \mathbf{n}_c dS\end{aligned} \tag{3.80}$$

$$\begin{aligned}\langle X_c \nabla \cdot \boldsymbol{\tau} \rangle^{\mathcal{V}} &= \nabla \cdot \langle X_c \boldsymbol{\tau} \rangle^{\mathcal{V}} - \langle \boldsymbol{\tau} \cdot \nabla X_c \rangle^{\mathcal{V}} \\ &= \nabla \cdot (\alpha_c \langle \boldsymbol{\tau} \rangle^{\mathcal{V}_c}) + \frac{1}{\mathcal{V}} \int_{S_i} \boldsymbol{\tau}_i \cdot \mathbf{n}_c dS\end{aligned} \tag{3.81}$$

and for the gravity term:

$$\langle X_c \rho_c \mathbf{g} \rangle^{\mathcal{V}} = \alpha_c \langle \rho_c \rangle^{\mathcal{V}_c} \mathbf{g}. \tag{3.82}$$

Rearranging:

$$\begin{aligned}\frac{\partial (\alpha_c \langle \rho_c \mathbf{u}_c \rangle^{\mathcal{V}_c})}{\partial t} + \nabla \cdot (\alpha_c \langle \rho_c \mathbf{u}_c \mathbf{u}_c \rangle^{\mathcal{V}_c}) &= -\nabla (\alpha_c \langle p \rangle^{\mathcal{V}_c}) + \nabla \cdot (\alpha_c \langle \boldsymbol{\tau} \rangle^{\mathcal{V}_c}) \\ &+ \alpha_c \langle \rho_c \rangle^{\mathcal{V}_c} \mathbf{g} \\ &- \frac{1}{\mathcal{V}} \int_{S_i} p_i \boldsymbol{I} \cdot \mathbf{n}_c dS + \frac{1}{\mathcal{V}} \int_{S_i} \boldsymbol{\tau}_i \cdot \mathbf{n}_c dS \\ &+ \frac{1}{\mathcal{V}} \int_{S_i} \rho_c \mathbf{u}_{c,i} (\mathbf{u}_i - \mathbf{u}_{c,i}) \cdot \mathbf{n}_c dS.\end{aligned} \tag{3.83}$$

At this point, care must be taken when identifying the interphase forces in the volume-averaged momentum equation for the continuous phase. It is very common to consider the surface integrals in Eq. (3.83) (excluding the last term, which obviously accounts for the momentum that the continuous phase gains or loses due to phase change) equal to the total hydrodynamic force (per unit volume) acting on the particles. However, as pointed out by Prosperetti [67], this might lead to a physically incorrect result. Consider for instance a system at rest without external forces. In this case, the LHS of Eq. (3.83) vanishes, as well as shear stresses, while the term $\langle p \rangle^{\mathcal{V}_c}$ is constant. Therefore, it is possible to write: $\nabla(\alpha_c \langle p \rangle^{\mathcal{V}_c}) = \langle p \rangle^{\mathcal{V}_c} \nabla \alpha_c$. This, if correct, would imply that an extra source of momentum exists only due to the spatial arrangement of the phases, which is clearly non-physical.

Therefore, the correct procedure – in line with Prosperetti's [67] arguments – must involve the rearrangement of pressure and shear stress terms. Thus:

$$\nabla(\alpha_c \langle p \rangle^{\mathcal{V}_c}) + \frac{1}{\mathcal{V}} \int_{S_i} p_i \boldsymbol{I} \cdot \mathbf{n}_c dS \;=\; \alpha_c \nabla \langle p \rangle^{\mathcal{V}_c} + \langle p \rangle^{\mathcal{V}_c} \nabla \alpha_c + \frac{1}{\mathcal{V}} \int_{S_i} p_i \boldsymbol{I} \cdot \mathbf{n}_c dS \tag{3.84}$$

$$\nabla \cdot (\alpha_c \langle \boldsymbol{\tau} \rangle^{\mathcal{V}_c}) + \frac{1}{\mathcal{V}} \int_{S_i} \boldsymbol{\tau}_i \cdot \mathbf{n}_c dS \;=\; \alpha_c \nabla \cdot \langle \boldsymbol{\tau} \rangle^{\mathcal{V}_c} + \langle \boldsymbol{\tau} \rangle^{\mathcal{V}_c} \cdot \nabla \alpha_c + \frac{1}{\mathcal{V}} \int_{S_i} \boldsymbol{\tau}_i \cdot \mathbf{n}_c dS \tag{3.85}$$

The terms $\langle p \rangle^{\mathcal{V}_c} \nabla \alpha_c$ and $\langle \boldsymbol{\tau} \rangle^{\mathcal{V}_c} \cdot \nabla \alpha_c$ can be recast as

$$\langle p \rangle^{\mathcal{V}_c} \nabla \alpha_c = \langle p \rangle^{\mathcal{V}_c} \frac{1}{\mathcal{V}} \int_V \underbrace{\nabla \mathbf{X}_c}_{\mathbf{n}_c \delta(\mathbf{x}-\mathbf{x}_i)} dV = \frac{1}{\mathcal{V}} \int_{S_i} \langle p \rangle^{\mathcal{V}_c} \boldsymbol{I} \cdot \mathbf{n}_c dS \tag{3.86}$$

and

$$\langle \boldsymbol{\tau} \rangle^{\mathcal{V}_c} \cdot \nabla \alpha_c = \langle \boldsymbol{\tau} \rangle^{\mathcal{V}_c} \frac{1}{\mathcal{V}} \int_V \underbrace{\nabla \mathbf{X}_c}_{\mathbf{n}_c \delta(\mathbf{x}-\mathbf{x}_i)} dV = \frac{1}{\mathcal{V}} \int_{S_i} \langle \boldsymbol{\tau} \rangle^{\mathcal{V}_c} \cdot \mathbf{n}_c dS, \tag{3.87}$$

respectively.

The momentum equation is now expressed as:

$$\begin{aligned}\frac{\partial(\alpha_c\langle\rho_c\mathbf{u}_c\rangle^{\mathcal{V}_c})}{\partial t}+\nabla\cdot(\alpha_c\langle\rho_c\mathbf{u}_c\mathbf{u}_c\rangle^{\mathcal{V}_c}) &= -\alpha_c\nabla\langle p\rangle^{\mathcal{V}_c}+\alpha_c\nabla\cdot\langle\boldsymbol{\tau}\rangle^{\mathcal{V}_c}\\ &+ \alpha_c\langle\rho_c\rangle^{\mathcal{V}_c}\mathbf{g}\\ &- \frac{1}{\mathcal{V}}\int_{S_i}(\langle p\rangle^{\mathcal{V}_c}-p_i)\boldsymbol{I}\cdot\mathbf{n}_c dS\\ &+ \frac{1}{\mathcal{V}}\int_{S_i}(\langle\boldsymbol{\tau}\rangle^{\mathcal{V}_c}-\boldsymbol{\tau}_i)\cdot\mathbf{n}_c dS\\ &+ \frac{1}{\mathcal{V}}\int_{S_i}\rho_c\mathbf{u}_{c,i}(\mathbf{u}_i-\mathbf{u}_{c,i})\cdot\mathbf{n}_c dS.\end{aligned} \tag{3.88}$$

Consider now that small air bubbles are immersed in a steady uniform water stream. In addition to the gravitational field, there is a contribution of stresses generated by gradients in the flow field (velocity, pressure). It will be basically assumed here that the characteristics of the interaction between individual particles and their immediate surroundings (which give rise to a drag force, for example) are approximately independent on the large scale structure of the stress field (such as macroscopic pressure gradient due to gravity for example). As shown before, the errors which derive from this assumption are expected to be less important for $Re_p \ll 1$. This argument has been also formalized by Prosperetti [67].

According to the above analysis, it might be useful to rewrite the RHS of Eq. (3.88) as (the momentum exchange due to phase change has been disregarded, for simplicity):

$$\begin{aligned}\text{RHS} &= -\nabla\langle p\rangle^{\mathcal{V}_c}+\nabla\cdot\langle\boldsymbol{\tau}\rangle^{\mathcal{V}_c}+\alpha_c\langle\rho_c\rangle^{\mathcal{V}_c}\mathbf{g}\\ &+ \alpha_d\nabla\langle p\rangle^{\mathcal{V}_c}-\alpha_d\nabla\cdot\langle\boldsymbol{\tau}\rangle^{\mathcal{V}_c}\\ &- \frac{1}{\mathcal{V}}\int_{S_i}(\langle p\rangle^{\mathcal{V}_c}-p_i)\boldsymbol{I}\cdot\mathbf{n}_c dS\end{aligned}$$

$$+ \quad \frac{1}{\mathcal{V}} \int_{S_i} (\langle \boldsymbol{\tau} \rangle^{\mathcal{V}_c} - \boldsymbol{\tau}_i) \cdot \mathbf{n}_c dS \tag{3.89}$$

Pressure and shear stress terms were rewritten with help of the constraint $\alpha_c + \alpha_d = 1$ (monodisperse). The fourth and fifth terms are identified as forces that arise due to large scale non-uniformities of the continuous phase flow. Again, for modeling purposes, it is clear that there exists a separation of "macroscale" forces, which appear due to large scale effects caused for instance by stress gradients in the main flow and "microscale" forces as a result of the strucure of the flow around each particle – represented by the surface integrals in the above equation. The latter can be modeled by drag or lift forces, as already pointed out before. Thus, it can be written in an explanatory manner:

$$\begin{aligned} -\mathbf{M} \quad = \quad & -\frac{1}{\mathcal{V}} \sum \mathbf{F} = \underbrace{-\alpha_d \nabla \langle p \rangle^{\mathcal{V}_c} + \alpha_d \nabla \cdot \langle \boldsymbol{\tau} \rangle^{\mathcal{V}_c}}_{\text{macroscale effects}} \\ & + \underbrace{\frac{1}{\mathcal{V}} \int_{S_i} (\langle p \rangle^{\mathcal{V}_c} - p_i) \boldsymbol{I} \cdot \mathbf{n}_c dS - \frac{1}{\mathcal{V}} \int_{S_i} (\langle \boldsymbol{\tau} \rangle^{\mathcal{V}_c} - \boldsymbol{\tau}_i) \cdot \mathbf{n}_c dS}_{\text{microscale effects}} \end{aligned} \tag{3.90}$$

The momentum transfer term **M** represents the sum of forces **F** (per unit volume) acting on the dispersed phase. Modeling of microscale effects in the momentum exchange between phases can only be achieved with *a priori* knowledge of the physical mechanisms behind it for the type of flow in question. That is, since the geometry of the flow is assumed in some sense (dilute dispersed flows of spherical particles), it is appropriate to model these effects through forces formulated as extensions of phenomenological expressions developed for single particle motion. These forces must be consistently formulated together with the dispersed phase equations, as will be seen later on.

In the volume-averaged convective term, $\nabla \cdot (\alpha_c \langle \rho_c \mathbf{u}_c \mathbf{u}_c \rangle^{\mathcal{V}_c})$ the average of the product between velocity components appears and still needs closure. For that purpose, it is possible to define a decomposition (similar to the Reynolds

decomposition for time average) in a volume-averaged and a fluctuating component: $\Psi_c = \langle \Psi_c \rangle^{\mathcal{V}_c} + \Psi_c^{'}$, such that:

$$\begin{aligned}
\langle \Psi_c \Psi_c \rangle^{\mathcal{V}_c} &= \langle \Psi_c \rangle^{\mathcal{V}_c} \langle \Psi_c \rangle^{\mathcal{V}_c} \\
&+ \underbrace{\langle \langle \Psi_c \rangle^{\mathcal{V}_c} \Psi_c^{'} \rangle^{\mathcal{V}_c}}_{=0} + \underbrace{\langle \Psi_c^{'} \langle \Psi_c \rangle^{\mathcal{V}_c} \rangle^{\mathcal{V}_c}}_{=0} \\
&+ \langle \Psi_c^{'} \Psi_c^{'} \rangle^{\mathcal{V}_c}, \\
\Rightarrow \alpha_c \langle \rho_c \mathbf{u}_c \mathbf{u}_c \rangle^{\mathcal{V}_c} &= \alpha_c \rho_c \langle \mathbf{u}_c \rangle^{\mathcal{V}_c} \langle \mathbf{u}_c \rangle^{\mathcal{V}_c} + \alpha_c \underbrace{\rho_c \langle \mathbf{u}_c^{'} \mathbf{u}_c^{'} \rangle^{\mathcal{V}_c}}_{\equiv -\boldsymbol{\tau}_c^{pt}}.
\end{aligned} \tag{3.91}$$

where it is implicitly assumed that the continuous phase is incompressible. The resulting term containing fluctuating velocity components (τ_c^{pt}) is often called *pseudo-turbulence* or *streaming* stress and is analogous to the Reynolds stress in single phase turbulence. It represents sub-volume fluctuations, which can be caused by the flow around particles. Even though the flow does not have to be turbulent to generate this stress, for the purpose of closure this term is usually joined together with the turbulent stresses, as will be discussed later.

3.3.3 Energy equation

For the applications studied in the present work (dispersed flows), mechanical energy effects are small compared to those of internal energy. It is therefore preferable to use a conservation equation for the latter, instead of a total energy equation. On the other hand, for instance when analyzing a multiphase pipeline for example, it might be important to retain all contributions to the total energy, because kinetic and potential energy variations are expected to be important.

The single phase (specific) internal energy equation is written as:

$$\frac{\partial(\rho_c i_c)}{\partial t} + \nabla\cdot(\rho_c \mathbf{u}_c i_c) = -\nabla\cdot\dot{q}_c - p\nabla\cdot\mathbf{u} + \Phi_v, \tag{3.92}$$

where $\dot{q}_c = k_c\nabla T$, $-p\nabla\cdot\mathbf{u}$ represents the flow work due to motion, Φ_v is the viscous dissipation function and volumetric source terms due to radiation or chemical reaction, for example, have been neglected.

Averaging of the energy equation is done the same way as for the momentum equation. On a term by term basis, starting with the LHS, the time derivative term is:

$$\langle X_c \frac{\partial(\rho_c i_c)}{\partial t}\rangle^{\mathcal{V}} = \frac{\partial(\alpha_c\langle\rho_c i_c\rangle^{\mathcal{V}_c})}{\partial t} + \frac{1}{\mathcal{V}}\int_{S_i}\rho_c i_{c,i}\mathbf{u}_i\cdot(-\mathbf{n}_c)dS, \tag{3.93}$$

while the convective term becomes:

$$\langle X_c\nabla\cdot(\rho_c\mathbf{u}_c i_c)\rangle^{\mathcal{V}} = \nabla\cdot(\alpha_c\langle\rho_c\mathbf{u}_c i_c\rangle^{\mathcal{V}_c}) + \frac{1}{\mathcal{V}}\int_{S_i}\rho_{c,i}i_{c,i}\mathbf{u}_{c,i}\cdot\mathbf{n}_c dS. \tag{3.94}$$

The diffusion term is derived similarly to the shear stress term:

$$\begin{aligned}\langle X_c\nabla\cdot\dot{q}_c\rangle^{\mathcal{V}} &= \nabla\cdot\langle X_c\dot{q}_c\rangle^{\mathcal{V}} - \langle\dot{q}_c\cdot\nabla X_c\rangle^{\mathcal{V}} \\ &= \nabla\cdot(\alpha_c\langle\dot{q}_c\rangle^{\mathcal{V}_c}) + \frac{1}{\mathcal{V}}\int_{S_i}\dot{q}_{ci}\cdot\mathbf{n}_c dS\end{aligned} \tag{3.95}$$

Flow work term and viscous dissipation are given by:

$$-\langle X_c p\nabla\cdot\mathbf{u}\rangle^{\mathcal{V}} = -\alpha_c\langle p\nabla\cdot\mathbf{u}\rangle^{\mathcal{V}_c} \tag{3.96}$$

and

$$\langle X_c \Phi_v \rangle^{\mathcal{V}} = \alpha_c \langle \Phi_v \rangle^{\mathcal{V}_c}, \tag{3.97}$$

respectively. The above terms can be put together in the following form:

$$\begin{aligned} \frac{\partial(\alpha_c \langle \rho_c i_c \rangle^{\mathcal{V}_c})}{\partial t} + \nabla \cdot (\alpha_c \langle \rho_c \mathbf{u}_c i_c \rangle^{\mathcal{V}_c}) &= \nabla \cdot (\alpha_c \langle \dot{q}_c \rangle^{\mathcal{V}_c}) \\ &- \alpha_c \langle p \nabla \cdot \mathbf{u} \rangle^{\mathcal{V}_c} + \alpha_c \langle \Phi_v \rangle^{\mathcal{V}_c} \\ &+ \frac{1}{\mathcal{V}} \int_{S_i} [\dot{q}_{ci} + \rho_c i_{c,i}(\mathbf{u}_i) - \mathbf{u}_{c,i}] \cdot \mathbf{n}_c dS. \end{aligned} \tag{3.98}$$

The conductive heat transfer term ($\langle \dot{q}_c \rangle^{\mathcal{V}_c}$) is given by: $\langle \dot{q}_c \rangle^{\mathcal{V}_c} = -k_c \nabla \langle T_c \rangle^{\mathcal{V}_c}$.

The thermal energy equation can be also formulated as:

$$\begin{aligned} \frac{\partial(\alpha_c \langle \rho_c i_c \rangle^{\mathcal{V}_c})}{\partial t} + \nabla \cdot (\alpha_c \langle \rho_c \mathbf{u}_c h_c \rangle^{\mathcal{V}_c}) &= \nabla \cdot (\alpha_c \langle \dot{q}_c \rangle^{\mathcal{V}_c}) \\ &- \alpha_c \langle \mathbf{u} \cdot \nabla p \rangle^{\mathcal{V}_c} + \alpha_c \langle \Phi_v \rangle^{\mathcal{V}_c} \\ &+ \frac{1}{\mathcal{V}} \int_{S_i} [\dot{q}_{ci} + \rho_c h_{c,i}(\mathbf{u}_i - \mathbf{u}_{c,i})] \cdot \mathbf{n}_c dS, \end{aligned} \tag{3.99}$$

with $h_c = i_c + \frac{p}{\rho_c}$, or in terms of the enthalpy itself:

$$\begin{aligned} \frac{\partial(\alpha_c \langle \rho_c h_c \rangle^{\mathcal{V}_c})}{\partial t} + \nabla \cdot (\alpha_c \langle \rho_c \mathbf{u}_c h_c \rangle^{\mathcal{V}_c}) &= \nabla \cdot (\alpha_c \langle \dot{q}_c \rangle^{\mathcal{V}_c}) \\ &- \alpha_c \langle \frac{\mathrm{d}p}{\mathrm{d}t} \rangle^{\mathcal{V}_c} + \alpha_c \langle \Phi_v \rangle^{\mathcal{V}_c} \\ &+ \frac{1}{\mathcal{V}} \int_{S_i} [\dot{q}_{ci} + \rho_c h_{c,i}(\mathbf{u}_i - \mathbf{u}_{c,i})] \cdot \mathbf{n}_c dS, \end{aligned} \tag{3.100}$$

with $\frac{\mathrm{d}p}{\mathrm{d}t} = \frac{\partial p}{\partial t} + \mathbf{u}_c \cdot \nabla p$

Closure for the energy equation represents one of the major challenges in multiphase flow modeling and is also one of the least explored aspects in Eulerian models. Difficulties arise due to the dissipation function and terms like $\langle p \nabla \cdot \mathbf{u} \rangle^{\mathcal{V}_c}$ and $\langle \mathbf{u} \cdot \nabla p \rangle^{\mathcal{V}_c}$, but also interfacial integrals. Closure of these terms rely on phenomenological models yet to be developed, which is out of the scope of this work. For low Mach numbers, low viscosity, incompressible flows, the contribution of viscous dissipation is known to be unimportant and will be neglected here. The flow work term is also not expected to play a decisive role (in comparison to the heat transfer between phases). Nevertheless, for completeness a simple model based on the description of Crowe et al. [22] will be presented. It is given by:

$$\alpha_c \langle p \nabla \cdot \mathbf{u}_c \rangle^{\mathcal{V}_c} = \langle p \rangle^{\mathcal{V}_c} \nabla \cdot \mathbf{U} \tag{3.101}$$

and

$$\alpha_c \langle \Phi_v \rangle^{\mathcal{V}_c} = \langle \boldsymbol{\tau} \rangle^{\mathcal{V}_c} : \nabla \mathbf{U}, \tag{3.102}$$

with the mixture velocity $\mathbf{U}$ given by $\mathbf{U} = \alpha_c \langle \mathbf{u}_c \rangle^{\mathcal{V}_c} + (1-\alpha_c) \langle \mathbf{u} \rangle^{\mathcal{V}_d}$.

Closure for the interfacial transfer terms will be worked out later.

Analogous to the convective term in the momentum equation, the convective term of the energy equation can be recast with help of the Reynolds decomposition given by Eq. (3.91). It is then rewritten as:

$$\alpha_c \langle \rho_c \mathbf{u}_c i_c \rangle^{\mathcal{V}_c} = \alpha_c \rho_c \langle \mathbf{u}_c \rangle^{\mathcal{V}_c} \langle i_c \rangle^{\mathcal{V}_c} + \alpha_c \underbrace{\rho_c \langle \mathbf{u}_c^{'} i_c^{'} \rangle^{\mathcal{V}_c}}_{\equiv -q_c^{pt}}, \tag{3.103}$$

where q_c^{pt} is analogous to τ_c^{pt} and represents the contribution of sub-volume fluctuations. This term will be modeled in a similar manner as the pseudo-turbulence stress, as will be shown later.

3.3.4 Transport equation for the fuel vapor mass fraction

In the droplet evaporation model, the fuel vapor mass fraction in the far field (i.e., away from the surface of the droplet) $Y_{v,\infty}$ ($\equiv Y_v$) appears in the determination of the mass transfer number – see Eq. (3.51). A transport equation for Y_v can be derived in the same context as above and is given by [22, 39]:

$$\begin{aligned}\frac{\partial(\alpha_c\rho_c Y_v)}{\partial t}+\nabla\cdot(\alpha_c\rho_c\langle\mathbf{u}_c\rangle^{\mathcal{V}_c}Y_v) &= \nabla\cdot\alpha_c(\mathbf{f}_c+\mathbf{f}_c^{pt}) \\ &- \frac{1}{\mathcal{V}}\int_{S_i}[\mathbf{f}_{ci}+\rho_c Y_S(\mathbf{u}_{c,i}-\mathbf{u}_i)]\cdot\mathbf{n}_c dS.\end{aligned} \tag{3.104}$$

$\mathbf{f}_c$ represents Fick's diffusive flux, which is given by $\mathbf{f}_c=\mathscr{D}_{cd}\nabla Y_v$. $\mathbf{f}_c^{pt}$ is the fluctuating part of the diffusive flux, analogous to the previous cases.

3.4 Dispersed phase equations

An heuristic approach will be pursued herein, in which the particle equations are used as a starting point to derive averaged equations for the dispersed phase. A similar strategy was also used before by Crowe et al. [22]. The main advantage is that it avoids the problem of interpretation of stress-like terms that arrise in the Eulerian framework for the dispersed phase (which is not, stricty speaking, a continuum), specially for dilute mixtures.

Consider the small averaging characteristic volume $\mathcal{V}$, which contains N_i particles of a certain size D. It is appropriate to define the volumetric average of an arbitrary quantity Ψ inside each particle:

$$\langle\Psi\rangle^{V_i}=\frac{\int_{V_i}\Psi dV_i}{V_i}. \tag{3.105}$$

The ensemble average of $\langle\Psi\rangle^{V_i}$ over all particles of the same size reads:

$$\frac{\sum^{N_i}\langle\Psi\rangle^{V_i}}{N_i}=\frac{\sum^{N_i}\langle\Psi\rangle^{V_i}V_i}{\alpha\mathcal{V}}=\frac{\sum^{N_i}\int_{V_i}\Psi dV_i}{\alpha\mathcal{V}}=\frac{\int_{\sum V_i=\mathcal{V}_i}\Psi dV_i}{\alpha\mathcal{V}}=\langle\Psi\rangle^{\mathcal{V}_d}. \tag{3.106}$$

3.4.1 Conservation of mass

The continuity equation states that the accumulation rate of mass in the characteristic volume $\mathcal{V}$ plus the net efflux through the surface enclosing this volume equals the total mass generated (or consumed) through phase change. The rate of variation of a single particle's mass is given by Eq. (3.50). This equation can be summed up as follows:

$$\frac{1}{\mathcal{V}}\sum^{N_i}\frac{\mathrm{d}m_i}{\mathrm{d}t} \;=\; \frac{1}{\mathcal{V}}\sum^{N_i}\dot{m}=\frac{N_i\dot{m}}{\mathcal{V}}=-\frac{1}{\mathcal{V}}\int_{S_i}\hat{\mathbf{u}}\cdot\mathbf{n}_d dS. \tag{3.107}$$

$\hat{\mathbf{u}}$ is the velocity through the interface, with respect to the interface velocity, given by $\hat{\mathbf{u}}=\mathbf{u}_{S_i}-\mathbf{u}_i$; $\mathbf{u}_{S_i}$ is the fluid velocity at the particle side of the interface.

Taking into account the source term above, the continuity equation can be written in an Eulerian frame as:

$$\frac{\partial(\rho_d\alpha)}{\partial t}+\nabla\cdot(\rho_d\alpha\langle\mathbf{u}\rangle^{\mathcal{V}_d}) \;=\; \frac{N_i\dot{m}}{\mathcal{V}}=\int_{S_i}\rho_d(\mathbf{u}_{S_i}-\mathbf{u}_i)\cdot\mathbf{n}_d dS, \tag{3.108}$$

where α is the local volume fraction corresponding to a certain size class ($\sum^{N_i}\alpha=\alpha_d$).

3.4.2 Particle equation of motion

The equation of motion for Stokes particles in a viscous fluid goes back to the pioneering works of Basset [6], Boussinesq [17] and Oseen [64]. Therefore, the

equation of motion is mostly referred to as Basset-Boussinesq-Oseen (BBO) equation.The BBO equation (without considering unsteady forces) is given below including the sum of the contributions of pressure ($\mathbf{F}_{F,p}$), shear stress ($\mathbf{F}_{F,\tau}$), drag ($\mathbf{F}_D$), and gravity forces:

$$\frac{\mathrm{d}\mathbf{v}}{\mathrm{d}t} = \frac{\langle \mathbf{u}_c \rangle^{\mathcal{V}_c} - \mathbf{v}}{\tau} - \frac{1}{\rho_d} \nabla \langle p \rangle^{\mathcal{V}_c} + \frac{1}{\rho_d} \nabla \cdot \langle \tau \rangle^{\mathcal{V}_c} + \mathbf{g}. \tag{3.109}$$

Equation (3.109) can be summed up for all particles of the same size and divided by the characteristic volume $\mathcal{V}$:

$$\frac{1}{\mathcal{V}} \sum^{N_i} \left(\rho_d V_i \frac{\mathrm{d}\mathbf{v}}{\mathrm{d}t} = \rho_d V_i \frac{\langle \mathbf{u}_c \rangle^{\mathcal{V}_c} - \mathbf{v}}{\tau} - V_i \nabla \langle p \rangle^{\mathcal{V}_c} + V_i \nabla \cdot \langle \tau \rangle^{\mathcal{V}_c} + \rho_d V_i \mathbf{g} \right). \tag{3.110}$$

The result will be handled on a term by term basis. For the gravity term, it is possible to write:

$$\frac{1}{\mathcal{V}} \sum^{N_i} \rho_d V_i \mathbf{g} = \frac{N_i \rho_d V_i}{\mathcal{V}} \mathbf{g} = \rho_d \alpha \mathbf{g}. \tag{3.111}$$

The pressure and shear stress terms are given by:

$$\frac{1}{\mathcal{V}} \sum^{N_i} V_i \nabla \langle p \rangle^{\mathcal{V}_c} = \frac{N_i V_i}{\mathcal{V}} \nabla \langle p \rangle^{\mathcal{V}_c} = \alpha \nabla \langle p \rangle^{\mathcal{V}_c}. \tag{3.112}$$

and

$$\frac{1}{\mathcal{V}} \sum^{N_i} V_i \nabla \cdot \langle \tau \rangle^{\mathcal{V}_c} = \frac{N_i V_i}{\mathcal{V}} \nabla \cdot \langle \tau \rangle^{\mathcal{V}_c} = \alpha \nabla \cdot \langle \tau \rangle^{\mathcal{V}_c}. \tag{3.113}$$

The drag term is

$$\frac{1}{\mathcal{V}} \sum^{N_i} \rho_d V_i \frac{\langle \mathbf{u}_c \rangle^{\mathcal{V}_c} - \mathbf{v}}{\tau} = \rho_d \alpha \frac{\langle \mathbf{u}_c \rangle^{\mathcal{V}_c} - \langle \mathbf{u} \rangle^{\mathcal{V}_d}}{\tau}. \tag{3.114}$$

The left hand side of the BBO equation becomes:

$$\begin{aligned}\frac{1}{\mathcal{V}}\sum^{N_i}\rho_d\,V_i\frac{\mathrm{d}\mathbf{v}}{\mathrm{d}t} &= \frac{\rho_d\,N_i\,V_i}{\mathcal{V}}\frac{\mathrm{d}}{\mathrm{d}t}\underbrace{\frac{\sum^{N_i}\mathbf{v}}{N_i}}_{\langle\mathbf{u}\rangle^{\mathcal{V}_d}} \\ &= \rho_d\,\alpha\,\frac{D}{Dt_p}\langle\mathbf{u}\rangle^{\mathcal{V}_d} \end{aligned} \tag{3.115}$$

with the derivative following a particle trajectory being replaced by a total derivative defined as:

$$\frac{D}{Dt_p} = \frac{\partial}{\partial t} + \langle\mathbf{u}\rangle^{\mathcal{V}_d}\cdot\nabla. \tag{3.116}$$

The final form of the particle equation of motion in an Eulerian frame is given by:

$$\begin{aligned}\rho_d\,\alpha\,\frac{\partial\langle\mathbf{u}\rangle^{\mathcal{V}_d}}{\partial t} + \rho_d\,\alpha\,\langle\mathbf{u}\rangle^{\mathcal{V}_d}\cdot\nabla\langle\mathbf{u}\rangle^{\mathcal{V}_d} &= -\alpha\,\nabla\langle p\rangle^{\mathcal{V}_c} + \alpha\,\nabla\cdot\langle\tau\rangle^{\mathcal{V}_c} \\ &+ \rho_d\,\alpha\,\frac{\langle\mathbf{u}_c\rangle^{\mathcal{V}_c} - \langle\mathbf{u}\rangle^{\mathcal{V}_d}}{\tau} \\ &+ \rho_d\,\alpha\,\mathbf{g}. \end{aligned} \tag{3.117}$$

Alternatively, with help of the continuity equation, it can be written in a conservative form:

$$\begin{aligned}\frac{\partial(\rho_d\,\alpha\langle\mathbf{u}\rangle^{\mathcal{V}_d})}{\partial t} + \nabla\cdot(\rho_d\,\alpha\,\langle\mathbf{u}\rangle^{\mathcal{V}_d}\langle\mathbf{u}\rangle^{\mathcal{V}_d}) &= -\alpha\,\nabla\langle p\rangle^{\mathcal{V}_c} + \alpha\,\nabla\cdot\langle\tau\rangle^{\mathcal{V}_c} \\ &+ \rho_d\,\alpha\,\frac{\langle\mathbf{u}_c\rangle^{\mathcal{V}_c} - \langle\mathbf{u}\rangle^{\mathcal{V}_d}}{\tau} \\ &+ \rho_d\,\alpha\,\mathbf{g} \\ &+ \frac{N_i}{\mathcal{V}}\dot{m}\langle\mathbf{u}\rangle^{\mathcal{V}_d}. \end{aligned} \tag{3.118}$$

3.4.3 Particle energy equation

The temperature equation for a single particle can be written as:

$$\rho_d V_i c_{p,d} \frac{\mathrm{d}T}{\mathrm{d}t} = \mathrm{Nu}\,\pi D k_c(\langle T_c\rangle^{\mathcal{V}_c} - T) + \dot{m} L_v, \tag{3.119}$$

with $\dot{m}$ given by Eq. (3.50).

Once again, summing up for all particles with the same size (and multiplying by $1/\mathcal{V}$) yields for the RHS:

$$\frac{1}{\mathcal{V}} \sum^{N_i} \mathrm{Nu}\,\pi D k_c(\langle T_c\rangle^{\mathcal{V}_c} - T) = \frac{N_i}{\mathcal{V}} \mathrm{Nu}\,\pi D k_c(\langle T_c\rangle^{\mathcal{V}_c} - \langle T\rangle^{\mathcal{V}_d}). \tag{3.120}$$

$$\frac{1}{\mathcal{V}} \sum^{N_i} \dot{m} L_v = \frac{N_i}{\mathcal{V}} \dot{m} L_v \tag{3.121}$$

For constant specific heat, one can simply write for the RHS:

$$\rho_d V_i c_{p,d} \frac{\mathrm{d}T}{\mathrm{d}t} = \rho_d V_i \frac{\mathrm{d}i}{\mathrm{d}t}, \tag{3.122}$$

where the internal energy i has been considered, such that $di = c_{p,d} dT$ for an incompressible phase. Furthermore:

$$\begin{aligned} \frac{1}{\mathcal{V}} \sum^{N_i} \rho_d V_i \frac{\mathrm{d}i}{\mathrm{d}t} = \quad &= \quad \frac{\rho_d N_i V_i}{\mathcal{V}} \frac{\mathrm{d}}{\mathrm{d}t} \underbrace{\frac{\sum^{N_i} i}{N_i}}_{\langle i\rangle^{\mathcal{V}_d}} \\ &= \quad \rho_d \alpha \frac{D}{D t_p} \langle i\rangle^{\mathcal{V}_d}. \end{aligned} \tag{3.123}$$

The internal energy equation for a given size class is therefore given by:

$$\rho_d \alpha \frac{\partial \langle i\rangle^{\mathcal{V}_d}}{\partial t} + \rho_d \alpha \langle \mathbf{u}\rangle^{\mathcal{V}_d} \cdot \nabla \langle i\rangle^{\mathcal{V}_d} \quad = \quad \frac{N_i}{\mathcal{V}} \mathrm{Nu}\,\pi D k_c(\langle T_c\rangle^{\mathcal{V}_c} - \langle T\rangle^{\mathcal{V}_d})$$

$$+ \quad \frac{N_i}{\mathcal{V}} \dot{m} L_v, \tag{3.124}$$

or

$$\begin{aligned} \frac{\partial(\rho_d \alpha \langle i \rangle^{\mathcal{V}_d})}{\partial t} + \nabla \cdot (\rho_d \alpha \langle \mathbf{u} \rangle^{\mathcal{V}_d} \langle i \rangle^{\mathcal{V}_d}) &= \frac{N_i}{\mathcal{V}} \mathrm{Nu} \pi D k_c (\langle T_c \rangle^{\mathcal{V}_c} - \langle T \rangle^{\mathcal{V}_d}) \\ &+ \frac{N_i}{\mathcal{V}} \dot{m} (L_v + \langle i \rangle^{\mathcal{V}_d}). \end{aligned} \tag{3.125}$$

3.5 Interface conditions

Consider a control volume $\mathcal{V}^*$ enclosing the interface S_i^* which separates both phases, as shown in Fig. 3.6. The following approximation is valid:

$$\mathcal{V}^* = \mathcal{V}_1 + \mathcal{V}_2 \approx (\overbrace{S_1 + S_2}^{\approx S^*}) \delta, \tag{3.126}$$

with $\mathcal{V}^*$ and S^* the total volume and surface area of the control volume, respectively.

The integral form of mass conservation for the total volume is:

$$\frac{\mathrm{d}}{\mathrm{d}t} \int_{\mathcal{V}^*} \rho dV + \int_{S^*} \rho (\mathbf{u} - \mathbf{u}_i) \cdot \mathbf{n} dS = 0, \tag{3.127}$$

or

$$\frac{\mathrm{d}}{\mathrm{d}t} \int_{\mathcal{V}_1} \rho_1 dV + \int_{S_1} \rho_1 (\mathbf{u}_1 - \mathbf{u}_i) \cdot \mathbf{n}_1 dS = -\frac{\mathrm{d}}{\mathrm{d}t} \int_{\mathcal{V}_2} \rho_2 dV + \int_{S_2} \rho_2 (\mathbf{u}_2 - \mathbf{u}_i) \cdot \mathbf{n}_2 dS, \tag{3.128}$$

while for the k-th ($k = 1$ or 2) phase control volume:

$$\frac{\mathrm{d}}{\mathrm{d}t} \int_{\mathcal{V}_k} \rho_k dV + \int_{S_k + S_i^*} \rho_k (\mathbf{u}_k - \mathbf{u}_i) \cdot \mathbf{n}_k dS \quad = \quad 0. \tag{3.129}$$

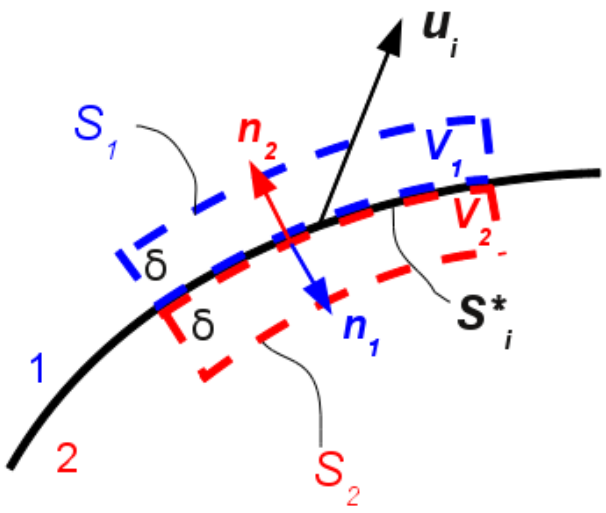

Figure 3.6: Control volume enclosing a surface S_i^* which locally separates the two phases.

By taking the limit $\delta \to 0$, which leads to $dV, \mathcal{V}^* \to 0$ (strictly speaking, the interface can not accumulate mass), the following result can be derived:

$$\int_{S_i^*} \rho_1(\mathbf{u}_1 - \mathbf{u}_i) \cdot \mathbf{n}_1 dS = -\int_{S_i^*} \rho_2(\mathbf{u}_2 - \mathbf{u}_i) \cdot \mathbf{n}_2 dS. \tag{3.130}$$

Since S_i^* is arbitrarily chosen, the integrand must vanish locally. Therefore:

$$\rho_1(\mathbf{u}_1 - \mathbf{u}_i) \cdot \mathbf{n}_1 = -\rho_2(\mathbf{u}_2 - \mathbf{u}_i) \cdot \mathbf{n}_2 = -\dot{m}^{''*}. \tag{3.131}$$

The balance of momentum for $\mathcal{V}^*$ states that the jump in phase tensions at the interface, combined with the momentum fluxes must be balanced by the action of surface tension (σ):

$$\dot{m}''^{,*}(\mathbf{u}_1-\mathbf{u}_2)+(p_2-p_1)\boldsymbol{I}\cdot\mathbf{n}+(\tau_2-\tau_1)\cdot\mathbf{n} \;=\; \nabla_s\sigma-\sigma\kappa\mathbf{n}, \tag{3.132}$$

where the relation $\mathbf{n}_1=-\mathbf{n}_2=\mathbf{n}$ was used. The first term on the RHS vanishes, unless the surface tension varies along the interface coordinate, s, due to surfactant effects for example (which is not the case here). κ is the local mean curvature of the interface, given by

$$\kappa=\nabla\cdot\mathbf{n}. \tag{3.133}$$

Surface tension effects in the normal direction do not need to be taken into account explicitly in the present work, since there is no need to link continuous and dispersed phase interfacial pressures (through a pressure-jump condition). The latter does not appear in the momentum equations as a consequence of the underlying assumptions involving the model derivation. In the examples studied in this work, particle sizes will be of order $\mathcal{O}(10^0-10^2\mu m)$. For particles of such sizes, the form of the interface will very unlikely change, and can be assumed to be known and remain constant (i.e. spherical particles).

Using the same procedure as for mass and momentum, the following condition for the energy balance is obtained (the energy associated to the interface, $e_i\approx S_i^*\,\sigma$, is not considered because the change in surface energy associated to the change in size due to evaporation is negligible compared to the enthalpy fluxes at the interface):

$$\begin{aligned}\dot{m}''^{,*}(e_1-e_2)-(-p_1\boldsymbol{n}_1+\tau_1\cdot\boldsymbol{n}_1)\cdot(\mathbf{u}_1-\mathbf{u}_i) \;&+\; (-p_2\boldsymbol{n}_2+\tau_2\cdot\boldsymbol{n}_2)\cdot(\mathbf{u}_2-\mathbf{u}_i)=\\ &=\; \mathbf{q}_2\cdot\mathbf{n}_2-\mathbf{q}_1\cdot\mathbf{n}_1,\end{aligned} \tag{3.134}$$

with $e_k=i_k+\frac{\mathbf{u}_k\cdot\mathbf{u}_k}{2}$ being the specific energy of a given phase. For the example of droplet evaporation, one normally neglects the work exerted by shear stresses and the above equation can be rewritten as:

$$\dot{m}''^{,*}(i_1+\frac{\mathbf{u}_1\cdot\mathbf{u}_1}{2}-i_2-\frac{\mathbf{u}_2\cdot\mathbf{u}_2}{2})+\frac{p_1}{\rho_1}\rho_1(\mathbf{u}_1-\mathbf{u}_i)\cdot\mathbf{n}_1 \;-\; \frac{p_2}{\rho_2}\rho_2(\mathbf{u}_2-\mathbf{u}_i)\cdot\mathbf{n}_2 = \\ = \mathbf{q}_2\cdot\mathbf{n}_2-\mathbf{q}_1\cdot\mathbf{n}_1 \tag{3.135}$$

Using the definition of specific enthalpy; $h_k = i_k + \frac{p_k}{\rho_k}$:

$$\dot{m}''^{,*}(h_1+\underbrace{\frac{\mathbf{u}_1\cdot\mathbf{u}_1}{2}}_{\ll h_1}-h_2-\underbrace{\frac{\mathbf{u}_2\cdot\mathbf{u}_2}{2}}_{\ll h_2}) = \mathbf{q}_2\cdot\mathbf{n}_2-\mathbf{q}_1\cdot\mathbf{n}_1.$$

$$\dot{m}''^{,*}(\underbrace{h_1-h_2}_{L_v}) = \mathbf{q}_2\cdot\mathbf{n}_2-\mathbf{q}_1\cdot\mathbf{n}_1, \tag{3.136}$$

which correponds to Eq. (3.49).

A similar analysis leads to the following constraint at the interface for the species (fuel vapor) mass fraction (see also Eq. 3.48):

$$\dot{m}''^{,*}(Y_1-Y_2) = \mathbf{f}_2\cdot\mathbf{n}_2-\mathbf{f}_1\cdot\mathbf{n}_1, \tag{3.137}$$

where $\mathbf{f}_k$ represents the Fick's diffusive fluxes at both sides of the interface. For the case of droplet evaporation, $Y_1 = 1$ and $\mathbf{f}_1 = 0$ (phase 1 is arbitrarily taken to be the liquid droplet).

The above conditions are useful in the formulation of closure models. Continuous phase equations must be coupled to the dispersed phase equations through the interfacial integrals, otherwise they remain undetermined. Each of the local interfacial conditions can be formulated in terms of the total surface representing the sum of all particles pertaining to a certain size class (monodisperse situation), by integration over S_i.Thus, comparing Eqs. (3.75), (3.108) and (3.131), the following condition can be written for the continuous phase continuity equation:

$$\frac{1}{\mathcal{V}}\int_{S_i}\rho_c(\mathbf{u}_i-\mathbf{u}_{c,i})\cdot\mathbf{n}_c\,dS = -\Gamma = -\frac{N_i\dot{m}}{\mathcal{V}}. \tag{3.138}$$

Similarly, unclosed momentum exchange terms due to microscale effects (here, only the drag force) and the momentum flux due to phase change are represented by:

$$\begin{aligned}\frac{1}{\mathcal{V}}\int_{S_i}(\langle p\rangle^{\mathcal{V}_c}-p_i)\boldsymbol{I}\cdot\mathbf{n}_c dS &- \frac{1}{\mathcal{V}}\int_{S_i}(\langle\boldsymbol{\tau}\rangle^{\mathcal{V}_c}-\boldsymbol{\tau}_i)\cdot\mathbf{n}_c dS = \\ &= -\rho_d\,\alpha\,\frac{\langle\mathbf{u}_c\rangle^{\mathcal{V}_c}-\langle\mathbf{u}\rangle^{\mathcal{V}_d}}{\tau} \qquad (3.139)\end{aligned}$$

and

$$\frac{1}{\mathcal{V}}\int_{S_i}\rho_c\mathbf{u}_{c,i}(\mathbf{u}_i-\mathbf{u}_{c,i})\cdot\mathbf{n}_c dS = -\frac{N_i}{\mathcal{V}}\dot{m}\langle\mathbf{u}\rangle^{\mathcal{V}_d}, \qquad (3.140)$$

respectively. At this point, the momentum transfer term $\mathbf{M}$ can be determined as:

$$\mathbf{M} = -\alpha\nabla\langle p\rangle^{\mathcal{V}_c}+\alpha\nabla\cdot\langle\boldsymbol{\tau}\rangle^{\mathcal{V}_c}+\rho_d\,\alpha\,\frac{\langle\mathbf{u}_c\rangle^{\mathcal{V}_c}-\langle\mathbf{u}\rangle^{\mathcal{V}_d}}{\tau}. \qquad (3.141)$$

Hence, the sum of the above interfacial integrals in the continuous phase momentum equation is

$$\frac{1}{\mathcal{V}}\int_{S_i}(...)dS = -\mathbf{M}-\Gamma\langle\mathbf{u}\rangle^{\mathcal{V}_d}. \qquad (3.142)$$

For the energy equation, it is possible to write:

$$\begin{aligned}\frac{1}{\mathcal{V}}\int_{S_i}[\dot{q}_{c\,i}+\rho_c i_{c,i}(\mathbf{u}_i-\mathbf{u}_{c,i})]\cdot\mathbf{n}_c dS &\approx -\frac{N_i}{\mathcal{V}}\mathrm{Nu}\,\pi\,D\,k_c(\langle T_c\rangle^{\mathcal{V}_c}-\langle T\rangle^{\mathcal{V}_d}) \\ &- \frac{N_i}{\mathcal{V}}\dot{m}(L_v+\langle i\rangle^{\mathcal{V}_d}), \qquad (3.143)\end{aligned}$$

where the pressure contribution at the interface was neglected in comparison to internal energy and latent heat contributions. The above terms can be conveniently redefined as:

$$\dot{Q} = 6\frac{\alpha}{D^2}\mathrm{Nu}\,k_c(\langle T_c\rangle^{\mathcal{V}_c} - \langle T\rangle^{\mathcal{V}_d}) + \Gamma(L_v + \langle i\rangle^{\mathcal{V}_d}), \tag{3.144}$$

representing the sum of convective heat transfer between phases and heat transfer associated to phase change.

For the species equation, the interface constraint is:

$$\frac{1}{\mathcal{V}}\int_{S_i}[\mathbf{f}_{ci} + \rho_c Y_S(\mathbf{u}_{c,i} - \mathbf{u}_i)]\cdot\mathbf{n}_c dS = -\Gamma. \tag{3.145}$$

3.6 Turbulence modeling and closure

Description of turbulence in single phase flows is extremely challenging, let alone multiphase flows. There are very few models available in the Eulerian framework, specially in the RANS context. The reason for that is the difficulty in obtaining reliable experimental data on particle-turbulence interaction, while multiphase resolved simulations in LES and DNS context are very expensive.

The procedure used to develop RANS equations in multiphase context is similar to that of single phase flows, i.e., by decomposing dependent variables into a mean and a fluctuating component (Reynolds decomposition)

$$\Psi = \overline{\Psi} + \Psi', \tag{3.146}$$

with $\overline{\Psi} = \frac{1}{T}\int_T \Psi\, dT$, and taking the time-average of the corresponding equation.

According to Oliveira [63], it is also interesting to define the α_k-weighted mean value of Ψ as:

$$\tilde{\Psi} \equiv \frac{\overline{\alpha_k \langle \Psi_k \rangle^{\gamma_k}}}{\overline{\alpha}_k}, \tag{3.147}$$

and the decomposition of Ψ into a phase-averaged component and its fluctuating part is: $\Psi = \tilde{\Psi} + \Psi''$.

In order to obtain a closed set of equations involving the dependent variables, many assumptions have to be made regarding the different correlations between fluctuating quantities. Only the most important results will be presented here; further details can be found in [43, 63].

With the above definitions, it is possible to rewrite the continuity, momentum, energy and species equations as follows:

$$\rho_c \frac{\partial \overline{\alpha}_c}{\partial t} + \rho_c \nabla \cdot (\overline{\alpha}_c \tilde{\mathbf{u}}_c) = -\overline{\Gamma}. \tag{3.148}$$

$$\begin{aligned} \rho_c \frac{\partial (\overline{\alpha}_c \tilde{\mathbf{u}}_c)}{\partial t} + \rho_c \nabla \cdot (\overline{\alpha}_c \tilde{\mathbf{u}}_c \tilde{\mathbf{u}}_c) &= -\nabla \tilde{p} + \nabla \cdot \tilde{\boldsymbol{\tau}} + \overline{\alpha}_c \rho_c \mathbf{g} \\ &+ \nabla \cdot \overline{\alpha}_c (\tilde{\boldsymbol{\tau}}_c^t + \tilde{\boldsymbol{\tau}}_c^{pt}) - \overline{\mathbf{M}} - \overline{\Gamma} \tilde{\mathbf{u}} \end{aligned} \tag{3.149}$$

$$\begin{aligned} \rho_c \frac{\partial (\overline{\alpha}_c \tilde{i}_c)}{\partial t} + \rho_c \nabla \cdot (\overline{\alpha}_c \tilde{\mathbf{u}}_c \tilde{i}_c) &= \nabla \cdot \overline{\alpha}_c (\tilde{\boldsymbol{q}}_c + \tilde{\boldsymbol{q}}_c^t + \tilde{\boldsymbol{q}}_c^{pt}) \\ &- \tilde{p} \nabla \cdot \tilde{\mathbf{U}} - \overline{\dot{Q}}. \end{aligned} \tag{3.150}$$

$$\rho_c \frac{\partial (\overline{\alpha}_c \tilde{Y}_v)}{\partial t} + \rho_c \nabla \cdot (\overline{\alpha_c} \tilde{\mathbf{u}}_c \tilde{Y}_v) = \nabla \cdot \overline{\alpha_c} (\tilde{\boldsymbol{f}}_c + \tilde{\boldsymbol{f}}_c^t + \tilde{\boldsymbol{f}}_c^{pt}) - \overline{\Gamma}, \tag{3.151}$$

Note that the gas density is taken out of the derivatives, since all fluid properties are for simplicity assumed to be constant. It is expected to be a good approximation due to the small pressure and temperature variations, as well as small fuel vapor mass fractions.

The fluctuating stress, heat and mass transfer terms are evaluated by means of the gradient diffusion hypothesis. For simplicity – and lack of a better approach, it is assumed that contributions due to turbulence and sub-volume fluctuations due to the presence of particles can be joined together and modeled by the usual turbulent diffusivity approach. They are given by:

$$\tilde{\boldsymbol{\tau}}_c^t + \tilde{\boldsymbol{\tau}}_c^{pt} \approx \mu_c^t(\nabla\tilde{\mathbf{u}}_c + \nabla\tilde{\mathbf{u}}_c^T) - \frac{2}{3}(\mu_c^t\nabla\cdot\tilde{\mathbf{u}}_c + \rho_c\tilde{\kappa}_c)\,\mathbf{I}, \tag{3.152}$$

with μ_c^t the turbulent viscosity of the continuous phase, κ_c the turbulence kinetic energy and $\tilde{\kappa}_c$ its phase averaged value.

$$\tilde{\boldsymbol{q}}_c + \tilde{\boldsymbol{q}}_c^t + \tilde{\boldsymbol{q}}_c^{pt} = k_c^{eff}\nabla\tilde{T}_c \tag{3.153}$$

with $k_c^{eff} = \frac{\mu_c^{eff}}{\mathrm{Pr}_c^t}$ and

$$\tilde{\boldsymbol{f}}_c + \tilde{\boldsymbol{f}}_c^t + \tilde{\boldsymbol{f}}_c^{pt} = \mathscr{D}_c^{eff}\nabla\tilde{Y}_v, \tag{3.154}$$

with $\mathscr{D}_c^{eff} = \frac{\nu_c^{eff}}{\mathrm{Sc}_c^t}$. In the above equations, the effective kinematic viscosity (ν_c^{eff}) is given by the sum of molecular and turbulent contributions, i.e., $\nu_c^{eff} = \nu_c + \nu_c^t$. Pr_c^t and Sc_c^t are the turbulent Prandtl and Schmidt numbers, respectively, taken to be unity.

The Eulerian particle equations for a single size class (monodisperse), on the other hand, are modified as follows:

$$\rho_d\frac{\partial\overline{\alpha}}{\partial t} + \rho_d\nabla\cdot(\overline{\alpha}\tilde{\mathbf{u}}) = \overline{\Gamma} \tag{3.155}$$

$$\rho_d\frac{\partial(\overline{\alpha}\tilde{\mathbf{u}})}{\partial t} + \rho_d\nabla\cdot(\overline{\alpha}\,\tilde{\mathbf{u}}\tilde{\mathbf{u}}) = \nabla\cdot(\overline{\alpha}\,\tilde{\boldsymbol{\tau}}_d^t) + \rho_d\,\overline{\alpha}\,\mathbf{g} + \overline{\mathbf{M}} + \overline{\Gamma}\tilde{\mathbf{u}}. \tag{3.156}$$

$$\rho_d \frac{\partial(\overline{\alpha}\tilde{i})}{\partial t} + \rho_d \nabla \cdot (\overline{\alpha}\tilde{\mathbf{u}}\tilde{i}) \quad = \quad \nabla \cdot (\overline{\alpha}\tilde{\boldsymbol{q}}_d^t) + \overline{\dot{Q}}. \tag{3.157}$$

The turbulence fluctuation terms in the above equations are also modeled using the Boussinesq approximation. Hence:

$$\tilde{\boldsymbol{\tau}}_d^t \approx \mu_d^t(\nabla\tilde{\mathbf{u}} + \nabla\tilde{\mathbf{u}}^T) - \frac{2}{3}(\mu_d^t \nabla\cdot\tilde{\mathbf{u}} + \rho_d\tilde{\kappa}_d)\,\mathbf{I}, \tag{3.158}$$

where μ_d^t is the turbulent viscosity of the dispersed phase and $\tilde{\kappa}_d$ its turbulence kinetic energy (phase-averaged); and

$$\tilde{\boldsymbol{q}}_d^t = k_d^t \nabla\tilde{T} \tag{3.159}$$

with $k_d^t = \frac{\mu_d^t}{\mathrm{Pr}_d^t}$.

Based on substitution of the time average velocities by $\overline{\mathbf{u}} = \tilde{\mathbf{u}} + \overline{\mathbf{u}''} = \tilde{\mathbf{u}} - \frac{\overline{\alpha\mathbf{u}'}}{\overline{\alpha}}$ (see [63] for details) and from the gradient diffusion hypothesis for the transport of α by turbulent fluctuations, that is $\overline{\alpha\mathbf{u}_k'} = \nu_k^t \nabla\overline{\alpha}$, the momentum transfer term can be approximated by:

$$\overline{\mathbf{M}} \quad \approx \quad -\overline{\alpha}\nabla\tilde{p} + \overline{\alpha}\nabla\cdot\tilde{\boldsymbol{\tau}} + \rho_d\overline{\alpha}\frac{(\tilde{\mathbf{u}}_c - \tilde{\mathbf{u}})}{\tau} + \underbrace{\frac{\rho_d}{\tau}\frac{\nu_d^t}{\sigma_\alpha}\nabla\overline{\alpha}}_{\text{Turbulent drag}}, \tag{3.160}$$

where σ_α is a turbulent dispersion coefficient, taken to be 0.7. The corresponding turbulent terms in the energy equations are neglected.

The turbulence model used herein is a two-equation, two-phase $\kappa - \epsilon$ model, as described by Oliveira and Issa [43]. The equations for the transport of turbulence kinetic energy k_c and its rate of dissipation ϵ_c, for the continuous phase, are written as:

$$\rho_c \frac{\partial(\overline{\alpha}_c \tilde{\kappa}_c)}{\partial t} + \rho_c \nabla \cdot (\overline{\alpha}_c \tilde{\mathbf{u}}_c \tilde{\kappa}_c) = \nabla \cdot (\overline{\alpha}_c \frac{\mu_c^t}{\sigma_k} \nabla \tilde{\kappa}_c) + \overline{\alpha}_c (G - \rho_c \tilde{\epsilon}_c) + S_d^k - \overline{\Gamma} \tilde{\kappa}_c \tag{3.161}$$

and

$$\rho_c \frac{\partial(\overline{\alpha}_c \tilde{\epsilon}_c)}{\partial t} + \rho_c \nabla \cdot (\overline{\alpha}_c \mathbf{u}_c \tilde{\epsilon}_c) = \nabla \cdot (\overline{\alpha}_c \frac{\mu_c^t}{\sigma_\epsilon} \nabla \tilde{\epsilon}_c) + \overline{\alpha}_c \frac{\tilde{\epsilon}_c}{\tilde{\kappa}_c} (C_1 G - C_2 \rho_c \tilde{\epsilon}_c) + S_d^\epsilon - \overline{\Gamma} \tilde{\epsilon}_c. \tag{3.162}$$

In the above equations, the turbulent viscosity μ_c^t and the generation of $\tilde{\kappa}_c$ are computed from:

$$\mu_c^t = \rho_c C_\mu \frac{\tilde{k}_c^2}{\tilde{\epsilon}_c} \tag{3.163}$$

and

$$G = \mu_c^t \nabla \tilde{\mathbf{u}}_c : (\nabla \tilde{\mathbf{u}}_c + \nabla \tilde{\mathbf{u}}_c^T). \tag{3.164}$$

$\overline{\Gamma} \tilde{\kappa}_c$ and $\overline{\Gamma} \tilde{\epsilon}_c$ are the additional source terms due to droplet evaporation. In addition, S_d^k and S_d^ϵ represent the interaction between disperse phase and continuous phase turbulence, which are given by:

$$S_d^k = -\frac{\rho_d}{\tau} \left[2 \overline{\alpha \alpha}_c (1 - C_k) \tilde{\kappa}_c + \frac{\nu_c^t}{\sigma_\alpha} \nabla \overline{\alpha} \cdot (\tilde{\mathbf{u}} - \tilde{\mathbf{u}}_c) \right] \tag{3.165}$$

$$S_d^\epsilon = -2 \overline{\alpha \alpha}_c (1 - C_k) \tilde{\epsilon}_c \frac{\rho_d}{\tau}. \tag{3.166}$$

In the above equations, C_k is given by:

$$C_k = \sqrt{C_t}. \tag{3.167}$$

The model for the response coefficient C_t employed here is based on the proposal of Oliveira and Issa [43]. It is given by:

$$C_t = \frac{3+\beta}{1+\beta+2\frac{\rho_d}{\rho_c}}, \tag{3.168}$$

with

$$\beta = \frac{\tau_{\epsilon_c}}{\tau}\left(1+2\frac{\rho_d}{\rho_c}\right). \tag{3.169}$$

τ_{ϵ_c} is the turbulence characteristic time scale, which is given by $\tau_{\epsilon_c} = 0.41\frac{\tilde{\kappa}_c}{\tilde{\epsilon}_c}$.

The turbulence kinetic energy ($\tilde{\kappa}_d$) and turbulent viscosity (ν_d^t) of the disperse phase are simply given by the relations: $\kappa_d = C_k\kappa_c$ and $\nu_d^t = C_k\nu_c^t$. Finally, the $\kappa-\epsilon$ constants used herein were that of the standard model (see, e.g., the work of Rusche [70]), with the turbulent quantities Pr^t and Sc^t taken to be unity for both phases.

4 Method of Moments

The last chapter was devoted to the thorough derivation of continuous phase and Eulerian particle phase equations, which form the basis of Eulerian-Eulerian models. Since a full size Multi-Fluid Model considers sets of Eulerian equations for a large number of size classes and is able to capture polydispersity automatically, it is reasonable that attempts to derive integral formulations, which relax the multi-size level of description – at the same time trying to retain a reasonable degree of accuracy – use as a starting point the Multi-Fluid equations (Fig. 4.1). A Moment Method of this type was systematically derived by Beck [10], based on the Eulerian equations presented by Mostafa and Mongia [62]. In the present thesis, a similar framework is used, but the Eulerian equations for dispersed phases derived in the last chapter in details are in line with Crowe et al. [22] and Prosperetti [67]. Before proceeding with the integration of these equations over the size spectrum, some definitions of important quantities related to the size distribution function will be provided next.

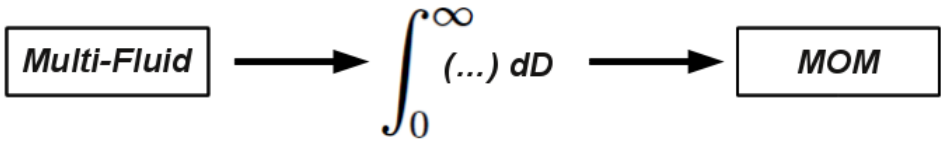

Figure 4.1: From Multi-Fluid to MOM formulation.

4.1 Definitions

The discrete number frequency distribution for the particle size, n_i, is first defined:

$$n_i = \frac{N_i}{N_t}, \tag{4.1}$$

where N_t is the total number of particles. It is straightforward to show that

$$\sum_{i=1}^{N_c} n_i = 1, \tag{4.2}$$

N_c is the total number of size classes present. The particle number density function (analogous to continuous distribution) $\tilde{f}(D)$ is defined as:

$$\tilde{f}(D) = \lim_{\Delta D \to 0} \frac{n_i}{\Delta D}, \tag{4.3}$$

such that the integral $\int_{D-}^{D+} \tilde{f}(D) dD$ represents the probability of having particles with sizes between $[D-, D+]$. Again, in analogy to the discrete case, it follows that:

$$\int_0^\infty \tilde{f}(D) dD = 1. \tag{4.4}$$

It is useful to define the size distribution function $f(D)$, as the particle number density function multiplied with the total number of particles per unit volume:

$$f(D) = \tilde{f}(D) \frac{N_t}{\mathcal{V}}. \tag{4.5}$$

The moments of the size distribution function are in turn defined as:

$$M^{(k)} \equiv \int_0^\infty D^k f(D) dD. \tag{4.6}$$

The definition of $f(D)$ allows a physical interpretation of the low order moments as follows:

- $M^{(0)}$: total number of particles (per unit volume)
- $M^{(1)}$: sum of the particle diameter (")
- $\pi M^{(2)}$: total surface area of particles (")
- $\frac{\pi}{6} M^{(3)}$: total volume of particles ("); or the local volume fraction of the disperse phase

The moment transport velocities, defined for the k^{th} moment as

$$\mathbf{u}^{(k)} \equiv \frac{1}{M^{(k)}} \int_0^\infty \mathbf{u}(D) D^k f(D) dD, \tag{4.7}$$

represent weighted integrals of the size-velocity correlation $\mathbf{u}(D)$ over the size spectrum[1]. As will be shown in the following sections, $\mathbf{u}^{(k)}$ is the velocity at which the k-th moment is transported. They will only be equal ($\mathbf{u}^{(l)} = \mathbf{u}^{(m)}$, $l \neq m$) in two limiting cases: for a monodisperse distribution, i.e. $f(D) = \delta(D - D^*)$, with $\mathbf{u}(D^*) = \mathbf{u}^*$; or if all particles have the same velocity, i.e. $\mathbf{u}(D) = \mathbf{u}^*$, $\forall D$. In both cases, $\mathbf{u}^{(k)} = \mathbf{u}^*$, $\forall k$. Otherwise, there is no reason, e.g., for $\mathbf{u}^{(2)}$ and $\mathbf{u}^{(3)}$ to be the same, as they represent surface area and volume weighted averages, respectively.

The motivation for the introduction of the moments and their transport velocities is to minimize computational costs by avoiding the discretization of the size distribution in several classes, and nevertheless to capture the polydispersity of the flow through the correct description of the evolution of the moments. The moments and the corresponding transport velocities appear naturally in the mathematical formulation as a direct consequence of the integration of the Eulerian particle equations over the diameter spectrum, as will be demonstrated next.

[1] Implicit here is the assumption that particles with the same size are represented by a unique local average velocity, denoted by $\mathbf{u}$

4.2 Moment transport equations

The objective here is the derivation of transport equations for the moments of the size distribution function in the form

$$\frac{\partial \phi}{\partial t} + \nabla \cdot (\mathbf{u}_\phi \phi) = \Gamma_\phi, \tag{4.8}$$

where ϕ is any property of the population of particles (per unit characteristic volume, $\mathcal{V}$) which travels with a characteristic velocity $\mathbf{u}_\phi$ and evolves according to source/sink terms incorporated in Γ_ϕ. Note that this is in some sense a generalization of the volume fraction equation:

$$\frac{\partial \alpha}{\partial t} + \nabla \cdot (\mathbf{u}\alpha) = \frac{\Gamma}{\rho_d}, \tag{4.9}$$

with α defined as the total volume occupied by particles of the same diameter (as seen in the previous chapter), i.e.:

$$\alpha = \frac{N_i \frac{\pi D^3}{6}}{\mathcal{V}}. \tag{4.10}$$

Note that, in Eq. (4.9), symbols denoting time and phase averages were droped for simplicity of notation – which will be continued from this point on.

Since $f(D)$ is related to α simply through

$$f(D) = \lim_{\Delta D \to 0} \frac{6}{\pi D^3} \alpha \frac{1}{\Delta D}, \tag{4.11}$$

a conservation equation for the third moment can be readily derived by integration of Eq. (4.9) over the size spectrum. Hence:

$$\frac{\left(\partial \int_0^\infty D^3 f dD\right)}{\partial t} + \nabla \cdot (\underbrace{\int_0^\infty \mathbf{u} D^3 f dD}_{M^{(3)}\mathbf{u}^{(3)}}) = \Gamma_{M^{(3)}}, \tag{4.12}$$

with $\Gamma_{M^{(3)}}$ the source term related to the variation of the total volume of the distribution (per unit volume).

The above equation can be directly generalized for any moment $M^{(k)}$ as:

$$\frac{\partial M^{(k)}}{\partial t} + \nabla \cdot (M^{(k)} \mathbf{u}^{(k)}) \quad = \quad \Gamma_{M^{(k)}}. \tag{4.13}$$

Note that the velocity which appears in the convective term is the moment transport velocity, $\mathbf{u}^{(k)}$. This results automatically from the integral over the size spectrum: $\int_0^\infty \mathbf{u} D^k f \, dD = M^{(k)} \mathbf{u}^{(k)}$. $\Gamma_{M^{(k)}}$ is a source term representing the overall effect of the population balance processes mentioned above; e.g. for $k = 3$ it represents the loss of mass (or volume) of a population of droplets due to evaporation.

4.2.1 Source terms due to evaporation

The overall effect of evaporation on size distribution is that of decreasing all moments $M^{(k)}$'s[2], once they represent integral characteristics of the whole spectrum of droplet sizes (total volume, surface, etc). The source terms $\Gamma_{M^{(k)}}$ can be developed from physical principles governing the evaporation process for a single particle – see section 3.2.4.

Consider first the (volume) rate of evaporation per unit volume for N_i droplets pertaining to a certain size class:

$$\frac{d}{dt}\left(\frac{N_i}{\mathcal{V}} D^3\right) = \left(\frac{N_i}{\mathcal{V}}\right) \frac{d}{dt} D^3 + \underbrace{D^3 \frac{d}{dt}\left(\frac{N_i}{\mathcal{V}}\right)\Big|_{D \to 0}}_{\equiv 0}. \tag{4.14}$$

Note that the last term is identically zero since, by definition, there can only be a variation of the number of droplets when they disappear, i.e. $D \to 0$ (Fig. 4.2

[2] In fact, as will be seen later in this section, unless the degree of vaporization is such that there is disappearance of droplets, $M^{(0)}$ remains unchanged.

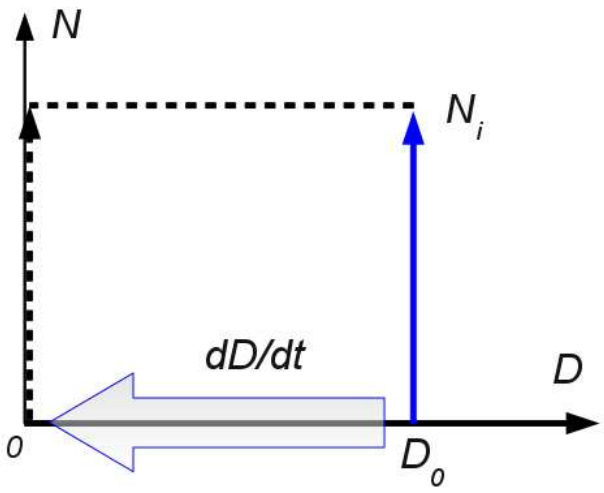

Figure 4.2: Schematic representation of evaporation of N_i droplets with initial diameter D_0.

illustrates the situation of the evaporation of N_i droplets with initial diameter D_0).

The source term $\Gamma_{M^{(3)}}$ is determined by integration over the whole spectrum of sizes of the above relation:

$$\Gamma_{M^{(3)}} = \int_0^\infty \left(\underbrace{\frac{N_i}{\mathcal{V}\, dD}}_{\equiv f;\ dD \to 0} \right) \frac{d(D^3)}{dt} dD = \int_0^\infty f(3D^2) \frac{dD}{dt} dD. \tag{4.15}$$

According to Eq. (3.53) (which defines the rate of variation of the droplet surface area) one can write:

$$\frac{\mathrm{d}D^2}{\mathrm{d}t} = \lambda^* \Rightarrow \frac{\mathrm{d}D}{\mathrm{d}t} = \frac{\lambda^*}{2D}. \tag{4.16}$$

Substituting the above expression for the rate of variation of the droplet diameter into Eq. (4.15):

$$\Gamma_{M^{(3)}} = \frac{3}{2}\lambda^* \int_0^\infty f\, D\, dD = -\frac{12}{\rho_d}\frac{k_c}{c_{p,c}} \ln(1+B_M) M^{(1)}. \tag{4.17}$$

$\Gamma_{M^{(2)}}$ and $\Gamma_{M^{(1)}}$ – i.e. the rate of variation of total surface area and sum of diameters – can be computed similarly, yielding:

$$\Gamma_{M^{(2)}} = -\frac{8}{\rho_d}\frac{k_c}{c_{p,c}} \ln(1+B_M) M^{(0)} \tag{4.18}$$

and

$$\Gamma_{M^{(1)}} = -\frac{4}{\rho_d}\frac{k_c}{c_{p,c}} \ln(1+B_M) M^{(-1)}, \tag{4.19}$$

respectively.

The disappearence rate of droplets per unit volume ($\Gamma_{M^{(0)}}$) requires a special analysis. The total number of droplets of a certain distribution will diminish only in the limit $D \to 0$. Consider the following expression, which sets the temporal variation of $\frac{N_i}{\mathcal{V}}$ to the number flux of "zero-size" droplets in the diameter space (see Fig. 4.2):

$$\frac{\partial}{\partial t}\left(\frac{N_i}{\mathcal{V}}\right)\Big|_{D\to 0} = \frac{\partial}{\partial D}\left(\frac{N_i}{\mathcal{V}}\frac{dD}{dt}\right)\Big|_{D\to 0}. \tag{4.20}$$

The above equality (with help of the definition for f) can be generalized and integrated to yield the source term for $M^{(0)}$, which shall include the sum of disappearence rates for all size classes. Therefore:

$$\begin{aligned} \Gamma_{M^{(0)}} &\propto \int_0^\infty \frac{\partial(f/D)}{\partial D} dD \\ &\propto \frac{f}{D}\Big|_{D\to 0}. \end{aligned} \tag{4.21}$$

Thus, $\Gamma_{M^{(0)}}$ is clearly indeterminate and its modeling is not trivial. Closure for this term will not be developed in this work (for details on the modeling of the disappearence rate of droplets, see the work of Massot et al. [56], for example). Thus, for the cases where droplet evaporation occurs, $M^{(0)}$ will not be chosen as transported moment. A further discussion on this subject will be given later.

4.3 Transport equation for moment fluxes

Analogously to the moment transport equations, it is possible to derive formulations representing balance equations for the moment fluxes, $\mathbf{u}^{(k)}M^{(k)}$:

$$\begin{aligned}\rho_d \frac{\partial\left(\int_0^\infty f D^k \mathbf{u}\, dD\right)}{\partial t} + \rho_d \nabla\cdot\left(\int_0^\infty f D^k \mathbf{u}\,\mathbf{u}\, dD\right) &= \int_0^\infty \mathbf{M} D^{(k-3)} dD \\ &+ \nabla\cdot\left(\int_0^\infty f D^k \boldsymbol{\tau}_{\boldsymbol{d}}^{\boldsymbol{t}}\, dD\right) \\ &+ \rho_d M^{(k)}\mathbf{g} \\ &+ \rho_d \Gamma_{M^{(k)}}\mathbf{u}^{(k)}, \end{aligned} \tag{4.22}$$

where gravity and momentum exchange terms (last terms on the RHS) are already given in an explicit manner. The integrals in the above equation will be dealt with on a term by term basis. The first term on the left hand side is given by:

$$\rho_d \frac{\partial\left(\int_0^\infty f D^k \mathbf{u}\, dD\right)}{\partial t} = \rho_d \frac{\partial\left(M^{(k)}\mathbf{u}^{(k)}\right)}{\partial t}. \tag{4.23}$$

To recast the second term on the LHS, following the decomposition first proposed by Beck [10], the particle velocities $\mathbf{u}$ are written in terms of the velocity $\mathbf{u}^{(k)}$ plus a relative velocity component (representing the deviation from the average) $\mathbf{u}'$: $\mathbf{u}(D) = \mathbf{u}^{(k)} + \mathbf{u}'^{(k)}(D)$. Note that $\mathbf{u}'^{(k)}(D)$ does not necessarily appear due to turbulent fluctuations of the particle movement, but represents

instead the deviation of individual velocities from the k-th average velocity of the "particle cloud" in a general way. Hence:

$$\begin{aligned}\nabla\cdot\left(\int_0^\infty f\mathbf{u}\mathbf{u}D^k dD\right) &= \nabla\cdot(M^{(k)}\mathbf{u}^{(k)}\mathbf{u}^{(k)}) + \nabla\cdot\left(\int_0^\infty f\mathbf{u}'\mathbf{u}'D^k dD\right)\\ &+ \underbrace{\nabla\cdot\left(\int_0^\infty f\mathbf{u}^{(k)}\mathbf{u}'D^k dD\right)}_{\equiv 0} + \underbrace{\nabla\cdot\left(\int_0^\infty f\mathbf{u}'\mathbf{u}^{(k)}D^k dD\right)}_{\equiv 0}.\end{aligned} \tag{4.24}$$

The third and fourth terms on the right side of the above equality are zero by definition.

On the RHS, the integral of the momentum exchange term $\mathbf{M}$ leads, for the pressure and shear stress contribution, to:

$$\int_0^\infty fD^k\nabla p\,dD + \int_0^\infty fD^k\nabla\cdot\boldsymbol{\tau}\,dD = M^{(k)}\nabla p + M^{(k)}\nabla\cdot\boldsymbol{\tau}, \tag{4.25}$$

and for drag and turbulent dispersion terms:

$$\begin{aligned}\int_0^\infty 18\mu_c f D^{k-2}(\mathbf{u}-\mathbf{u}_c)dD &= 18\mu_c M^{(k-2)}(\mathbf{u}^{(k-2)}-\mathbf{u}_c)\\ \nabla\int_0^\infty 18\mu_c\frac{\nu_d^t}{\sigma_\alpha}fD^{k-2}dD &= 18\mu_c\frac{\nu_c^t}{\sigma_\alpha}\nabla M^{(k-2)},\end{aligned} \tag{4.26}$$

respectively. In the above expressions, it is the dependence of the Stokes relaxation time with the particle diameter, $\tau\propto D^2$ that gives rise to lower order powers of moment and transport velocity. This will be further discussed later on.

The turbulent stress term is approximately evaluated with the velocity $\mathbf{u}^{(k)}$ and moment $M^{(k)}$, yielding the approximate expression:

$$\nabla\cdot\left(\int_0^\infty fD^k\boldsymbol{\tau}_{\boldsymbol{d}}^{\boldsymbol{t}}dD\right) \equiv \nabla\cdot\left(M^{(k)}\boldsymbol{\tau}_{\boldsymbol{d}}^{\boldsymbol{t}\,(k)}\right), \tag{4.27}$$

with

$$\boldsymbol{\tau}_{\boldsymbol{d}}^{\boldsymbol{t}\,(k)} \approx \rho_d\,\nu_d^t(\nabla\mathbf{u}^{(k)}+\nabla\mathbf{u}^{(k)^T}-\frac{2}{3}\nabla\cdot\mathbf{u}^{(k)}\mathbf{I})-\rho_d\frac{2}{3}k_d\mathbf{I}. \tag{4.28}$$

According to the above results, the following form of the (k-th) averaged momentum equation for the particle phase is obtained:

$$\begin{aligned}\rho_d\frac{\partial\left(M^{(k)}\mathbf{u}^{(k)}\right)}{\partial t}+\rho_d\nabla\cdot(M^{(k)}\mathbf{u}^{(k)}\mathbf{u}^{(k)}) &= M^{(k)}\nabla p+M^{(k)}\nabla\cdot\boldsymbol{\tau}\\ &+ 18\mu_c M^{(k-2)}(\mathbf{u}^{(k-2)}-\mathbf{u}_c)+18\mu_c\frac{\nu_c^t}{\sigma_\alpha}\nabla M^{(k-2)}\\ &+ \nabla\cdot\left(M^{(k)}\boldsymbol{\tau}_{\boldsymbol{d}}^{\boldsymbol{t}\,(k)}\right)\\ &+ \rho_d M^{(k)}\mathbf{g}\\ &+ \rho_d\Gamma_{M^{(k)}}\mathbf{u}^{(k)}.\end{aligned} \tag{4.29}$$

The above equation for $k=3$ is the volume-averaged momentum equation of a dispersed phase (since $M^{(3)}\mathbf{u}^{(3)}$ represents the volume-flux of the population of particles). Thus:

$$\begin{aligned}\rho_d\frac{\partial\left(M^{(3)}\mathbf{u}^{(3)}\right)}{\partial t}+\rho_d\nabla\cdot(M^{(3)}\mathbf{u}^{(3)}\mathbf{u}^{(3)}) &= M^{(3)}\nabla p+M^{(3)}\nabla\cdot\boldsymbol{\tau}\\ &+ 18\mu_c M^{(1)}(\mathbf{u}^{(1)}-\mathbf{u}_c)+18\mu_c\frac{\nu_c^t}{\sigma_\alpha}\nabla M^{(1)}\\ &+ \nabla\cdot\left(M^{(3)}\boldsymbol{\tau}_{\boldsymbol{d}}^{\boldsymbol{t}\,(3)}\right)\\ &+ \rho_d M^{(3)}\mathbf{g}\\ &+ \rho_d\Gamma_{M^{(3)}}\mathbf{u}^{(3)}.\end{aligned} \tag{4.30}$$

4.4 Volume-averaged internal energy equation

The droplet temperature at a given position is considered here independent of the diameter. This hypothesis will be shown to suffice for the present purposes, but the more general case requires the consideration of other average quantities (for example, a length scale or surface average temperature to be used with the evaporation models) and is not going to be taken into account in the present work. Recent developments in this direction can be found in [32] and [84]. Thus, integration of the energy equation – with a similar treatment for the convective term as used in the momentum equation – leads to the conservation equation of the volume average internal energy:

$$\rho_d \frac{\partial (M^{(3)} i^{(3)})}{\partial t} + \rho_d \nabla \cdot (M^{(3)} \mathbf{u}^{(3)} i^{(3)} - M^{(3)} \frac{\nu_d^t}{\mathrm{Pr}_t^d} \nabla T^{(3)}) \quad = \quad \dot{Q}^{(3)}, \tag{4.31}$$

where, for the convective term, it was implicitly assumed that:

$$\begin{aligned} \nabla \cdot \left(\int_0^\infty f \mathbf{u} i D^3 dD \right) \quad &= \quad \nabla \cdot (M^{(3)} \mathbf{u}^{(3)} i^{(3)}) + \underbrace{\nabla \cdot \left(\int_0^\infty f \mathbf{u}' i' D^3 dD \right)}_{\approx 0} \\ &+ \quad \underbrace{\nabla \cdot \left(\int_0^\infty f \mathbf{u}^{(3)} i' D^3 dD \right)}_{\equiv 0} + \underbrace{\nabla \cdot \left(\int_0^\infty f \mathbf{u}' i^{(3)} D^3 dD \right)}_{\equiv 0}. \end{aligned} \tag{4.32}$$

Note that the velocity and energy fluctuations are considered uncorrelated, for simplicity. The integral heat flux $\dot{Q}^{(3)}$ is given by:

$$\dot{Q}^{(3)} \quad \approx \quad \rho_d \Gamma_{M^{(3)}} \hat{h}^{(3)} + 6 \mathrm{Nu} k_c M^{(1)} (T^{(3)} - T_c), \tag{4.33}$$

with $\hat{h}^{(3)}$ determined by: $\hat{h}^{(3)} = i^{(3)} + L_v$.

4.5 Exchange terms with the gas phase

The averaged equations for the continuous phase derived in the previous chapter considered exchange terms with a single dispersed phase (monodisperse situation). However, the exchange of mass, momentum and heat takes place between the continuous phase and a population of particles with different sizes and velocities. Therefore, the models extended in the previous sections also need to be incorporated into the continuous phase equations. Since the exchange terms are formulated in the previous section for equations involving $M^{(3)}$, a factor of $\pi/6$ has to be incorporated in corresponding terms for the gas equations. Equations (3.148), (3.149), (3.150) and (3.151) are then rewritten as follows:

$$\rho_c \frac{\partial \alpha_c}{\partial t} + \rho_c \nabla \cdot (\alpha_c \mathbf{u}_c) = -\rho_d \frac{\pi \Gamma_{M^{(3)}}}{6}. \tag{4.34}$$

$$\begin{aligned} \rho_c \frac{\partial (\alpha_c \mathbf{u}_c)}{\partial t} + \rho_c \nabla \cdot (\alpha_c \mathbf{u}_c \mathbf{u}_c) &= -\alpha_c \nabla p + \alpha_c \nabla \cdot \boldsymbol{\tau} \\ &+ \nabla \cdot \alpha_c (\boldsymbol{\tau}_c^t + \boldsymbol{\tau}_c^{pt}) \\ &- 3\pi\mu_c M^{(1)} (\mathbf{u}^{(1)} - \mathbf{u}_c) - 3\pi\mu_c \frac{\nu_c^t}{\sigma_\alpha} \nabla M^{(1)} \\ &+ \alpha_c \rho_c \mathbf{g} \\ &- \rho_d \frac{\pi \Gamma_{M^{(3)}}}{6} \mathbf{u}^{(3)} \end{aligned} \tag{4.35}$$

$$\begin{aligned} \rho_c \frac{\partial (\alpha_c i_c)}{\partial t} + \rho_c \nabla \cdot (\alpha_c \mathbf{u}_c i_c) &= \nabla \cdot \alpha_c (\boldsymbol{q}_c + \boldsymbol{q}_c^t + \boldsymbol{q}_c^{pt}) \\ &- p \nabla \cdot \mathbf{U} - \frac{\pi}{6} \dot{Q}^{(3)} \end{aligned} \tag{4.36}$$

$$\rho_c \frac{\partial (\alpha_c Y_v)}{\partial t} + \rho_c \nabla \cdot (\alpha_c \mathbf{u}_c Y_v) = \nabla \cdot \alpha_c (\boldsymbol{f}_c + \boldsymbol{f}_c^t + \boldsymbol{f}_c^{pt}) - \rho_d \frac{\pi \Gamma_{M^{(3)}}}{6}. \tag{4.37}$$

Note that the following constraint is valid for the volume fraction α_c: $\alpha_c = 1 - \pi M^{(3)}/6$.

The two-phase $\kappa-\epsilon$ equations are also modified to account for the integral exchange terms with the whole population of particles. They are then rewritten as:

$$\begin{aligned}\rho_c\frac{\partial(\alpha_c\kappa_c)}{\partial t}+\rho_c\nabla\cdot(\alpha_c\mathbf{u}_c\kappa_c) &= \nabla\cdot(\alpha_c\frac{\mu_c^t}{\sigma_k}\nabla\kappa_c)+\alpha_c(G-\rho_c\epsilon_c)\\ &- 18\mu_c M^{(1)}\left[2(1-\alpha_c)\alpha_c(1-C_k)\kappa_c-\frac{\nu_c^t}{\sigma_\alpha}\nabla\alpha_c\cdot(\mathbf{u}^{(3)}-\mathbf{u}_c)\right]\\ &- \rho_d\frac{\pi\Gamma_{M^{(3)}}}{6}\kappa_c \end{aligned} \tag{4.38}$$

$$\begin{aligned}\rho_c\frac{\partial(\alpha_c\epsilon_c)}{\partial t}+\rho_c\nabla\cdot(\alpha_c\mathbf{u}_c\epsilon_c) &= \nabla\cdot(\alpha_c\frac{\mu_c^t}{\sigma_\epsilon}\nabla\epsilon_c)+\alpha_c\frac{\epsilon_c}{\kappa_c}(C_1G-C_2\rho_c\epsilon_c)\\ &- 2(1-\alpha_c)\alpha_c(1-C_k)\epsilon_c(18\mu_c M^{(1)})\\ &- \rho_d\frac{\pi\Gamma_{M^{(3)}}}{6}\epsilon_c. \end{aligned} \tag{4.39}$$

The parameter β for the calculation of C_t in Eq. (3.168) is given approximately by:

$$\beta = \rho_d\frac{\tau_{\epsilon_c}}{18\mu_c M^{(1)}}\left(1+2\frac{\rho_d}{\rho_c}\right), \tag{4.40}$$

where the contribution of the population of particles is considered implicitly through $M^{(1)}$. Note that the time scale has been substituted by the factor $\rho_d/(18\mu_c M^{(1)})$.

4.6 Size distribution closure

Due to the form of the expressions for exchange terms in the particle equations of motion, unknown moments and transport velocities (e.g. $M^{(k-2)}$,

$\mathbf{u}^{(k-2)}$) appear in the formulation. For instance, as seen before, the expression for the drag force per unit volume in the equation for $\mathbf{u}^{(k)}$ is given by:

$$\mathbf{F}_{Drag}^{(k)} = 18\mu_c M^{(k-2)}(\mathbf{u}^{(k-2)} - \mathbf{u}_c). \tag{4.41}$$

The closure problem for the moments has been studied for the first time in the pioneer work of Hulburt and Katz [40]. Since then, the majority of the literature is concerned with the determination of source terms due to interactions such as agglomeration or break-up, but not due to size-dependent particle movement. In the present work, the closure problem for the drag term is treated in a similar manner.

A simple way to overcome the issue of determining unknown moments is to assume a certain functional form for $f(D)$. Then the distribution can be reconstructed approximately from a few (usually low-order) "prognostic moments", for which transport equations are solved. Unknown "diagnostic moments", which may be required to achieve closure, can then be computed by integration of the presumed size distribution.

When using pNDFs, it is intrinsically assumed that the shape of the distribution is preserved during the simulated process, which might not be strictly true. However, even if its shape varies, it might be possible to capture the most important features of the flow through the description of the moments, which represent integral quantities associated to the population as whole. Thus, hypothetically, the exact shape of a droplet size distribution in an evaporating spray might be poorly reproduced, without deteriorating predictions of the total number/length scale/surface area/volume of droplets; so it might be expected that exchange terms with the gas phase are still satisfactory. One can try to minimize this problem by choosing distribution shapes which are known to be flexible; or, develop methods which do not need to assume the shape of the distribution (e.g., MEF or spline methods, as mentioned before). Here, the first approach will be pursued. It shall be however pointed out that critical situations involving bi- or multi-modal distributions will not be handled in this thesis.

Different types of reconstruction schemes using Gamma and Beta distribution functions will be outlined next, while a closure method for the moment transport velocities will be proposed in section 4.7.

4.6.1 Gamma distribution

The Gamma distribution function used here is similar to the one proposed by Watkins [83]. The present version, however, is defined such that it has 3 free parameters, while the previous one had only 2. Another version of a 2-parameter Gamma scheme was also presented by Carneiro et al. [19]. It was shown that the 3-parameter scheme performed better in a real spray configuration analyzed. The two-parameter Gamma scheme will not be used in this work.

The expression for the Gamma distribution function is given by:

$$f(D) = C_0 \frac{D^{q-1} e^{-\frac{D}{p}}}{p^q \Gamma(q)}, \tag{4.42}$$

with the Gamma function

$$\Gamma(q) = \int_0^\infty t^{q-1} e^{-t} dt. \tag{4.43}$$

Moments can be calculated explicitly by the general expression:

$$M^{(k)} = C_0 \frac{\Gamma(q+k) p^k}{\Gamma(q)}. \tag{4.44}$$

The parameters p, q and C_0 can be expressed in terms of 3 prognostic moments,

$$p = \frac{M^{(k_{min}+2)} M^{(k_{min})} - (M^{(k_{min}+1)})^2}{M^{(k_{min})} M^{(k_{min}+1)}}$$

$$q = \frac{(k_{min}+1)(M^{(k_{min}+1)})^2 - k_{min}M^{(k_{min}+2)}M^{(k_{min})}}{M^{(k_{min}+2)}M^{(k_{min})} - (M^{(k_{min}+1)})^2} \tag{4.45}$$

$$C_0 = \begin{cases} \frac{M^{(k_{min})}}{p^{k_{min}}\Pi_{l=0}^{k_{min}-1}(q+l)} & \text{, if } k_{min} \in N^+ \\ M^{(0)} & \text{, if } k_{min} = 0. \end{cases}$$

Hence, these relations provide a simple way to reconstruct the Gamma distribution function from any three consecutive moments known. In the present work two alternatives will be tested: $M^{(0)}$-$M^{(2)}$ ($k_{min} = 0$) and $M^{(1)}$-$M^{(3)}$ ($k_{min} = 1$).

4.6.2 Beta distribution

The Beta distribution function with minimum diameter equal to zero is defined as [83]:

$$f(D) = \frac{C_0}{B(p,q)} \frac{D^{p-1}(D_{max}-D)^{q-1}}{{D_{max}}^{p+q-1}}, \tag{4.46}$$

with $D \in [0, D_{max}]$ and the Beta function

$$B(p,q) = \int_0^1 t^{p-1}(1-t)^{q-1}dt = \frac{\Gamma(p)\Gamma(q)}{\Gamma(p+q)}. \tag{4.47}$$

Moments are given by the general expression:

$$M^{(k)} = C_0 D_{max}^k \frac{B(p+k,q)}{B(p,q)}, \tag{4.48}$$

with the parameters C_0, D_{max}, p and q being determined by:

$$C_0 = M^{(0)}$$

$$
\begin{aligned}
D_{max} &= \frac{-M^{(1)}(M^{(2)})^2 + 2(M^{(1)})^2 M^{(3)} - M^{(0)} M^{(2)} M^{(3)}}{(M^{(1)})^2 M^{(2)} - 2M^{(0)}(M^{(2)})^2 + M^{(0)} M^{(1)} M^{(3)}} \\
p &= \frac{-M^{(1)}(D_{max} M^{(1)} - M^{(2)})}{D_{max}[(M^{(1)})^2 - M^{(0)} M^{(2)}]} \\
q &= -\frac{D_{max} M^{(0)} M^{(1)} - (M^{(1)})^2 - M^{(0)} M^{(2)} + \frac{M^{(1)} M^{(2)}}{D_{max}}}{(M^{(1)})^2 - M^{(0)} M^{(2)}}.
\end{aligned} \tag{4.49}
$$

Clearly, the reconstruction of the Beta distribution requires in general knowledge of the first four moments ($M^{(0)}$-$M^{(3)}$). If the maximum diameter D_{max} of the distribution is kept constant, however, only three moments ($M^{(0)}$-$M^{(2)}$) are sufficient, since $M^{(3)}$ does not appear explicitly in the expressions for p and q. Both possibilities will be assessed in the present study. The main advantage of the presumed function approach is the simplicity of the reconstruction methods; indeed, for the Gamma and Beta functions the distribution parameters are calculated in an algebraic manner. Furthermore, these functions are able to represent a wide variety of shapes. Figure 4.3 shows the variation of Gamma and Beta distribution functions for typical values of the shape and scale parameters, maintaining $M^{(0)}$ and D_{max} invariant. Even for the small range of variation of p and q, very distinct forms can be reproduced in both cases. Some important differences can be observed between the two functions, however. While the Gamma distribution extends the diameter range indefinetely, remaining positively skewed for all combinations of p and q (a limitation of its functional form), the Beta distribution has a fixed diameter range and is able to represent positively skewed ($p < q$), symetrical ($q = p$) and negatively skewed ($p > q$) shapes. Note in Fig. 4.4 that for values of $p, q < 2$, overshoots ($f \to \infty$) at the limits $D \to 0$ or $D \to D_{max}$ can be produced.

As will be demonstrated later, the use of different distribution shapes and a different number of moments to reconstruct the distribution functions have a strong influence on the performance of the model.

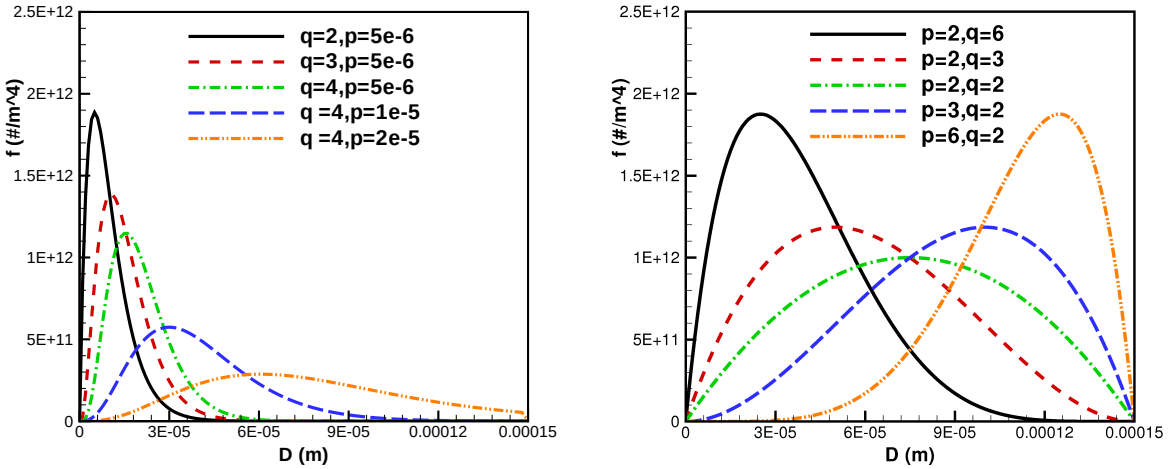

Figure 4.3: Variation of the Gamma (left) and Beta (right) distribution functions with the parameters p and q.

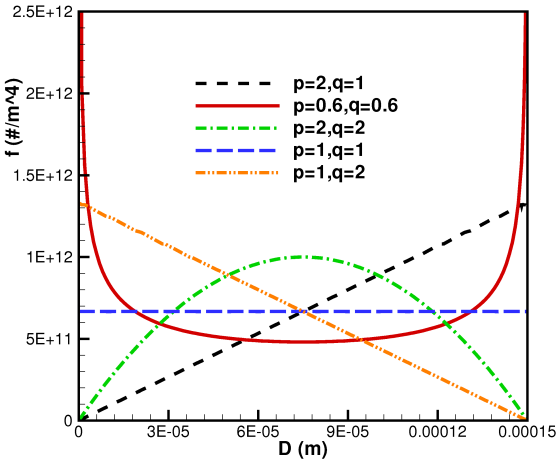

Figure 4.4: Different forms of the Beta distribution functions $p \leq 2$ and $q \leq 2$.

4.6.3 Validity of a moment set

Given a set of moments $(M^{(k)}, k = k_{min}, \ldots, k_{max})$, there is no guarantee that there is a realizable distribution function associated with it. In that case, the set of moments is considered "invalid". In Eulerian simulation models, invalid sets may occur for two reasons, even if boundary and initial conditions are valid: the independent advection of moments $M^{(k)}$ with different moment transport velocities ($\mathbf{u}^{(l)} \neq \mathbf{u}^{(m)}$, $l \neq m$); or the presence of different source terms in the moment transport equations (e.g. due to coalescence, break-up or evaporation).

Recall the formulation of the Stieltjes moment problem [3, 74]:

To prove the existence of a distribution function $f(D)$, with $f(D) \geq 0$ defined in the range $D \in [0, \infty)$, given a set of moments defined as

$$M^{(k)} \equiv \int_0^\infty D^k f(D) dD. \tag{4.50}$$

In order to uniquely characterize $f(D)$, knowledge of all its moments is in theory necessary. In fact, White [87] give examples showing that even dissimilar size distributions can have identical moments of all orders. One way or the other, only a finite set is available in practice. Clearly, there exists an infinite variety of functions whose moments coincide with the given finite set, and the unique reconstruction of $f(D)$ is impossible. Therefore, the problem of distribution reconstruction is two-fold: first, the realizability of these distributions must be consistently checked in the simulation models; second, classes of functions of interest must be chosen in order to reasonably reproduce the shapes of experimentally observed distributions for the physical problem in question.

4.6.3.1 Convexity

An invalid moment set is characterized by the non-existence of an underlying distribution function associated to it. The most straightforward way to check the validity of a moment set is by verifying the so called "convexity conditions" (also frequently called "Schwarz's Inequalities"):

$$M^{(k)}\,M^{(k-2)} - (M^{(k-1)})^2 \quad > \quad 0, \tag{4.51}$$

which must hold for all k. This property of the moment set is a direct consequence of the definition of the moments: for a non-negative $f(D)$, since the ratio of consecutive moments $\frac{M^{(k)}}{M^{(k-1)}}$ increases with k, one can simply write:

$$\frac{M^{(k-1)}}{M^{(k-2)}} < \frac{M^{(k)}}{M^{(k-1)}} < \frac{M^{(k+1)}}{M^{(k)}}\ (...), \tag{4.52}$$

which implies Eq. (4.51). This mathematical constraint must always be met in order for the distribution function to be realizable.

A direct consequence of Eq. (4.52) is that the usual mean diameters used to characterize droplet size distributions occurring in spray applications are such that: $D_{10} < D_{21} < D_{32} < D_{43}\ (...) < D_{max}$. This, as seen above, must be true for all realizable distribution functions.

4.6.3.2 Hankel-Hadamard determinants

Equation (4.52), however, is a necessary but not sufficient condition for a valid moment set. Necessary and sufficient conditions which guarantee the existence of a distribution function, given a sequence of moments $M^{(k)}$, $k = 0, 1, 2 \ldots \underbrace{2l/2l+1}_{k_{max}}$[3], are non-negative Hankel-Hadamard determinants [46,74]:

[3]The expression for $k_{max}(l)$ depends if the number of prognostic moments is even ($k_{max} = 2l+1$) or odd ($k_{max} = 2l$).

$$\Delta_{k,l} = \begin{vmatrix} M^{(k)} & M^{(k+1)} & \dots & M^{(k+l)} \\ M^{(k+1)} & M^{(k+2)} & \dots & M^{(k+l+1)} \\ \vdots & \vdots & \ddots & \vdots \\ M^{(k+l)} & M^{(k+l+1)} & \dots & M^{(k+2l)} \end{vmatrix} \geq 0$$

with $k = 0, 1$; $l \geq 0$; $\Delta_{k,l} = 0$ for a monodisperse distribution.

A compact way of writing the above criteria including a formula for the matrix elements is: $\Delta_{k,l} = \det|B| \geq 0$ $(k = 0, 1)$ and $B_{ij} = M^{(k+i+j-2)}$, with $i, j = 1, 2, ..., l+1$.

Note that:

- $\Delta_{k,0} \geq 0$ corresponds to the physical condition of positivity of the moments.
- $\Delta_{k,1}$ (2x2 determinants) are a compact form of the convexity inequalities: $\frac{M^{(k+1)}}{M^{(k)}} < \frac{M^{(k+2)}}{M^{(k+1)}}$.

The Hankel-Hadamard conditions guarantee the existence of $f(D)$ whose first $(k_{max}+1)$ moments are equal to the given ones. If the existence of a distribution function is proven for a sequence of moments $M^{(0)}...M^{(kmax)}$, the remaining moments $M^{(j)}$, $j = k_{max}+1, ...$ are such that all determinants $\Delta_{k,r}$, $r = l+1, l+2...$ will necessarily be positive. Here, the first few moments are used to compute the distribution function by means of presumed forms of $f(D)$. The relevant conditions depending on the number of prognostic moments are given as follows:

- 2 Moments

  As mentioned before, the criterion reduces to $M^{(k)} \geq 0$, since $l = 0$.

- 3 Moments; $M^{(0)} - M^{(2)}$

  The following restrictions apply:

$M^{(0)}, M^{(1)} \geq 0$ ($l = 1$)

and

$$\Delta_{0,1} = \begin{vmatrix} M^{(0)} & M^{(1)} \\ M^{(1)} & M^{(2)} \end{vmatrix} \geq 0$$

(it is clearly not enough that $M^{(2)} \geq 0$, since convexity must also be satisfied: $M^{(2)} \geq \frac{(M^{(1)})^2}{M^{(0)}}$)

- 4 Moments; $M^{(0)} - M^{(3)}$

  Also here, $l = 1$. Hence: $M^{(0)}, M^{(1)} \geq 0$

  and

$$\Delta_{0,1} = \begin{vmatrix} M^{(0)} & M^{(1)} \\ M^{(1)} & M^{(2)} \end{vmatrix} \geq 0$$

$$\Delta_{1,1} = \begin{vmatrix} M^{(1)} & M^{(2)} \\ M^{(2)} & M^{(3)} \end{vmatrix} \geq 0$$

4.6.3.3 Further remarks

The conditions outlined above obviously allow the definition of bounds for the moments. There are some reconstruction approaches that might require some additional considerations. For example, if the moments $M^{(k_{min})}, M^{(k_{min}+1)}, \ldots$ are available, there is a problem with directly using the Hankel-Hadamard criteria as presented here, since $M^{(0)}$ is unknown. However, this problem can be readily avoided by defining an auxiliary distribution $f'(D)$

$$f'(D) = D\, f(D), \tag{4.53}$$

such that $M^{(k)'} = M^{(k+1)}$, and the Hankel-Hadamard inequalities are applied to $f'(D)$. Hence, if $f'(D)$ exists, $f(D)$ also does. The following restrictions must be then fulfilled:

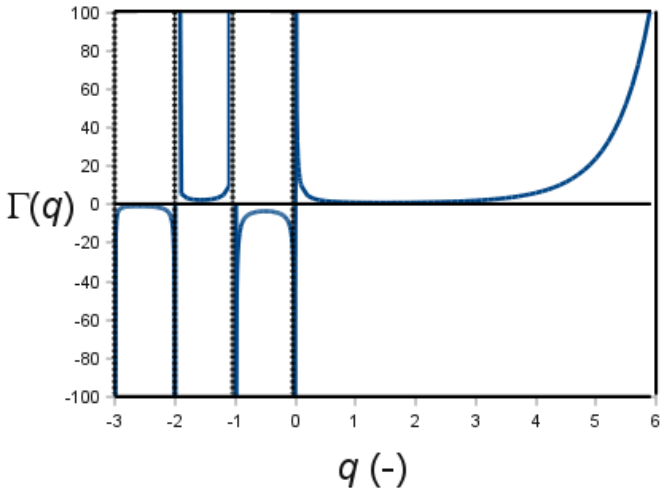

Figure 4.5: Variation of the Gamma function with the argument q.

$k_{min} = 1$ ($M^{(1)} - M^{(3)}$ as prognostic moments): $M^{(1)}, M^{(2)} \geq 0$

and

$$\Delta_{1,1} = \begin{vmatrix} M^{(1)} & M^{(2)} \\ M^{(2)} & M^{(3)} \end{vmatrix} \geq 0,$$

leading to $M^{(3)} \geq \frac{(M^{(2)})^2}{M^{(1)}}$.

However, as will be seen in an example, some extra care might be needed in order to reconstruct the distribution function. If the distribution function is assumed to have a Gamma shape with $k_{min} = 0$, it is sufficient to prove the conditions outlined before (which lead to $C_0, p, q \geq 0$ – in fact, the monodisperse case has to be disconsidered to avoid q from exploding, and $C_0, p, q > 0$). However, for $k_{min} = 1$, the criteria outlined above only guarantee that $C_0, p > 0$, but not q. This might be problematic, since $\Gamma(q < 0)$ may assume negative values – see Fig. 4.5. To ensure that $q > 0$, one can define lower and upper bounds, e.g., for the moment $M^{(2)}$ as a function of $M^{(1)}$ and $M^{(3)}$:

$$\sqrt{\frac{1}{2}M^{(1)}\,M^{(3)}} < M^{(2)} < \sqrt{M^{(1)}\,M^{(3)}}. \tag{4.54}$$

In fact, depending on which low-order moments appear in the sub-models used, the above condition might become more restrictive. For instance, for the problem of droplet evaporation, source terms might depend on moments with negative order (e.g. $M^{(-1)}$). In that case, according to Eq. (4.44), $q > 1$ is desired. More generally: $q > |k_l|$ ($k_l < 0$) must be satisfied; otherwise $M^{(k_l)}$ might become negative. thus, it is possible to write for $M^{(2)}$:

$$\sqrt{\frac{|k_l|+1}{|k_l|+2}M^{(1)}\,M^{(3)}} < M^{(2)} < \sqrt{M^{(1)}\,M^{(3)}}, \tag{4.55}$$

k_l is the order of the moment with lowest (negative) order.

Some similar results on the bounds of moments for maximum entropy distributions are also presented by Frontini and Tagliani [35].

Concerning the Beta distribution, a discussion on the Stieltjes formulation is provided in Appendix A.1. It remains to be investigated, under which conditions for both 3- and 4-moment schemes, the Beta distribution is realizable allowing the reconstruction of the functional form. Hence:

- D_{max}=D_0 = const. (> 0); three-moments scheme

$$\begin{aligned} p &= \frac{M^{(1)}(D_0 M^{(1)} - M^{(2)})}{D_0[\underbrace{M^{(0)}M^{(2)} - (M^{(1)})^2}_{\Delta_{0,1}}]} \\ p &= \frac{(M^{(1)})^2}{\Delta_{0,1}}\left(1 - \frac{D_{21}}{D_0}\right) \end{aligned} \tag{4.56}$$

  Thus, if $M^{(1)} > 0$, $\Delta_{0,1} > 0$ and $D_0 > D_{21}$ (see section 4.6.3.1), $p > 0$. q can be rewritten in dependence of p as:

$$q = p\left(\frac{D_0}{D_{10}} - 1\right). \tag{4.57}$$

Obviously, if $p > 0$ and $D_0 > D_{10}$, $q > 0$.

- four-moments scheme

  The conditions derived above are also valid here. It remains to be to be analyzed under which conditions $D_{max} > 0$. The expression for D_{max} can be rewritten as:

$$\begin{aligned} D_{max} &= \frac{(D_{32} - D_{21})\,(M^{(1)})^2\,M^{(2)} - (D_{21} - D_{10})\,M^{(0)}\,M^{(1)}\,M^{(3)}}{(D_{32} - 2D_{21} + D_{10})\,M^{(0)}\,M^{(1)}\,M^{(2)}} \\ D_{max} &= \frac{1}{D_{32} - 2D_{21} + D_{10}}\left[(D_{32} - D_{21})\,D_{10} - (D_{21} - D_{10})\,D_{32}\right] \\ D_{max} &= \frac{D_{32}\,D_{10}}{D_{32} - 2D_{21} + D_{10}}\left[2 - D_{21}\left(\frac{1}{D_{10}} + \frac{1}{D_{32}}\right)\right] \\ D_{max} &= \frac{D_{32}\,D_{21}\,D_{10}}{D_{32} - 2D_{21} + D_{10}}\left[\left(\frac{1}{D_{21}} - \frac{1}{D_{32}}\right) - \left(\frac{1}{D_{10}} - \frac{1}{D_{21}}\right)\right] \end{aligned} \tag{4.58}$$

  As will be seen below, the difference $(D_{k,k-1} - D_{k-1,k-2}$ decreases with k, where $D_{k,k-1} = M^{(k)}/M^{(k-1)})$. This can be verified using the expression for the moments of the Beta distribution, Eq. (4.48), observing that

$$M^{(k)} = C_0\,D_{max}^k\,\Pi_{i=0}^{k-1}\frac{p+i}{p+q+i}, \tag{4.59}$$

  which allows to derive an expression for the mean diameters of the distribution, as a function of k:

$$D_{k,k-1} = D_{max}\frac{p+k-1}{p+q+k-1}. \tag{4.60}$$

  The above expression has the following property: $\lim_{k\to\infty} D_{k,k-1} = D_{max}$. The dependence of $D_{k,k-1}$ on k can be visualized in Fig. 4.6, for the Beta distributions shown in Fig. 4.3. Hence, as $D_{k,k-1}$ tends asymptotically to D_{max} with increasing order k, it is apparent that the difference $(D_{k,k-1} - D_{k-1,k-2})$ decreases. With help of Eq. (4.60), expressions for $D_{k,k-1}$ can be substituted in the conditions $(D_{32} + D_{10})/2 < D_{21}$ and $(1/D_{32} + 1/D_{10})/2 > 1/D_{21}$. It is possible to conclude that p, q must be positive, otherwise they are not satisfied. Note that D_{10}, D_{21} and D_{32} must also be positive.

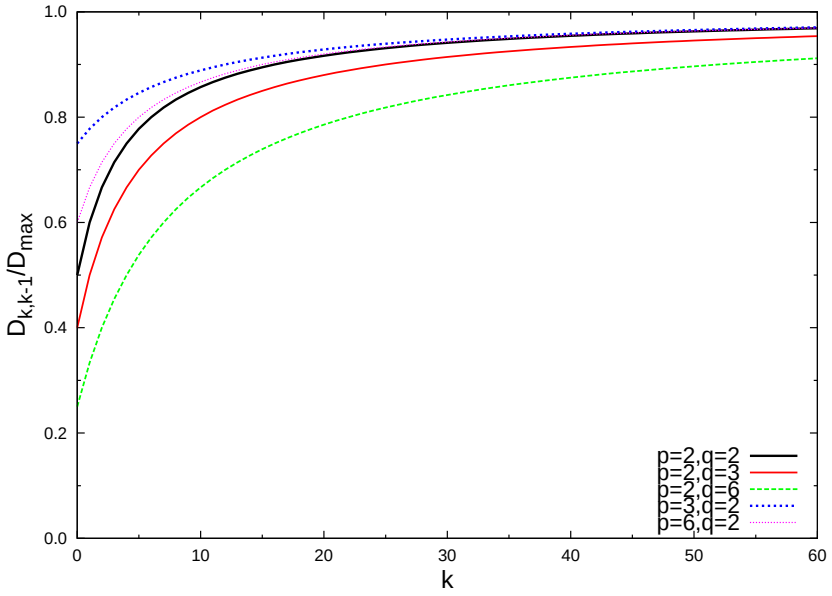

Figure 4.6: Variation of the ratio $D_{k,k-1}/D_{max}$ with the order k.

4.6.3.4 Geometry of the moment space

As seen above, the Hankel-Hadamard determinants establish whether or not there is a set of positive functions which obey the Stjelties moment condition. The realizability of specific functional forms might require additional considerations, which depend both on the underlying mathematical functions and reconstruction schemes. Therefore, the geometry of the valid moment space varies accordingly.

As shown by Dems et al. [25], e.g. for the Beta scheme using four moments the condition that both the enumerator and denominator of D_{max} have to be negative leads to the following inequalities for $M^{(2)}$:

$$M^{(2)} \geq \sqrt{\frac{M^{(0)^2} M^{(3)^2}}{4M^{(1)^2}} + 2M^{(1)} M^{(3)}} - \frac{M^{(0)} M^{(3)}}{2M^{(1)}} \tag{4.61}$$

and

$$M^{(2)} \geq \sqrt{\frac{M^{(1)^4}}{16M^{(0)^2}} + \frac{M^{(1)}M^{(3)}}{2}} + \frac{M^{(1)^2}}{4M^{(0)}}, \tag{4.62}$$

for enumerator and denominator, respectively.

Such constraints can be illustratively plotted together for the Beta schemes (see Fig. 4.7), in order to visualize the valid moment space projected at the $M^{(1)}-M^{(2)}$ plane (i.e., for given values of $M^{(0)}$ and $M^{(3)}$). The map is normalized by the maximum values of $M^{(1)}$ and $M^{(2)}$. They can be determined taking into account the intersection of the several conditions outlined above, from which it follows that:

$$M^{(1)}_{max} = D_0 M^{(0)} \qquad M^{(1)}_{max} = D_0^2 M^{(0)}, \tag{4.63}$$

for the 3-moment scheme (with $D_{max} = D_0 = \text{constant}$), and

$$M^{(1)}_{max} = \sqrt[3]{M^{(0)^2} M^{(3)}} \qquad M^{(1)}_{max} = \sqrt[3]{M^{(0)} M^{(3)^2}}, \tag{4.64}$$

for the 4-moment scheme.

4.6.3.5 Replacement and correction schemes

The outcome of the numerical solution of the equation systems comprising moment methods might give rise to moment sets that violate the mathematical constraints which must be met in order to calculate the local distribution function.

Bo and Watkins [15], for example, reported serious difficulties in the simulation of sprays. At the spray edges, particularly at the front, it is observed that moments of higher order tend towards zero much faster than the lower order ones. The authors applied restrictions in the moment transport velocities in order to prevent this situation from occurring. Watkins [83], on the other

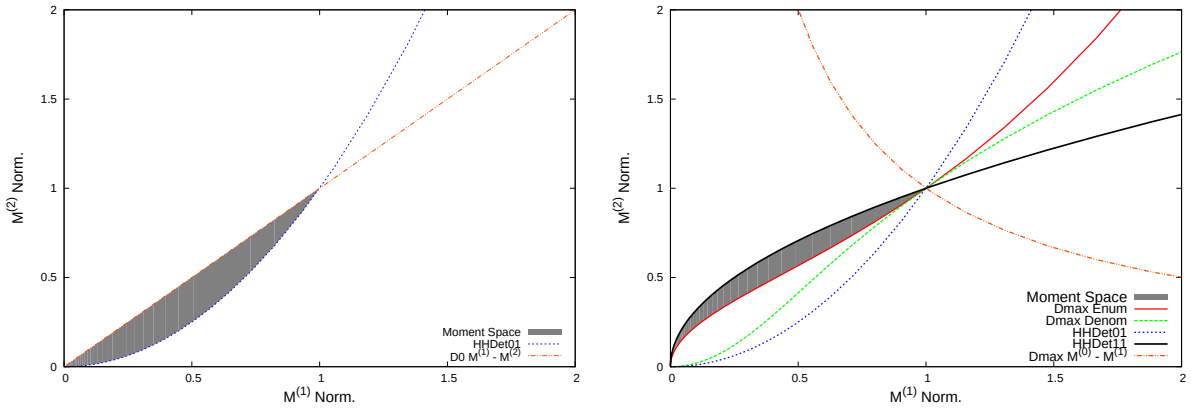

Figure 4.7: Region of valid moment sets shown in the moment space projected at the $M^{(1)} - M^{(2)}$ plane. 3-moment Beta scheme (left) and 4-moment Beta scheme (right). Moments are normalized by the maximum allowed values, $(M^{(1)}_{\text{max}}, M^{(2)}_{\text{max}})$

.

hand, bounded the Gamma and Beta parameters obtained in the reconstruction process in order to avoid out-of-range values in the transport equations. A method using Hankel-Hadamard determinants and the construction of difference tables for the correction of invalid sets moments of aerosol size distributions was proposed by McGraw [58] and used by Petitti et al. [66] in the simulations of gas-liquid stirred reactors with QMOM. Replacement schemes were also proposed in the literature, based on, e.g., polynomial interpolation of unknown moments [5] or log-normal schemes [14, 46]. DQMOM [53] might also be an interesting alternative, because it tracks abscissas and weights directly, which can be shown to be always positive and realizable for univariate smooth distribution functions, avoiding moment set validity concerns. If the distribution is multivariate, however, the moment set must be carefully chosen in order to avoid nonunique abscissas and negative weights [34].

In the present work, potential situations will be described which might give rise to invalid sequences during the simulations. In order to avoid singularities in the distribution reconstruction during the solution procedure, it is made sure that the moments do not fall below minimum values, which must respect the conditions outlined above. By doing this, it will be shown that the

converged solution of the equation system always presents positive Hankel Hadamard determinants, allowing the reconstruction of realizable distribution functions. The integration of other procedures described in the literature with the presumed functional forms and reconstruction schemes used here will not be undertaken in this study.

4.7 Relaxation approach for size-dependent particle velocity

The "equilibrium Eulerian method" was introduced by Ferry and Balachandar [30,31]. The method assumes that for very small particle relaxation times, it is appropriate to express the particle velocity $\mathbf{u}$ as a first order expansion around the continuous phase velocity $\mathbf{u}_c$ in terms of its relaxation time τ given by Eq. (2.3). By doing so, particle velocities can be determined in a computationally efficient manner by simply introducing a correction of $\mathcal{O}(\tau)$ on $\mathbf{u}_c$. In the light of this idea, Bollweg et al. [16] proposed a linear interpolation between the continuous phase and reference particle velocities (with a size larger than all "minor" particles) to determine minor particle size velocities. Thus only one particle velocity field needs to be solved for in addition to $\mathbf{u}_c$. In this work, a similar concept is used to determine moment transport velocities, thus achieving closure for Eq. (4.13).

Considering the particle relaxation time τ as dependent variable, the particle velocity $\mathbf{u}$ can be expanded formally around a reference velocity $\mathbf{u}|_{\tau_{ref}}$:

$$\mathbf{u}|_{\tau} = \mathbf{u}|_{\tau_{ref}} + (\tau - \tau_{ref}) \frac{\partial \mathbf{u}}{\partial \tau}\Big|_{\tau_{ref}} + \mathcal{O}(\tau^2). \tag{4.65}$$

For the special case $\tau_{ref} = 0$, $\mathbf{u}|_{\tau_{ref}=0} = \mathbf{u}_c$ and the above expression may be written as

$$\mathbf{u}|_{\tau} = \mathbf{u}_c + \tau \frac{\partial \mathbf{u}}{\partial \tau}\Big|_{\tau_{ref}=0}, \tag{4.66}$$

where the higher order terms were droped for simplicity. Obviously, in the limit $\tau \to 0$ the particle follows the continuous phase, $\mathbf{u}|_{\tau} \to \mathbf{u}_c$.

The derivative $\partial \mathbf{u}/\partial \tau\big|_{\tau_{ref}=0}$ can be determined by rewriting the particle equa-

tion of motion given by Eq. (3.109) as[4]:

$$\mathbf{u} = \mathbf{u}_c + \tau \left[\left(1 - \frac{\rho_c}{\rho_d}\right)\mathbf{g} + \frac{\rho_c}{\rho_d}\frac{\mathrm{D}\mathbf{u}_c}{\mathrm{D}t} - \frac{\mathrm{d}\mathbf{u}}{\mathrm{d}t} \right]. \tag{4.67}$$

Taking the derivative with respect to τ yields for $\tau_{ref} = 0$:

$$\left.\frac{\partial \mathbf{u}}{\partial \tau}\right|_{\tau_{ref}=0} = \left(1 - \frac{\rho_c}{\rho_d}\right)\mathbf{g} + \frac{\rho_c}{\rho_d}\frac{\mathrm{D}\mathbf{u}_c}{\mathrm{D}t} - \left.\frac{\mathrm{d}\mathbf{u}}{\mathrm{d}t}\right|_{\tau_{ref}=0} = \left(1 - \frac{\rho_c}{\rho_d}\right)\left(\mathbf{g} - \frac{\mathrm{D}\mathbf{u}_c}{\mathrm{D}t}\right). \tag{4.68}$$

In the above equations, the Lagrangian derivative of the particle velocity $\mathrm{d}\mathbf{u}/\mathrm{d}t$, evaluated at $\tau_{ref} = 0$, is replaced by the material derivative $\mathrm{D}\mathbf{u}_c/\mathrm{D}t$ following a fluid particle, which is given by Eq. (3.6). Ferry and Balachandar [30] have shown that this is accurate for sufficiently small τ.

The above analysis can be extended by expanding $\mathbf{u}$ around a reference velocity $\mathbf{u}_0 \equiv \mathbf{u}|_{\tau_{ref}}$ with corresponding relaxation time $\tau_0 > 0$ (which shall nevertheless be sufficiently small to allow the first order approximation), leading to:

$$\mathbf{u}|_\tau = \underbrace{\mathbf{u}_0}_{\mathbf{u}_c + \tau_0 \left.\frac{\partial \mathbf{u}}{\partial \tau}\right|_{\tau_0}} + (\tau - \tau_0)\left.\frac{\partial \mathbf{u}}{\partial \tau}\right|_{\tau_0} = \mathbf{u}_c + \tau \left.\frac{\partial \mathbf{u}}{\partial \tau}\right|_{\tau_0}. \tag{4.69}$$

Furthermore, according to Eq. (4.68), one can write:

$$\left.\frac{\partial \mathbf{u}}{\partial \tau}\right|_{\tau_0} = \left(1 - \frac{\rho_c}{\rho_d}\right)\mathbf{g} + \frac{\rho_c}{\rho_d}\frac{\mathrm{D}\mathbf{u}_c}{\mathrm{D}t} - \left.\frac{\mathrm{d}\mathbf{u}}{\mathrm{d}t}\right|_{\tau_0}. \tag{4.70}$$

Substituting $\mathbf{u} = \mathbf{u}_0$ and $\tau = \tau_0$ in Eq. (3.109) allows to finally arrive at the following expression for $\mathbf{u}|_\tau$:

$$\mathbf{u}|_\tau = \mathbf{u}_c + \tau \frac{\mathbf{u}_0 - \mathbf{u}_c}{\tau_0}. \tag{4.71}$$

These results exhibit a number of important properties:

1. The limiting case $\mathbf{u}|_\tau \to \mathbf{u}_c$ for $\tau \to 0$ is satisfied.

[4] Note that the particle center of mass velocity $\mathbf{v}$ is now the Eulerian mean velocity $\mathbf{u}$.

2. If the continuous phase is not accelerating, $\mathrm{D}\mathbf{u}_c/\mathrm{D}t = 0$, the particle terminal rise/fall velocity

$$\mathbf{u}_T = \mathbf{u}_c + \tau\left(1 - \frac{\rho_c}{\rho_d}\right)\mathbf{g} \tag{4.72}$$

is recovered.

3.

$$\frac{\partial}{\partial\tau}\mathbf{u}|_\tau = \frac{\mathbf{u}_0 - \mathbf{u}_c}{\tau_0} = \left(1 - \frac{\rho_c}{\rho_d}\right)\left(\mathbf{g} - \frac{\mathrm{D}\mathbf{u}_c}{\mathrm{D}t}\right) \approx \text{constant}, \tag{4.73}$$

hence $\partial\mathbf{u}/\partial\tau\big|_{\tau=\tau_{ref}}$ does not depend on the particle diameter. Differences appear only in higher order terms $\mathscr{O}(\tau^2)$.

It is now shown how this framework can be applied to determine first order approximations for the moment transport velocities. In order to do so, the expression 4.71 for $\mathbf{u}|_\tau$ is integrated over the size spectrum, yielding:

$$\mathbf{u}^{(k)} \approx \frac{1}{M^{(k)}}\int_0^\infty f\,\mathbf{u}|_\tau\, D^k dD = \mathbf{u}_c + \frac{\tau^{(k)}}{\tau_0}(\mathbf{u}_0 - \mathbf{u}_c), \tag{4.74}$$

where the k-th order response time $\tau^{(k)}$ is defined as:

$$\tau^{(k)} = \frac{1}{M^{(k)}}\int_0^\infty \tau D^k f(D) dD. \tag{4.75}$$

Substituting Eq. (2.3) into (4.75), one obtains:

$$\tau^{(k)} = \frac{\rho_d}{18\,\mu_c}\frac{M^{(k+2)}}{M^{(k)}}. \tag{4.76}$$

Therefore, this closure corresponds to a linear interpolation between continuous phase velocity $\mathbf{u}_c$ and reference velocity $\mathbf{u}_0$ (see Fig. 4.8) in the response times space. It is hence clear that the size-velocity correlation (and consequently any $\mathbf{u}^{(k)}$) is fully determined with knowledge of $\mathbf{u}_c$ and $\mathbf{u}_0$. Transport equations for $\mathbf{u}_c$ and $\mathbf{u}_0$ based on momentum conservation will be presented later.

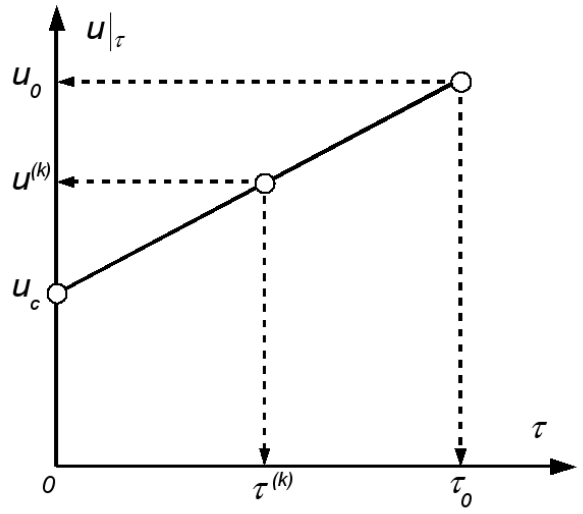

Figure 4.8: Schematic representation of the expression given by Eq. (4.74).

This framework is named "relaxation approach", because it allows to consider the relaxation process towards the equilibrium condition. The relaxation approach and the presumed function closure presented in this work comprise what is called presumed function Method of Moments (refered to as "PMOM").

4.7.1 A simple example for constant $f(D)$

To illustrate the concept of the relaxation approach, two cases are considered. One can imagine the simple situation of particles in a box (0D), where the distribution function (and consequently its moments) is constant in space and time, and only the evolution of the velocities due to drag (first case) or buoyancy and drag (second case) is computed for the initial value problem of solving Eq. (3.17) in a Lagrangian frame. The expression for the time evolution of a given velocity component u(t) for each particle class is given by:

$$\mathrm{u}(t) = \mathrm{u}_T\,(1 - \mathrm{e}^{-\frac{t}{\tau}}), \tag{4.77}$$

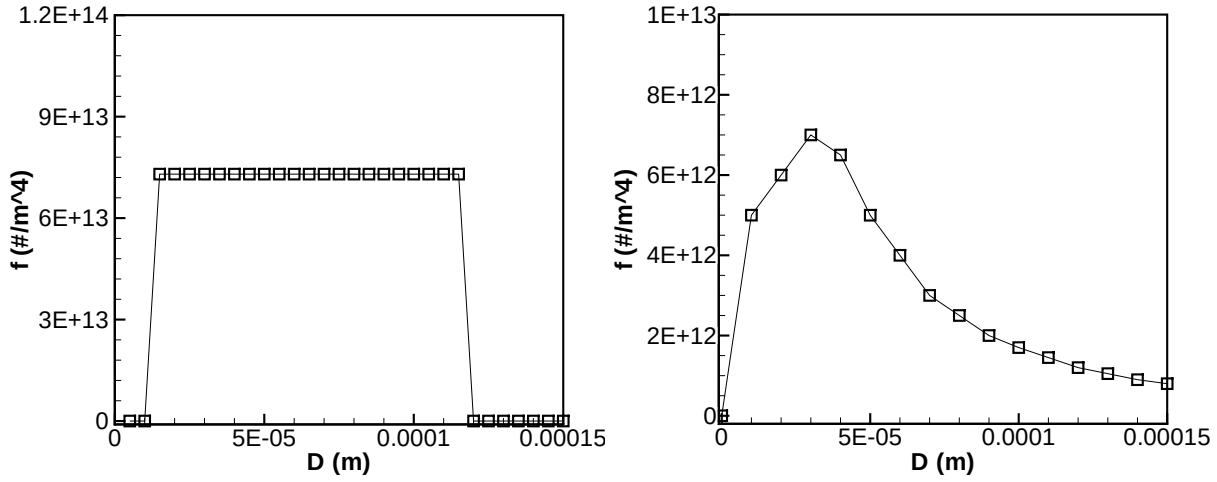

Figure 4.9: Initial distributions considered for the droplet deceleration (left) and bubble rise (right) cases.

u_T is a given component of the terminal velocity. The size distribution for the first case is "Top-Hat" with minimum diameter D_{min} = 15 μm, maximum diameter D_{max} =115 μm and $f \approx 7\text{x}10^{13}$ 1/m^4. Particles have density ρ = 998 kg/m^3 (water droplets) and the continuous phase (air at standard conditions) has a constant velocity of 0.5 m/s. The moment transport velocities at t = 0 s are: $u^{(0)}$ = 0.79 m/s, $u^{(1)}$ = 0.87 m/s, $u^{(2)}$ = 0.94 m/s and $u^{(3)}$ = 1 m/s. For the second case, a distribution of air-bubbles initially at rest is considered, with $M^{(0)} - M^{(3)}$ given by: $M^{(0)} = 4.81\text{x}10^8$ 1/m^3, $M^{(1)} = 2.58\text{x}10^4$ 1/m^2, $M^{(2)}$ = 1.99 1/m and $M^{(3)} = 1.91\text{x}10^{-4}$. The initial distributions for both cases are given in Fig. 4.9.

The analytical solution for the time evolution of the particle velocities and moment average velocities are shown in Fig. 4.10. The moment average velocities are compared to the interpolated values with Eq. (4.74), where the reference velocity $\mathbf{u}_0$ is chosen to be $\mathbf{u}^{(3)}$, the volume averaged velocity. For the case where particles decelerate to the continuous phase velocity (Fig. 4.10, left), the size dependence of the drag term dictates that $\mathbf{u}^{(m)} < \mathbf{u}^{(n)}$ for $m < n$, since bigger particles will tend to take longer to reach equilibrium. A similar situation occurs in the case where bubbles accelerate in a stagnant medium

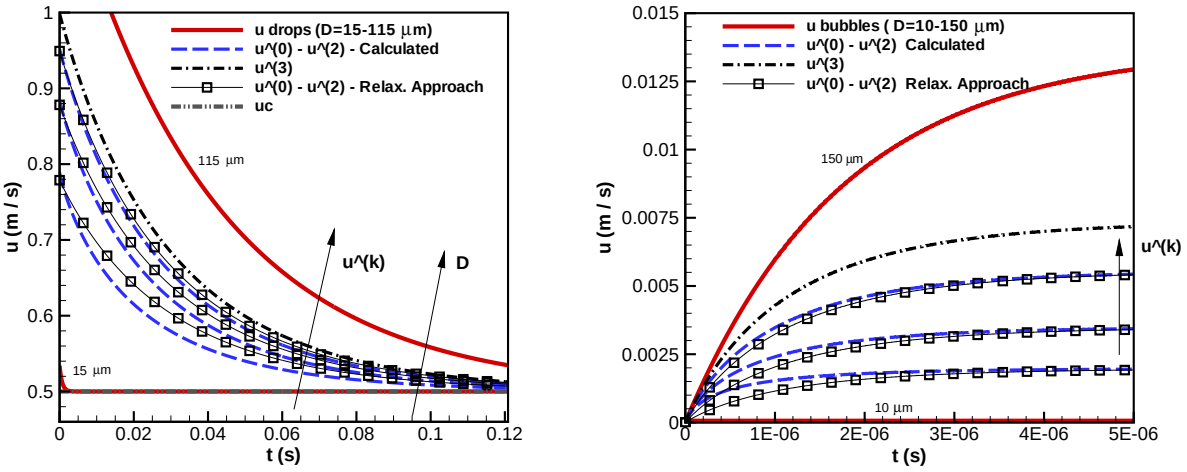

Figure 4.10: 0D solution of the Lagrangian equation of motion for particle deceleration (left) and bubble rise velocity (right) and comparison with the relaxation approach.

towards the terminal rise velocity (Fig. 4.10, right), and the evolution of the moment transport velocities reflects the effect of bubble size on buoyancy. In both cases, the first order interpolation between $\mathbf{u}_c$ and $\mathbf{u}^{(3)}$ is a reasonable approximation for the lower order moment average velocities. Furthermore, the interpolated values of $\mathbf{u}^{(k)}$, $k < 3$ tend to the exact velocities as they approach the equilibrium values. Note that the error (in Fig. 4.11, the error is defined as $(\mathbf{u}^{(k)}_{interp} - \mathbf{u}^{(k)})/\mathbf{u}^{(k)}_{eq}$, with the equilibrium velocity $\mathbf{u}_{eq}$ being given by the continuous phase and terminal rise velocities, for the first and second cases, respectively) decreases with k and tend to zero as the velocities approach the equilibrium values.

4.7.2 Closure for the moment transport equations and drag term

For the general case, one has to find the spatio-temporal evolution of the moments of the size distribution function. In the presumed function approach, $f(D)$ is fully determined if a few prognostic moments are known, for which transport equations are solved. This allows the calculation of any diagnostic

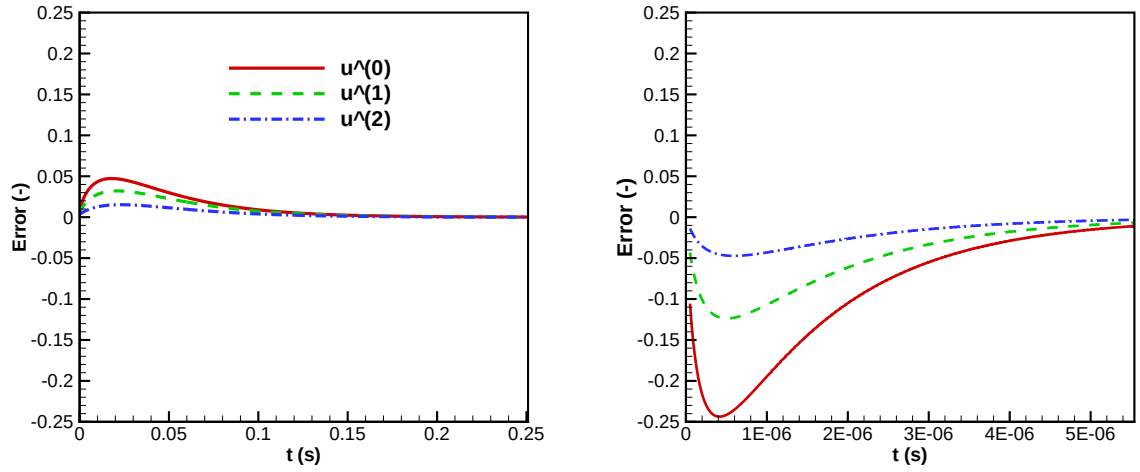

Figure 4.11: Time evolution of the error between the moment average velocities obtained by analytical integration of the Lagrangian equation of motion and interpolation through the relaxation approach.

moment needed by the model – as described in section 4.6 for the Gamma and Beta distributions.

It follows from the moment transport equation with Eq. (4.74), that:

$$\frac{\partial M^{(k)}}{\partial t} + \nabla \cdot (M^{(k)} \mathbf{u}_c) = \nabla \cdot [M^{(k)} \underbrace{(\mathbf{u}_c - \mathbf{u}^{(k)})}_{\frac{\tau^{(k)}}{\tau_0}(\mathbf{u}_c - \mathbf{u}_0)}]. \tag{4.78}$$

Hence, all moment transport equations contain a term, which represents convection by the continuous phase, and a correction term, which depends on the order of the kth-moment through the average response times $\tau^{(k)}$. It is also possible to formulate the above equation such that the common convective velocity is $\mathbf{u}_0$ and the correction is: $\nabla \cdot [M^{(k)} \left(1 - \frac{\tau^{(k)}}{\tau_0}\right)(\mathbf{u}_c - \mathbf{u}_0)]$. In both cases, the relative velocity $(\mathbf{u}_c - \mathbf{u}_0)$ is common to all equations, independent of k. Therefore, only two equations are needed to determine these velocities. It is clear that a closure problem also exists here, since in order to determine $\tau^{(k)}$, $M^{(k+2)}$ is required. This will be handled similar to any moment closure prob-

lem, i.e. diagnostic moments are calculated after the distribution function is reconstructed from prognostic moments.

The choice of additional transport equations for the prognostic moments will depend on the presumed functional form and reconstruction algorithm chosen. The volume (or mass) of the dispersed phase is a very – if not the most – important characteristic to be conserved. Furthermore, in many situations, the transport velocities of the moments $M^{(0)}$-$M^{(2)}$ lie between $\mathbf{u}_c$ and $\mathbf{u}^{(3)}$ (as demonstrated by Fig. 4.10), which makes the interpolation procedure between these velocities most appropriate. Hence, $\tau^{(3)}$ and $\mathbf{u}^{(3)}$ are chosen here for the reference properties to be used in the interpolation procedure for $\mathbf{u}^{(k)}$ (in this case, the hypothetical "reference particle size" of Bollweg et al. [16] should be chosen to have exactly these properties, i.e. $D_0 = \sqrt{\frac{M^{(5)}}{M^{(3)}}}$). Closure for the moment transport velocities requires, therefore, solution of Eq. (4.29), for $k = 3$.

In order to close the integral drag term given in section 4.6, it is useful to rewrite Eq. (4.74), with help of Eq. (4.76) as:

$$\mathbf{u}^{(k)} = \mathbf{u}_c + \mathscr{K}\,\frac{M^{(k+2)}}{M^{(k)}}, \tag{4.79}$$

where $\mathscr{K}$ is a constant according to Eq. (4.73) and is given for $\tau_0 = \tau^{(3)}$ and $\mathbf{u}_0 = \mathbf{u}^{(3)}$ by:

$$\mathscr{K} = \frac{\rho_d}{18\mu_c}\frac{\mathbf{u}^{(3)} - \mathbf{u}_c}{\tau^{(3)}}. \tag{4.80}$$

Hence, the following equality is valid, $\forall\, k$:

$$M^{(k-2)}\,(\mathbf{u}_c - \mathbf{u}^{(k-2)}) = \mathscr{K}\,M^{(k)}. \tag{4.81}$$

Equation (4.41) for $k = 3$ can be written in a closed form as:

$$\mathbf{F}^{(3)}_{Drag} = 18\mu_c\,M^{(3)}\,\mathscr{K} = \rho_d\,M^{(3)}\,\frac{\mathbf{u}_c - \mathbf{u}^{(3)}}{\tau^{(3)}}. \tag{4.82}$$

The above formulation of the drag term offers the advantage that it explicitly depends on the velocity which is solved for, $\mathbf{u}^{(3)}$. Thus, Eq. (4.29) for $k = 3$, which in fact represents the volume averaged momentum equation for the dispersed phase, can be written as:

$$\begin{aligned}
\rho_d \frac{\partial \left(M^{(3)}\mathbf{u}^{(3)}\right)}{\partial t} + \rho_d \nabla \cdot (M^{(3)}\mathbf{u}^{(3)}\mathbf{u}^{(3)}) &= M^{(3)}\nabla p + M^{(3)}\nabla \cdot \boldsymbol{\tau} \\
&+ \rho_d M^{(3)} \frac{\mathbf{u}_c - \mathbf{u}^{(3)}}{\tau^{(3)}} + 18\mu_c \frac{\nu_c^t}{\sigma_\alpha} \nabla M^{(1)} \\
&+ \nabla \cdot \left(M^{(3)} \boldsymbol{\tau}_{\boldsymbol{d}}^{\boldsymbol{t}\,(3)} \right) \\
&+ \rho_d M^{(3)} \mathbf{g} \\
&+ \Gamma_{M^{(3)}} \mathbf{u}^{(3)}. \qquad (4.83)
\end{aligned}$$

The momentum equation for the gas phase is in turn given by:

$$\begin{aligned}
\rho_c \frac{\partial (\alpha_c \mathbf{u}_c)}{\partial t} + \rho_c \nabla \cdot (\alpha_c \mathbf{u}_c \mathbf{u}_c) &= -\alpha_c \nabla p + \alpha_c \nabla \cdot \boldsymbol{\tau} \\
&+ \nabla \cdot \alpha_c (\boldsymbol{\tau}_c^t + \boldsymbol{\tau}_c^{pt}) \\
&- \rho_d \frac{\pi}{6} M^{(3)} \frac{\mathbf{u}_c - \mathbf{u}^{(3)}}{\tau^{(3)}} - 3\pi\mu_c \frac{\nu_c^t}{\sigma_\alpha} \nabla M^{(1)} \\
&+ \alpha_c \rho_c \mathbf{g} \\
&- \rho_d \frac{\pi \Gamma_{M^{(3)}}}{6} \mathbf{u}^{(3)} \qquad (4.84)
\end{aligned}$$

Note that the absolute value of the total drag force per unit volume ($\rho_d \mathbf{F}_{Drag}^{(3)}$) is equal for both phases, and the outcome of the relaxation approach is such that it consistently depends on the relative velocity between $\mathbf{u}^{(3)}$ (a volume, or mass, weighted value) and $\mathbf{u}_c$, with a corresponding relaxation time, $\tau^{(3)}$. This relaxation time can be interpreted as a volume averaged response time of all particles, and depends on the diagnostic moment $M^{(5)}$. The Gamma and Beta distributions presented in this work offer some possibilities of closure, as outlined before. Table 4.1 summarizes prognostic and diagnostic moments involved in each of the reconstruction methods used:

Table 4.1: Summary of presumed functions used with corresponding prognostic and diagnostic moments.

Distribution	Prognostic Moments	Diagnostic Moments
Gamma	$M^{(0)}$-$M^{(2)}$	$M^{(3)}$-$M^{(5)}$
Gamma	$M^{(1)}$-$M^{(3)}$	$M^{(0)}$,$M^{(4)}$,$M^{(5)}$
Beta	$M^{(0)}$-$M^{(2)}$	$M^{(3)}$-$M^{(5)}$
Beta	$M^{(0)}$-$M^{(3)}$	$M^{(4)}$-$M^{(5)}$

The assumption of $\mathbf{u}|_\tau$ also allows to assess the order of magnitude of the term that contains the velocity deviation tensor $\mathbf{u}'\mathbf{u}'$ neglected in Eq. (4.29), otherwise unclosed[5]. It can be shown (see A.2) by substituting the expressions derived in the relaxation approach, that it is proportional to the integral over size of a term with order $\mathcal{O}(\tau'^2)$; τ' is the deviation of the particle relaxation time with respect to the average value, $\tau^{(k)}$. It is identically zero only in the monodisperse case and its contribution is expected to be more important for distributions that present wider size spectra, including bigger, inertial particles, which tend to respond very differently to the flow.

4.7.3 Extension for larger particle relaxation times

The key underlying assumption of the relaxation approach presented in the previous sections is that particles are assumed to have small relaxation times. To illustrate the consequences of that assumption, consider the two distinct situations of section 4.7.1. First, a population of droplets is decelerated in a constant air-stream; the initial relative velocity is 0.5 m/s. Figure 4.12 shows the evolution of the size-velocity correlation (left) and τ-velocity correlation (right). The relaxation approach considers a linear expression for the particle velocities in τ, i.e. $\propto D^2$, according to the Stokes expression for the drag force. This tends to be accurate for small τ or near the equilibrium – note that this also applies for a population of bubbles rising in a stagnant fluid, where terminal velocities are different for different bubble sizes (4.13). However, the

[5] As discussed by [22], in the literature this term is either simply neglected or incorporated into turbulent fluctuating quantities using a diffusion hypothesis

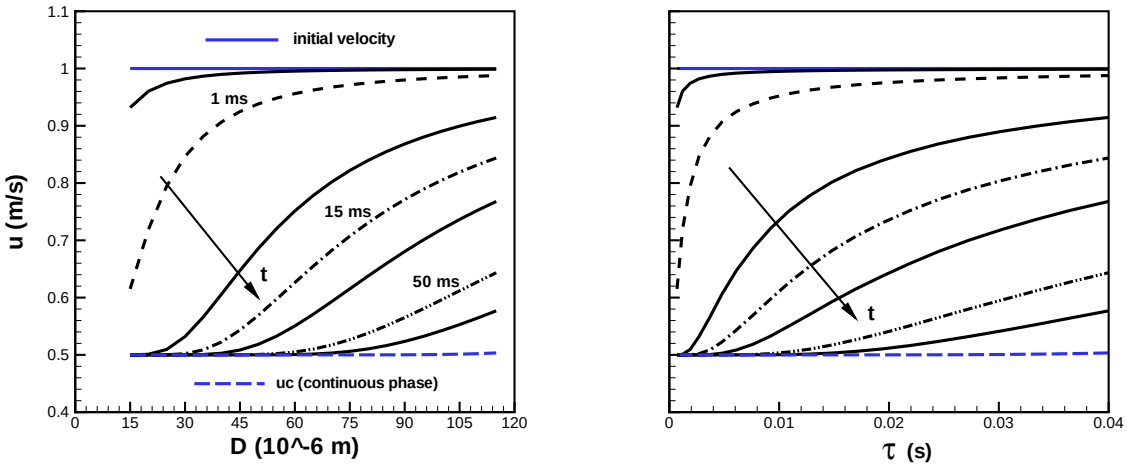

Figure 4.12: Evolution of the size-velocity correlation and relaxation times for a population of droplets decelerating in a gas.

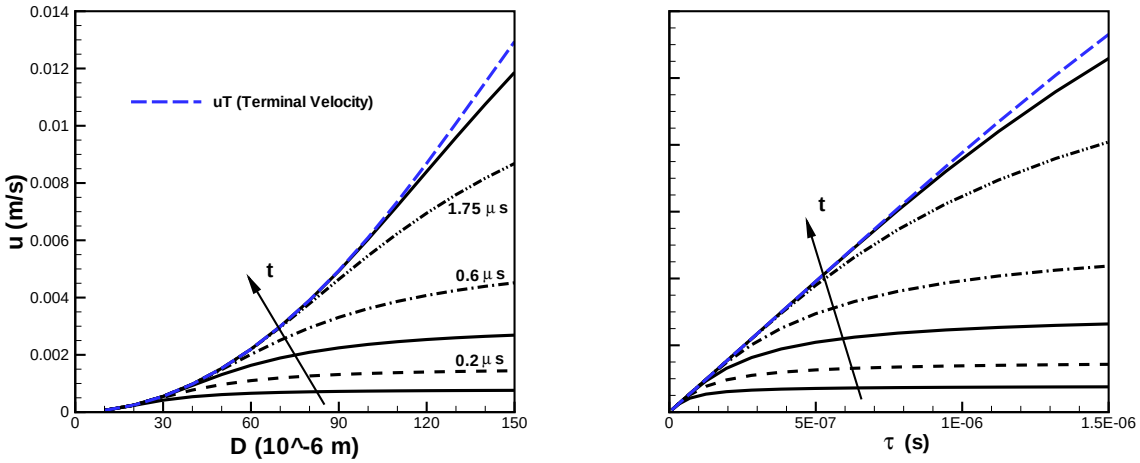

Figure 4.13: Evolution of the size-velocity correlation and relaxation times for a population of bubbles rising in stagnant liquid.

assumption of linear dependence in τ breaks down specially for big particles and non-equilibrium conditions.

In order to account for inertial effects (i.e., larger response times to changes in the flow) in non-equilibrium situations, an extension of the standard relax-

ation approach is suggested here. The idea is to limit the velocity of particles with diameter greater than a certain critical value D^*, such that

$$\mathbf{u}(D) = \begin{cases} \mathbf{u}_c + \mathscr{K}' D^2 & \text{if } D < D^*, \\ \mathbf{u}^* & \text{if } D \geq D^* \end{cases}$$

with $\mathbf{u}^* = \mathbf{u}_c + \mathscr{K}' D^{*2}$. The new proposed function is schematically represented in Fig. 4.14.

Hence, the size-velocity correlation is now divided in two regions: the first one, for particles with $D < D^*$, so that $\mathbf{u} \sim D^2$ (as in the relaxation approach, i.e. the linear dependence in τ is recovered); and the second one, for inertial particles with $D > D^*$, which are considered to have a constant velocity. Note that this function satisfies the following (physical) constraints:

- $\lim \mathbf{u}(D)_{D\to 0} = \mathbf{u}_c$: tracer particles follow the continuous phase perfectly.
- $\lim \mathbf{u}(D)_{D\to \infty} = \mathbf{u}^*$: the motion of very big, "inertial particles" is essentially unaffected by the continuous phase.
- $\lim \frac{d\mathbf{u}(D)}{dD} = 0$ in the limits $D \to 0, \infty$: the size-velocity correlation tends asymptotically to the above limits.

The characteristics of $\mathbf{u}(D)$ are also in accordance with the typical behavior for the mean droplet size-velocity correlation at a single point experimentally measured in a spray by Schulte [75], who measured simultaneously drop sizes and velocity at a single point with PDA in the spray of a pressure atomizer. A similar type of approach to determine the size-velocity correlation was also proposed before by Mossa [61], where a polynomial expression for $\mathbf{u}(D)$ was used with a presumed size distribution function of Gaussian type. Mossa's polynomial expression also takes into account the physical limits incorporating different particle behavior depending on particle size.

A simple way to determine the critical diameter D^* which divides these two regions is to use a time scale of the size distribution τ^* which corresponds to a characteristic response time beyond which particles are considered to be in

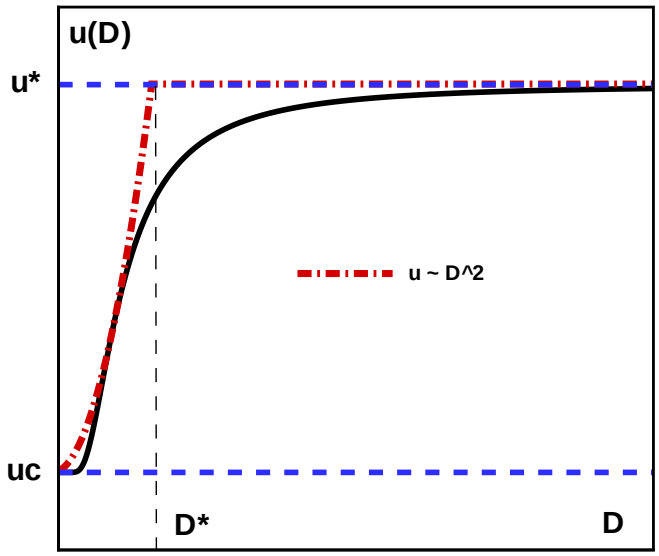

Figure 4.14: Schematic representation of new proposed function.

the inertial region. The characteristic response time τ^* is related to the maximum response time corresponding to the maximum diameter of the spectrum (in line with the Beta distribution function) according to: $\tau^* = \mathrm{St}^* \tau_{max}$. Thus, D^* can be determined by

$$D^* = \sqrt{\frac{18\mu_c}{\rho_d} \mathrm{St}^* \tau_{max}}. \tag{4.85}$$

St^* is given by the following expression:

$$\mathrm{St}^* = \frac{|\mathbf{u}^{(3)}|}{\left|\mathbf{u}_c + \tau^{(3)} \left(1 - \frac{\rho_c}{\rho_d}\right) \mathbf{g}\right|}. \tag{4.86}$$

Note that the relaxation approach is recovered for $\mathrm{St}^* \to 1$, since $D^* \to D_{max}$. This happens when the transport velocity for the third moment, $\mathbf{u}^{(3)}$, approaches its equilibrium value.

The new expression for the size-velocity correlation can be integrated over the size spectrum, assuming that the distribution function $f(D)$ has a Beta shape given by Eq. (4.46):

$$\mathbf{u}^{(k)} = \frac{1}{M^{(k)}} \left[\int_0^{D^*} \mathbf{u}(D) D^k f(D) dD + \int_{D^*}^{D_{max}} \mathbf{u}(D) D^k f(D) dD \right], \tag{4.87}$$

which results in

$$\begin{aligned} \mathbf{u}^{(k)} = \mathbf{u}_c \quad &+ \quad \mathscr{K}' \{ C_0 D_{max}^{k+2} \frac{I_{D^*/D_{max}}(p+k+2, q)}{B(p,q)} \\ &+ \quad C_0 D_{max}^k D^{*2} [\frac{M^{(k)}}{C_0 D_{max}^k} - \frac{I_{D^*/D_{max}}(p+k, q)}{B(p,q)}] \}. \end{aligned} \tag{4.88}$$

The incomplete Beta integral $I_x(a,b)$ is defined as

$$I_x(a,b) = \int_0^x t^{a-1} (1-t)^{b-1} dt \tag{4.89}$$

and is evaluated numerically with the algorithm of Majumder and Battacharjee [51].

Analogously to the relaxation approach, any unknown velocity $\mathbf{u}^{(k)}$ can be determined with knowledge of the reference velocity $\mathbf{u}_0 = \mathbf{u}^{(3)}$, such that:

$$\mathbf{u}^{(k)} = \mathbf{u}_c + \frac{\Phi^{(k)}}{\Phi^{(3)}}(\mathbf{u}^{(3)} - \mathbf{u}_c), \tag{4.90}$$

with the ratio $\frac{\Phi^{(k)}}{\Phi^{(3)}}$ given by

$$\frac{\Phi^{(k)}}{\Phi^{(3)}} = \frac{D_{max}^{k+2}}{D_{max}^{5}} \left\{ \frac{\frac{I_{D^*/D_{max}}(p+k+2,q)}{B(p,q)} + \left(\frac{D^*}{D_{max}}\right)^2 \left[\frac{M^{(k)}}{C_0 D_{max}^k} - \frac{I_{D^*/D_{max}}(p+k,q)}{B(p,q)}\right]}{\frac{I_{D^*/D_{max}}(p+5,q)}{B(p,q)} + \left(\frac{D^*}{D_{max}}\right)^2 \left[\frac{M^{(3)}}{C_0 D_{max}^3} - \frac{I_{D^*/D_{max}}(p+3,q)}{B(p,q)}\right]} \right\}. \tag{4.91}$$

5 Model Development

5.1 OpenFOAM

The Method of Moments presented in previous chapters (PMOM) was implemented in the open source CFD tool OpenFOAM [86], based on the Two-Fluid solver `twoPhaseEulerFoam` [70]. The framework of PMOM with the relaxation approach is comparable to a standard Two-Fluid formulation in terms of implementation and costs. Additional computational effort is related mostly to the solution of the moment transport equations. At the same time, PMOM framework offers the possibility of incorporating polydisperse effects into standard Two-Fluid solvers in a relatively simple manner. Details on the implementation of moment transport equations in OpenFOAM are found below (as also shown by Carneiro et al. [18]).

OpenFOAM is a C++ class library which can be easily used to develop CFD codes for a wide variety of problems, including multiphase flows. This can be done either by starting from existing solvers or by developing completely new ones, using capabilities of the finite volume method [44, 86].

The solution of additional transport equations for the moments within `twoPhaseEulerFoam` is possible with help of the closure for $\mathbf{u}^{(k)}$ through the relaxation approach. Regarding the implementation in the code itself, the moment transport equations can be defined within the tensor derivative class `fvScalarMatrix`, with all terms being treated implicitly through the class `fvm`, as depicted below:

```
surfaceScalarField C = tauk*(phib-phia)/taua;

fvScalarMatrix mkEqn
```

```
(
      fvm::ddt(mk)
    + fvm::div(phib, mk)
    + fvm::div(C, mk) //convective correction
);

mkEqn.relax();
mkEqn.solve();
```

According to Weller's notation [85], the discretised form of the moments transport equations is given by:

$$[\![\frac{\partial [M^{(k)}]}{\partial t}]\!] + [\![\nabla \cdot (\phi_b \, [M^{(k)}]_{f(\phi_b,UD,)})]\!] + [\![\nabla \cdot (C \, [M^{(k)}]_{f(C,UD,)})]\!] = 0, \tag{5.1}$$

where the Euler implicit scheme for the time derivative and upwind differencing face values of $M^{(k)}$'s for the convective terms were used.

It has been shown before that first order schemes guarantee realizability of moment sets at the numerical level [26,46]. A recent study [81] presented ideas for developing realizable high-order finite-volume schemes for quadrature-based moment methods. The investigation of the model behavior with higher order numerical schemes is out of the scope here and will be left for future work.

The relaxation times `taua` and `tauk` for the correction coefficient `C` are defined as `surfaceScalarField` types. Thus, segregation of the moments throughout the flow field is achieved by considering different convective corrections for each transport equation. Further details of the implementation and discretization strategies can be found in [70] and [18]. Note however that the model described in [70] is essentialy a Two-Fluid Model and the exchange terms are obviously adapted to encompass the framework presented here.

5.2 Particle relaxation

The following test case comprises the one-dimensional flow of a population of small particles that are injected into a domain with length L_c = 20 cm. The advantage of such a test case is that there is an analytical solution to compare with (see A.3 for details). The dispersed and continuous phase properties as well as the inlet distribution were described in section 4.7.1. The continuous phase velocity is given by $\mathbf{u}_c = (\mathrm{u}_{c,x}, 0, 0)$, with $\mathrm{u}_{c,x}$ = 0.5 m/s (case 1, particle deceleration) and $\mathrm{u}_{c,x}$ = 2 m/s (case 2, particle acceleration). The inlet size distribution for the analytical solution is "Top-Hat" as described before. The Gamma and Beta distributions used to approximate the Top-Hat distribution have the following low-order moments: $M^{(0)} = 7.05\mathrm{x}10^9$ 1/m^3, $M^{(1)} = 4.65\mathrm{x}10^5$ 1/m^2, $M^{(2)}$ = 36.15 1/m and $M^{(3)} = 3.15\mathrm{x}10^{-3}$. The inlet moment transport velocities are: $\mathbf{u}^{(k)} = (\mathrm{u}_x^{(k)}, 0, 0)$, with $\mathrm{u}_x^{(0)}$ = 0.79 m/s, $\mathrm{u}_x^{(1)}$ = 0.87 m/s, $\mathrm{u}_x^{(2)}$ = 0.94 m/s and $\mathrm{u}_x^{(3)}$ = 1 m/s. The Stokes number based on the biggest particle size ($\mathrm{St}_{max} = \tau_{max} \frac{|\mathbf{u}_c|}{L_c}$) compares the characteristic time scales of both phases and is approximately 0.1 for the first case and 0.4 for the second case.

As will be shown next, the test cases demonstrate that, despite the fact that Gamma- and Beta-based reconstruction methods can poorly describe Top-Hat or monotonic shaped functions (which will unlikely occur in a practical situation), the moments of the distribution and its transport velocities are well reproduced by the model.

5.2.1 Results and discussion – case 1

In this test case, particles have a higher inlet velocity than the continuous phase, hence they will be decelerated towards the gas velocity. The axial variation of the steady state analytical distributions (normalized by the initial distribution) can be found in Fig. 5.1. The maximum values occur for smaller diameters near the inlet and shift towards the maximum diameter of the distribution closer to the outlet. This happens because bigger particles have initially a higher inertia, but also larger relaxation times than smaller ones, and tend to accumulate further downstream in the domain. Figure 5.2 shows the

steady state distribution functions obtained with the various moment closure methods presented in section 4.6 for three different axial positions (x = 0, 2 and 20 cm); the corresponding analytical distributions are shown here too. Generally, the correct trend is captured by PMOM: as the particles are decelerated by the continuous phase, they accumulate upstream, and a small shift towards the bigger particles of the spectrum occurs. Regarding the Beta reconstruction schemes, in addition to the 4-moment scheme (where D_{max} is evaluated depending on prognostic moments), two variants were tested here for the 3-moment scheme: the first, with D_{max} equal to that calculated by the 4-moment scheme at the inlet, and the second, with maximum diameter corresponding to that of the initial Top-Hat distribution of the reference solution, $D_{max} = D_{max,init}$. Note that reconstructed distributions at the inlet are different and none of the Beta forms is symmetric (while a Top-Hat shape is), since the minimum diameter is forced to be null. While no substantial difference can be seen between the 4-moment Beta scheme and the 3-moment scheme with same D_{max}, the 3-moment scheme with $D_{max,init}$ was able to obtain negatively skewed distributions which agreed qualitatively better to the analytical solution. This occurs because of the smaller maximum diameter used by this scheme, which forces the Beta shape to have stronger influence of particles with diameters towards D_{max}. The reconstructed Gamma function with $k_{min} = 1$ presents a higher peak than that with $k_{min} = 0$ for all axial positions, but both schemes produced distributions with very similar shapes to the 4-moment Beta scheme.

Figure 5.3 gives the spatial relaxation of the moment transport velocities towards the gas phase velocity until the steady state condition is reached. Since all particles relax towards the continuous phase velocity, the same happens to all moment transport velocities. However, since the influence of bigger particles is less pronounced in $\mathbf{u}^{(0)}$ than $\mathbf{u}^{(3)}$, it takes slightly longer for $\mathbf{u}^{(3)}$ to reach a value close to the continuous phase velocity. A very good agreement is obtained between all reconstruction methods and the analytical solution.

The time evolution of the axial profiles of the 0^{th} and 3^{rd} moments can be seen in Fig. 5.4. In the simulations, the domain is initialized with the inlet values of the moments resulting from the reconstructed distributions using

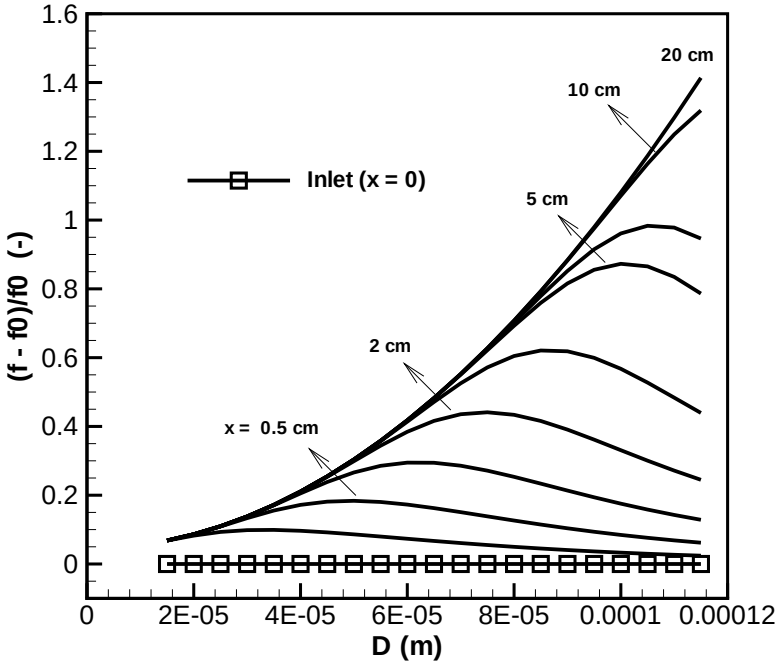

Figure 5.1: Steady state distribution functions at several axial positions for test case 1 (analytical solution).

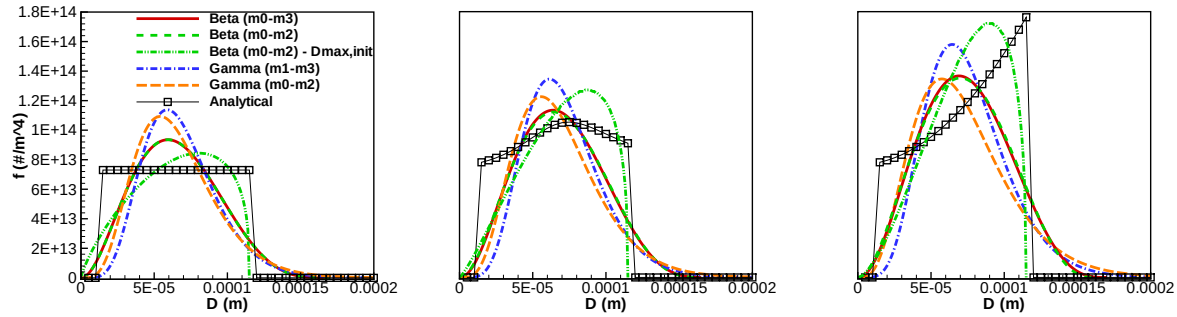

Figure 5.2: Steady state distribution functions computed with PMOM vs. analytical solution at three different axial positions: $x = 0$ (left), $x = 2$ cm and $x = 20$ cm (right).

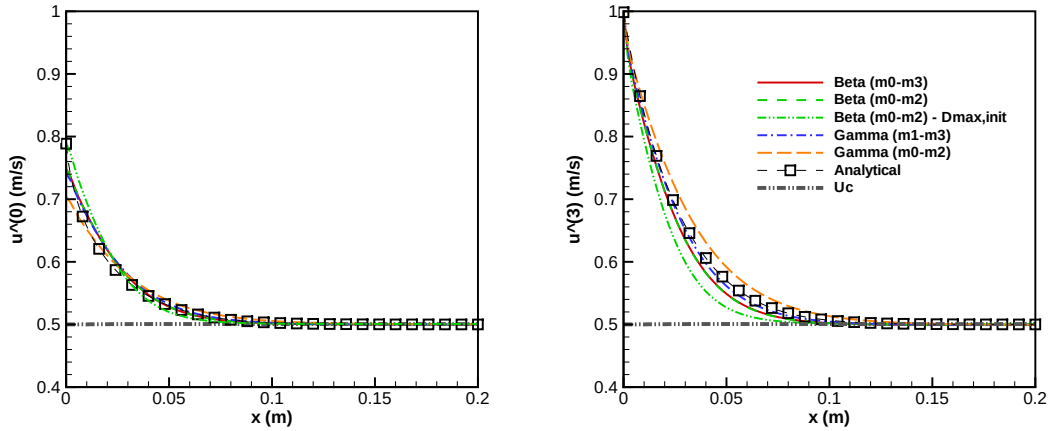

Figure 5.3: Variation of the moment transport velocities $\mathbf{u}^{(0)}$ and $\mathbf{u}^{(3)}$ along the axial position.

the different methods investigated. As mentioned before, bigger particles of the population will travel faster and segregate from the smaller ones, thus accumulating further downstream in the domain. In the moments context, this translates into a "continuity wave" for the moments, that propagates towards the outlet until the equilibrium state is reached at approximately 0.2 s. This wave has a higher concentration of particles on its peak, and its characteristic diameters increase with axial position while traveling in the domain. The analytical solution of Eq. (4.13), at the steady state, requires that $\mathbf{u}^{(k)}M^{(k)}$ =constant. Since $\tau^{(k)}$ and τ_0 are determined differently by the various reconstruction methods and the interpolation between $\mathbf{u}^{(3)}$ and $\mathbf{u}_c$ in Eq. (4.74) results in different boundary values for $\mathbf{u}^{(0)}$ in each method, the 0^{th} moment evolves to different values, with the Beta approaches presenting closer values to the analytical profiles. Regarding $M^{(3)}$, because $\mathbf{u}^{(3)}$ decelerates from 1 (at the inlet) to 0.5 m/s, the equilibrium value must be twice as high as the inlet value. However, it is apparent that for the Gamma distribution with $k_{min} = 0$, $M^{(3)}$ is not conserved, since it is not used explicitly in the reconstruction process. This can be a serious drawback for this reconstruction approach, because the total volume of the distribution is a very important physical parameter. This seems not to be an issue for the presumed Beta function using three moments, even though it also uses only $M^{(0)}$-$M^{(2)}$ in the distribution re-

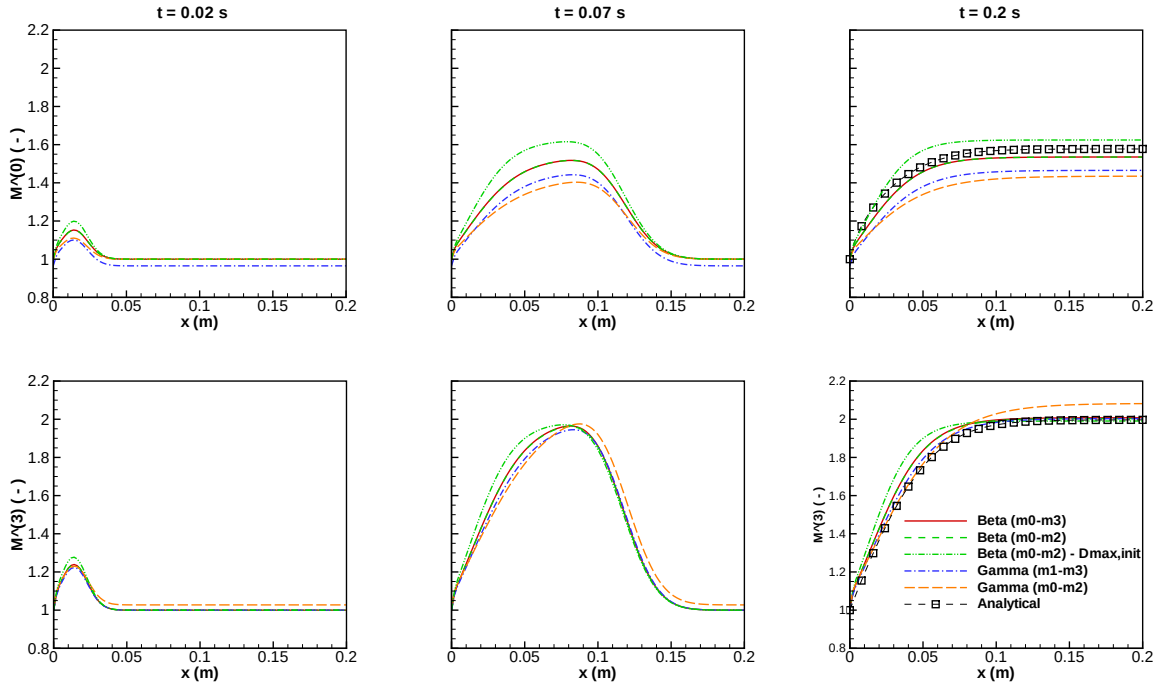

Figure 5.4: Temporal evolution of the normalized moments – $M^{(0)}$ (top) and $M^{(3)}$ (bottom) – along the axial direction at times t = 0.02 (left), 0.07 (middle) and 0.2 s (right).

construction process.

The analysis of the first four Hankel-Hadamard determinants ($\Delta_{0,1}$, $\Delta_{1,1}$, $\Delta_{0,2}$ and $\Delta_{1,2}$, normalized with their inlet values), which contain the most important low-order moments used in the reconstruction schemes or appearing directly in the model equations, reveals that they remain positive throughout the whole domain (see Fig. 5.5). This guarantees the realizability of distribution functions for all sets of moments obtained. Furthermore, the axial variation of the Hankel-Hadamard determinants is similar to that of the moments, increasing asymptotically to a constant value corresponding to the equilibrium distribution function. The variants of the Beta and Gamma methods are compared to each other and it is possible to observe that the discrepancy between the curves increases with the introduction of higher order moments in the determinants, which carry a greater uncertainty irrespective of the reconstruction method used. For the Beta distributions with equal initial D_{max} (left in

Fig. 5.5), since they were very similar everywhere, and therefore must also have similar moments, its corresponding determinants differed only marginally, even for $\Delta_{0,2}$ and $\Delta_{1,2}$ (which depend on $M^{(4)}$ and $M^{(5)}$). The variant of the 3-moment scheme with $D_{max} = D_{max,init}$ (Fig. 5.5, right) presented smaller determinants than the 4-moment scheme. In the case of the Gamma functions (Fig. 5.5, bottom), a greater difference is observed between the two methods. This aspect might be critical for the suitability of the different reconstruction approaches, since it shows that the conditions for a valid set are sensible to the moment sequence chosen.

Figure 5.6 illustrates that the pairs of $(M^{(1)}, M^{(2)})$ obtained with the 4-moment Beta scheme obviously fall within the bounds of the moment space, also illustrating the validity of this reconstruction scheme for all moment combinations obtained for this test case.

Figure 5.7 shows the size-velocity correlations obtained by PMOM (with the 4-moment Beta scheme) and the analytical solution for different axial positions. A good qualitative agreement can be observed, with all curves being reasonably reproduced by a parabolic profile given by the relaxation approach. It should be noted that the flow conditions were chosen such that effects of larger relaxation times in non-equilibrium situations were not important. This will be investigated later on.

5.2.2 Results and discussion – case 2

In this test case, particles have a smaller inlet velocity than the continuous phase and will be accelerated towards the gas velocity, $u_{c,x} = 2$ m/s. For simplicity, the boundary and initial conditions are otherwise identical to test case 1.

The analytical solutions for this configuration can be seen in Fig. 5.8. The effect of particle acceleration is that of decreasing the size distribution in the axial direction. The more pronounced decrease for smaller particles reflects the smaller response times and faster acceleration towards equilibrium with the continuous phase.

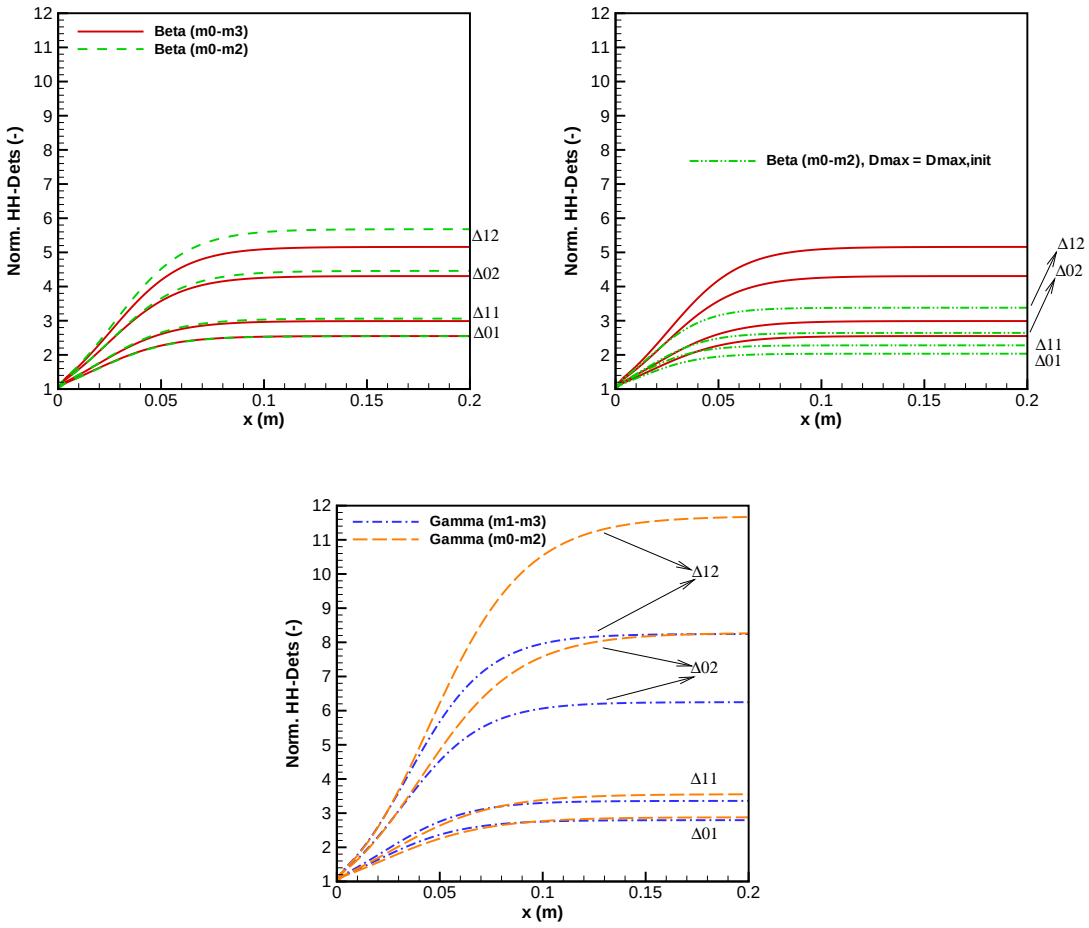

Figure 5.5: Normalized Hankel-Hadamard determinants within the domain for the Beta (left and right) and Gamma (bottom) distributions.

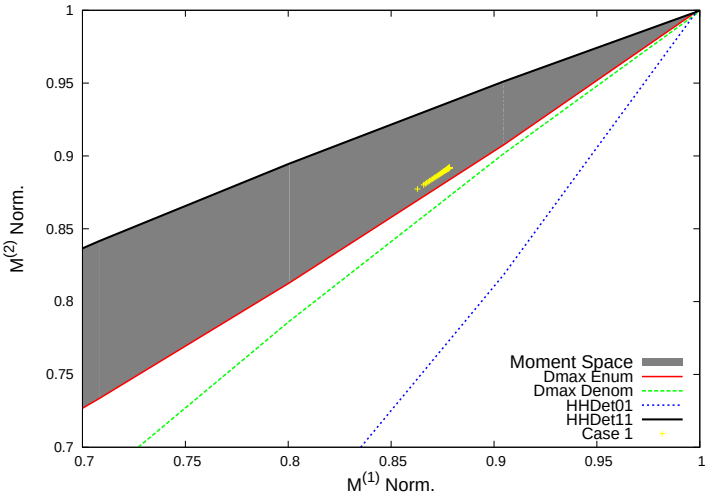

Figure 5.6: Moment space projected at the $(M^{(1)},M^{(2)})$ plane and sets of normalized moments obtained.

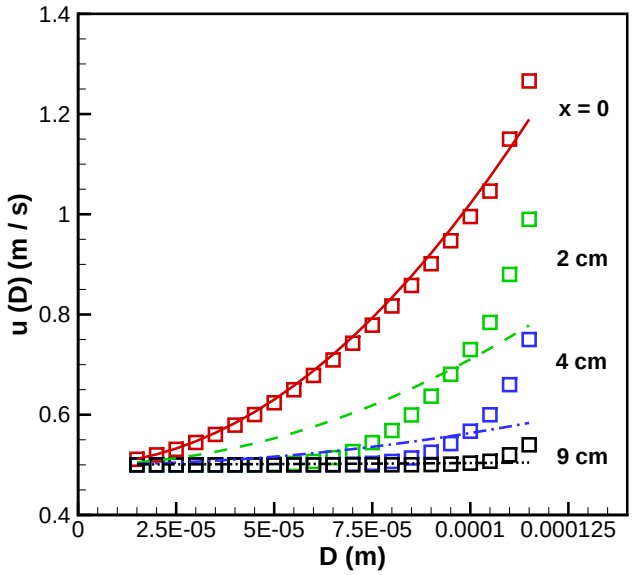

Figure 5.7: Size velocity correlations for different positions along the axial coordinate: analytical solution (symbols) vs. PMOM (lines).

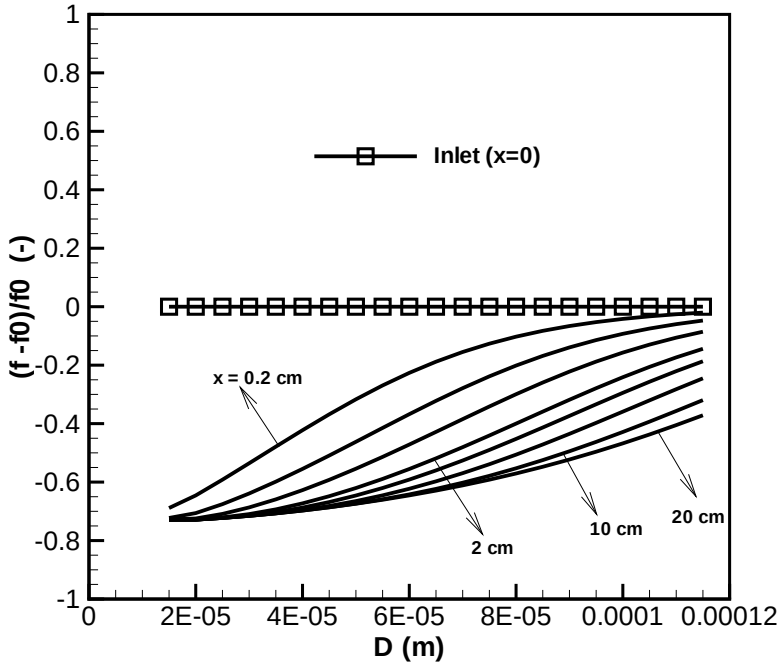

Figure 5.8: Evolution of the distribution functions at several axial positions for test case 2 (analytical solution).

The distribution functions obtained with the Gamma reconstruction method using $M^{(1)}$-$M^{(3)}$, the 4-moment Beta scheme, as well as the 3-moment Beta with $D_{max} = D_{max,init}$ are compared to the analytical results in Fig. 5.9. Once again, the exact shape of the analytical distributions (a consequence of the initial Top-Hat distribution chosen) is very difficult to be captured, but the general trend is reasonably reproduced by the Beta distributions. Note that, unlike the previous case, the 4-moment scheme shifts the skewness towards the maximum diameter of the distribution. This can be attributed, first, to the fact that particle segregation leads to a decrease of the moments in the axial direction. According to Eq. (4.48), $M^{(k)} \propto D_{max}^k$, and a decrease in D_{max} occurs. But also the higher "drift" in this case – the average relative velocity ($|\mathbf{u}_r^{(3)}| = |\mathbf{u}_c - \mathbf{u}^{(3)}| = 1$ m/s) is twice as much as in the previous case ($|\mathbf{u}_r^{(3)}| = 0.5$ m/s) – contributes to stronger variations in the shapes of the distribution.

The evolution of the parameters p and q for the Beta distribution using four moments is shown in Fig. 5.10 for the first (left) and second (right) cases. While in the first case, it is clear that the condition $p < q$ leads to negatively skewed distributions along the axial position (Fig. 5.9); the second case is more interesting since the value of p exceeds that of q inside the domain, leading to positively skewed distributions. The reason for that, as seen above, is the stronger acceleration experienced by the particles due to a higher relative velocitiy.

The agreement of the axial evolution of the normalized third moment (Fig. 5.11, left) is very good for all methods. It is also interesting to analyze the evolution of the normalized Hankel-Hadamard determinants along the axial position. While for the decelerating case the effect of particle accumulation towards the outlet of the domain led to an increase of the determinants, here the inverse occurs: particles tend to segregate along the axial position, which leads to a decrease of the determinants (once again, it follows the variation of the moments). According to the criteria described in section 4.6.3, positive Hankel-Hadamard determinants are the necessary and sufficient conditions for a valid moment set. Thus, this is an example of a potential situation where these constraints might not be fully met, revealing a critical aspect of the formulation which must be confronted. This issue will be addressed further in the next example.

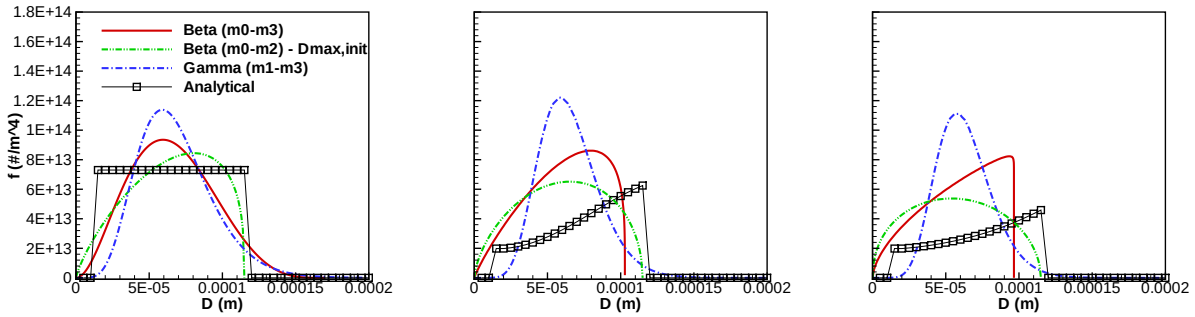

Figure 5.9: Distribution functions at three different axial positions for test case 2: $x = 0$ (left), $x = 2$ cm and $x = 20$ cm (right).

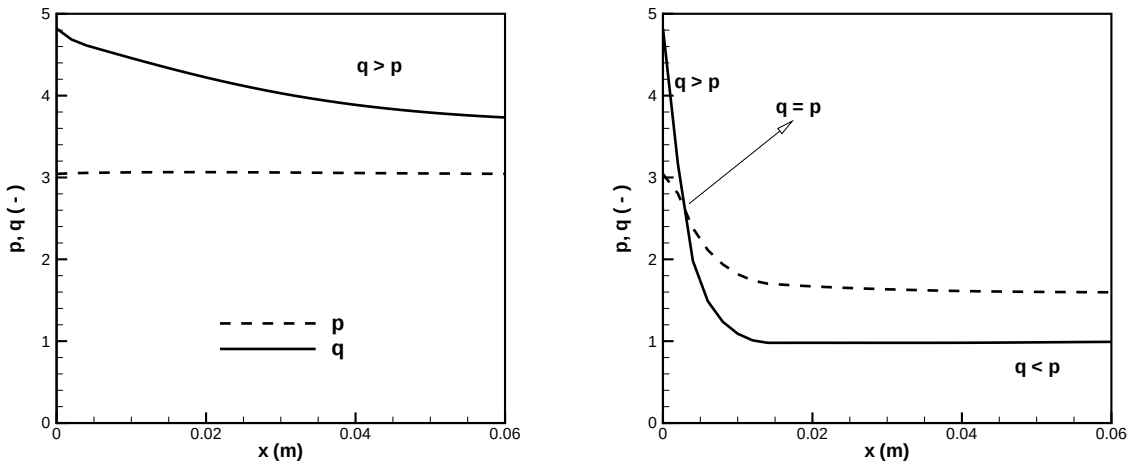

Figure 5.10: Parameters p and q of the Beta distributions for cases 1 (left) and 2 (right).

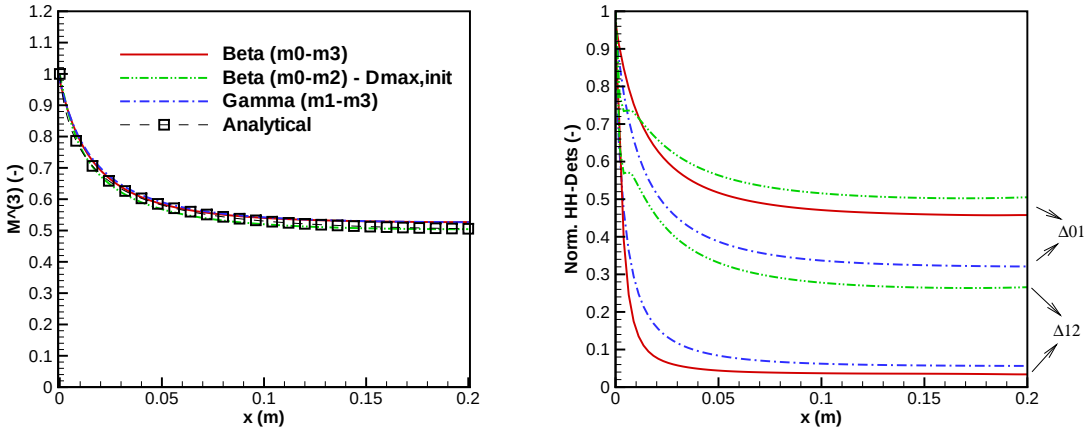

Figure 5.11: Evolution of the normalized 3^{rd} moment $M^{(3)}$ and Hankel-Hadamard determinants along the axial position for test case 2.

5.3 Particle segregation due to buoyancy

In this section, two cases are presented to demonstrate the segregation of populations of bubbles or solid particles due to the combined effect of buoyancy and drag. In section 5.3.1, flow of a dilute mixture of water and air bubbles at standard conditions is considered in a channel with 2 cm height and 10 cm length. At the inlet, axial velocities $u_{c,x}$=u_x=$u_x^{(k)}$=0.1 m/s were defined; the other components were set to null. The low-order moments of the size distribution of the dispersed phase are the same described in section 4.7.1 for the case with bubbles. A constant pressure was kept at the outlet, with zero gradient boundary conditions for all other variables. For simplicity, slip conditions at the walls were applied for both phases, in order to mimic the situation of segregation of particles in a quasi-uniform continuous phase velocity field, with a constant pressure gradient given by the static equation: $\nabla P \approx \rho_c \mathbf{g}$. The maximum Stokes number based on the height of the channel is in this case of order $\mathcal{O}(10^{-5})$. The same configuration will be investigated for the sedimentation of solid particles (ρ = 2500kg/m^3; $St_{max} \approx \mathcal{O}(10^{-1})$) in section 5.3.2, with identical boundary conditions. In the second case, the much higher Stokes number indicates that particle inertia is more important than in the first case.

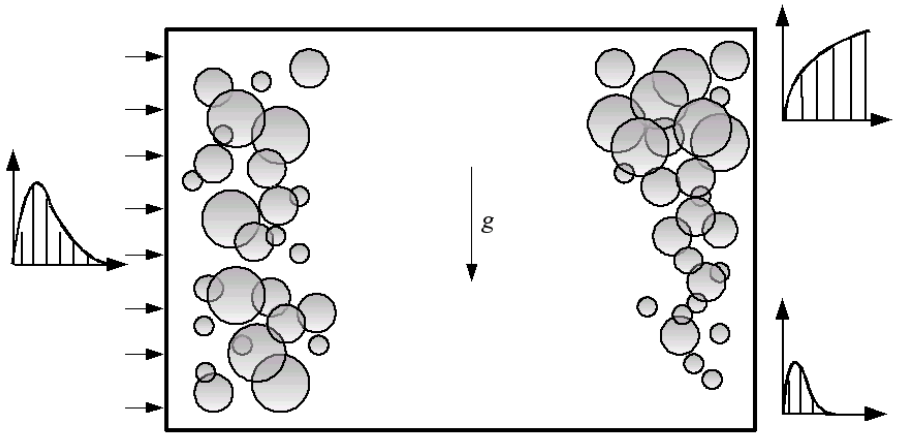

both

Figure 5.12: Schematic representation for the test case of bubble segregation due to buoyancy.

Results obtained with PMOM using the Beta and Gamma approaches will be compared to Multi-Fluid solutions with 15 size classes ($D = 10 - 150\mu$m; $\Delta D = 10\mu$m) obtained with the commercial software ANSYS CFX-11.0. The Inhomogeneous-MUSIG approach of Krepper et al. [48] solves equations for the velocities $\mathbf{u}(D_i)$ and volume fractions α_i of each size class i. In order to provide a correct comparison with PMOM, the molecular viscosity of the dispersed phases is set to a very small value, which is consistent with the dilute limit (particles do not influence each other's motion). The size distribution function can be recovered from the MUSIG simulations with the relation: $f(D_i) = \frac{6\alpha_i}{\pi D_i^3}\Delta D$. Moments and moment transport velocities used for comparison with PMOM are calculated, respectively, by:

$$M^{(k)} = \sum_{i=1}^{15} f(D_i) D_i^k \Delta D \tag{5.2}$$

and

$$\mathbf{u}^{(k)} = \frac{\sum_{i=1}^{15} \mathbf{u}(D_i) f(D_i) D_i^k \Delta D}{\sum_{i=1}^{15} f(D_i) D_i^k \Delta D}. \tag{5.3}$$

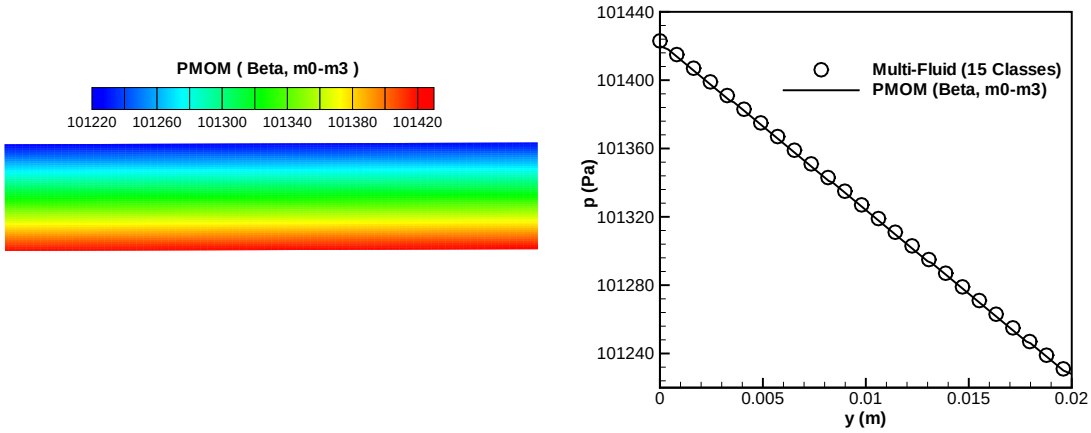

Figure 5.13: Pressure contours inside the channel and vertical pressure profile at $x = 0.05$ m.

5.3.1 Results and discussion – bubbles

First, the contours of the pressure field, as well as its vertical profile at the center of the channel are shown in Fig. 5.13. As expected, the hydrostatic linear profile (with mean value equal to the atmospheric pressure) was obtained by both Multi-Fluid and Moment Methods, with an almost exact match observed between both approaches.

Figure (5.14) shows the contours of the mean diameters – defined as $D_{mn} = \left(\frac{M^{(m)}}{M^{(n)}}\right)^{\frac{1}{m-n}}$ – inside the channel obtained with PMOM using the Beta approach with $M^{(0)}$-$M^{(3)}$ (left) and the Multi-Fluid Model (right), respectively. An increase towards the upper wall can be clearly observed for all D_{mn}. This reflects the fact that the vertical velocity induced by buoyancy tends to increase with bubble diameter. Since the contribution of bigger bubbles is more pronounced for the higher order moments, $M^{(m)}$ rises faster than $M^{(n)}$ $(m > n)$ and leads consequently to an increase in D_{mn}. Marginal discrepancies between both methods can be seen, with the Beta approach predicting a slightly larger region with small mean diameters downstream near the bottom wall, while at the top wall larger mean diameters are observed at the first half of the channel in the Multi-Fluid solution.

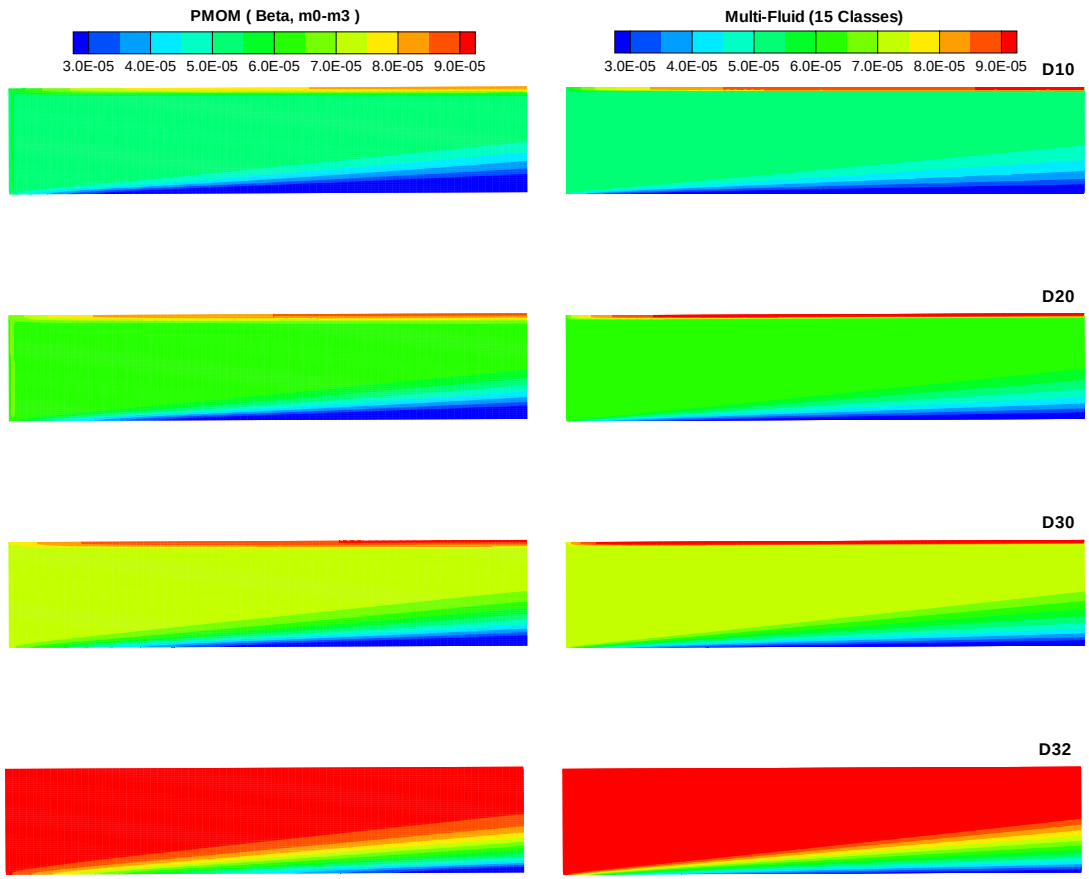

Figure 5.14: Contours of mean diameters of the size distribution inside the channel.

The reconstructed distribution functions at several positions inside the channel (corresponding to axial positions x = 2; 5; 8 cm and vertical positions y = 0.035; 0.1; 1 and 1.97 cm) are compared to the reference solution obtained with the Multi-Fluid approach using 15 classes in Fig. 5.15. As bubbles migrate inside the channel, $f(D)$ increases towards the top wall for all size classes. Furthermore, because of the greater velocity of bigger size bubbles due to buoyancy, they tend to segregate from the smaller ones, while rising to the upper side of the channel. Hence, for the vertical positions y = 0.035 and 0.1 cm, bigger bubbles gradually disappear from the spectrum, accumulating in the upper part (y = 1 and 1.97, cm). The distributions at y = 1 cm are nearly constant along the length of the channel, indicating that the bubbles leaving the central region of the channel are being replenished by the region near the bottom wall.

Generally, a reasonable agreement can be noticed between the Multi-Fluid approach and PMOM using different presumed functions, with all reconstruction approaches reproducing the effect of polydispersity on bubble rise. Concerning the shape of the distribution functions, important differences must be pointed out. The Beta distributions present very distinct shapes here. The reconstruction approach using $M^{(0)}$-$M^{(3)}$ results in distributions with a positive skewness through the whole domain, while the Beta distributions with constant D_{max} adjust their shapes depending on the relative influence of small and big bubbles of the spectrum, in order to reproduce the moments $M^{(0)}$-$M^{(2)}$ correctly. This is a consequence of the fact that the 3-moment scheme has one degree of freedom less than the 4-moment scheme, since D_{max} has a fixed value throughout the channel. Thus, near the bottom of the channel, they produce unphysical peaks towards D = 0μ m[1], while the other approaches are in better agreement with the shape of the reference solution. Near the upper wall, particularly at the most downstream axial position in the channel, the Beta distribution using four moments deviates the most from that of the Multi-Fluid solution, even though it correctly reproduces the negative skewness. It underestimates the influence of the bigger bubbles, while predicting a much higher peak towards smaller size bubbles. On the other hand, the Beta distributions reconstructed with three moments seem to be approximately

[1] Note that, for the Beta distribution function, $\lim_{D\to 0} \to \infty$, for $p < 1$.

null-skewed near the top wall, with small negative skewness at $x = 2$ cm, shifting towards a small positive skewness at $x = 8$ cm. Furthermore, the shape of the Gamma distribution seems to be the best fit to the size distributions obtained by the Multi-Fluid near the top wall. The parameters p and q for the three-moment Beta scheme can be observed in Fig. 5.16 for $y = 0.035$ and 1.97 cm. As seen above, near the bottom wall the distribution remains negatively skewed towards the smaller bubbles of the spectrum, while near the top walla change in skeweness is observed towards the bigger bubbles.

In Fig. 5.17, the axial evolution of the zeroth and third normalized moments for several vertical positions inside the channel obtained by PMOM is compared against the reference Multi-Fluid solution. The overall behavior is well represented by the model: as bigger bubbles migrate faster to the upper side of the channel, higher order moments tend to decrease faster near the bottom wall and increase faster near the top wall, while the distribution (and its moments) in the central region stays nearly constant until very close to the outlet. Also, the model compares quantitatively well against the Multi-Fluid approach, with the best performance being achieved by the Beta presumed function using four moments in almost the whole domain. Even though the shape of the gamma distribution seems to reasonably reproduce the spectral distributions (see Fig. 5.15), its moments are not well captured, being overestimated through the whole domain. This probably happens because the spectrum of the Gamma distribution ranges from $D = 0$ to $D \rightarrow \infty$, and the residual influence of very big bubbles might be significant, even though their number density values are very small. At $y = 1.97$ cm, however, the Gamma distribution is able to better reproduce the axial increase of the moments, which seems to be an artifact caused by the presence of very big bubbles in the spectrum, being able to compensate the underestimation of the number density for $D = 100$-150μm.

The profiles of the vertical component of the moment transport velocities for $x = 5$ cm can be found in Fig. 5.18. $\mathbf{u}^{(0)}$ and $\mathbf{u}^{(3)}$ increase with the vertical position until a constant level is reached, corresponding to the region in the channel where the distribution function is approximately invariant. Furthermore, the contribution of big bubbles to $\mathbf{u}^{(k)}$ increases with the order k of the aver-

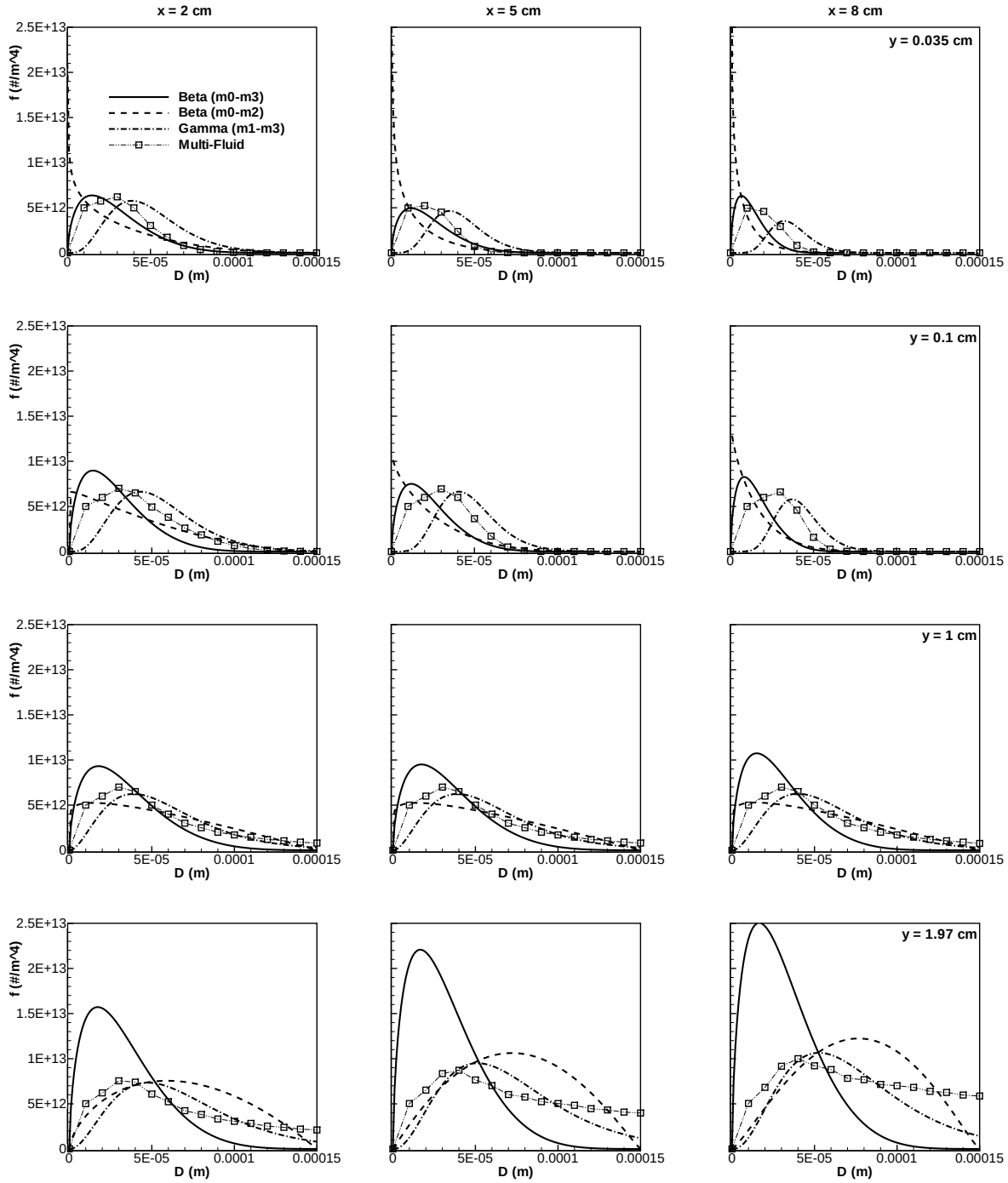

Figure 5.15: Distribution functions at three different axial positions – $x = 2$ cm (left), $x = 5$ cm (middle) and $x = 8$ cm (right) – and four different vertical positions (from top to bottom) $y = 0.035$, 0.1, 1 and 1.97 cm.

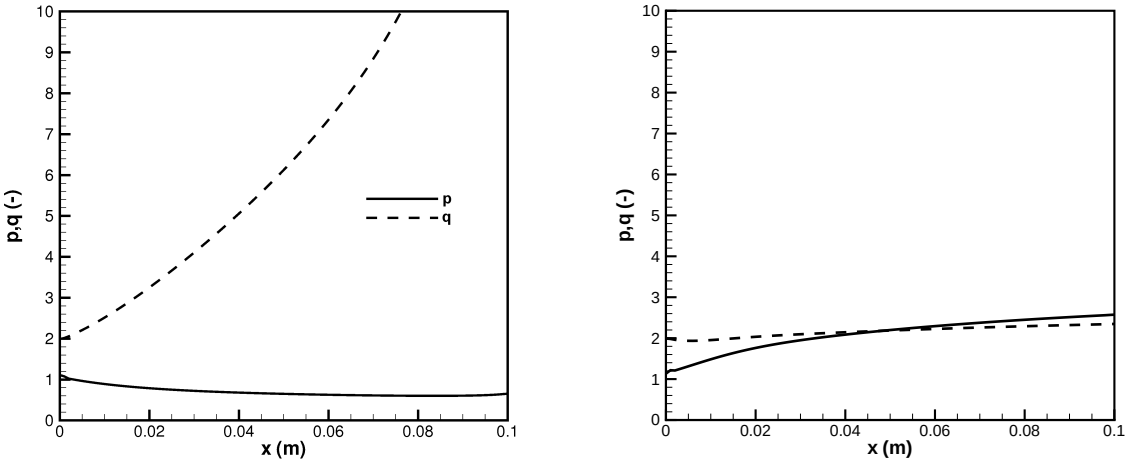

Figure 5.16: Parameters p and q of the 3-moment Beta scheme for $y = 0.035$ cm (left) and $y = 1.97$ cm(right).

age, leading to a higher value of $\mathbf{u}^{(3)}$ in comparison to $\mathbf{u}^{(0)}$. This, as observed before and leads to an increase on the mean diameters towards the upper part of the channel. A better agreement is obtained for the Beta approaches, while the Gamma reconstruction significantly underpredicts the velocities, particularly for higher k. This also explains the overprediction of the moments in the bottom half of the channel seen in Fig. 5.17. The 4-moment scheme performs better for $\mathbf{u}^{(0)}$ and in the upper half of the channel for $\mathbf{u}^{(3)}$. On the other hand, the fixed maximum diameter Beta approach agrees better with the Multi-Fluid Model in the constant region of $\mathbf{u}^{(3)}$. The relaxation times of the small bubbles considered in this example are of the order of μs, thus can be considered small when compared to the characteristic time scale of the continuous phase flow ($\mathrm{St}_{max} \approx \mathcal{O}(10^{-5})$). The variation of the moment transport velocities with the vertical position occurs mainly due to the spatial heterogeneity of the distribution function itself (which translates into the variation of the moments and the moment average relaxation times, $\tau^{(k)}$), and much less due to acceleration of the bubbles, since they can be considered to travel nearly at their terminal velocities in most part of the channel.

The Hankel-Hadamard determinants were also investigated inside the chan-

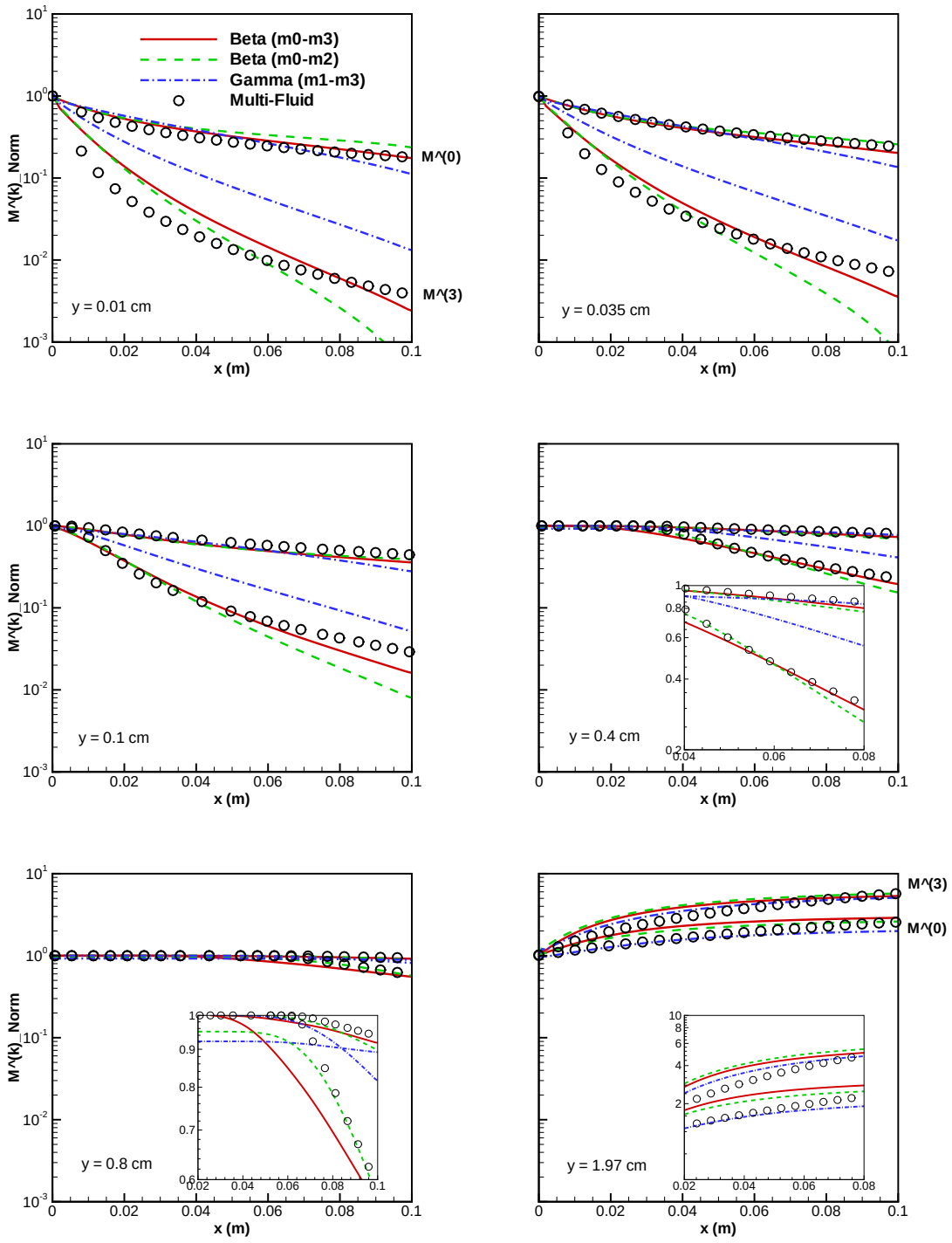

Figure 5.17: Axial evolution of normalized moments for several vertical positions inside the channel: $y = 0.01$, 0.035, 0.1, 0.4, 0.8 and 1.97 cm.

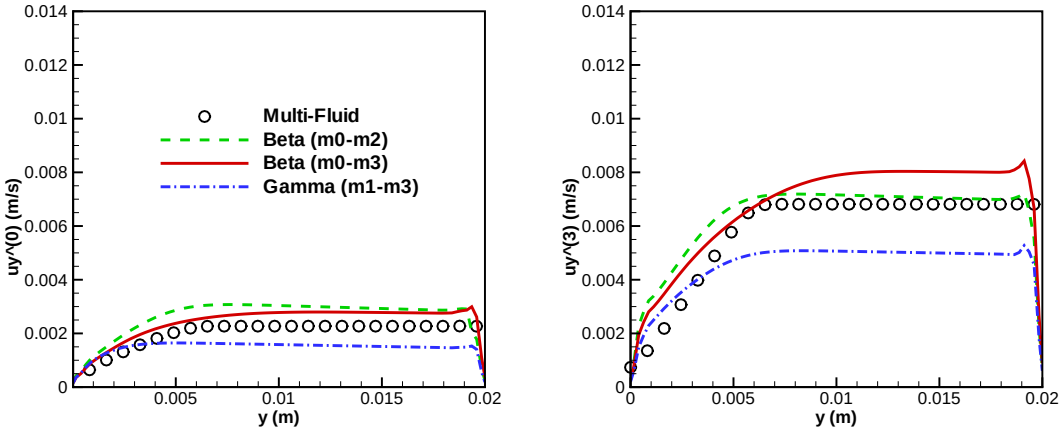

Figure 5.18: Vertical evolution of the moments transport y-velocities for $x = 5$ cm.

nel (Figs. 5.19 and Fig. 5.20). Once again, positiveness of the determinants could be confirmed, which guaranteed the existence of distributions for the moment sets obtained by PMOM for all presumed functions presented. An interesting characteristic is also demonstrated here: the contours of the Hankel-Hadamard determinant Δ_{11} resembles the characteristics of the moments, i.e. tend to vanish where bubbles are less and increase when they accumulate. Hence, the evolution of the profiles for $y = 0.035$ and $y = 1.97$ cm is analogous to the evolution of the moments for the same positions. While an increase of the determinants is observed near the top wall, near the bottom wall, where the bubbles gradually disappear, they tend to zero. This once again reveals that situations where the moments tend to zero, i.e., transitions between regions with and without particles within the flow field, might be critical for the stability of the simulation. Since the moments are transported differently through the domain, it is natural that they also tend to zero at a different rate. In the test cases presented here, this is a direct effect of size dependent drag and buoyancy forces on the transport of particles. For example, the vertical transport velocity of the third moment is larger than that of the zeroth moment, reflecting the fact that bigger bubbles contribute more to the volume average than smaller ones. If a particular moment is convected faster than other moments, there is a possibility that the former vanishes in a computational cell,

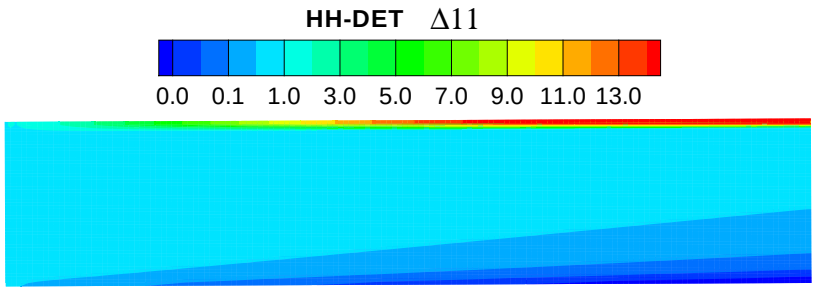

Figure 5.19: Contours of the Hankel-Hadamard determinant inside the channel.

while the latter remain present. This situation is clearly unphysical (since all moments refer to the same distribution), and might give rise to invalid sets in the numerical domain, making strictly necessary the introduction of bounding procedures or replacement schemes (as mentioned in section 4.6.3.5).

5.3.2 Results and discussion – solid particles sedimentation

The sedimentation of a population of solid particles in the channel flow configuration is investigated here with PMOM using the presumed Beta approach with the 3- and 4-moment schemes and the Multi-Fluid Model. The boundary conditions of the previous case are used again in order to assess the behavior of the model for larger particle relaxation times, which is achieved by significantly increasing the dispersed phase density ($\rho = 2500$ kg/m^3, with $\mathrm{St}_{max} \approx \mathcal{O}(10^{-2})$). Since the buoyancy term in the momentum equation changes sign ($\rho_c/\rho_d < 1$), particles will gradually sink towards the bottom wall while traveling inside the channel.

Figure (5.21) compares the mean diameters obtained with PMOM (left) and the Multi-Fluid Model (right). An increase towards the bottom of the channel can be observed for all D_{mn}. When compared to the previous test case, a smaller region where the distribution function remains nearly constant is ob-

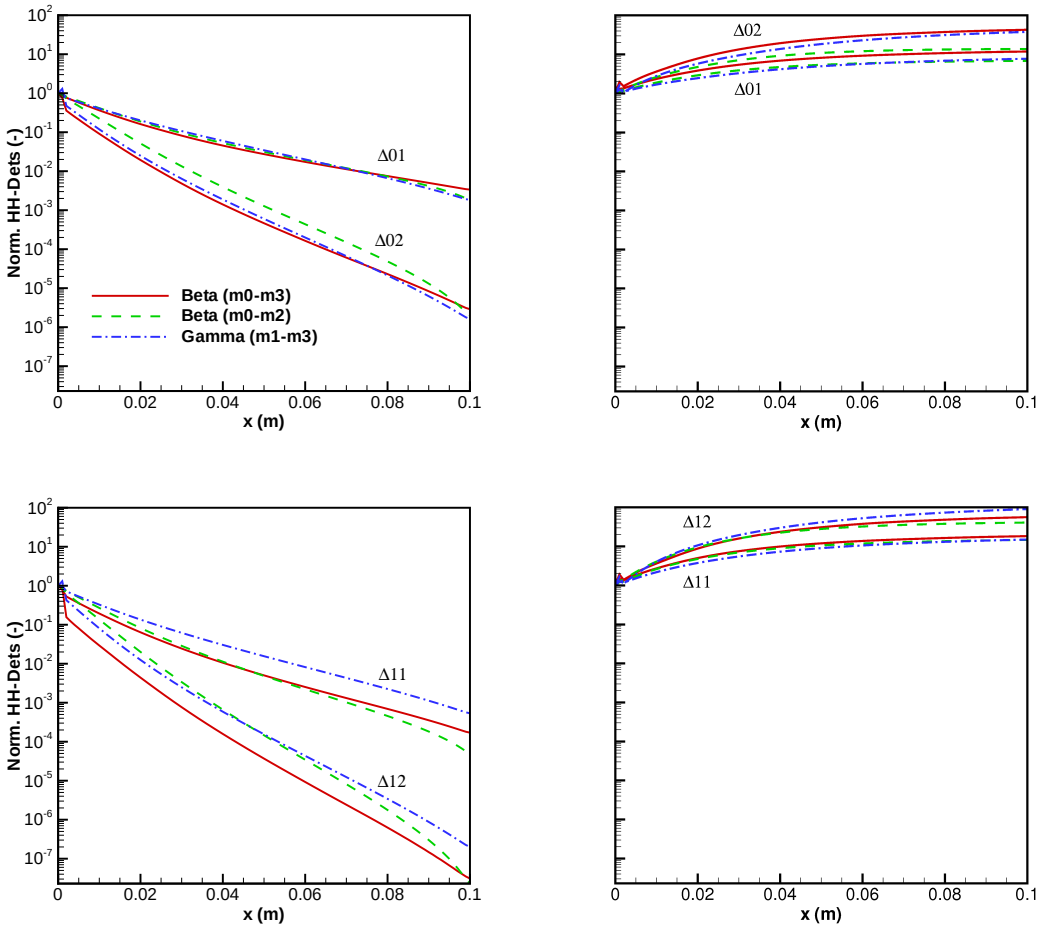

Figure 5.20: Axial evolution of the normalized Hankel-Hadamard determinants for $y = 0.035$ cm (left) and $y = 1.97$ cm (right).

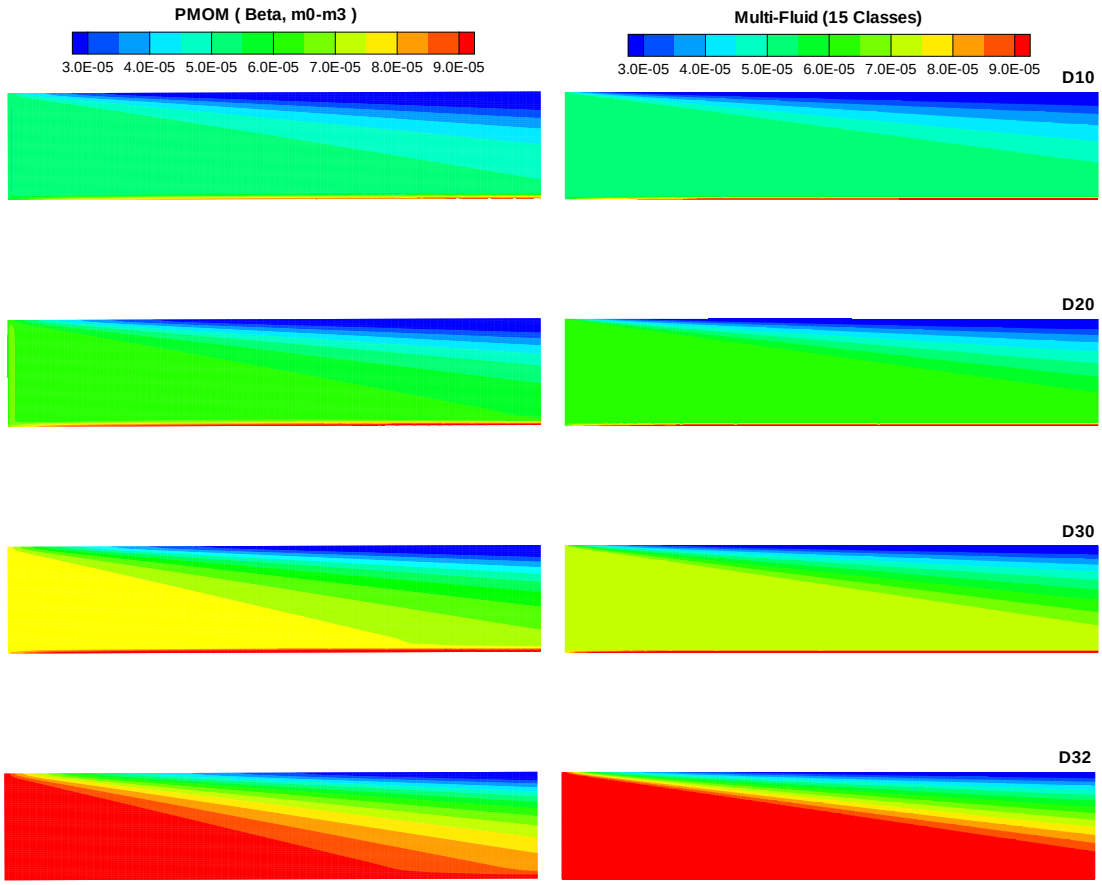

Figure 5.21: Contours of mean diameters of the size distribution inside the channel.

served with a more significant variation on the characteristic diameters inside the channel, which occurs due to the larger relaxation times used here. Furthermore, a greater difference (specially for D_{30} and D_{32}) is observed between the Multi-Fluid Model and PMOM, where particles seem to settle with a higher velocity. The larger discrepancy in this case than in the previous case possibly points to the extension of the relaxation approach to large relaxation times, where the approach is not strictly valid.

The distribution functions obtained with PMOM at three different axial posi-

tions (x = 2 cm, x = 5 cm and x = 8 cm) and three different vertical positions (y = 0.035, 1 and 1.97 cm) inside the channel are compared to the reference solution of the Multi-Fluid Model in Fig. 5.22. An overall good agreement is obtained between both solutions. Particles continuously disappear from the region near the top wall, settling towards the bottom of the channel as the mixture flows along the domain. Again the distribution function in the middle of the channel stays nearly uniform along the axial position. The biggest particles of the spectrum completely disappear from the upper part of the channel at x = 8 cm; an effect which is also well captured by the 4-moment Beta approach, as can be observed through the decrease in the predicted maximum diameters. Near the bottom at y = 0.035 cm, the distributions predicted by PMOM deviate the most from the Multi-Fluid distributions, with the underestimation of the bigger size classes being compensated both by the high peaks in the smaller diameters and the presence of particles with diameter range between $[150\mu m, D_{max}]$. When compared to the previous test case for the channel flow with bubbles, a similar behavior was observed. Note that this region contains a high accumulation of big particles with high τ, where the relaxation approach is also supposed to fail. The Beta approach with the 4-moment reconstruction scheme performs better than the 3-moment scheme, specially at the top of the channel, where the latter approach produces again unphysical high peaks towards the very small diameters of the distribution.

The position of the moment sets at the $(M^{(1)},M^{(2)})$ plane for the present test case are shown in Fig. 5.23 (left), corresponding to the soltuion obtained with the 4-moment Beta scheme at three different vertical positions. While all points are located inside the valid moment space, the $(M^{(1)},M^{(2)})$ moment pairs corresponding to the vertical position close to the top wall are closer to the lower bound curve given by Eq. (4.62). In this region, as indicated before, there is a smaller concentration of particles, which leads to a decrease of all Hankel-Hadamard determinants and possibly to moment set validity concerns (i.e., irrespective of functional form chosen) - see Fig. 5.23 (right).

The evolution of the normalized moments and their transport velocities are shown in Figs. (5.24) and (5.25), respectively. Generally, results for the 4-moment Beta approach compare reasonably well against the Multi-Fluid so-

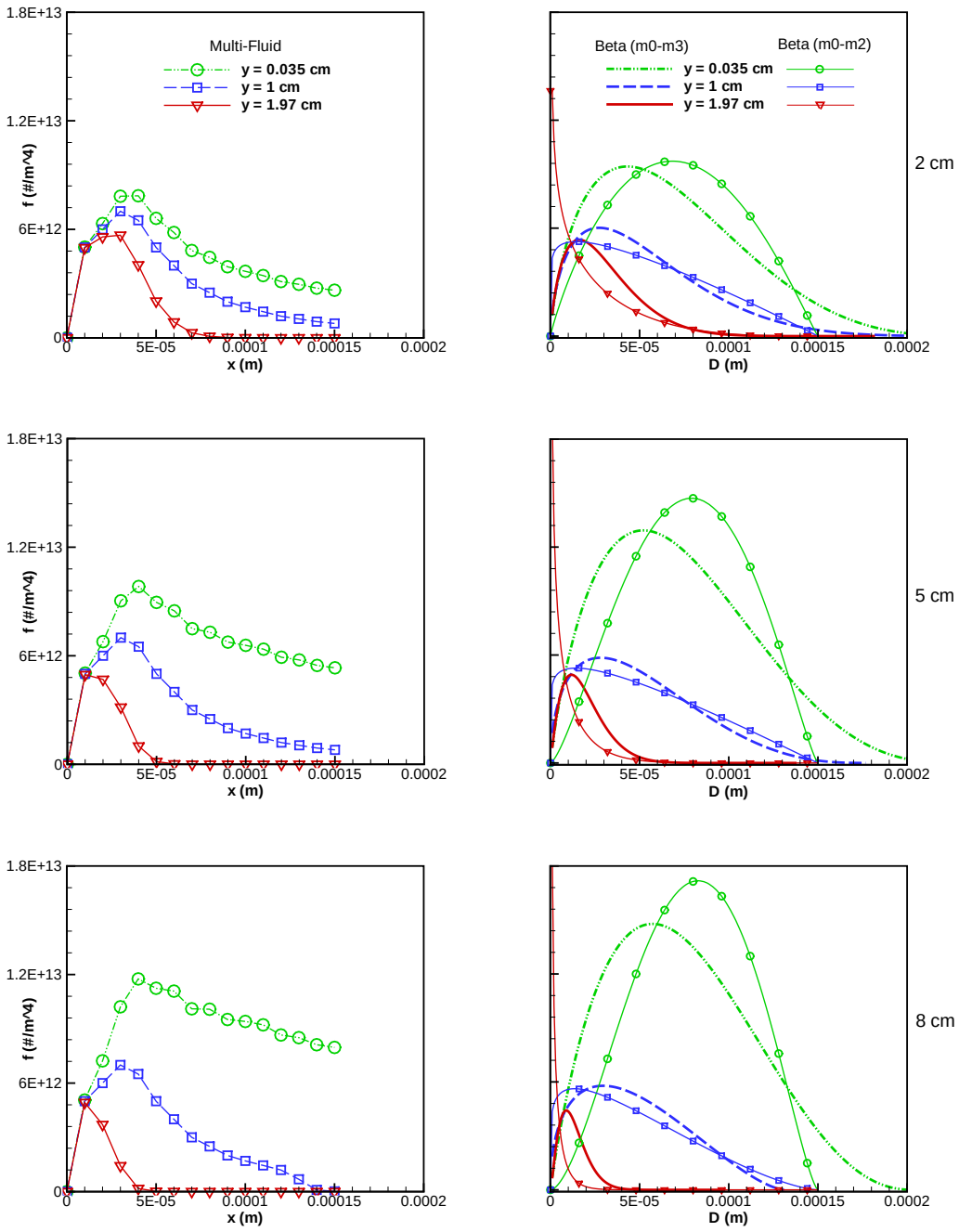

Figure 5.22: Distribution functions at three different axial positions – $x = 2$ cm, $x = 5$ cm and $x = 8$ cm (from top to bottom) – and three different vertical positions $y = 0.035$, 1 and 1.97 cm for the Multi-Fluid Model (left) and PMOM (right).

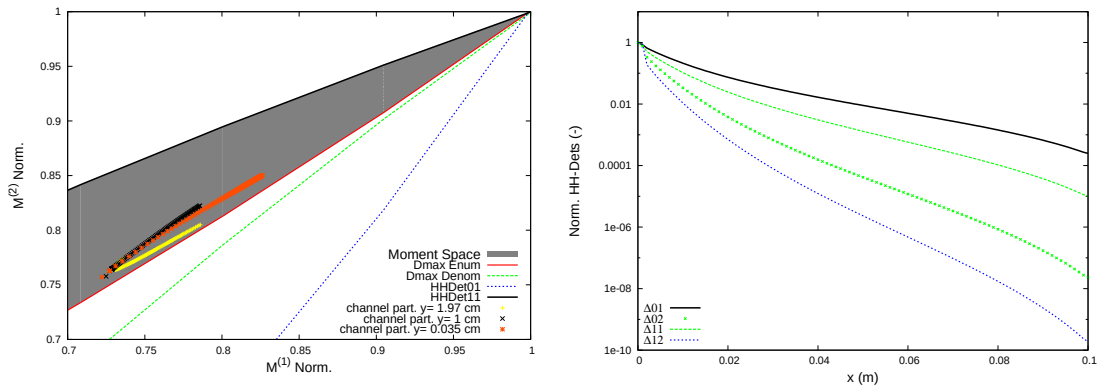

Figure 5.23: Moment space projected at the $(M^{(1)}, M^{(2)})$ plane with sets of normalized moments obtained at $y = 0.035, 1, 1.97$ cm (left) and axial variation of normalized Hankel-Hadamard determinants at $y = 0.035$ cm (right).

lution. While the agreement for the normalized moments at intermediate vertical positions is very good, specially for the low order moments, they are overpredicted near the bottom wall at the first half of the channel ($y = 0.035$ cm) and underpredicted near the top wall in the downstream part of the channel ($y = 1.97$ cm).

The profiles of the moment vertical velocities at $x = 5$ cm for both Beta approaches are compared with the Multi-Fluid profiles in Fig. 5.25. The effect of the inclusion of the velocity deviation tensor term – as given by Eq. (A.4) – on the vertical velocity profile was also investigated. In general, only small differences are observed, as expected. However, near the bottom wall, the inclusion of this term removed the sharp gradients in the profiles in the region with highest accumulation of particles. In that region, the influence of big particles becomes more significant and the size spectra of the distributions wider (see Fig. 5.22), which makes the contribution of the velocity deviation tensor term more important. The overall behavior of both schemes is similar to the previous test case, but higher discrepancies are observed here between PMOM and the Multi-Fluid solution for $\mathbf{u}^{(0)}$ and $\mathbf{u}^{(3)}$. Specially for $\mathbf{u}^{(3)}$, the 4-moment scheme significantly overpredicts the vertical velocities at the lower half of the channel (where the influence of bigger particles is more important) and fails

to predict a constant region in the profile, while the Beta approach with fixed maximum diameter still captures reasonably well this behavior. The more pronounced difference between PMOM and Multi-Fluid when compared to the previous case occurs due to the larger particle relaxation times, since inertia plays a more important role in the segregation of solid particles than bubbles, given that the initial distribution is the same. The relaxation approach is based on the assumption of sufficiently small relaxation times, so that the first order expansion for τ can still be accurate. Hence, the closure given by Eq. (4.74) is not as accurate as in the previous case, since the errors in the underlying approximations become larger.

Nevertheless, the above findings suggest that a combination of both Beta methods to reconstruct the distribution function might yield better overall results for the transport of the moments. A hybrid reconstruction scheme is proposed here for the computation of diagnostic moments, which determines the maximum diameter through a linear combination between the expression given by Eq. (4.49) and the maximum diameter of the initial distribution, $D_{max,init}$: $D_{max,new} = \frac{1}{2}(D_{max} + D_{max,init})$. The new scheme prevents the maximum diameter from becoming excessively large, overestimating the influence of bigger particles. Indeed, significant improvements can be evidenced by the predictions of the mean diameters inside the channel, as can be seen in Figs. 5.28 and 5.29 (compare also to Fig. 5.21). PMOM's results with the new Beta scheme are in closer agreement with the Multi-Fluid Model.

In order to better assess the validity of the relaxation approach, the size-velocity correlations in the y-direction $\mathrm{u}_y(D)$ obtained with the Multi-Fluid Model and the hybrid Beta reconstruction approach are compared to each other for various vertical positions at the center of the channel (Fig. 5.26, left). The curves obtained with the Multi-Fluid Model reveal a considerable effect of particle inertia, specially for diameters greater than 40 μm. While the smallest particles reach their terminal velocities (parabolic profile) close to the top wall, this is only observed at approximately y =1.3 cm for the biggest particles. On the other hand, the relaxation approach implicitly assumes that the size-velocity correlation is always parabolic, varying according to the values of $\mathbf{u}_c$ and $\mathscr{K}$ – see section 4.7.2. Therefore, results obtained with PMOM, even

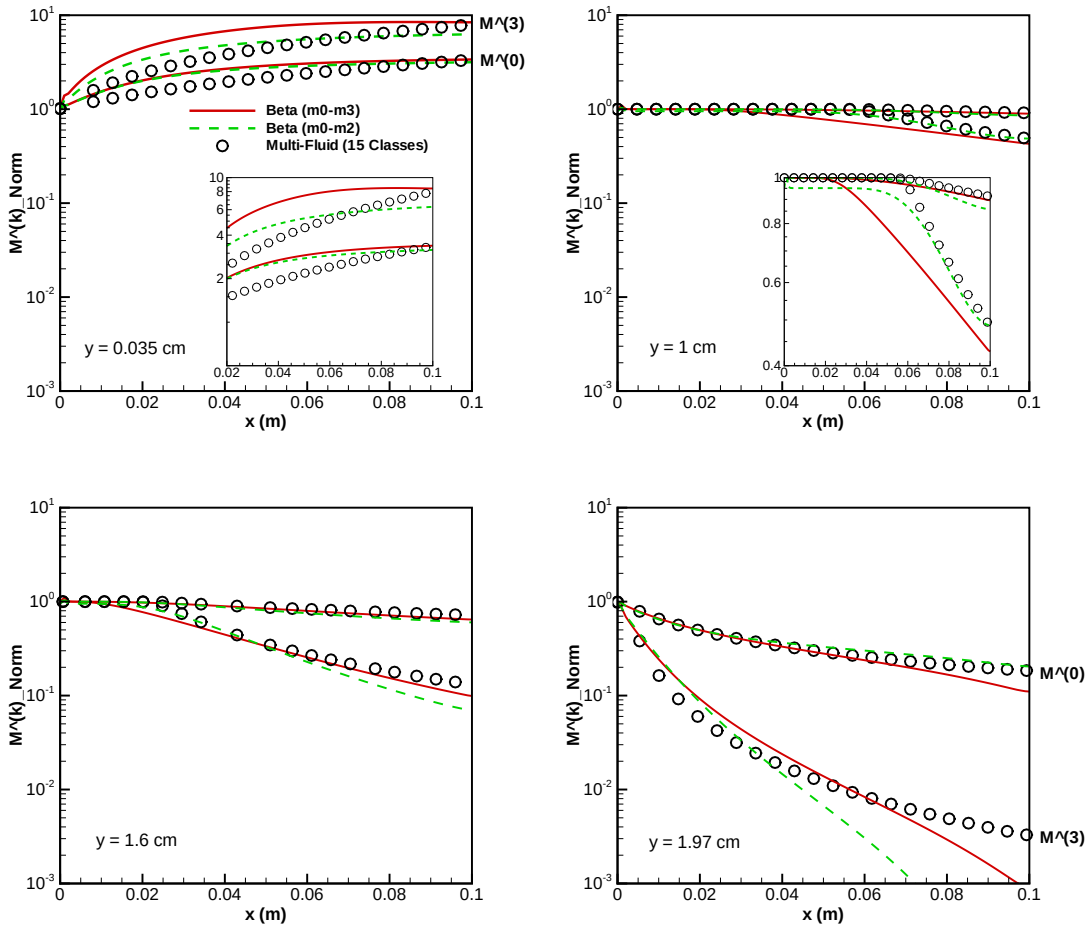

Figure 5.24: Axial evolution of normalized moments for four vertical positions inside the channel: $y = 0.035$, 1, 1.6 and 1.97 cm.

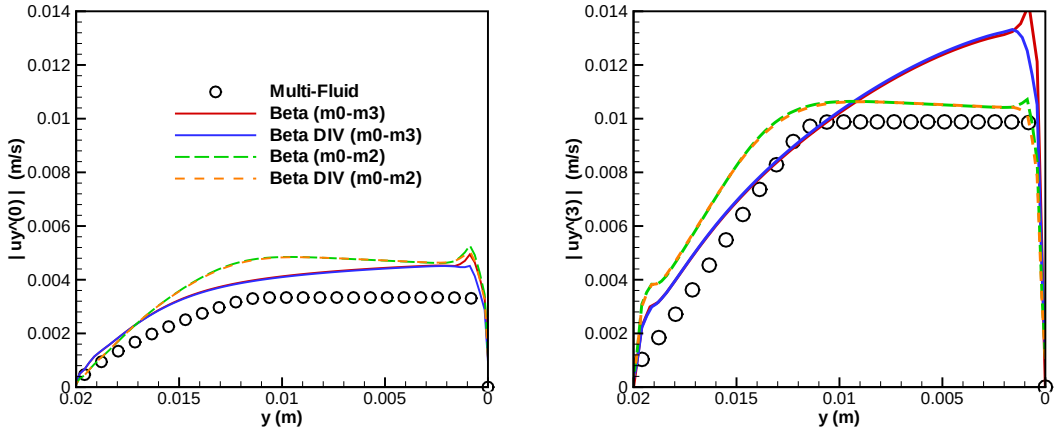

Figure 5.25: Vertical evolution of the moments transport y-velocities for $x = 5$ cm: Multi-Fluid solution vs. PMOM (Beta); with and without velocity deviation term.

with the modified Beta reconstruction, deviate considerably from the reference Multi-Fluid solution, specially for bigger particles. Indeed, the accuracy of the relaxation approach is expected to deteriorate if relaxation times are sufficiently high. Figure 5.26 (right) shows the size-velocity correlations at the center of the channel obtained by the extended PMOM (new hybrid Beta with extended relaxation approach). The modifications in the standard PMOM led to a better representation of the mean diameters inside the channel than obtained by the standard Beta reconstruction, which can be seen in Fig. 5.29 (compare to Fig. 5.21), as well as the axial profile at the center of the channel (Fig. 5.28). The combination of the hybrid Beta with the extended relaxation approach presented the best performance, with a very good agreement against the Multi-Fluid results.

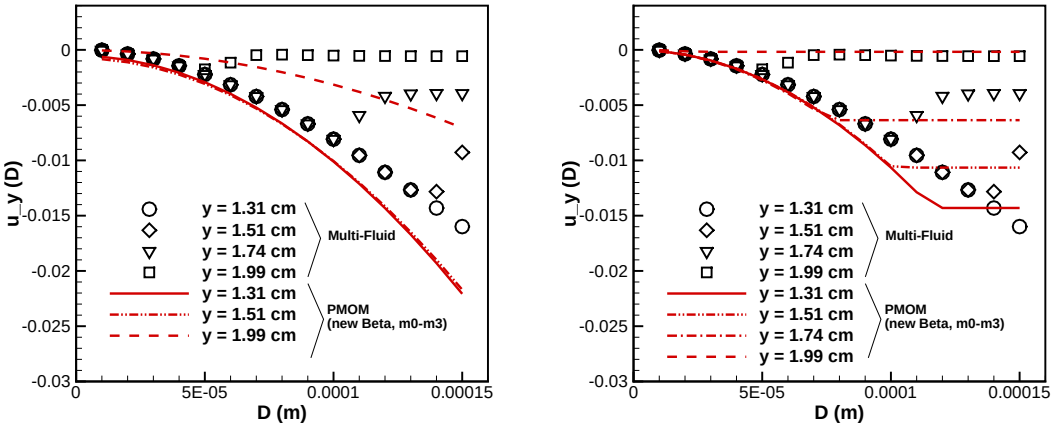

Figure 5.26: Comparison of size-velocity correlations for $x = 5$ cm and various vertical positions obtained by PMOM with the new hybrid Beta reconstruction vs. Multi-Fluid Model: standard relaxation approach (left) and the extended version (right).

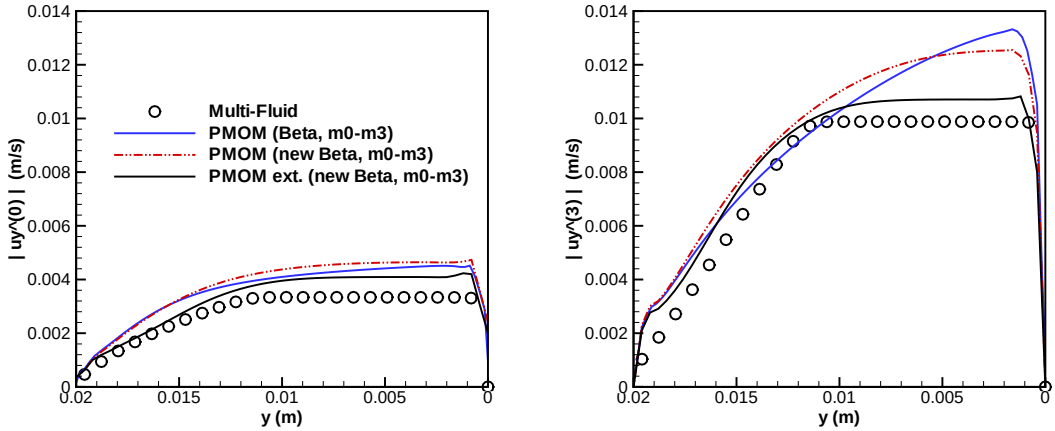

Figure 5.27: Vertical evolution of the moments transport y-velocities for $x = 5$ cm: Multi-Fluid solution vs. PMOM with the new hybrid Beta reconstruction; standard relaxation approach and the extended version.

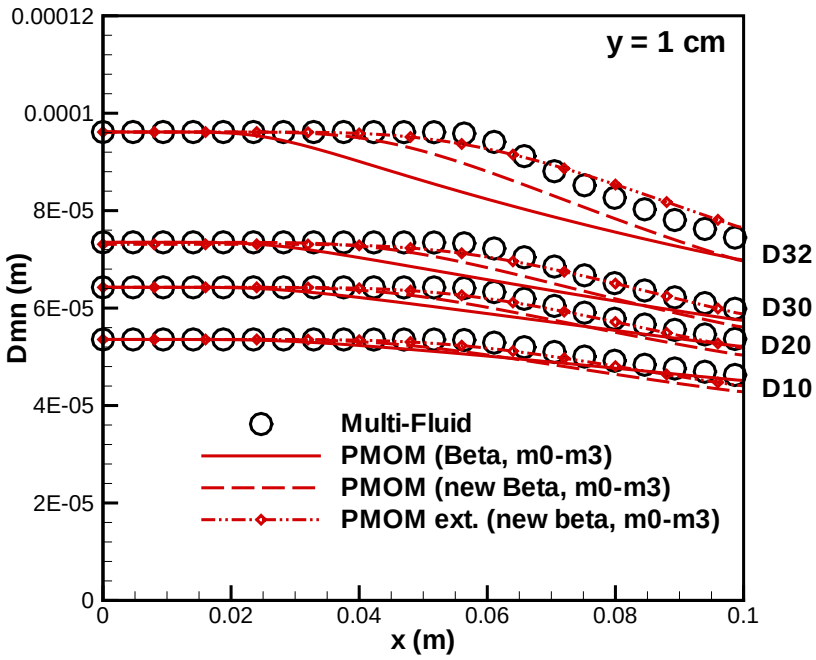

Figure 5.28: Axial evolution of the mean diameters inside the channel for $y = 1$ cm.

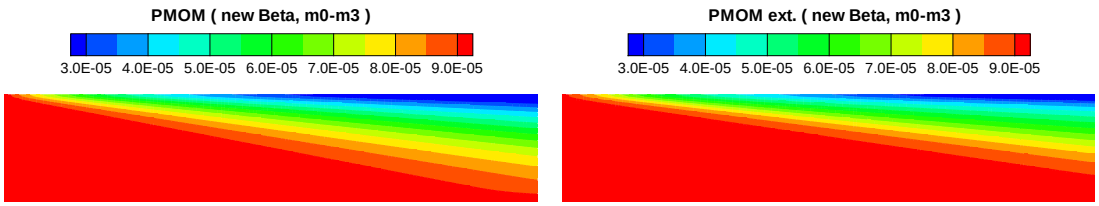

Figure 5.29: Contours of the Sauter Mean Diameter of the size distribution inside the channel: new Beta approach with standard relaxation approach (left) and extended model (right).

6 Droplet Dispersion and Evaporation

6.1 Ultra-sonic atomizer

The following test case represents the configuration of a spray generated by an Ultra-sonic atomizer. Figure (6.1) sketches the geometry of the test case. An axisymmetric domain is used to represent the experimental set-up of Bässler et al. [8]. The atomizer is placed centrally in a tube with 71 mm diameter and 400 or 610 mm length (non-evaporative and evaporative cases, respectively). Fuel is fed to an ultrasonic nozzle at 15 ml/min, which uses a small mass flow of carrier air to improve droplet dispersion. Main air is injected at a substantially higher flow rate (285 ln/min) than the atomizing air (15-20 ln/min), flowing through an annular passage 71 mm long, mixing with secondary (carrier) air flow and spray. Main air temperature was 90 C for the evaporating case, otherwise all fluids were at 25 C. The outlet section was prescribed at 1 atm and all walls were considered adiabatic. Boundary conditions for the moments were calculated from the experimental distribution measured at 8 mm behind the oscillating plate where droplets were generated: $M^{(1)} = 3.83 \cdot 10^5$ m^{-2}, $M^{(2)} = 1.43 \cdot 10^1$ m^{-1} and $M^{(3)} = 6.36 \cdot 10^{-4}$.

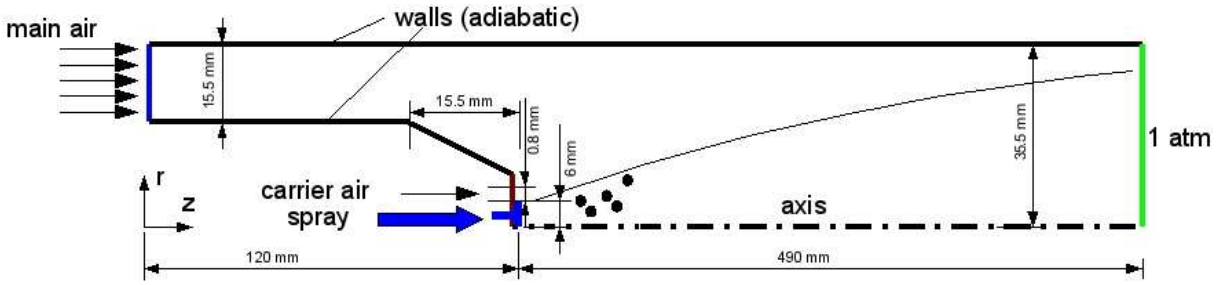

Figure 6.1: Sketch of the geometry used in the test case.

6.1.1 Monodisperse simulations

Results for monodisperse simulations with a Two-Fluid Model based on the algorithm described by Rusche [70] are shown for different droplet diameters (D =15, 30, 45 and 60 μm). The axial velocity profiles at two positions along the z-coordinate (8 mm and 150 mm behind the oscillating plate, i.e. z =128 mm and 270 mm) are shown in Fig. 6.2 with the experimental profiles obtained from PDA measurements of [8]. Two distinct streams are observed near the spray inlet, which tend to mix while traveling towards the outlet of the pipe, where a more uniform axial velocity profile is observed. It is possible to notice that a given mean diameter is not necessarily appropriate for different regions of the spray. For example, while at z =128 mm the profile seems to be better represented with D =30 μm (although the peak is slightly better captured by D =15 μm), further downstream this is not the case anymore, with the bigger diameters showing better results near the axis of symmetry. This illustrates the need for a polydisperse approach, which is able to represent the population of droplets and the exchange processes with the gas phase in a consistent manner. Results obtained with PMOM for the same case will be shown in the next section.

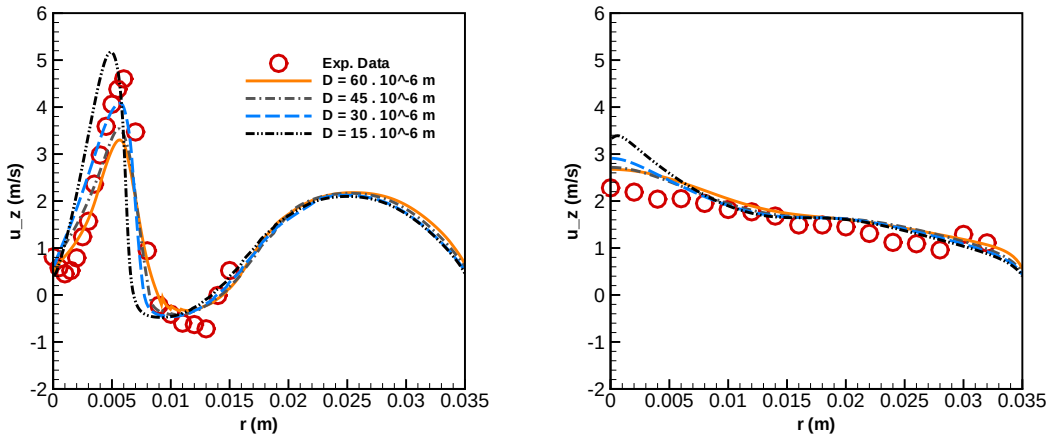

Figure 6.2: Axial velocity profiles obtained by the monodisperse simulations and experimental profiles at z =128 mm and 270 mm.

6.1.2 Polydisperse simulations

For the polydisperse cases, PMOM is used with two distribution reconstruction approaches: a three-moment Gamma scheme ($M^{(1)} - M^{(3)}$) and the four-moment Beta scheme ($M^{(0)} - M^{(3)}$). For stability reasons, the moments are initially transported with equal velocities ($\mathbf{u}^{(3)}$) and the converged solution is used as starting condition for the full polydisperse case, where the correction terms in the Moment Transport Equations (see section 4.7.2) are then activated. This procedure was not necessary in the simplified test cases of the previous chapter. The reconstructed size distribution functions at the inlet for the Gamma and Beta approaches are shown in Fig. 6.3 and their shapes are compared to the experimentally measured droplet number frequency distribution function. f's are reconstructed using the integral moments, which in turn are calculated with knowledge of some properties of the experimental function. For example, since $M^{(3)}$ and D_{32} are known, $M^{(2)}$ can be promptly determined, and so on. Both Beta and Gamma functions are able to reasonably reproduce the experimental shape.

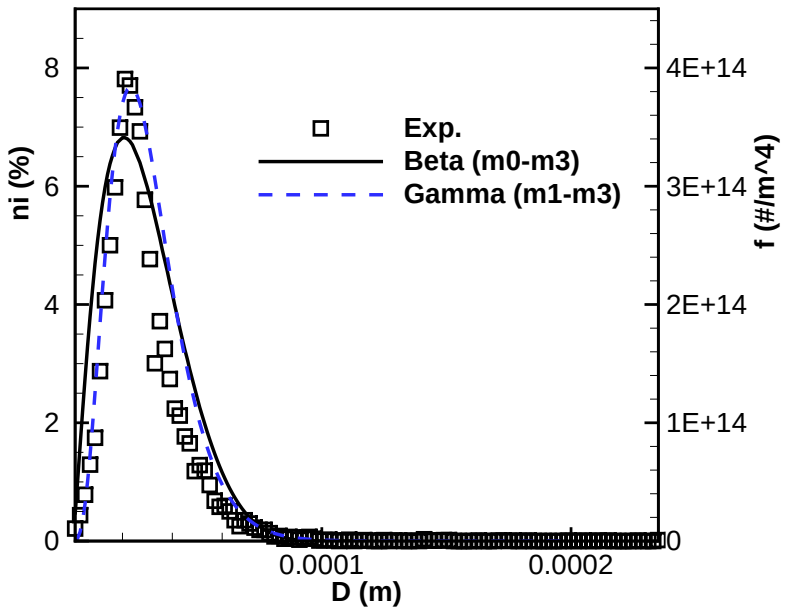

Figure 6.3: Experimentally measured distribution function at $z = 128$ mm and reconstructed Gamma and Beta distributions.

Contours of the continuous phase velocity magnitude obtained by the PMOM using the four-moment Beta scheme are shown in Fig. 6.4. The two different air streams can be easily identified, with higher velocities induced by the carrier jet, while a strong recirculating region is created by the detachment of the main flow in the annular region. The two streams mix inside the tube while flowing towards the outlet of the domain.

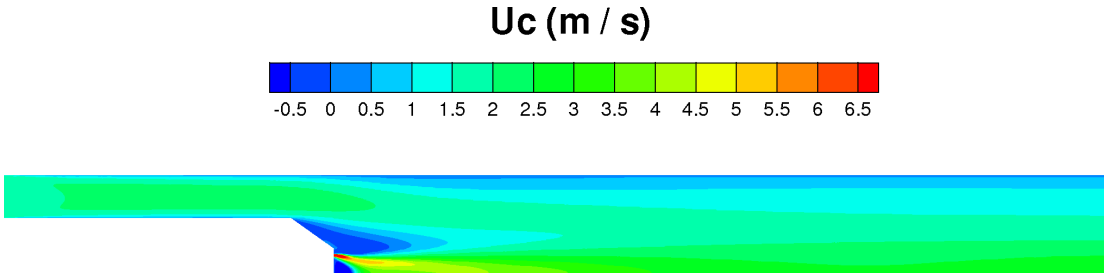

Figure 6.4: Contours of the gas phase velocity magnitude.

The axial and radial velocity profiles are investigated for PMOM using the presumed Gamma and Beta functions. The differences between both reconstruction approaches are not significant, with a good agreement obtained against the experimental profiles. Since the experimental profiles represent a number average value of the droplet velocities, it is natural that the transport velocity of $M^{(0)}$ ($\mathbf{u}^{(0)}$) agrees better with the data. Near the spray inlet, smaller droplets accelerate faster due to the higher continuous phase inlet velocity, having a bigger contribution to $\mathbf{u}^{(0)}$, while the contribution of bigger droplets is more important to $\mathbf{u}^{(3)}$. The width of the peak in the axial velocity profile is underpredicted by the model, with smaller velocities obtained between the highest value and the recirculation zone. This might be a direct consequence of the interpolation procedure of the relaxation approach, which in this case forces the intermediate moment transport velocities to lie between the reference velocity ($\mathbf{u}^{(3)}$) and $\mathbf{u}_c$. The radial component is qualitatively well predicted by both approaches. The two distinct streams observed near the spray inlet tend to mix towards the outlet of the pipe, where a more uniform axial velocity profile is observed and the radial component becomes marginal.

The typical structure of the spray obtained with the Beta approach can be identified in Fig. 6.6 (top). The spray is concentrated near the centerline and

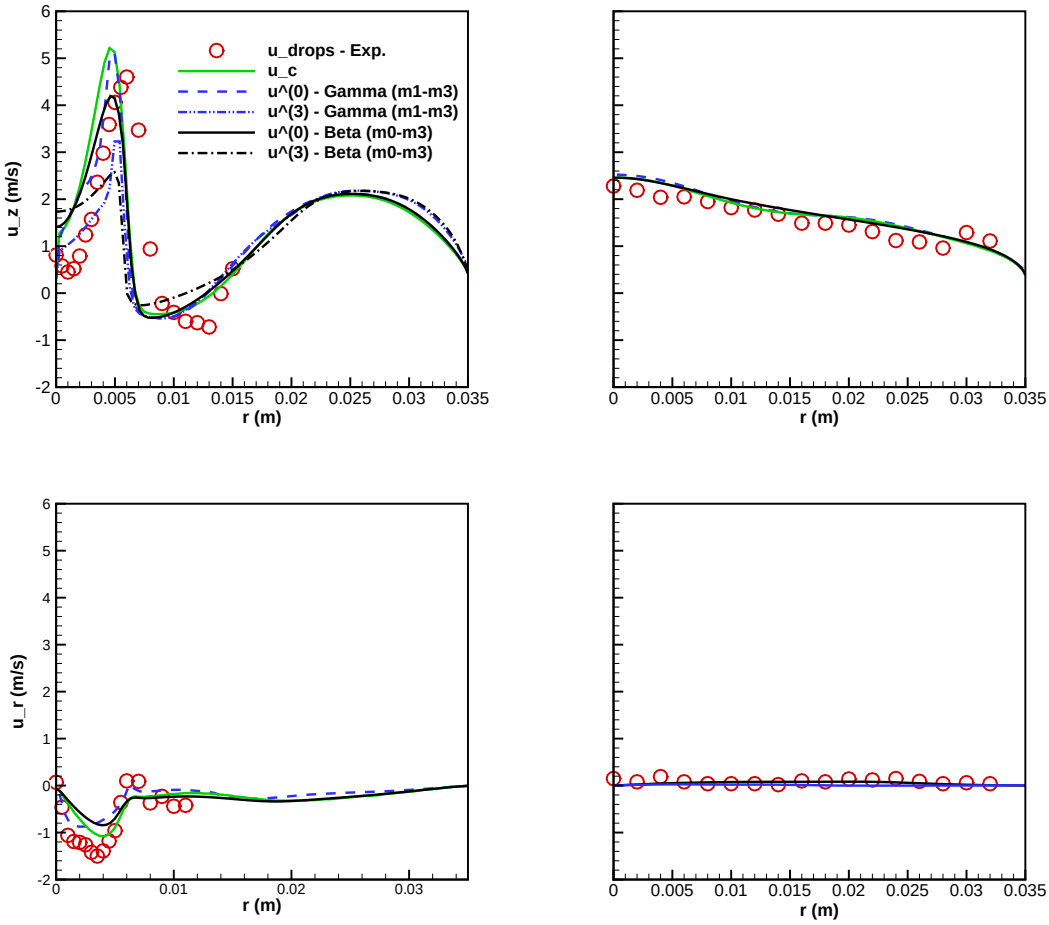

Figure 6.5: Comparison of axial (top) and radial (bottom) velocity profiles obtained with PMOM against experimental data.

in the first half of the mixing tube. The radial dispersion of the droplets (due to turbulent dispersion and drag) can be observed inside the domain, with a consequent gradual decrease on the normalized number of droplets per unit volume ($M^{(0)}$) in the region near the symmetry axis. Contours of the normalized third moment ($M^{(3)}$) are depicted in Fig. 6.6 (bottom). When compared to $M^{(0)}$, $M^{(3)}$ penetrates further downstream in the tube, which reflects the more pronounced influence of bigger droplets on this moment.

Contours of the Hankel-Hadamard determinants Δ_{01} and Δ_{11} for the Beta approach are shown in Figs. 6.7, respectively. Throughout the whole domain, positiveness of the determinants was observed. Note that also for the main air

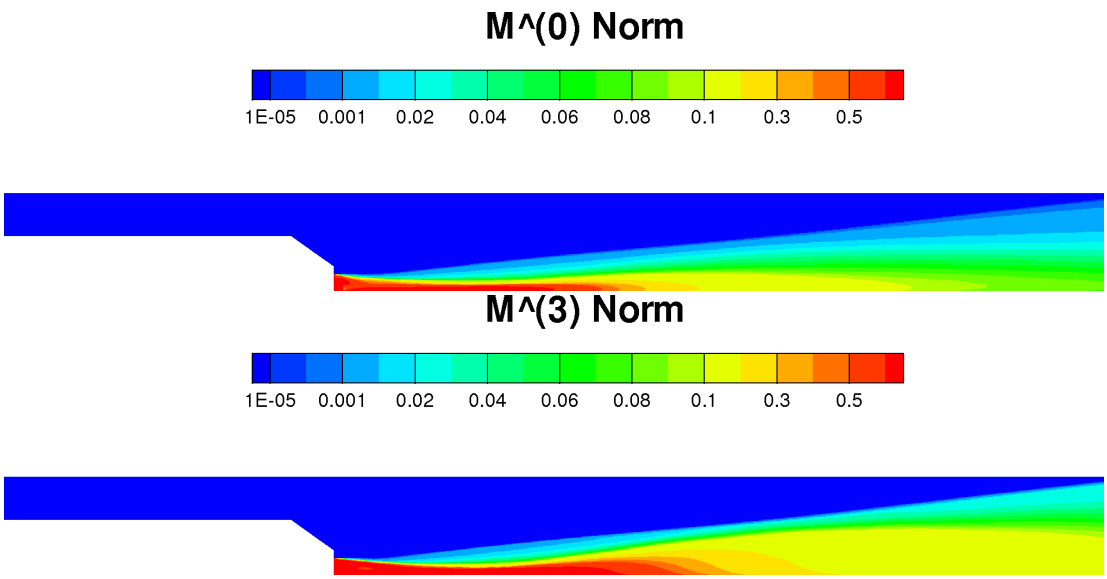

Figure 6.6: Contours of $M^{(0)}$ and $M^{(3)}$ obtained by PMOM with the Beta approach.

stream in the annular region a pseudo-distribution with very few droplets was also defined at the inlet; this distribution obviously has positive determinants and this information is also transmitted through the domain. Furthermore, an interesting feature is observed here: Δ_{01} and Δ_{11} reach their minimum values (close to zero) in the recirculation zone, which is "out of the reach" of droplets. It highlights, once more (as observed in the 1D relaxation cases and the channel flow with bubbles/particles) that regions without particles represents the greatest risk of generation of invalid sets. In the spray itself, the determinants tend to remain positive and far from the “critical condition”, i.e. $\Delta_{kl} \rightarrow 0$ and the distributions are always realizable.

Figure 6.8 shows that the radial profiles of Δ_{01} obtained by both reconstruction approaches at 8 mm behind the spray inlet are qualitatively similar. The sudden drop in the profiles corresponds to the recirculation zone in the gas phase.

The reconstructed Gamma and Beta distributions for two axial positions at the centerline are shown in Fig. 6.9. First, the variation in f observed for both cases reflects the decrease in the total number of droplets along the centerline due to the radial dispersion of the spray (i.e., $M^{(0)}$ decreases – compare also

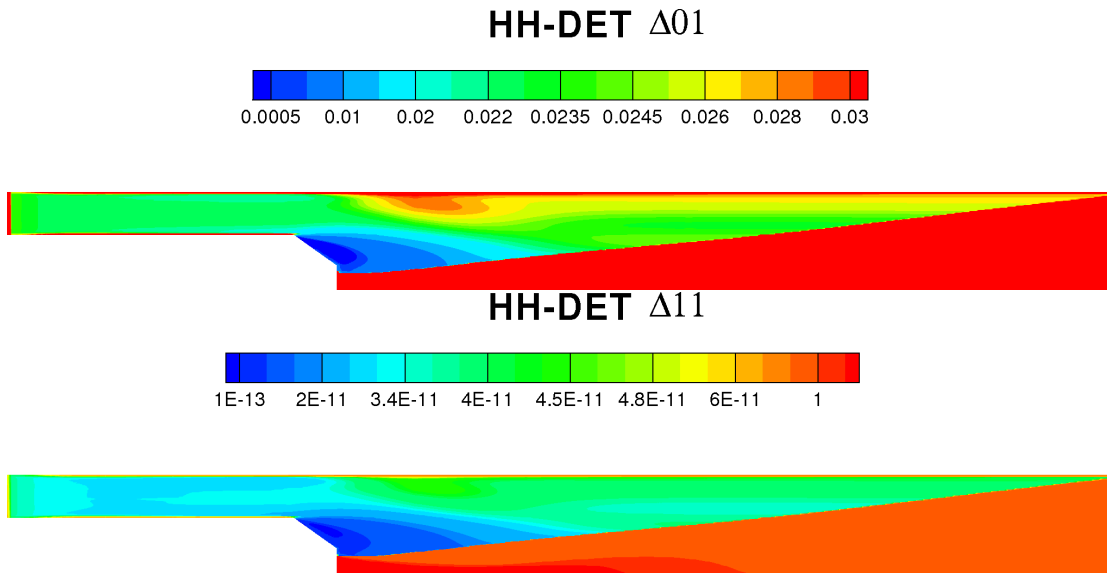

Figure 6.7: Contours of Δ_{01} and Δ_{11} for the Beta approach.

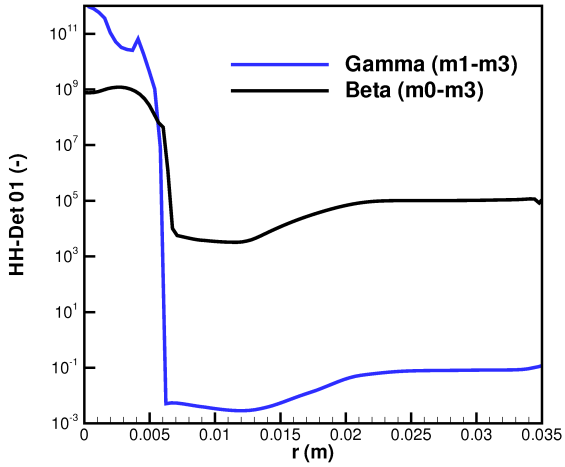

Figure 6.8: Profiles of Δ_{01} at $z = 128$ mm obtained by both Gamma and Beta approaches.

to Fig. 6.6). Furthermore, the Beta distribution presents a clear shift torwards larger diameter droplets of the spectrum. This can not be reproduced by the Gamma function, whose shape presents necessarily a positive skewness.

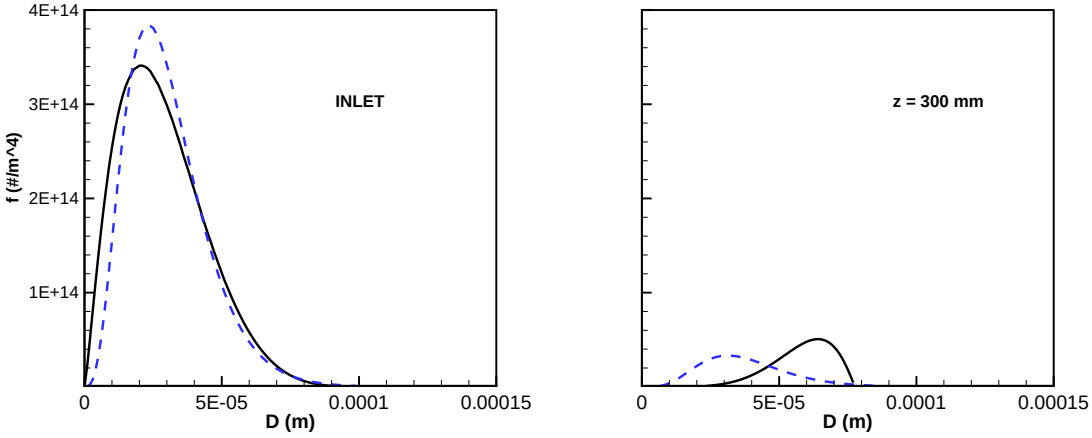

Figure 6.9: Reconstructed Gamma ($M^{(1)} - M^{(3)}$) and Beta ($M^{(0)} - M^{(3)}$) distributions at the inlet and z = 300 mm.

6.1.3 Droplet evaporation

6.1.3.1 D^2-Law

The evaporation model for the population of droplets is based on the D^2-Law for a single droplet, which is integrated over the size spectrum to yield source terms for the moments $M^{(k)}$.

In order to assess the adequacy of the D^2-Law and the Gamma distribution to describe the evaporation process of the spray simulated here, a comparative study was carried out using the experimental data of Bässler [7]. The number frequency distribution n_i measured near the spray inlet is used as initial condition and is discretized using 103 size classes ($N_c = 103$) with $\Delta D = 2$ μm and maximum diameter equal to 235 μm. The variation on the number density of a given size class i during a time interval Δt is simply computed by

$$dn_i = n_i \frac{dD_i}{\Delta D}, \tag{6.1}$$

with n_i the number density corresponding to the time instant $t - \Delta t$ and dD_i the change in size due to evaporation for all droplets pertaining to class i. dD_i can be calculated according to the D^2-Law as

$$dD_i = D_i - (D_i^2 - \lambda^* \Delta t)^{\frac{1}{2}}, \tag{6.2}$$

with D_i the diameter corresponding to class i droplets at time instant $t - \Delta t$.

The evolution of the number frequency distribution as described by the above relations is schematically represented in Fig. 6.10.

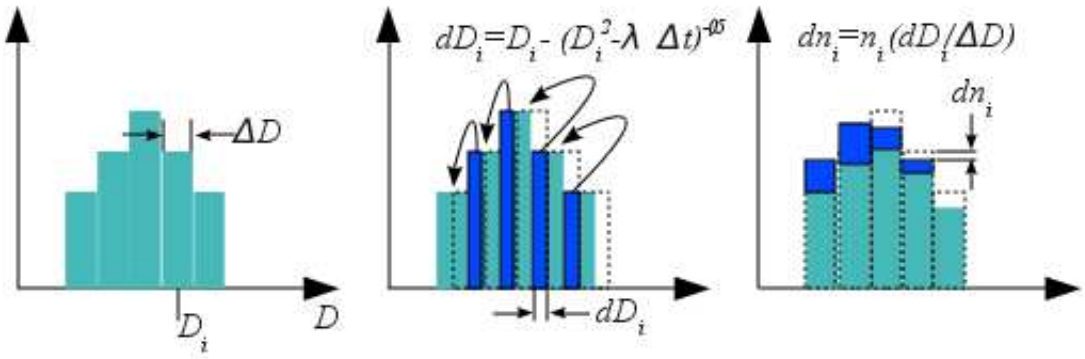

Figure 6.10: Schematic representation of the evaporation process of a population of particles as governed by the D^2-Law.

At each time instant, the moments of the number frequency distribution can be computed as:

$$M^{(k)} = \sum_i^{N_c} n_i D_i^k \Delta D. \tag{6.3}$$

With knowledge of $M^{(k)}$, the number frequency distribution can also be reconstructed, at each time instant, with the presumed function approach described in this work. Here, the suitability of a three-moment Gamma scheme will be tested for the description of the process of droplet evaporation.

Figure 6.11 shows the evolution of the number frequency distribution for subsequent time instants $t = 0.001, 0.002, 0.004, 0.006$ s as computed directly by the D^2-Law (the droplets-air mixture is considered at boiling conditions). The reconstructed distributions calculated with the low order moments $M^{(1)} - M^{(3)}$

using a presumed Gamma scheme are also shown. As droplets evaporate, the number density obviously decreases for both the direct (spectral) distributions and the reconstructed ones. The Gamma reconstruction scheme is able to reasonably reproduce the shapes of the number frequency distributions.

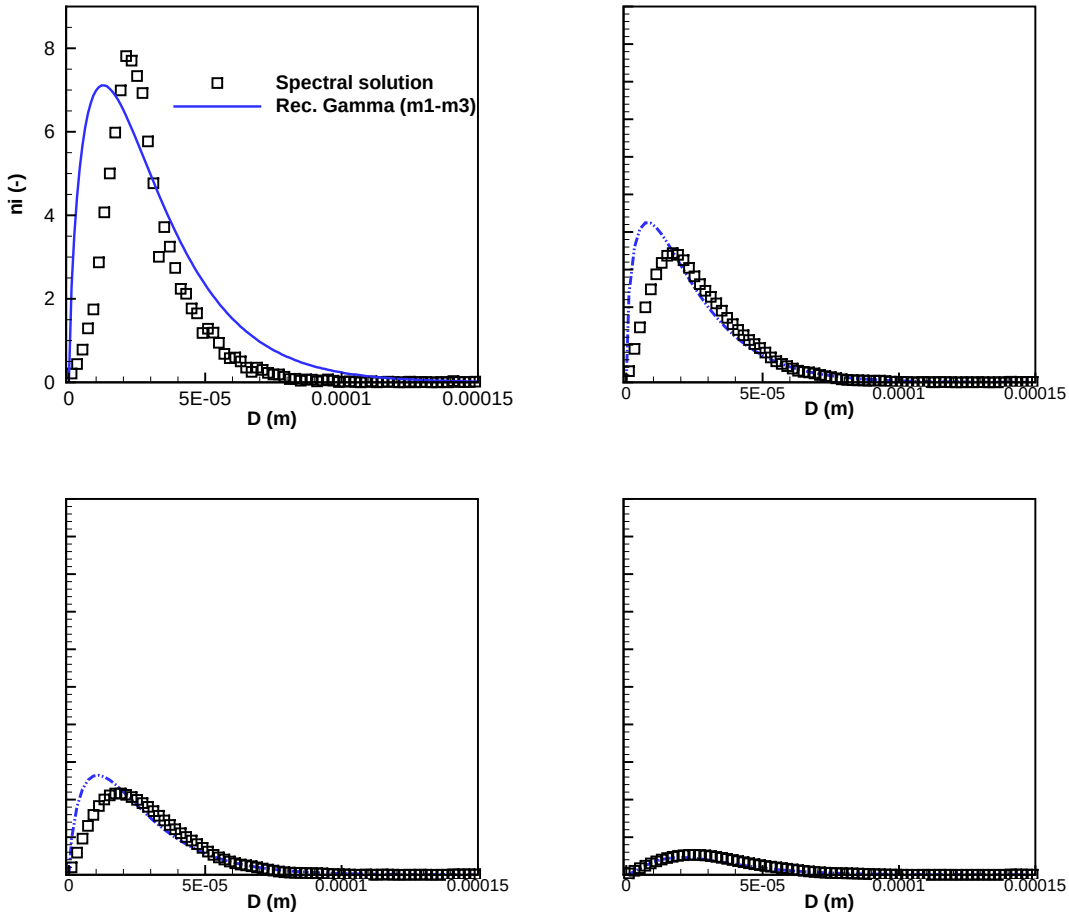

Figure 6.11: Evolution of the number frequency distribution as directly computed by the D^2-Law and reconstructed number frequency distributions by the Gamma approach.

The evolution of the total number of droplets with the degree of vaporization φ is shown in Fig. 6.12. φ is defined as:

$$\varphi = 1 - \frac{M^{(3)}}{M_0^{(3)}}, \tag{6.4}$$

$M_0^{(3)}$ is the third moment of the initial droplet number frequency distribution. Thus, the limit $\varphi \rightarrow 1$ represents the complete disappearance of droplets.

The evolution of the total number of droplets is compared for the direct solution, the Gamma approach and experimental values of Bässler [7]. The experimental data is collected for a number of different cases, given the mass-flow rate, varying the air temperature and the length of the mixing tube (see Fig.6.1), yielding different φ's measured at the outlet of the tube [7]. The evolution of N_t in the simulations is therefore an idealization of the real process, neglecting for example effects of convection, heat-up and interaction between droplets.

Even though the Gamma scheme does not use $M^{(0)}$ explicitly in the reconstruction process, the deviations observed from the spectral solution are small. Both can represent the evolution of N_t qualitatively well, underpredicting however the total number of droplets for high degrees of vaporization ($\varphi > \approx 50\%$). Bässler [7] argues that this occurs probably due to the presence of vaporized fuel in the droplets vicinity, decreasing the concentration gradient, which drives the evaporation process at the surface.

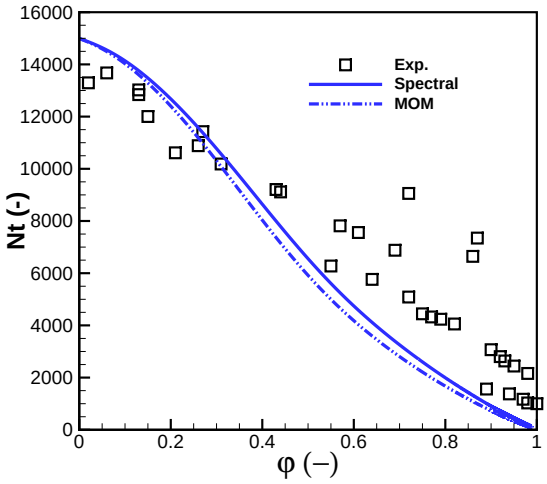

Figure 6.12: Evolution of the total number of droplets with the degree of vaporization.

The mean droplet diameters are also compared to the experimentally mea-

sured values. First, it is observed that $D_{10} < D_{32} < D_{43}$. This is obviously a requirement for a realizable distribution according to the convexity condition, as mentioned before. For D_{32} and D_{43}, a good agreement is obtained between the model and experimental data. The observed increase in the mean diameters is explained by the fact that the rate of decrease of droplet diameter is higher for smaller droplets, since according to the D^2-Law: $dD/dt \propto 1/D$. For D_{10}, this increase was not observed in the experiments. This might be a consequence of the underprediction of the total number of droplets by the model, leading to the excessive increase in D_{10}.

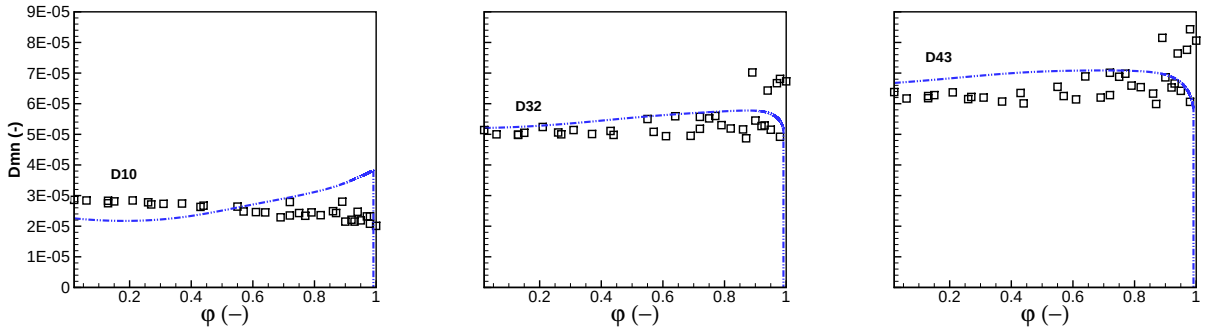

Figure 6.13: Evolution of mean diameters with the degree of vaporization.

The variation of the normalized Hankel-Hadamard determinant Δ_{01} as the distribution of droplets evaporate is also computed (Fig. 6.14). As expected, Δ_{01} gradually decreases with φ and when droplets completely evaporate ($\varphi \rightarrow 1$), the determinant vanishes ($\Delta_{01} \rightarrow 0$). Hence, sprays with a high degree of vaporization are expected to represent a potential situation for the occurance of invalid moment sets.

6.1.3.2 Ultra-sonic atomizer with droplet transport and evaporation

As mentioned before, the source term for the zeroth moment due to evaporation presents a singularity problem. As for the present version of PMOM, this moment can not be chosen to be transported; development of a model for $\Gamma_{M^{(0)}}$ will not be undertaken in the present work. Therefore, only the Gamma approach as used in the non-evaporative situation will be presented, since it

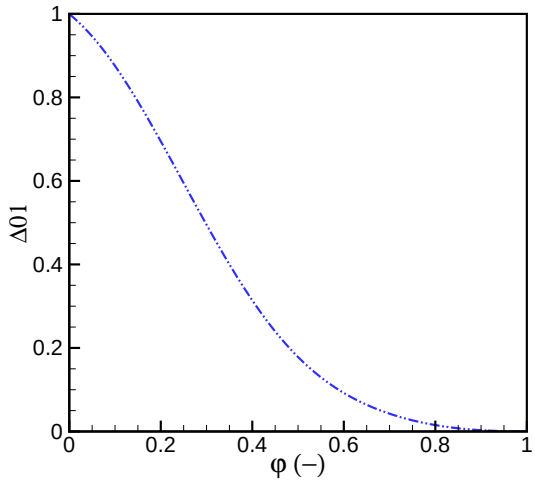

Figure 6.14: Evolution of the normalized determinant Δ_{01}.

does not use $M^{(0)}$ explicitly in the distribution reconstruction. As seen above, the Gamma reconstruction scheme with $M^{(1)} - M^{(3)}$ was able to reasonably reproduce the process of droplet evaporation described by a D^2-Law, and presented a reasonable agreement with experimentally measured values of D_{10}, D_{32} and D_{43} for different degrees of vaporization. Therefore, it is assumed that the D^2-Law with this reconstruction scheme is a good approximation for the evaporation process of the spray in question. It will be shown next that PMOM with simultaneous moment transport and evaporation yields reasonable results for the configuration analyzed. In order to avoid a higher propensity for the generation of invalid sets due to the simultaneous consideration of polydisperse transport and evaporation in the moments transport equations, a two-step procedure is recommended, where evaporation source terms are considered first, and the convective correction by the relaxation approach is subsequently incorporated. As shown in the previous section, the evaporation model considered in the moments context, with no transport, presented a reasonable comparison with the real spray for the evolution of the droplet population with the degree of vaporization. It is assumed that polydisperse transport may be considered less important in this particular case. Therefore, for simplicty, moments are transported with the same velocity, given by $\mathbf{u}^{(3)}$, in the simulation results shown next.

Contours of the dispersed phase volume fraction ($\propto M^{(3)}$) and vapor mass fraction (Y_v) are shown in Fig. (6.15). A higher concentration of droplets is observed near the inlet, which gradually decreases towards the end of the pipe due to both dispersion and evaporation of the droplets, while the amount of vaporized fuel increases.

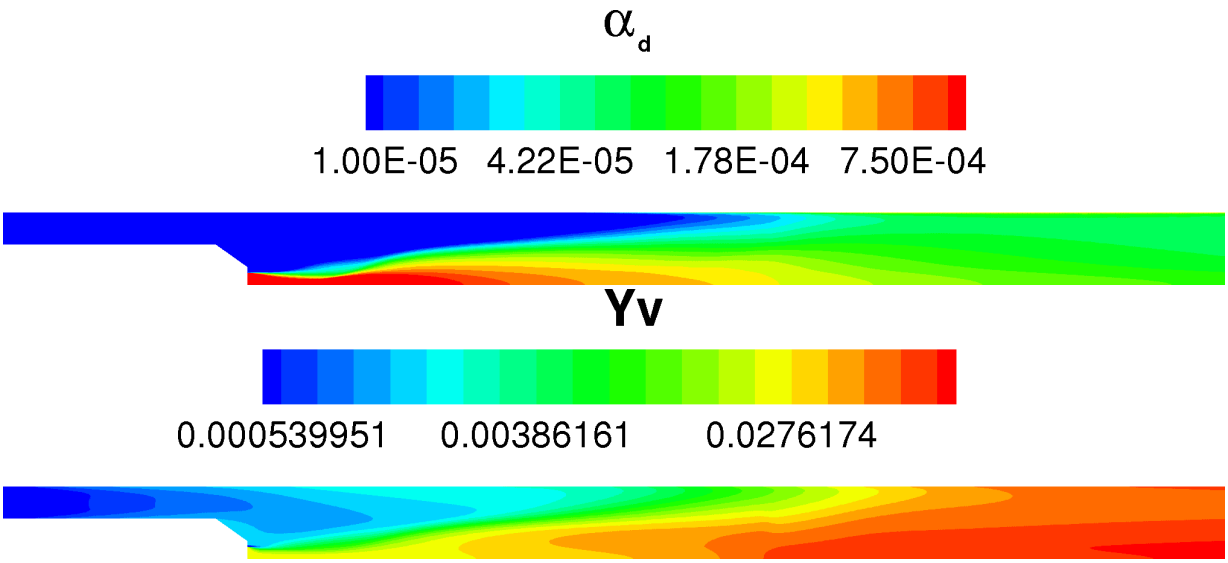

Figure 6.15: Contours of dispersed phase volume fraction (top) and vapor mass fraction (bottom).

The low order Hankel-Hadamard determinants Δ_{02} and Δ_{11} containing the most relevant moments were assessed in order to check the signature of invalid moment sets throughout the solution domain (Figs. 6.16 and 6.17, left). Contours of Δ_{11} are qualitatively similar to the ones obtained in the non-evaporative cases, being positive within the spray and tending to zero towards the outside region. It is also observed here, however, that Δ_{11} decreases axially towards the outlet, where the degree of vaporization is higher. This was observed in the previous computation where the initial distribution of droplets is made to evaporate according to the D^2-Law with the moments and Hankel-Hadamard determinants being calculated at each time instant. It was shown that they decrease with the degree of vaporization and vanish at the limit when droplets completely evaporate. For combustion simulations, for example, where it is generally desired to achieve a high degree of spray vaporization, this issue must be addressed in more details.

The reconstructed distributions at the centerline (Fig. 6.17, right) show the effect of evaporation as the droplets travel downstream in the pipe, diminishing the total population in the spray.

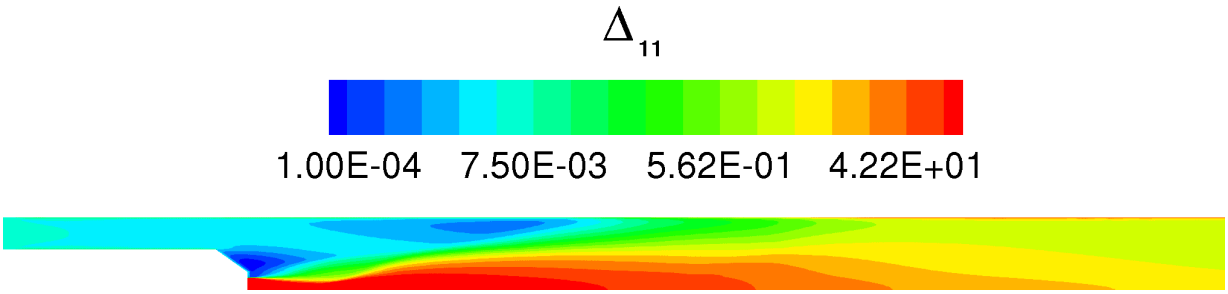

Figure 6.16: Contours of Δ_{11}.

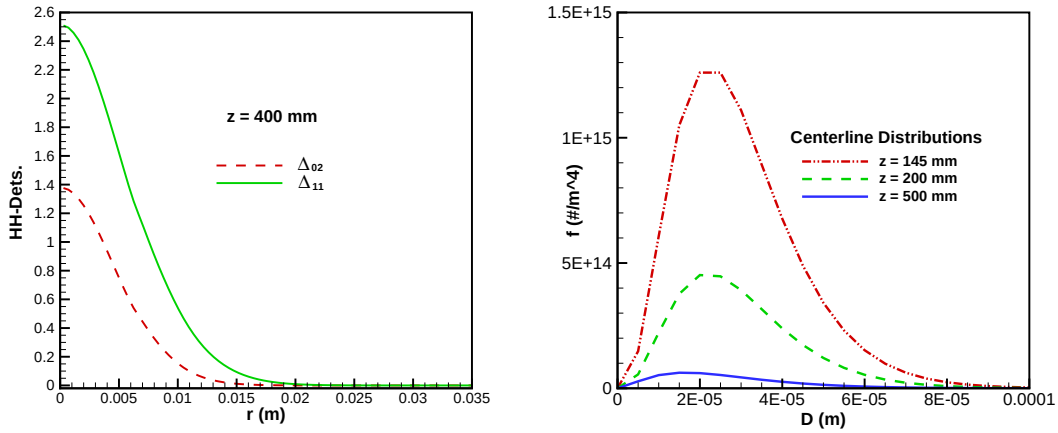

Figure 6.17: Radial profiles of Δ_{02} and Δ_{11} (left) and reconstructed distributions.

Profiles of droplet mean diameters corresponding to $z = 600$ mm are depicted in Fig. (6.18). As shown by the experimental measurements, the mean diameters are approximately constant at $z = 600$ mm in most part of the spray and tend to slightly diminish in the main hot air stream, mainly because the temperature is higher there (but probably also because bigger droplets tend to travel near the centerline). This effect was also captured by the Moments Model through the implementation of source terms described earlier but an increase is also observed in the trends of the curves. This occurs due to the nature of the source terms for the moments, which reproduces the D^2-Law:

smaller droplets have higher rate of evaporation, which translates into higher rates of evaporation for low order moments. Towards the spray tip and near the wall, only a few smaller droplets are likely to be found leading to a decrease in the mean diameters.

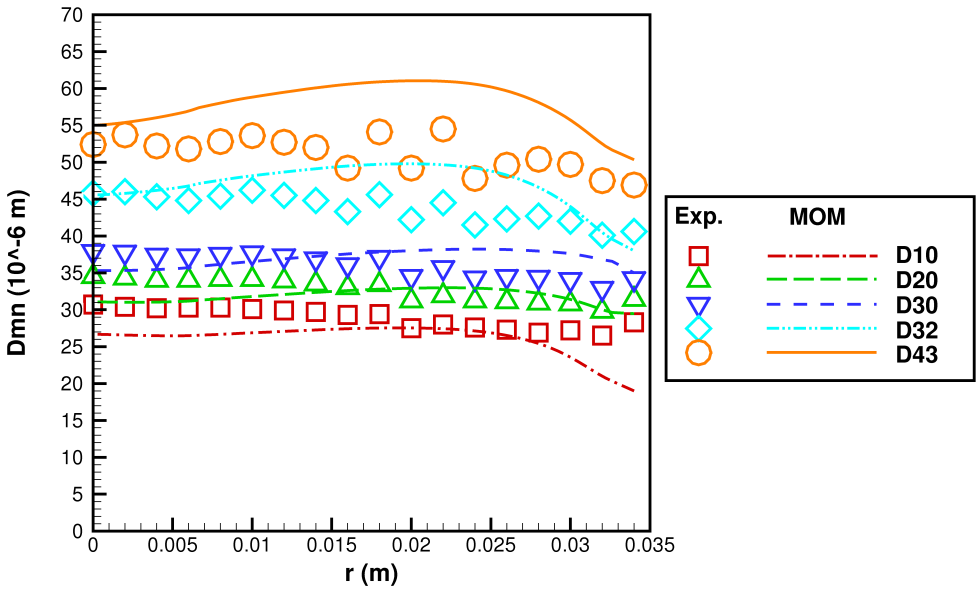

Figure 6.18: Droplet mean diameters (z = 600 mm) obtained with the Moments Model and PDA data.

7 Discussion and Future Developments

A Method of Moments of polydisperse multiphase flows in the Eulerian-Eulerian framework was formulated and validated. Closure was based on presumed functions for the particle size distribution and a novel relaxation approach for the size-velocity correlation. The method (called "PMOM") was implemented in the open source tool OpenFOAM in an existing Two-Fluid solver. The proposed model was able to reproduce polydisperse effects in the particle motion in an efficient manner, by transporting a few moments of the size distribution function.

First, one-dimensional test cases consisting of a population of particles being decelerated or accelerated in a constant gas phase velocity field were investigated. Different particle relaxation times due to Stokes drag generate axially heterogeneous distributions. Results for the model using different reconstruction schemes involving Gamma and Beta distribution functions were analyzed and compared to an analytical solution. In general, the agreement was very good, with the best performance achieved by the Beta approach. It became also apparent that reconstruction methods that use only a few prognostic moments, might present conservation issues with respect to the diagnostic moments, since the latter are not explicitly used in the reconstruction process itself. Since the moments also represent physical characteristics of the distribution, non-conservativeness is in certain situations unacceptable. This is the case, for example, of the Gamma approach using $M^{(0)}$-$M^{(2)}$, which does not conserve the volume of the distribution. In this sense, the Beta approach using the same moments presented a better performance.

A numerical experiment representing a channel flow of water and two different disperse phase densities (corresponding to bubbles or solid particles) was also carried out to investigate the polydisperse segregation due to size-dependent buoyancy effects. Results obtained with PMOM were compared

to reference solutions carried out with the Multi-Fluid Model using 15 size classes. Also in this configuration, very reasonable agreement with the reference solution was obtained in both test cases. Predictions for the evolution of the moments and their transport velocities for the case with bubbles were slightly superior than for the one with solid particles – the reason for the discrepancies observed was the larger average response times involved in the second case. The relaxation approach was extended to account for inertial effects and combined with a hybrid Beta reconstruction method. Improvements were achieved in comparison with the standard version of PMOM, since the size-velocity correlations are better reproduced by the extended approach.

The model was also applied in a configuration consisting of a spray generated by an ultra-sonic atomizer. Results show that the basic structure of the spray is well captured by the model, with a good quantitative agreement with the experimental velocity profiles, showing that overall momentum exchange was reasonably reproduced. For the evaporative case, experimentally determined mean diameters could be well reproduced by the model through the implementation of moments source terms derived from the D^2-Law, which was shown to be a good approximation of the evaporation process.

The analysis of the Hankel-Hadamard determinants was introduced in order to check the validity of the moment sets generated in the solutions. In the cases investigated here, positiveness of the determinants was observed in the converged solutions. However, it was revealed that the determinants increase where particles tend to accumulate and decrease where they tend to disappear, following the moments characteristics in some sense. This observation suggests that transition regions with and without particles within the flow field represent potential situations for the generation of invalid sets. Since the moments are transported with different velocities in the flow field, the rate at which they tend to zero is also different. Hence, it is possible that the numerical schemes produce invalid sets during the solution of the equation system. Some practical situations can be perceived in which the Hankel-Hadamard criteria might not be fulfilled, such as in sedimentation systems with strong particle segregation, at the edges of high velocity sprays or the front of precipitating droplet clouds. In such situations, it will be important to investigate dif-

ferent reconstruction schemes and to which extent bounding and correction procedures do not violate moment conservation. The Hankel-Hadamard determinants establish the existence or not of a family of distribution functions, given a set of moments, and the realizability of especific functional forms require further analysis. Here, limits on the moment space for the Gamma and Beta distributions were established and may help to construct replacement or correction schemes in the future, in case invalid sets appear during the solution procedure. Other functions and reconstruction schemes need to be separately evaluated.

Future work should primarily be concerned with the extension of the model concerning the simplifying hypothesis introduced here. Tentative general guidelines are listed below:

- Extension to larger particle Reynolds number

  The basic closure for the drag force is based on the Stokes law and correlations for heat and mass exchange do not account for Reynolds number corrections in the calculation of Nusselt and Sherwood numbers. This simplification allowed the derivation of an analytical closure for these terms. However, it is usual for most applications involving spray evaporation to consider larger particle Reynolds numbers, making necessary the extension of momentum, heat and mass exchange models considered here.

- Closure for the energy equation

  Hitherto, most of the Eulerian models assume that all particles have a single temperature, as also done here. It is possible to develop a closure in a similar framework as in the relaxation approach for particle velocities, by expanding the particle temperature around the continuous phase temperature in terms of thermal response times (see [32], for details). The expression can be then integrated over the size spectrum in order to develop expressions for moment averaged temperatures, $T^{(k)}$.

- Closure for $\mathbf{u}'\mathbf{u}'$

  The assessment of the importance of the velocity deviation tensor term

and its dependence on the particle relaxation time is also still needed. A suggestion using the framework of the relaxation approach was presented in this work (see A.2).

- Droplet evaporation

  Eventhough reasonable results were achieved in the examples studied here, the evaporation model presented is not built on the conservation of zero-th moment, since it is not chosen a prognostic moment. Closure with a Beta reconstruction scheme using four moments, for example, requires the development of a source term for $M^{(0)}$. However, as seen before, $\Gamma_{M^{(0)}}$ presents a singularity problem and its formulation involves modeling in some way. One idea is to formulate $\Gamma_{M^{(0)}}$ as a function of $\Gamma_{M^{(3)}}$, for example, as: $\Gamma_{M^{(0)}} = \frac{M^{(0)}}{M^{(3)}}\Gamma_{M^{(3)}}$ (i.e., the ratio of source terms is equivalent to the ratio of the moments themselves). Schneider [72] and Massot et al. [56] tackle the problem by parameterizing the distribution function with the droplet's surface area, using an approximate NDF [72] or a maximum entropy approach [56], respectively.

- Particle Trajectory Crossing (PTC)

  In contrast to Lagrangian approaches, one of the major drawbacks of standard Eulerian models for disperse flows is the assumption that particles of the same size are only allowed to have a single local velocity. This can be a serious handicap in situations such as those of impinging particle jets and jet crossing (as in multiple spray injection systems), but also for LES and DNS of the gas phase. It is illustrated in A.4, in the framework of PMOM, that approaches considering a single velocity field fail to capture PTC. It is necessary to allow the co-existence, locally, of multiple distributions and size-velocity correlations. It is important to point out, however, that quadrature-based methods have been proven to efficiently overcome this issue allowing the local velocity to be multi-valued (see [33], [23] and [72], for example).

Finally, it is believed that the foundations were laid in this work for the application of the methodology in more complex configurations such as in gas turbines or Diesel engines, where it is obviously still necesssary to include other

interaction phenomena, such as droplet break-up and collision and possibly extend the framework to turbulence resolved reacting flows.

Bibliography

[1] M. R. Archambault, C. F. Edwards, and R. W. MacCormack. Computation of spray dynamics by moment transport equations I: theory and development. *Atomization and Sprays*, 13:63–87, 2003.

[2] M. R. Archambault, C. F. Edwards, and R. W. MacCormack. Computation of spray dynamics by moment transport equations II: application to calculation of a quasi-one dimensional spray. *Atomization and Sprays*, 13:89–115, 2003.

[3] G. A. Jr Baker. *Essentials of Padé Approximants*. New York: Academic, 1975.

[4] S. Balachandar and J. K. Eaton. Turbulent dispersed multiphase flow. *Annual Review of Fluid Mechanics*, 42:111–133, 2010.

[5] J. C. Barrett and J. S. Jheeta. Improving the accuracy of the moments method for solving the aerosol general dynamic equation. *Journal of Aerosol Science*, 27:1135–1142, 1996.

[6] A. B. Basset. On the motion of a sphere in a viscous liquid. *Philosophical Transactions of the Royal Society of London*, 179:43–63, 1888.

[7] S. Bässler. *Einfluss der Vorverdampfung auf die Stickoxidbildung in Sprayflammen*. PhD thesis, Lehrstuhl für Thermodynamik, TU-München, Germany, 2007.

[8] S. Bässler, K. Moesl, and T. Sattelmayer. NOx emissions of a premixed partially vaporized kerosene spray flame. *Journal of Engineering for Gas Turbines and Power, Vol. 129, pages 695-702*, 2007.

[9] J. Bataille and M. Lance. Two-fluid modeling versus mechanistic approach and lift effects in bubbly sheared flows. *International Journal of Thermophysics*, 14:661–669, 1993.

[10] J. C. Beck. *Computational modelling of polydisperse sprays without seggregation into size classes.* PhD thesis, UMIST, UK, 2000.

[11] J. C. Beck and A. P. Watkins. On the development of spray submodels based on droplet size moments. *Journal of Computational Physics*, 182:586–621, 2002.

[12] J. C. Beck and A. P. Watkins. On the development of a spray model based on drop-size moments. *Proceedings of the Royal Society of London A*, 459:1365–1394, 2003.

[13] A. Berlemont, P. Desjonqueres, and G. Gouesbet. Particle lagrangian simulation in turbulent flows. *International Journal of Multiphase Flow*, 16:19, 1990.

[14] F. S. Binkowski and S. J. Roselle. Models-3 community multiscale air quality (CMAQ) model aerosol component 1. model description. *Journal of Geophysical Research*, 108:4183, 2003.

[15] Y. Bo and A. P. Watkins. Mathematical development and numerical analysis of further transport equations for the droplet size moment theory. *19th Annual Meeting of ILASS-Europe, Nottingham, UK, September*, 2004.

[16] P. Bollweg, A. Kaufmann, and W. Polifke. Derivation and application of a poly-celerid method for poly-dispersed two-phase flows. *6th International Conference on Multiphase Flow, Leipzig, Germany*, 2007.

[17] V. J. Boussinesq. Sur la resistance qu'oppose un liquide indéfini en repos. *Comptes Rendus Mécanique*, 100:935–937, 1885.

[18] J. N. E. Carneiro, V. Kaufmann, and W. Polifke. Implementation of a moments model in openfoam for polydispersed multiphase flows. *Open Source CFD International Conference 2008, Berlin, Germany*, 2008.

[19] J. N. E. Carneiro, V. Kaufmann, and W. Polifke. Eulerian simulations of polydisperse flows using a moments model with a relaxation approach for the moment transport velocities. *7th International Conference on Multiphase Flow, Tampa, USA*, 2010.

[20] G. F. Carrier. Shock waves in a dusty gas. *Journal of Fluid Mechanics*, 4:376–382, 1958.

[21] C. T. Crowe and E. E. Michaelides. Basic concepts and definitions. In C. T. Crowe, editor, *Multiphase Flow Handbook*. CRC Mechanical Engineering, 2006.

[22] C. T. Crowe, M .Sommerfeld, and Y. Tsuji. *Multiphase flows with droplets and particles*. CRC Press, NY, 1998.

[23] S. de Chaisemartin, L. Freret, D. Kah, F. Laurent, R. O. Fox, J. Reveillon, and M. Massot. Eulerian models for turbulent spray combustion with polydispersity and droplet crossing. *Comptes Rendus Mécanique*, 337:438–448, 2009.

[24] L. G. M. de Souza, G. Janiga, V. John, and D. Thévenin. Reconstruction of a distribution from a finite number of moments with an adaptive spline-based algorithm. *Chemical Engineering Science*, 65:2741–2750, 2010.

[25] P. Dems, J. N. E. Carneiro, and W. Polifke. Large eddy simulation of particle-laden swirling flow with a presumed function method of moments. *8th International Conference on CFD in Oil & Gas, Metallurgical and Process Industries, Trondheim, Norway*, 2011.

[26] O. Desjardins, R. O. Fox, and P. Villedieu. A quadrature-based moment method for dillute fluid-particle flows. *Journal of Computational Physics*, 227:2514–2539, 2008.

[27] S. E. Elghobashi. Particle-laden turbulent flows: direct simulation and closure models. *Journal Applied Scientific Research*, 48:301–314, 1991.

[28] S. E. Elghobashi. On predicting particle-laden turbulent flows. *Journal Applied Scientific Research*, 52:309–329, 1994.

[29] A. Ferrante and S. E. Elghobashi. On the physical mechanism of two-way coupling in particle-laden isotropic turbulence. *Physics of Fluids*, 15:315–329, 2003.

[30] J. Ferry and S. Balachandar. A fast Eulerian method for dispersed two-phase flow. *International Journal of Multiphase Flow*, 27:1199–1226, 2001.

[31] J. Ferry and S. Balachandar. Equilibrium expansion for the Eulerian velocity of small particles. *Powder Technology*, 125:131–139, 2002.

[32] J. Ferry and S. Balachandar. Equilibrium Eulerian approach for predicting the thermal field of a dispersion of small particles. *International Journal of Heat and Mass Transfer*, 48:681–689, 2005.

[33] R. O. Fox. Introduction and fundamentals of modeling approaches for polydisperse multiphase flows. In D. L. Marchisio and R. O. Fox, editors, *Multiphase Reacting Flows: Modelling and Simulation*. SpringerWienNewYork, 2007.

[34] R. O. Fox. Optimal moment sets for multivariate direct quadrature method of moments. *Industrial & Engineering Chemistry Research*, 48:9686–9696, 2009.

[35] M. Frontini and A. Tagliani. Maximum entropy in the finite Stieltjes and Hamburger moment problem. *Journal of Mathematical Physics*, 35(12):6748–6756, 1993.

[36] E. Gharaibah. *Entwicklung und Validierung eines Modells polydisperser Zweiphasenströmungen unter Berücksichtigung von Koaleszenz und Dispersion*. PhD thesis, Lehrstuhl für Thermodynamik, TU-München, Germany, 2008.

[37] E. Gharaibah and W. Polifke. A numerical model of dispersed two-phase flow in aerated stirred vessels based on presumed shape number density functions. In M. Sommerfeld, editor, *Bubbly Flows*, pages 295–306. Springer Verlag, 2003.

[38] A. D. Gosman and E. Ioannides. Aspects of computer simulation of liquid-fueled combustors. *AIAA Paper 81-0323*, 1981.

[39] B. H. Hjertager. Multi-fluid CFD analysis of chemical reactors. In D. L. Marchisio and R. O. Fox, editors, *Multiphase Reacting Flows: Modelling and Simulation*. SpringerWienNewYork, 2007.

[40] H. M. Hulburt and S. Katz. Some problems in particle technology. *Chemical Engineering Science*, 19:555–574, 1964.

[41] F. P. Incropera and D. P. DeWitt. *Fundamentals of Heat and Mass Transfer*. Wiley, 5th Edition, 2001.

[42] M. Ishii. *Thermo-Fluid Dynamic Theory of Two-Phase Flow*. Eyrolles, Paris, 1975.

[43] R. I. Issa and P. J. Oliveira. Numerical prediction of particle dispersion in a mixing layer using an eulerian two-phase flow model. *Proceedings of FEDSM98 ASME Fluids Engineering Division Summer Meeting, Washington, DC*, 1998.

[44] H. Jasak. *Error analysis and estimation for the finite volume method with applications to fluid flows*. PhD thesis, Imperial College of Science Technology and Medicine, London, UK, 1996.

[45] V. John, I. Angelov, A. A. Öncül, and D. Thévenin. Techniques for the reconstruction of a distribution from a finite number of moments. *Chemical Engineering Science*, 62:2890–2904, 2007.

[46] D. L. Wright Jr. Numerical advection of moments of the particle size distribution in eulerian models. *Journal of Aerosol Science*, 38:352–369, 2007.

[47] D. Kah, Q. H. Tran, S.Jay, F. Laurent, and M. Massot. A high order moment method with mesh movement for the description of a compressible polydisperse evaporating spray. *7th International Conference on Multiphase Flow, Tampa, USA*, 2010.

[48] E. Krepper, D. Lucas, T. Frank, H.-M. Prasser, and P. J. Zwart. The inhomogeneous MUSIG model for the simulation of polydispersed flows. *Nuclear Engineering Design*, 238:1690–1702, 2008.

[49] S. Lo. Application of the MUSIG model to bubbly flows. *AEAT-1096, AEA Technology, June*, 1996.

[50] E. Loth. Modeling. In C. T. Crowe, editor, *Multiphase Flow Handbook*. CRC Mechanical Engineering, 2006.

[51] K. L. Majumder and G. P. Bhattacharjee. The incomplete Beta integral. *Journal of the Royal Statistical Society. Series C (Applied Statistics)*, pages 409–411, 1973.

[52] M. Manninen, V. Taivassalo, and S. Kallio. On the mixture model for multiphase flow. Technical report, Technical Research Centre of Finland, Espoo, 1996.

[53] D. L. Marchisio and R. O. Fox. Solution of population balance equations using the direct quadrature method of moments. *Journal of Aerosol Science*, 36:43–73, 2005.

[54] D. L. Marchisio and R. O. Fox. *Multiphase Reacting Flows: Modelling and Simulation*. SpringerWienNewYork, 2007.

[55] M. Massot. Eulerian multi-fluid models for polydisperse evaporating sprays. In D. L. Marchisio and R. O. Fox, editors, *Multiphase Reacting Flows: Modelling and Simulation*. SpringerWienNewYork, 2007.

[56] M. Massot, F. Laurent, D. Kah, and S. de Chaisemartin. A robust moment method for evaluation of the disappearence rate of evaporating sprays. *SIAM Journal on Applied Mathematics*, 70:3203–3234, 2010.

[57] M. R. Maxey. The gravitational settling of aerosol particles in homogeneous turbulence and random flow fields. *Journal of Fluid Mechanics*, 174:441–465, 1987.

[58] R. McGraw. *Correcting moment sequences for errors associated with advective transport*, 2006. `http://www.ecd.bnl.gov/pubs/momentcorrection_mcgraw2006.pdf`.

[59] S. M. Monahan and R. O. Fox. Linear stability analysis of a two-fluid model for air-water bubble columns. *Chemical Engineering Science*, 62:3157–3177, 2007.

[60] S. M. Monahan, V. S. Vitankar, and R. O. Fox. CFD predictions for flow-regime transitions in bubble columns. *AIChe Journal*, 51:1897–1923, 2005.

[61] J.-B. Mossa. *Extension Polydisperse pour la Description Euler-Euler des Ecoulements Diphasiques Réactifs*. PhD thesis, Institut National Polytechnique de Toulouse, Toulouse, France, 2005.

[62] A. A. Mostafa and H. C. Mongia. On the modeling of turbulent evaporating sprays: Eulerian versus Lagrangian approaches. *International Journal of Heat and Mass Transfer*, 30:2583–2593, 1987.

[63] P. J. Oliveira. *Computer Modelling of Multidimensional multiphase Flow and Application to T-Junctions*. PhD thesis, Imperial College of Science Technology and Medicine, London, UK, 1992.

[64] C. W. Oseen. Über den Gültigkeitsbereich der Stokesschen Widerstandsformel. *Arkiv för Matematik Astronomi och Fysik*, 9, 1913.

[65] Y. Pan and S. Banerjee. Numerical investigation of the effects of large particles on wall turbulence. *Physics of Fluids*, 9:3786, 1997.

[66] M. Petitti, A. Nasuti, D. L. Marchisio, M. Vanni, G. Baldi, N. Mancini, and F. Podenzani. Bubble size distribution modeling in stirred gas–liquid reactors with qmom augmented by a new correction algorithm. *AIChe Journal*, 56:36–53, 2010.

[67] A. Prosperetti. Averaged equations for multiphase flow. In A. Prosperetti and G. Tryggvason, editors, *Computational Methods for Multiphase Flow*. Cambridge University Press, UK, 2007.

[68] W. E. Ranz and W. R. Marshall. Evaporation from drops. *Chemical Engineering Progress*, 48:141–146, 1952.

[69] E. Riber, V. Moureau, M. Garcia, T. Poinsot, and O. Simonin. Evaluation of numerical strategies for large eddy simulation of particulate two-phase recirculating flows. *Journal of Computational Physics*, 228:539–564, 2009.

[70] H. Rusche. *Computational Fluid Dynamics of Dispersed Two-Phase Flows at High Phase Fractions*. PhD thesis, Imperial College of Science Technology and Medicine, London, UK, 2002.

[71] L. Schiller and A. Naumann. Über die grundlegende Berechnung bei der Schwerkraftaufbereitung. *Zeitschrift Verein Deutscher Ingenieure*, 44:318–320, 1933.

[72] L. Schneider. *A concise moment method for unsteady polydisperse sprays*. PhD thesis, Technische Universität Darmstadt, 2009.

[73] A. Seifert and K. D. Beheng. A two-moment cloud microphysics parameterization for mixed-phase clouds: Part i: Model description. *Meteorology and Atmospheric Physics*, 92:45–66, 2006.

[74] J. A. Shohat and J. D. Tamarkin. *The Problem of Moments*. Providence, RI: American Mathematical Society, 1963.

[75] G. Shulte. *Zweidimensionale Verteilungen von Partikeleigenschaften: Anwendung auf Systeme ruhender und bewegter Partikeln*. Shaker Verlag, Aachen, 1995.

[76] M. Sommerfeld, B. van Wachem, and R. Oliemans. *Best Practice Guidelines. Special Interest Group on Dispersed Turbulent Multi-Phase Flow*. ERCOFTAC, 2007.

[77] G. G. Stokes. On the theories of internal friction of the fluids in motion. *Transactions of the Cambridge Philosophical Society*, 8:287–319, 1845.

[78] A. Tagliani. On the application of the maximum entropy to the moments problem. *Journal of Mathematical Physics*, 34(1):326–337, 1993.

[79] J. R. Travis, F. H. Harlow, and A. A. Amsdem. Numerical calculations of two-phase flows. *Nuclear Science and Engineering*, 61:1–10, 1975.

[80] M. Uhlmann. Interface-resolved direct numerical simulation of vertical particulate channel flow in the turbulent regime. *Physics of Fluids*, 20:053305, 2008.

[81] V. Vikas, Z. J. Wang, A. Passalacqua, and R. O. Fox. Realizable high-order finite volume schemes for quadrature-based moment methods. *Journal of Computational Physics*, 230:5328–5352, 2011.

[82] U. Wacker and A. Seifert. Evolution of rain water profiles resulting from pure sedimentation: spectral vs. parameterized description. *Atmospheric Research*, 58:19–39, 2001.

[83] A. P. Watkins. The application of Gamma and Beta number size distributions to the modelling of sprays. *Proceedings of the 20th ILASS-Europe, Orléans, France, September*, 2005.

[84] A. P. Watkins. Modelling the mean temperatures used for calculating heat and mass transfer in sprays. *International Journal of Heat and and Fluid Flow*, 28:388–406, 2007.

[85] H. G. Weller. A code independent notation for finite volume algorithms. Technical report, TR/HGW/01, OpenCFD, 2005.

[86] H. G. Weller, G. Tabor, H. Jasak, and C. Fureby. A tensorial approach to computational continuum mechanics using object-oriented techniques. *Computers in Physics*, 12(6):620–631, 1998.

[87] W. H. White. Particle size distributions that cannot be distinguished by their integral moments. *Journal of Colloid and Interface Science*, 135(1):297–299, 1990.

[88] F. A. Williams. Spray combustion and atomization. *Physics of Fluids*, 1:541–545, 1958.

[89] Y. Yamamoto, M. Potthoff, T. Tanaka, T. Kajishima, and Y. Tsuji. Large eddy simulation of turbulent gas-particle flow in a vertical channel: effect of considering interparticle collisions. *Journal of Fluid Mechanics*, 442:303–334, 2001.

[90] S. Yuu, N. Yasukouchi, Y. Hirosawa, and T. Jotaki. Particle diffusion in a dust laden round jet. *AIChe Journal*, 24:5, 1978.

A Appendix

A.1 Stieltjes formulation and Beta function

The Stieltjes formulation (see section 4.6.3) applies to $D \in [0,\infty)$. However, the Beta function might assume negative values if D is outside the interval $[0, D_{max}]$. To avoid this situation occuring, one can redefine $f(D)$ by splitting the intervals in $D \in [0, D_{max}]$ and outside.

Consider $f|_{[0,D_{max}]}(D)$ the part of $f(D)$ defined in $[0, D_{max}]$.

In order to guarantee that $f(D)$ is non-negative throughout the entire real axis, it is necessary that

$$f(D) \begin{cases} f|_{[0,D_{max}]}(D) \geq 0, & D \in [0, D_{max}] \\ 0, & \text{elsewhere.} \end{cases}$$

A schematic representation is found in Fig. A.1.

The moments of $f(D)$ are simply given by:

$$M^{(k)} = \int_0^{D_{max}} f|_{[0,D_{max}]}(D) D^k dD + \underbrace{\int_{D_{max}}^{\infty} (...) dD}_{\equiv 0}. \tag{A.1}$$

Therefore, the use of Hankel-Hadamard determinants in the sense of Stieltjes will also be considered valid for the realizability of the Beta distribution used here.

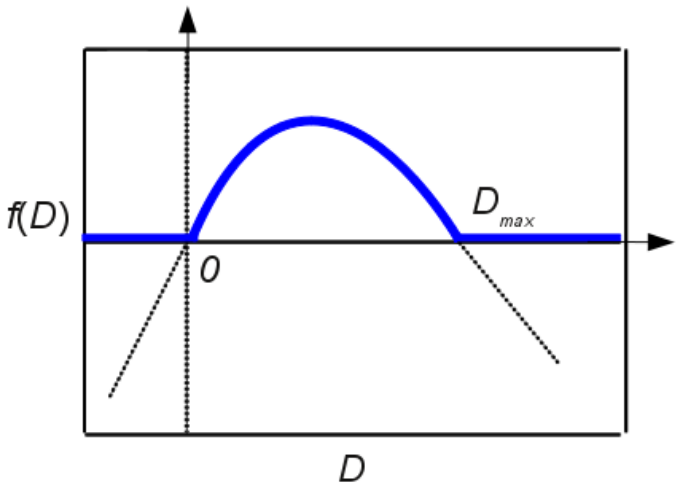

Figure A.1: Schematic representation of $f|_{[0,D_{max}]}(D)$.

A.2 Closure for $\mathbf{u}'\mathbf{u}'$

The expression for the first order expansion of the particle velocity in τ allows the development of a closure for the velocity deviation tensor $\mathbf{u}'\mathbf{u}'$. If $\mathbf{u}' = \mathbf{u}|_\tau - \mathbf{u}^{(k)}$ one can write, with help of Eq. (4.74):

$$\nabla \cdot \left(\int_0^\infty f\mathbf{u}'\mathbf{u}' D^k dD\right) = \nabla \cdot \left[\frac{\mathbf{u}_{0r}\mathbf{u}_{0r}}{\tau_0^2}\int_0^\infty (\tau')^2 f D^k dD\right], \tag{A.2}$$

with τ' the deviation of the particle relaxation time from the average relaxation time, given by

$$\tau' = \tau - \tau^{(k)}, \tag{A.3}$$

and $\mathbf{u}_{0r} = \mathbf{u}_0 - \mathbf{u}_c$. The divergence of the velocity deviation tensor can be neglected if $(\tau')^2$ is sufficiently small, which occurs, for example, in distributions where the size spectrum contains mostly very small particles and does not extend through a wide range. The term obviously tends to zero in the monodisperse case, where all particles have equal response times. The framework introduced here allows us to develop a model to account for the contribution of the velocity deviation, which can be done by substituting back the expression for τ' in Eq. (A.2), giving rise to:

$$\nabla \cdot \left(\int_0^\infty f\mathbf{u}'\mathbf{u}' D^k dD\right) = \nabla \cdot \left[\mathbf{u}_{0r}\mathbf{u}_{0r}\left(\frac{\tau^{(k)}}{\tau_0}\right)^2 M^{(k)}\right] + \nabla \cdot \left[\mathbf{u}_{0r}\mathbf{u}_{0r}\left(\frac{\tau^{(k+2)}}{\tau_0^2}\right) M^{(k+2)}\right]. \tag{A.4}$$

Both terms on the RHS of the above equation need closure, which can be done by means of presumed distribution functions as presented in this work.

A.3 Analytical solution for the 1D particle relaxation case

The steady-state one-dimensional momentum equation – considering the flux $f\,\mathrm{u}_x$ in the axial direction – with no gravity can be written as:

$$\frac{\mathrm{d}(f\mathrm{u}_x^2)}{\mathrm{d}x} = \frac{f}{\tau}(\mathrm{u}_{c,x} - \mathrm{u}_x) \tag{A.5}$$

and

$$\frac{\mathrm{d}(f\mathrm{u}_x)}{\mathrm{d}x} = 0, \tag{A.6}$$

respectively.

For a constant gas velocity, Eq. (A.5) can be analytically integrated from $x = 0$ to x and $\mathrm{u}_x(x=0) = \mathrm{u}_{I,x}$ to $\mathrm{u}_x(x)$ to give:

$$\mathrm{u}_x(x) + \mathrm{u}_{c,x}\ln\Big[\frac{\mathrm{u}_x(x) - \mathrm{u}_{c,x}}{\mathrm{u}_{I,x} - \mathrm{u}_{c,x}}\Big] = \mathrm{u}_{I,x} - \frac{x}{\tau}. \tag{A.7}$$

Solution of the above transcendental equation in $\mathrm{u}_x(x)$ together with Eq. (A.6) results in:

$$\frac{f(x)}{f_I} = \frac{1}{1 + \mathbf{W}(\Phi)}, \tag{A.8}$$

with

$$\Phi = \frac{\mathrm{u}_{c,x}}{\mathrm{u}_{I,x} - \mathrm{u}_{c,x}}\,\mathbf{exp}\Big(\frac{\mathrm{u}_{c,x}}{\mathrm{u}_{I,x} - \mathrm{u}_{c,x}} - \frac{x}{\mathrm{u}_{c,x}\tau}\Big). \tag{A.9}$$

The Lambert-function $\mathbf{W}(\Phi)$ is the inverse function of

$$F(\Phi) = \Phi\,\mathbf{exp}(\Phi). \tag{A.10}$$

A.4 Particle Trajectory Crossing (PTC)

An intrinsic assumption of classic Two-Fluid formulations consists in considering a single velocity field for the dispersed phase. This, in a moments model context, translates to the restriction that particles of the same size have locally the same velocity.

Here, a "Multi-Moments" approach is evaluated, in order to capture macroscopic particle-crossing trajectories in two-dimensional flows, maintaining the type of closure models presented in this work. It consists of solving multiple sets of equations for the moments of the size distributions and its transport velocities. By doing so, it is possible to represent multi-modal velocity distributions which are primary condition to represent crossing particle jets. It remains to be investigated how to account for interactions between the underlying distributions, such as when collisions or break-up take place.

Assuming that only Stokes drag is the relevant force acting on the particles and unknown moments and average velocities are determined through the presumed function closure described before, the governing equations for the disperse phase are:

$$\frac{\partial M_i^{(k)}}{\partial t} + \nabla \cdot (\mathbf{u}_i^{(k)} M_i^{(k)}) = 0, \tag{A.11}$$

$$\frac{\partial M_i^{(k)} \mathbf{u}_i^{(k)}}{\partial t} + \nabla \cdot (\mathbf{u}_i^{(k)} \mathbf{u}_i^{(k)} M_i^{(k)}) = \frac{18\mu_c}{\rho_d} M_i^{(k-2)} (\mathbf{u}_c - \mathbf{u}_i^{(k-2)}). \tag{A.12}$$

The distribution function is assumed to be e.g. a sum of multiple Gamma distributions:

$$f(D) = \sum_i C_{0_i} \frac{D^{\beta_i - 1} e^{-\frac{D}{\alpha_i}}}{\alpha_i^{\beta_i} \Gamma(\beta_i)}, \tag{A.13}$$

and the "total" moments are simply given by the sum of the individual mo-

ments:

$$M^{(k)} = \sum_i M_i^{(k)}. \tag{A.14}$$

The test case consists of a 0.1m x 0.1m squared domain and water droplets (jets) are introduced centered at the bottom and right-hand sides of the domain with velocities of equal magnitude (1 m/s). For the sake of simplicity, a very large Stokes number is chosen (so that the drag force vanishes). Additionally, no collisional interaction is taken into account. First, results obtained with a classical Two-Fluid Moments Model approach are shown in Fig. (A.2). The jets "collide" at the center of the domain and move off diagonally in one stream towards the upper left-hand corner of the domain. This is clearly unphysical, since no collisional interaction is explicitly taken into account in the model. This artifact demonstrates the inability of classical Two-Fluid approaches to cope with such situations.

For the same conditions of the previous example, a Multi-Moments approach was also used and results are shown in Fig. (A.3). At early times, the jets advance towards the center point, until they begin to overlap and the local third moment doubles. Distinct from the classical model, however, for subsequent times, the jets continue along their original trajectories and finally exit the flow domain at the top and left-hand sides, respectively.

The model is now applied to a situation where three distinct jets co-exist inside the domain, thus three sets of moments equations are needed. Two different distribution functions are considered, so that a pair of equal distributions, and a pair of different ones, cross perpendicularly. The idea behind this configuration is to demonstrate the ability to represent different types of distributions simultaneously (including distributions containing multiple peaks).

As highlighted in Fig. (A.4), the three jets cross at two positions inside the domain, namely "a" (distribution 1 + distribution 1) and "b" (distribution 1 + distribution 2). The reconstructed size distributions at these positions, as well as at both inlets, are shown in Fig. (A.5). At position "a" (bottom left), the resulting distribution has the same shape as distribution 1 (in fact, it is exactly the

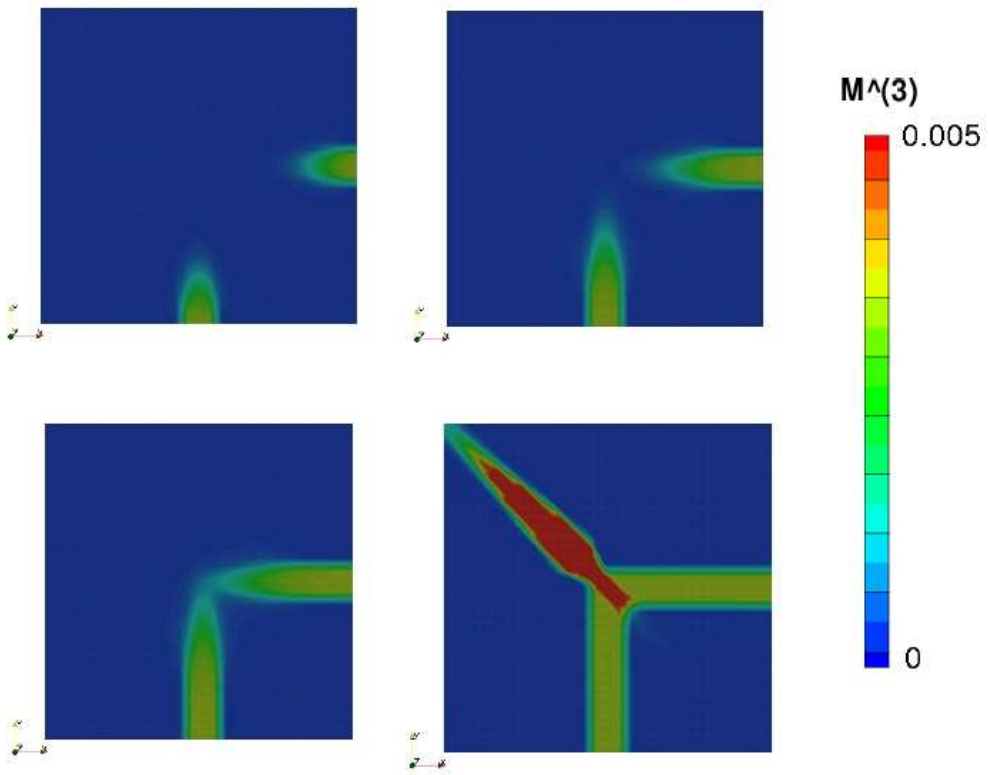

Figure A.2: Crossing Jets with a classical Moments approach – contours of the third moment, $M^{(3)}$.

distribution 1 scaled by a factor of 2), but at "b", the distribution presents a double-peak shape resulting from the addition of the two underlying distributions 1 and 2. It is clear that it can be easily extended to include more jets (and more distributions), even distribution functions having different shapes (for example, Beta, Log-normal, etc).

The previous test can also be extended to consider three jets crossing at the same point. In order to do so, the three inlets are located at the bottom plane of the square, with the central jet being directed upwards and the two side jets having opposite inclinations, as shown in Fig. (A.6). Once again, the model succeeds in capturing the crossing trajectories effect, with the overlapping and subsequent separation of the three distribution functions. The high numerical diffusion observed for the inclined jets is caused by the upwind schemes used here, and will be subject of future improvement. The multi-

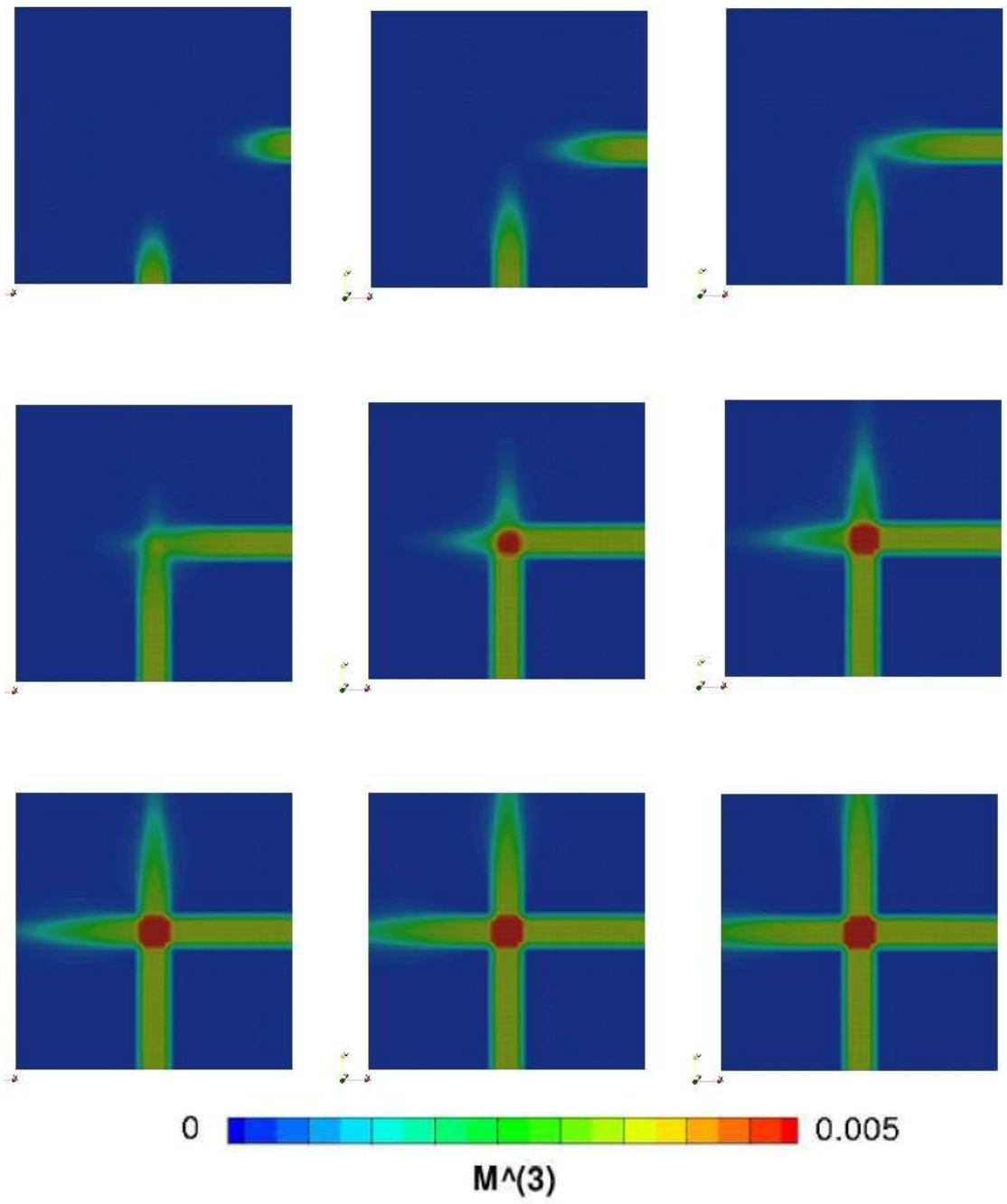

Figure A.3: Crossing jets with a Multi-Moments approach – contours of the third moment, $M^{(3)}$.

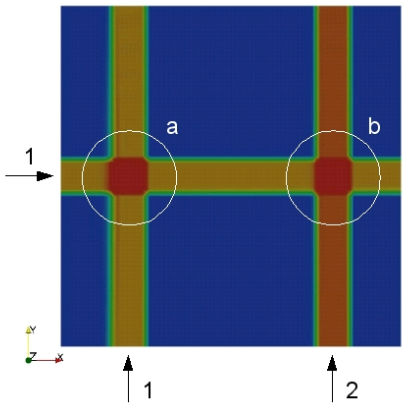

Figure A.4: Configuration with three jets using the Multi-Moments approach – contours of the third moment, $M^{(3)}$.

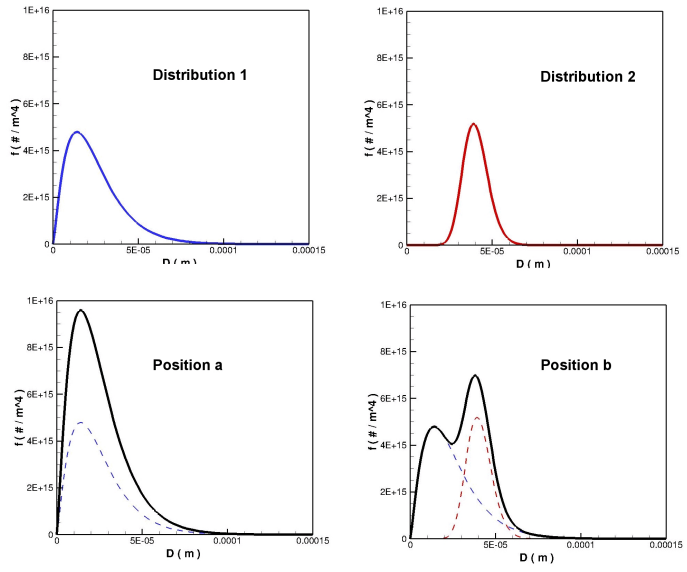

Figure A.5: Inlet distributions and reconstructed distributions at positions a and b.

peak reconstructed distribution at the intersection point of the three jets is shown in Fig. (A.7).

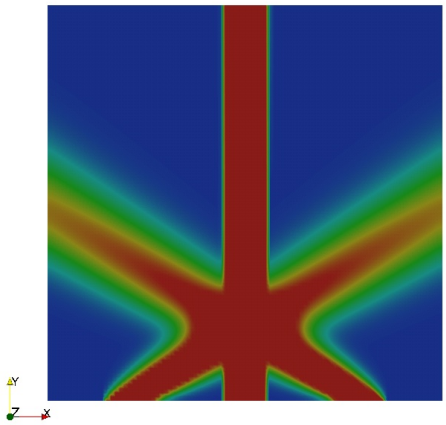

Figure A.6: Configuration with three crossing jets using the Multi-Moments approach – contours of the third moment, $M^{(3)}$.

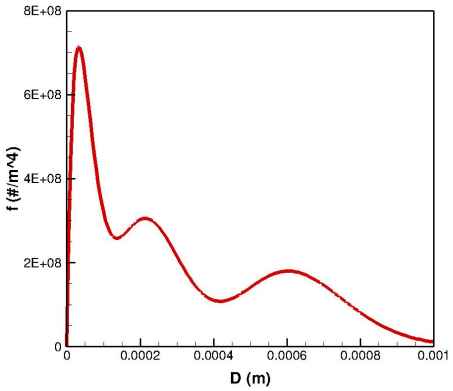

Figure A.7: Reconstructed distribution at the intersection point of the three jets.